UNIVERSITAT DE BARCELONA

Development and Characterization of Bioprintable Physiomimetic Scaffolds for Tissue Engineering

Héctor Sanz Fraile

UNIVERSITAT DE BARCELONA

Development and Characterization of Bioprintable Physiomimetic Scaffolds for Tissue Engineering

by

Héctor Sanz Fraile

Memòria de tesi doctoral presentada per Héctor Sanz Fraile per optar al grau de Doctor per la Universitat de Barcelona

Programa de Doctorat Biomedicina

Línia d'Enginyeria Biomèdica

Dirigida per Prof. Ramon Farré i Dr. Jorge Otero (Universitat de Barcelona)

Unitat de Biofísica i Bioenginyeria

Facultat de Medicina i Ciències de la Salut

Universitat de Barcelona

Barcelona, Gener 2023

Ramon Farré

Jorge Otero

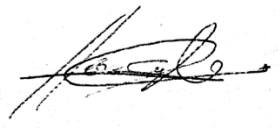

Héctor Sanz

A mi madre

A mi padre

A mi *doctor*

A mi *cachito*

A todos los que me habéis empujado hasta aquí

Agradecimientos

OTRA ETAPA que finaliza. Otra etapa que comienza. Es difícil no mirar atrás y preguntarse cómo es posible. Cómo aquel chaval que suspendía hasta el recreo está escribiendo hoy esto. Supongo que algo falló. Quizás no era el momento. Quizás no era el lugar. Sea como fuere, todo formó parte del camino. Un camino que continúa. Un camino que he recorrido con tanta y tanta gente que, aun con el miedo de dejarme a alguien en algún rincón de mi memoria, no puedo evitar agradecérselo uno por uno.

Primeramente, me gustaría agradecer a mis dos directores de tesis, el Prof. Ramon Farré y el Dr. Jordi Otero, por su guía continua a través de estos años en los que he desarrollado mi tesis doctoral en la unidad de biofísica y bioingeniería de la Universitat de Barcelona. Vuestra continua disponibilidad ante cualquier duda, vuestra disposición infinita a ayudar y vuestro compañerismo es algo que siempre me guiará en mis futuros pasos. Sin duda, vuestro aporte a mi formación no termina aquí; más bien no ha hecho más que empezar.

También quería agradecer en especial al Prof. Daniel Navajas. Aunque tu reciente jubilación hizo que no pudiésemos compartir tantas discusiones como me habría gustado tener con alguien con tu sabiduría, he podido disfrutar de algunas de ellas en nuestros fantásticos *lab meetings*. Sin duda, aquel mail que me respondiste un 30 de octubre 2017 citándome a una reunión en la unidad dio lugar a esto. Sin ti tampoco habría sido posible.

De la misma forma, me gustaría agradecer al resto de profesores de la unidad, Isaac, Jordi Alcaraz, Roser, Domènec, Nùria y Raimon, los cuales siempre han estado dispuestos a ayudar en todo lo necesario.

No puedo olvidarme de todos los compañeros que han compartido estos años de laboratorio. A algunos de vosotros puedo consideraros amigos, sin duda. Empezando por Jordi, que además de director se ha convertido en amigo; como tú siempre dices:

“te puedo enseñar a convertirte en científico”. Y vaya si lo has hecho. Bryan, mi codirector de TFM favorito. No me extraña nada todo lo que estás consiguiendo en la ciencia. Realmente creo que has nacido para esto. Y sabes que espero que algún día volvamos a trabajar codo con codo en un lab… o en una bachata. Ignasi…. La de horas que habremos echado en el AFM charlando de ciencia y no ciencia. Saber con certeza que tú y yo sí que coincidiremos nuevamente en un laboratorio es una de las mejores noticias que la ciencia me ha dado. Esther, sin duda tú has sido una alegría en el lab; otra excelente científica y compañera de bachata. Llegarás a donde quieras. Pero eso ya lo sabes. Álvaro, el madrileño guapo del laboratorio. Contigo las risas estaban aseguradas. Anna, mi compi de cafés favorita y la alegría de la tercera planta. Otra gran científica que llegará donde quiera. Eli, tú sí que has llegado donde has querido y cuando has querido. Ojalá tener la mitad de la determinación que tienes tú. Eres una crack. Rafa, espero que no te hayas puesto celoso por llamar guapo a Álvaro. Se te echa mucho de menos en el laboratorio. Jair, qué genial sería que volvieras. Marta y Paula… mis acompañantes de ópera favoritas. Marta, es una alegría seguir compartiendo laboratorio contigo. Paula…. Tú eres la definición de alegría. Cada vez que pienso en alguien riendo en el lab, sólo me puede venir a la cabeza tu risa. Se te echará muchísimo de menos. Nanthilde, ahora que sé que entiendes esto, quiero que sepas que eres otra gran científica, y que los experimentos contigo han sido geniales. Constança, amiguita, qué pena que la pandemia paró esas noches de juegos de mesa con tu familia portuguesa. Miguel Ángel, el mejor técnico que un laboratorio podría tener. Cuando necesites a alguien que te apague la impresora 3D por la tarde, ya sabes que soy experto en ello. Siento que este párrafo se esté alargando demasiado, pero no lo cerraré sin agradeceros a todas las demás personas con quien he compartido laboratorio estos años, en mayor o menor medida: Edolie, Cristina, Reihana, Ignacio, Irene, Susana, Lluis, Alejandro, Alejandro, Alejandro (os toca a vosotros adivinar cuál es cada uno), María Leonor, Àfrica, Marina, Carol, Alicia, Patri, Nata, Kate, Elba, Agnès, Fer, Rodrigo, Mariona, Carmen, Sheila, Llorenç y Andressa. Juro que creo que no me olvide a nadie. Y si lo he hecho y estás leyendo esto… te lo agradezco a ti también.

Otra de las ventajas que tiene hacer un doctorado en un laboratorio tan reconocido es la posibilidad de colaborar con otros laboratorios. En particular, quiero

nombrar a tres personas que ha sido una bendición encontrarme con ellas en el camino. Tres científicas y tres profesionales maravillosas:

Ceci. Mi primera colaboración oficial en el laboratorio y la que más quebraderos de cabeza me dio con el maldito chip. En serio, en un placer trabajar contigo. Y charlar. Y tomar algo. Eres una compañía fantástica. Creo que estamos en el mismo camino de la ciencia, así que estoy seguro de que nos encontraremos muchas más veces. Gracias por tus didácticas charlas sobre biología.

Ana. Los cerebros nunca fueron tan divertidos como cuando los medíamos juntos. La persona que más rápidamente ha aprendido a hacer reología. Y estoy seguro de que el día que quieras, dominarás el AFM. Gracias por los desayunos, y seguro que nos volveremos a encontrar.

Nona. Llegaste a la mitad de mi tesis para tomar el relevo a Victoria y a nuestras medidas de mocos y la verdad, ojalá tu llegada no hubiese significado la marcha de Victoria, pero sin duda ha sido una suerte que tú fueses quien entrase a ese puesto.

Victoria. El último párrafo tenía que ser para ti. Contigo descubrí el maravilloso mundo de los mocos (aspirados bronquiales. Perdón). Aun después de tu marcha hemos seguido trabajando juntos. Eres una profesional enorme. Trabajar contigo es muy fácil. Te lo he dicho muchas veces: el día que tengas tu propio grupo tienes que contratarme. O si no te contrataré yo a ti.

No quiero terminar la parte de agradecimientos académicos sin nombrar a Pepe. Mi profesor de física de bachillerato y la persona que despertó en mí por primera vez el gusanillo de la enseñanza. Ojalá algún día ser la mitad de buen profesor que has sido tú. De mi etapa universitaria en Madrid tengo que hacer una especial mención a Alberto. Fuiste mi primer contacto con la ciencia. La persona que me dio la primera oportunidad para entrar en un laboratorio. Quien vio en mí algo lo suficientemente bueno como para invitarme a colaborar aquel verano de 2013. Contigo empezó todo. Gracias.

Llega el momento de agradecer a mis amigos por todos los buenos momentos que me han hecho pasar durante estos años, aun estando lejos. María, gracias por estar siempre ahí. Por venir a verme cada vez que has podido. Por estar cada día al otro lado. Rober, eres la definición de amigo. Alguien que es capaz de recorrerse 600 km sólo

porque tienes un mal día y necesitas escapar. Kike, desde los 3 años juntos y siempre has estado ahí. Desde la distancia siempre te he podido notar cerca. Serguey, qué pena que estemos tan lejos. Eres de esos amigos que, aunque estés un tiempo sin hablar, sabes que están ahí para cuando lo necesites. Silvia, otro de mis grandes apoyos en la distancia. Alguien que, aunque no me coja el teléfono, sé que siempre me devuelve la llamada. Y no te enfades por aparecer al final, que sabes que los últimos serán los primeros. Os quiero.

Agradecérselo también a mi familia, que siempre me ha apoyado en cada paso que he dado para llegar hasta aquí. A mi madre, quien siempre confió en mi capacidad, incluso cuando ni yo mismo lo hacía. Eres un ejemplo. Mi ejemplo. Ojalá alguien esté algún día tan orgulloso de mí como yo lo estoy de ti. A mi padre, por enseñarme a ser un gran profesional haga lo que haga; sea pasar un punto de luz o montar una bioimpresora. A Dori, por ayudarme en todo lo que he pedido y por tratarme siempre como uno más. Es una suerte saber que estás siempre ahí. A mi tía Dioni; mi cachito. Siempre has sido una madre para mí. No hay recuerdo de mi vida en el que no aparezcas. No existe persona más buena que tú en este mundo. Tú me has enseñado los valores para ser una buena persona. Y a mi tío Amador; mi doctor. Mi mejor amigo. Me cuesta plasmar con palabras lo que estoy sintiendo mientras te escribo esto. Es duro llevarte en mi piel y no poderte abrazar. Estés donde estés, te echo mucho de menos.

Y por último agradecerte a ti, Virginia, por todo el apoyo que me has dado en esta última etapa del doctorado. Por apoyarme en los días malos y en los buenos. Eres la mejor compañera que jamás habría imaginado. Eres un regalo. Gracias.

Y es hora de ir cerrando estos agradecimientos, que acabarán ocupando más que la propia tesis a este paso. Pero es que sería injusto dejarme a alguien. Porque todos y cada uno de los que aquí salen me han ayudado, de una manera u otra, a conseguir esto. De corazón, GRACIAS

INDEX

List of figures

Abbreviations and acronyms

$<\Delta d^2>$	Average of the square fluctuations
3D	Three-dimensional
A_0	Cross-sectional area
AFM	Atomic force microscopy
AM	Additive manufacturing
B3	Bioactive borate glass
BM-MSCs	Bone marrow mesenchymal stromal cells
cCM	Chicken embryonic cardiomyocytes
cECM	Cardiac extracellular matrix
COL I	Type I collagen
Cx43	Connexin 43
d	Deflection
d_0	Offset
DLP	Digital light processing
DNA	Deoxyribonucleic acid
E	Elastic modulus / Young's modulus
ECM	Extracellular matrix
EEP	Energy equipartition method
G	Shear modulus
G'	Storage modulus
G''	Loss modulus
G*	Sinusoidal stress
GAGs	Glycosaminoglycans
GelMA	Gelatin methacrylate
GG-PEGDA	Gelan gum-poly diacrylate
Gly	Glycine
hBM-MSCs	Human bone marrow mesenchymal stromal cells
HCAECs	Human coronary artery endothelial cells
hCPC	Human cardiac progenitor cells
iPC	Intrapericardial region
iPS-CPCs	Induced pluripotent stem cell-derived cardiac progenitors
k	Spring's elasticity constant
k_B	Boltzman constant
L	Length
L_0	Initial length
LIFT	Laser-induced forward transfer
m	Mass
MSC	Mesenchymal stem cells
n	Fluid flow behavior index
PBS	Phosphate buffered saline
PCL	Polycaprolactone
PLA	Polylactic acid
PVA	Polyvinyl alcohol
R	Radius

RASMCs	Rat aortic smooth muscle cells
Rz	Mean roughness depth
Sa / Ra	Areal arithmetic mean
SDC	Sodium deoxycholate
SDS	Sodium duodecil sulfate
SEM	Scanning electron microscopy
SiO_2	Silicon dioxide
Sku / Rku	Kurtosis
SLA	Stereolithography
Ssk / Rsk	Skewness
T	Temperature
UV	Ultraviolet light
V	Voltage
VEGF	Vascular endothelial growth factor
YSZ	Yttria-stabilized zirconia
z	Displacement of the cantilever with the piezo actuator
z_c	Vertical displacement when the tip contacts the sample
α chains	Polypeptide chains
α-SMA	α-Smooth muscle actin
γ	Strain
δ	Indentation
ε	Deformation
η	Viscosity
η'	Dynamic viscosity
η''	Storage viscosity
η*	Complex viscosity
Θ	Mean angle of the pyramid
ρ	Density
σ	Applied stress
τ	Shear stress
ω	Angular velocity
υ	Poisson's ratio

Thesis in compendium of publications format. The thesis consists of one general objective and three specific objectives, containing two already published articles and two articles currently *in manuscript* status:

Published articles:

- ***Hector Sanz-Fraile**, Susana Amoros, Irene Mendizabal, Carolina Galvez-Monton, Cristina Prat-Vidal, Antoni Bayes-Genis, Daniel Navajas, Ramon Farre, and Jorge Otero. Silk-Reinforced Collagen Hydrogels with Raised Multiscale Stiffness for Mesenchymal Cells 3D Culture. Tissue Eng Part A. 2020 Mar;26(5-6):358-370. doi:10.1089/ten.TEA.2019.0199. IF: 3.845. Q2 (35/89)*
- *Irene Buj-Corral, **Héctor Sanz-Fraile**, Anna Ulldemolins, Aitor Tejo-Otero, Alejandro Domínguez-Fernández, Isaac Almendros, Jorge Otero. Characterization of 3D Printed Metal-PLA Composite Scaffolds for Biomedical Applications. Polymers (Basel). 2022 Jul 5;14(13):2754. doi: 10.3390/polym14132754.*
  IF: 4.967. Q1 (16/90)

In manuscript format:

- **Héctor Sanz-Fraile,** Carolina Herranz-Diez, Anna Ulldemolins, Bryan Falcones, Isaac Almendros, Núria Gavara, Raimon Sunyer, Ramon Farré and Jorge Otero. *Characterization of Bioinks Developed from the Gelification of the Extracelullar Matrix obtained from Decellularized Porcine Myocardia.*
- *Buj-Corral, Irene; **Sanz-Fraile, Hector**; Tejo Otero, Aitor; Xuriguera, Elena; Otero, Jorge. Biocompatible 3D Yttria-Stabilized Zirconia Parts using Direct Ink Writing.*

Thesis summary

Development and Characterization of Bioprintable physiomimetic Scaffolds for Tissue Engineering.

TISSUE ENGINEERING is a field of study in which engineers use technology to mimic the structure of human tissue as closely as possible. The development of 3D tissue culture is a major area of research because cells behave differently in 3D microenvironments compared to 2D microenvironments.

Natural and synthetic polymers can be processed to be 3D printable and form hydrogels. Tissue decellularization is a commonly used method to isolate extracellular matrix (ECM). To create functional 3D tissues, cells need to be embedded in the ECM. The mechanics of the ECM can modulate physiological processes, so characterization of biomaterials for tissue-engineered scaffolds must be done at both macroscopic and microscopic scales.

Bioprinting using additive manufacturing (3D printing) is a widely used method in biomedical research to create, replace, or regenerate damaged tissues. Different biomaterials or cell-laden solutions can be deposited layer by layer with precision using 3D bioprinting, which has opened the door to personalized medicine. Biocompatible synthetic materials are also available and have tunable properties, making them good candidates for use in 3D printing.

In this thesis, we hypothesize that we can develop a hydrogel that mimics the mechanical properties of cardiac tissue using collagen type I (COL I) as the main component. Furthermore, this thesis hypothesizes that 3D printed synthetic composites are suitable for direct culture of stem cells on them, showing cell viability and osteocalcin markers after several days of culture. Therefore, the main objective of this work is to develop and characterize the mechanical properties of biomaterials for 3D bioprinting. To this end, a protocol for decellularization of porcine myocardium was

developed for the development of ECM-derived hydrogels. In addition, a protocol for the addition of silkworm silk dissolved in COL I hydrogels was developed to modify the stiffness and printability of the scaffolds and to characterize the multi-scale mechanical properties. Finally, printable synthetic composites suitable for direct cell culture on their surfaces have been developed.

The macromechanics of a material is determined by the mechanical properties of its components and the ratio of these elements. To perform the multi-scale characterization, well-known techniques were used: To characterize the micromechanics, an atomic force microscope (AFM) was used to measure forces in the nanonewton range, getting the elastic modulus (E) of the material. To quantify E at the macroscopic level, tensile test method was used, which stretches a sample by a certain percentage and measures the force required to deform the sample. For the viscoelastic properties of the hydrogels, the rheology technique was used to quantify storage modulus (G') and viscosity (η). Finally, scanning electron microscopy (SEM) was used to image the ultrastructure of the materials and quantify the diameter of the fibers. To study cell viability, cells embedded in the hydrogels or on the developed structures were stained with different antibodies and visualized with a confocal microscope.

The main findings of the four articles presented in this dissertation are as follows:

Sericin-preserved silk improves the mechanical properties of collagen scaffolds for tissue engineering.

A silk-reinforced collagen hydrogel was developed to create an ECM-derived material with mechanical properties similar to native myocardium. Cells were cultured within the bioink, which showed increased viability compared to the pure collagen hydrogel. Microscale elastic moduli were higher in the silk-reinforced hydrogels, with maximum values at 50% (E_m = 1.26 kPa) and 100% (E_m = 1.31 kPa) silk content. Macroscale mechanical properties were also improved with silk reinforcement, with maximum values at 75% silk content (E = 31 kPa). The rheological properties of the hydrogel were improved, including increased storage modulus regarding to COL I hydrogels and no change in viscosity at 4 ˚C, making it easier to print. Overall, silk reinforcement improved the mechanical and rheological properties of the hydrogel.

Cardiac ECM-derived hydrogels can be optimized for developing 3D bioscaffolds.

A cECM bioink for 3D cell culture in cardiac tissue engineering was developed from decellularized porcine myocardium. The structure, viability, and behavior of the hydrogel with hBM-MSCs were investigated by imaging, staining, and a contraction assay. The hydrogel exhibited a fibrillar network and was mechanically stable with gelation from 16 h (G' = 5 Pa) to 24 h (G' = 24 Pa) pepsin digestion time. The cell-laden hydrogel was characterized by rheological analysis and showed softening than acellular hydrogels after 7 days of cell culture. The crosstalk between cECM and hBM-MSCs was evaluated, and the cells showed a spindle shape, well-formed cytoskeleton, and positive expression of Cx43 and α-SMA.

Yttria-Stabilized Zirconia (YSZ) scaffolds can be 3D printed by using direct ink writing.

The viability of hBM-MSCs on 3D printed YSZ with different surface roughness was investigated due to limited in vitro studies with this biocompatible ceramic material. Surface roughness was compared for two 3D printed samples with 80% and 95% infill. No differences were found between the two infills. The samples were coated with collagen for cell adhesion testing, and cells were found to adhere to both coated and uncoated surfaces, so it seems to be a suitable biomaterial for cell culture.

3D Printed Metal-PLA composite scaffolds induce osteogenic differentiation of Mesenchymal Stromal Cells.

3D printing was used to fabricate three PLA/metal composites in a study that analyzed porosity, roughness, and biocompatibility. Steel was found to be cytocompatible, while copper and bronze were not. The roughness of the samples was measured, and collagen coating was performed to analyze cytocompatibility. hBM-MSCs were cultured on steel/PLA scaffolds and showed the presence of osteocalcin after 21 days, indicating successful osteogenic differentiation. The results suggest that steel-filled scaffolds are suitable for biomedical applications.

In conclusion, bioinks for 3D cell culture have been developed and characterized for use in tissue-engineered scaffolds. They have been evaluated for macro- and micromechanical properties and rheological behavior. Natural composite biomaterials have also been developed, showing improved mechanical and rheological properties

when combined with collagen. Synthetic composites have been evaluated for biocompatibility and found to be suitable for 3D bioprinting, offering potential for use in future medical prosthetics.

Resumen (ES)

Development and Characterization of Bioprintable physiomimetic Scaffolds for Tissue Engineering.

LA INGENIERÍA de tejidos es un campo de estudio que, entre otras cosas, busca utilizar la tecnología para imitar la estructura del tejido humano. El desarrollo del cultivo celular en 3D es uno de los principales campos de investigación, ya que las células se comportan de forma diferente en microambientes 3D que en microambientes 2D.

La descelularización de tejidos es un método muy utilizado para aislar la matriz extracelular (ECM). Para crear tejidos tridimensionales funcionales es necesario embeber las células en la ECM. La mecánica de la ECM puede modular los procesos fisiológicos, por lo que la caracterización de los biomateriales para estructuras de ingeniería tisular debe hacerse tanto a escala macroscópica como microscópica.

La bioimpresión es un método muy utilizado en la investigación biomédica para crear, sustituir o regenerar tejidos dañados. Mediante la bioimpresión 3D pueden depositarse con gran precisión, capa por capa, distintos biomateriales con o sin células en su interior, lo que abre la puerta a la medicina personalizada. También existen materiales sintéticos biocompatibles y con propiedades ajustables, lo que los convierte en buenos candidatos para la impresión 3D.

En esta tesis, planteamos la hipótesis de que podemos desarrollar un hidrogel que alcance la rigidez del tejido cardíaco utilizando colágeno tipo I (COL I) como componente principal. Además, esta tesis plantea también la hipótesis de que los materiales compuestos sintéticos impresos en 3D son adecuados para el cultivo directo de células madre sobre ellos. El objetivo principal de este trabajo es desarrollar y caracterizar las propiedades mecánicas de biomateriales para bioimpresión 3D. Para ello, se desarrolló un protocolo de descelularización de miocardio porcino para obtener hidrogeles derivados de ECM. Además, se desarrolló un protocolo para la adición de

seda disuelta en hidrogeles de COL I para modificar la rigidez y la printabilidad, así como caracterizar sus propiedades mecánicas multiescalares. Por último, se han desarrollado compuestos sintéticos imprimibles aptos para el cultivo celular directo sobre su superficie.

La macromecánica de un material viene determinada por las propiedades mecánicas de sus componentes y su disposición. Para realizar la caracterización multiescalar se utilizaron diversas técnicas: Para caracterizar la micromecánica, se utilizó un microscopio de fuerza atómica (AFM) para medir fuerzas en el rango de nanonewtons, obteniendo el módulo elástico (E) del material. Para cuantificar E a nivel macroscópico, se utilizó el método de ensayo de tracción. Para evaluar las propiedades viscoelásticas de los hidrogeles, se utilizó la técnica de reología para cuantificar el módulo de almacenamiento (G') y la viscosidad (η). Por último, se utilizó microscopía electrónica de barrido (SEM) para obtener imágenes de la ultraestructura de los materiales y cuantificar el diámetro de las fibras. Para estudiar la viabilidad celular, las células embebidas en los hidrogeles o sembradas sobre las estructuras impresas en 3D se tiñeron con diferentes anticuerpos y se visualizaron con un microscopio confocal.

Las principales conclusiones y resultados de los cuatro artículos presentados en esta tesis son:

La adición de seda con sericina preservada mejora la rigidez de los hidrogeles de colágeno para su uso en ingeniería de tejidos.

Se desarrolló un hidrogel de colágeno reforzado con seda para crear un material derivado de ECM con rigidez similar a la del miocardio nativo. Se embebieron células en el interior de la biotinta. Estos hidrogeles mostraron una elevada viabilidad celular. La rigidez zonal aumentó en los hidrogeles reforzados con seda, con valores máximos al 50% (Em = 1,26 kPa) y al 100% (Em = 1,31 kPa) de contenido de seda. El módulo de Young también mejoró con el refuerzo de seda, con valores máximos alcanzados con un 75% de contenido de seda (E = 31 kPa). Además, se mejoraron las propiedades reológicas del hidrogel, obteniendo valores superiores con respecto a los hidrogeles COL I y sin visualizar ningún cambio en la viscosidad a 4 ˚C, lo que facilitó su bioimpresión.

Los hidrogeles derivados de ECM cardíaca pueden ser optimizados para desarrollar bioestructuras en 3D.

A partir de miocardio porcino descelularizado se desarrolló una biotinta para el cultivo de células 3D. La estructura, la viabilidad y el comportamiento del hidrogel con hBM-MSC se investigó mediante imágenes, tinción y reología. El hidrogel presentó una ultraestructura fibrilar y estabilidad mecánica, gelificando después de 16 h (G' = 5 Pa) a 24 h (G' = 24 Pa) de digestión con pepsina. El hidrogel celular mostró una rigidez inferior al de los hidrogeles acelulares tras 7 días de cultivo celular. Se evaluó la interacción entre la ECM y la hBM-MSCs, las cuales mostraron una morfología expandida, un citoesqueleto bien formado y una expresión positiva de Cx43 y α-SMA.

Estructuras de Yttria estabilizada con Zirconia (YSZ) pueden ser impresas en 3D utilizando direct ink writing.

Se investigó la viabilidad de las hBM-MSC en YSZ impresa en 3D con diferente rugosidad superficial. Se comparó la rugosidad superficial de dos muestras impresas en 3D con 80% y 95% de relleno. Las muestras se recubrieron con colágeno para realizar pruebas de adhesión celular, y se observó que las células se adherían tanto a las superficies recubiertas como a las no recubiertas, por lo que parece ser un biomaterial adecuado para el cultivo celular.

Estructuras compuestas de PLA/metal impresas en 3D inducen la diferenciación osteogénica de las células mesenquimales.

Se imprimieron en 3D tres compuestos de PLA/metal, analizando seguidamente la porosidad, la rugosidad y la biocompatibilidad de las estructuras impresas. El refuerzo de acero mostró citocompatibilidad, mientras que el cobre y el bronce no. Se analizó la capacidad de adhesión celular cultivando hBM-MSC en estructuras de PLA/acero y se observó presencia de osteocalcina en las células después de 21 días. Los resultados sugieren que las estructuras de PLA/acero son adecuadas para su utilización en aplicaciones biomédicas.

En conclusión, se han desarrollado y caracterizado biotintas para el cultivo celular en 3D. Se han evaluado sus propiedades macro y micromecánicas y su reología. También se han desarrollado biomateriales compuestos naturales, que muestran

mejores propiedades mecánicas y reológicas cuando se combinan colágeno y seda. Se ha evaluado la biocompatibilidad de determinados compuestos sintéticos, mostrando viabilidad para la bioimpresión tridimensional.

Chapter I. Introduction

TISSUE ENGINEERING is a discipline that focuses on developing strategies to create, maintain, and repair tissues and organs using techniques from engineering, biology, and medicine.

Among these different techniques, we can highlight cell therapy, organ engineering and 3D bioprinting. Cell therapy is a technique that uses living cells to treat disease or injury. For example, stem cells can be used to repair damaged tissues or immune cells can be used to treat diseases of the immune system. Organ engineering is a technique used to create new tissue or repair damaged tissue. This can be done by using living cells and synthetic materials to create a tissue-like structure.

3D bioprinting uses specialized equipment (3D printers) to create tissue and organ structures in an automated way. This is done through the use of bioinks, which are biocompatible materials that may incorporate living cells as well other components necessary for cell growth and differentiation.

3D bioprinting has many potential applications in medicine, including the creation of engineered tissues and organs to replace damaged or missing ones, the fabrication of tissue models for research and development of new therapies, and the customization of medical treatments for individual patients.

Although 3D bioprinting is an emerging technology and it is still in its early stages of development, it has the potential to revolutionize medicine and improve the health of people around the world. However, there are still many challenges facing this technology, such as the need to develop more advanced bioinks and improve the efficiency and accuracy of 3D printing of tissues and organs.

The development of bioinks is important for 3D bioprinting as they are the material from which tissues and organs are printed. They must be able to withstand 3D printing and allow cells to grow and develop properly. The development of more

advanced bioinks is essential to improve the efficiency of 3D bioprinting and make it more accessible to more users.

1 Scaffolds for tissue engineering: the extracellular matrix

The extracellular matrix (ECM) is a complex and dynamic structure that provides support and structure to cells and tissues. ECM also has a major impact on cell behavior by regulating cell-cell and cell-tissue interactions (1).

The ECM is three-dimensional, and it serves as a biophysical and biochemical support for different cell types (2). Due to the great multicellular variety that can be present in the ECM, its composition and characteristics vary greatly among different tissues, giving rise to tissues as different as brain or bone (3).

In addition to giving physical support, ECM regulates important cellular processes such as migration, differentiation, and morphogenesis (4, 5). The main ECM constituents are, among other fibrous proteins, collagens, elastin, glycosaminoglycans (GAGs), and fibronectin. Of these proteins, the most abundant in the ECM of most tissues is type I collagen (COL I), which associates with other collagens and ECM proteins to form complex fibrillar structures (1). In turn, this complex structure interconnects with other molecules present in the ECM itself to re-modulate and give rise to the ECM. In summary, the formation and remodeling of the ECM is a cyclical and uninterrupted process that varies when conditions within the ECM change (6).

Cells synthesize and secrete molecules that interact with the ECM to remodel it. Furthermore, variations in the composition and structure of the ECM modulate the response of the cells (1).

1.1 Collagens

Among the proteins, collagens are the most abundant ones in the ECM of the majority of human tissues (7). Fibroblasts are the main cells responsible for synthesizing and secreting collagens. In addition, through tensions and fibroblast/matrix interactions, these cells influence collagen fiber alignment. In turn, collagen scaffolds provide signals

to the cells, thereby modifying basic cellular functions such as migration, adhesion or tissue repair (4).

There are 28 different types of collagens, which are made up of a minimum of 46 different polypeptide chains (α chains) (1, 8). There is a structural characteristic shared between the different types of collagens, namely the presence of a triple helix (three α chains linked together) that varies in different percentages, depending on the type of collagen (9). Each of these chains is formed by 3 amino acids that follow the same pattern (Gly-X-Y)n, where X and Y can be any amino acid, although they are frequently occupied by proline, hydroxyproline or glycine. To achieve consistency, all these helices are held together by hydrogen bonds and Van der Waals forces (10).

Some types of collagens are called fibrillar collagens, including types I, II, III, V, XI, XXIV and XXVII (8). The formation of fibrillar tissue is promoted by the presence of other matrix macromolecules, such as decorin and biglycan (11). Among these fibrillar collagens, type I (COL I) is the most abundant in the different tissues of vertebrates (11).

From the biomechanical point of view, COL I is the main protein providing structure to the ECM, being the stiffer component of all those that compose it and the one that supports the structural loads that tissues undergo (12). Structurally speaking, collagen fibers are composed of an aggregation of collagen fibrils combined with other molecules, such as proteoglycans. In turn, these collagen fibrils are formed by clusters of triple helices (three α-chains covalently linked together) in different densities (13, 14, 15).

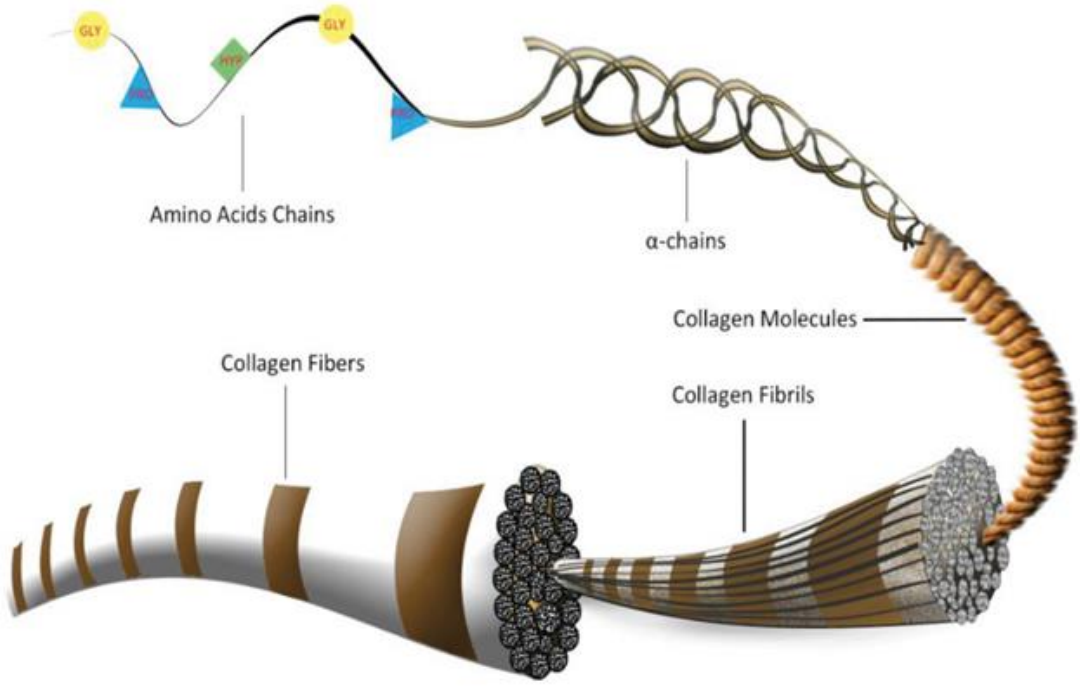

Figure 1.- Sketch of the structure of a collagen fiber (16)

Several authors have characterized the mechanical properties of the different components of COL I, from the triple helix to the collagen fiber. Thus, it has been shown that the elastic modulus of the collagen fiber (0.07-0.43 GPa (17, 18, 19, 20)) is up to two orders of magnitude lower than the elastic modulus of the triple helix (1.3-7.8 GPa (21, 22, 23, 24)). Similarly, the anisotropy of collagen fibers has been also demonstrated (19). Thus, it has been proposed that the elastic modulus of the fibers of the different types of collagens is determined by the specific packing of the triple helices that compose it (12).

1.2 Elastin

Elastin is the main protein of the elastic fibers, which are responsible for giving the ECM its elasticity. It is mostly present in tissues that undergo cyclic deformation, such as cardiac and lung tissues, or blood vessels. The elastic fibers that form part of ECM tissues are composed of elastin (approximately 90%) and cellular microfibrils (1).

Elastin is an insoluble biopolymer formed by a precursor chain of amino acids with a hydrophobic region (valine, proline and glycine) and a hydrophilic region (lysine

and alanine) called tropoelastin. It is the hydrophobic region that gives the protein its elastic properties (25). Microfibrils are the first component present in the ECM when elastic tissue develops, acting as a scaffold on which tropoelastin monomers are oriented and assembled (26).

Mechanically, the elastic fibers of the different tissues have an elastic modulus of ≈300-700 kPa. The main characteristic that elastic fibers exhibit when they are subjected to a tensile test is that the elastic zone of the curve has an extension of approximately 70% (25). In addition, they are capable of withstanding billions of extension/relaxation cycles without modifying their mechanical response (27).

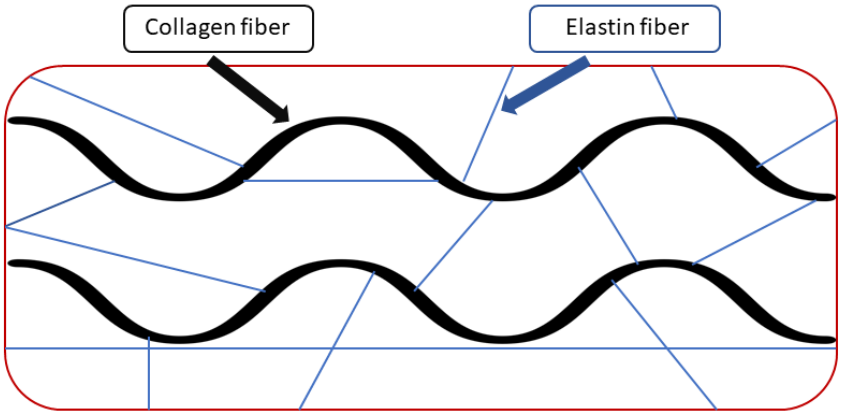

Figure 2.- Representation of collagen (black) and elastin (blue) fibers in the ECM. When a force is applied, elastin fibers are the first to elongate in the direction of the applied force. When that force exceeds a certain value, recruitment of the collagen fibers begins and they begin to stretch, giving rise to the beginning of the nonlinear zone of a stress-strain curve.

1.3 Fibronectin

Fibronectin plays an important role in cell adhesion, migration and differentiation (28). It also helps to maintain tissue integrity and promote wound healing. Its function is essential for maintaining the integrity and organization of tissues in the body.

Fibronectin formation in the ECM occurs when cells (primarily fibroblasts) secrete soluble fibronectin dimers. These soluble fibronectin dimers then bind to cells in the tissue via small structures called integrins, which are found on the cell surface. This binding allows cells to adhere to the ECM and maintain their organization in tissues (29). Fibronectin can also act as a signaling molecule, which means that it can transmit

chemical signals from the ECM to the cells, allowing them to respond to changes in their environment.

In addition, fibronectin also plays an important role in wound healing. When an injury to the skin occurs, cells in the extracellular matrix begin to produce fibronectin, which helps to form a layer of granulation tissue over the wound. This layer of granulation tissue is necessary so that cells can migrate and begin to repair the wound (30).

1.4 Glycosaminoglycans

Glycosaminoglycans (GAGs) are a group of molecules found in the ECM of the human tissues. They consist of a long chain of sugars that are linked together by glucosamine- or galactosamine-type bonds. GAGs are essential for the formation and maintenance of the structure and function of tissues in the body.

GAGs are found in high concentrations in cartilage, where they form a layer that lines the surface of joints. This layer helps to protect the cartilage and absorb the shocks generated by joint movement. GAGs are also found in the skin, blood vessels and the ECM of other tissues, such as the lung, where they play an important role in the structure and function of these organs (31).

GAGs are made up of a chain of monosaccharides, which are small sugar molecules. These chains are linked together by covalent bonds, which gives them a rigid and tough structure. GAGs also bind to proteins in the ECM, allowing them to interact with cells in the body and transmit chemical signals (32).

There are several different types of GAGs, including hyaluronic acid, chondroitin sulfate and dermatan sulfate (33). Each type of GAG has a slightly different structure and function in the body. For example, hyaluronic acid is a GAG found in high concentrations in cartilage and skin (34), where it helps maintain the elasticity and hydration of these tissues. Chondroitin sulfate, on the other hand, is found in cartilage and helps to absorb the shocks generated by joint movement (35).

The synthesis of GAGs in the body tissues takes place through a complex process involving the production of monosaccharides, their binding into long chains and their

binding to proteins in the extracellular matrix. This synthesis is carried out by specialized cells found in the ECM of tissues, such as fibroblasts (36, 37).

1.5 Cell-matrix interactions

Interactions between cells and the ECM are essential for the physiology of tissues and organs in the human body. The ECM provides support and allows cells to adhere and communicate, while cells use enzymes and proteins to interact with the ECM and respond to environmental signals (1).

To do this, cells have several mechanisms to interact with the extracellular matrix. For example, cells can release enzymes that degrade the extracellular matrix, allowing them to move and change shape. They can also produce adhesion proteins that allow them to attach to the ECM, allowing them to anchor and maintain their position in the tissue (38).

In addition, cells have receptors on their surface that bind to extracellular matrix proteins, allowing them to receive signals from the environment and respond appropriately. For example, collagen receptors can help cells detect when they are being subjected to mechanical stress, allowing them to contract and protect themselves (39).

The interaction between cells and the extracellular matrix is also important for the formation and maintenance of the structure of the body tissues (40). This degradation process is balanced by deposition in healthy tissues (41). A mismatch in cell-matrix interactions could lead to the progression of diseases such as fibrosis (42) or cancer (43).

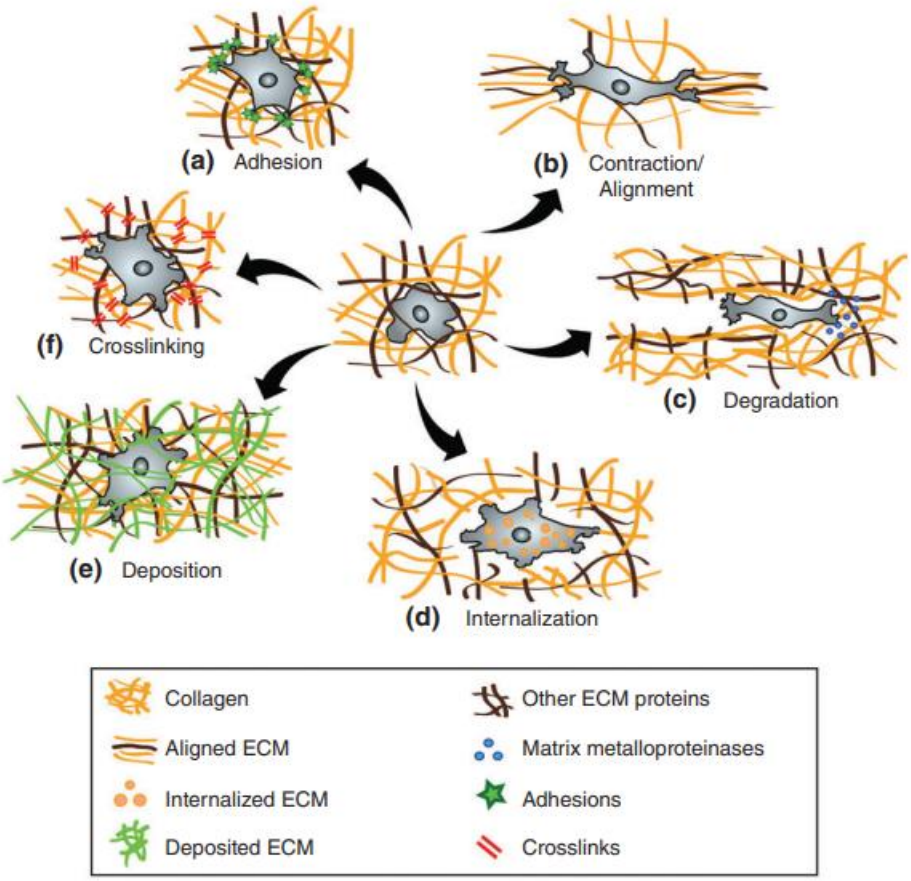

Figure 3.- Remodeling of the ECM by different mechanisms (38).

2 Decellularization

One of the most common methods to study the ECM is organ and tissue decellularization. Decellularization protocols aim to remove all cellular components of a tissue while preserving the ECM as much as possible (44, 45). The first reported case of obtaining ECM by decellularization of a tissue and its subsequent use as a scaffold was the use of small intestinal submucosa as a raw material for vascular applications in 1989 (46, 47, 48).

Subsequently, many protocols have been developed to achieve decellularization of while minimizing the changes in the ECM. Decellularization protocols are usually based on the combination of three major types of methods: physical, chemical and biological (49).

Physical methods include techniques such as pressure application (50, 51), freezing and thawing cycles (52, 53) or electroporation (54, 55). Chemical methods, which are the most used, include the use of ionic solvents, such as sodium dodecyl

sulfate (SDS) (56, 57) or sodium deoxycholate (SDC) (58, 59); and non-ionic solvents, such as triton X-100 (60, 61). Finally, biological methods include the use of enzymes such as trypsin (62, 63) or dispase (53, 64).

Implementing a decellularization protocol must be done with care, as the removal of cells and genetic material from a tissue can lead to alterations and even to damage to the ECM. Therefore, decellularization protocols are different for every tissue type (49, 65).

There are two main approaches for decellularizing a tissue or an organ: by perfusion (66) (the whole organ is decellularized by sequential perfusion of the reagents through the airways or blood vessels of the tissue) and by diffusion (67) (small pieces of the organ are decellularized by immersing them subsequentially in the different reagents). The same organ/tissue can be decellularized in both ways. For example, there are protocols for the decellularization of the heart by perfusion (68) and by diffusion (69).

3 Hydrogels derived from the extracellular matrix.

The potential of decellularized ECM alone as a scaffold for tissue engineering has been studied in terms of inflammatory response after decellularization and the applicability of animal studies to humans (70). Therefore, to generate a functional and viable three-dimensional tissue is essential to embed cells within the ECM (71). With this in mind, an evolution of the direct use of the decellularized ECM is reconstituting the matrix proteins in the form of hydrogels, which are hydrophilic structures capable of holding large amounts of water.

Since pioneering works with hydrogels in 1960 (72), hydrogels have been used in numerous biological and biomedical applications, such as drug delivery, injectable bioink, or tissue engineering (73, 74, 75). In the PubMed database alone, there are currently more than 1500 papers describing the use of ECM-derived hydrogels from almost every organ in the human body. The mechanism by which the ECM hydrogel modulates cell behavior is not yet well described, although different hypotheses have been postulated. Among others, it has been proposed that hydrogels influence the

regulation of tissue homeostasis by extracellular vesicles, the biologically active degradation products derived from ECM or the biomaterial-host interaction (76, 77, 78).

ECM-derived hydrogels are formed by means of a collagen-based self-assembly process, which is mainly regulated by the proteins of the ECM and the presence of glycosaminoglycans and proteoglycans (79). For hydrogel formation to occur, it is important to maintain the original composition of the ECM as much as possible. Therefore, choosing a mild decellularization protocol is crucial in determining the physicochemical properties of the ECM-derived hydrogels obtained (80). Once the correct decellularization of the tissue has been achieved, the tissue is freeze-dried and converted into a fine powder by cryo-milling (to ease further solubilization).

In addition to adequate decellularization, choosing the correct solubilization protocol (since not all the ECM proteins are acid-soluble) highly determines the properties of the obtained hydrogels.

The most widely used solubilization method is by digesting the ECM powder with pepsin from the porcine gastric mucosa (81). Pepsin is a protease that breaks down polypeptides into smaller ones, i.e. peptides and amino acids, carrying out the protein hydrolysis reaction. This action is essential for protein digestion since our body cannot absorb proteins in their complete form. Instead, our we need to break down proteins into smaller fragments to absorb and utilize the amino acids that they contain. Pepsin is activated in an acidic environment. When a peptide bond is broken by pepsin action, two new peptides are formed with a C-terminus and an N-terminus, producing one carboxylic and one amino group (82). In acidic conditions, the amino group reacts with a proton, establishing a balance in favor of the protonated form (NH_3^+) and consuming protons (Figure 4), which leads to an increase in pH and the inhibition of pepsin digestion if the pH reaches high values.

To solubilize the ECM, primarily, the most used methods are the Freytes (83) method (0.1M hydrochloric acid + pepsin) and the Voytik-Harbin (84) method (0.5M acetic acid + pepsin). Pepsin breaks non-acid soluble proteins of the ECM, but it may also break the telopeptide bonds of the collagen triple helix (85), which a major impact on the mechanical properties of the obtained hydrogels (86).

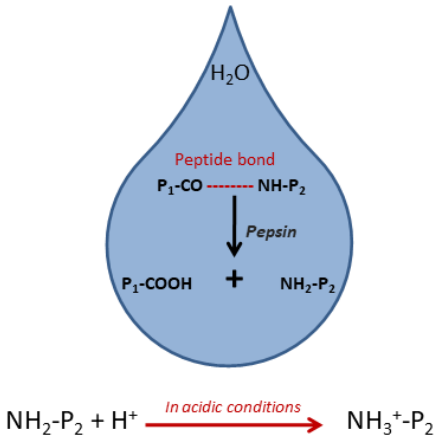

Figure 4.- Visual representation of protein hydrolysis and proton consumption in acidic conditions.

The ECM is considered solubilized when the liquid is homogeneous and has no visible particles (83). Once the ECM has been solubilized, the next step is to bring the ECM solution to physiological pH (7.4), salt concentration (1X) and temperature (37 ˚C). Then, a self-assembly process begins as the entropy of the reaction increases when the collagen monomers lose water and start to form aggregates. These aggregates are oriented in such a way that the hydrophobic part of the protein remains inside the collagen fibril, while the hydrophilic part is oriented towards the outer end (85, 87).

Johnson *et al*. investigated the effect of modifying a single neutralization parameter while maintaining the rest of the parameters in cardiac ECM-derived hydrogel (88). As an example, increasing the salt concentration from 0.5x PBS to 1.5x PBS decreased the mechanical properties of the hydrogels by 2-3 fold. Furthermore, the gelation time increases from 20 minutes (0.5x PBS) to more than 8 hours (1.5x PBS).

Brightman *et al*. demonstrated that matrix assembly kinetics, fibrillar network and network morphology were distinct between extracellular matrix-derived hydrogels and hydrogels formed from purified collagen I. On the one hand, matrix-derived hydrogels showed an increased rate of assembly and fibril density; on the other hand, type I collagen hydrogel revealed a higher opacity and increased fibril diameter (79). Furthermore, the study demonstrated how ECM glycoproteins and proteoglycans played a crucial role in ECM fibril regulation and formation.

3.1 Impact of decellularization methods on ECM-derived hydrogels

The biochemical composition of the hydrogel, its transparency, mechanical properties, gelation kinetics and cytocompatibility, among others, are characteristics to be considered when choosing the most appropriate decellularization protocol for each tissue.

Fernández-Pérez *et al*. compared porcine corneas-derived hydrogels fabricated from different decellularization methods, evaluating the impact of using two detergent-based techniques (SDS and Triton X-100) and the freeze-thaw cycling technique (89).

Briefly, the amount of collagen obtained in the hydrogel remained constant in the three treatments. Regarding the gelation kinetics, the SDS treatment resulted in longer gelation times (27.53 ± 1.36 min); however, the hydrogels obtained by SDS decellularization of the tissues were the ones that exhibited stronger rheological properties (when compared with rat tail-derived collagen hydrogels). Evaluation of the hydrogel ultrastructure confirmed that all of them presented a porous and fibrillar structure, with no significant changes between groups. Interestingly, all groups showed good cytocompatibility except for the SDS group, where no viable cells were visible after 1 day of cell culture. In summary, decellularization with SDS provided stiffer but non-biocompatible hydrogels.

Gaetani *et al*. also compared different hydrogels, in this case, derived from porcine pancreas, using decellularization with Triton X-100 and SDS at different concentrations (90). In addition to the results showed by Fernandez-Perez *et al*. in their research, Gaetani *et al*. demonstrated that the variability between the properties of obtained hydrogels was much lower in the SDS groups. Therefore, the choice of the appropriate detergent is fundamental to preserve as much as possible the biochemical composition of the native organ, as well as to obtain a hydrogel with the desired physicochemical properties.

3.2 Crosslinked hydrogels

Both ECM decellularization techniques and those used to obtain pure collagen involve the extraction of the tissue-forming collagen, which leads to the destruction of

the collagen fibrillar structure and its natural crosslinkers during collagen extraction (91, 92), resulting in a collagen structure with poorer mechanical properties and lower mechanical stability. This aspect is one of the major limitations of the use of type I collagen-based biomaterials in tissue engineering.

Intending to overcome these drawbacks, numerous researchers have used crosslinkers to obtain collagen-based biomaterials with higher stiffness (93, 94) or compressive modulus (95). A crosslinker could be defined as a material capable of inducing a bond or sequence of bonds between one polymeric chain or polypeptide and another (96). These links can be covalent or ionic in nature. It has even been shown that the use of crosslinking results in higher thermal stability of the obtained structures (97, 98). Although the different crosslinking techniques have proven to be effective in obtaining more stable collagen-based biomaterials with improved mechanical properties, there is no standard crosslinking technique, but it is necessary to use the most appropriate depending on the concrete application.

There are three general crosslinking techniques: chemical, physical, and enzymatic crosslinking.

Chemical crosslinking uses an external agent to create covalent bonds between collagen fibers, while physical crosslinking uses ionizing radiation, ultraviolet light or photo-oxidation to create weak bonds (99, 100). Enzymatic crosslinking uses enzymes to catalyze the formation of covalent bonds. Glutaraldehyde is a widely used chemical crosslinker because of its low cost, but it has high cytotoxicity and generates an inflammatory response in surrounding tissues (101, 102). Natural cross-linkers, such as genipin (103) and polyphenols (104), are less toxic but have a lower degree of crosslinking (101). Physical and enzymatic cross-linkers showed to produce more biocompatible scaffolds but with lower stability and enzyme resistance (105, 106).

4 Scaffold mechanical characterization

Cells are mechanosensitive. Therefore, substrate mechanics can modulate physiological processes at the cellular, molecular and systemic levels (107). In particular, cells sense the microenvironment in which they find themselves through focal

adhesions. Focal adhesions have an area of approximately 1 μm^2 (108), which is an order of magnitude larger than the diameter of collagen fibers (109). Therefore, the cells will not only sense the mechanical properties of the collagen fibers but their behavior will be modulated by all the components present in the adhesion area.

Then, to properly characterize a biomaterial, its mechanical properties must be measured either at the macroscopic and microscopic scales (110, 111, 112, 113).

The mechanical behavior of any material defines its resistance to stress, as well as to the deformation that this stress causes in the material. Stress is defined as the internal resistance of the material per unit area to externally applied forces. There are different types of stress: tensile, compressive, torsional, biaxial, hydrostatic pressure, and shear stress.

$$\sigma = \frac{F}{A} \tag{1}$$

Where:

σ: Applied stress (Pa).

F: Force applied (N).

A: Area over which the stress is applied (m^2).

Deformation, on the other hand, quantifies how much the shape of a material changes in response to an external force. Types of deformation are categorized into tensile, compressive, torsional and shear strain. A linear strain is calculated as shown in Equation 2.

$$\varepsilon = \frac{L - L_0}{L_0} \tag{2}$$

Where:

ε: Deformation (dimensionless).

L: Length after deformation (m).

L_0: Initial length (m).

Materials can have the same mechanical properties in all directions (isotropic), or they can have different mechanical properties depending on the test direction (anisotropic). Materials can be mechanically characterized in terms of stiffness, toughness, or hardness, among many other properties. The most commonly used parameter to define the mechanical properties of a material is stiffness. Stiffness is defined by the elastic modulus (E, in Pa) or Young's modulus (named in honor of Thomas Young), which relates the stress and strain parameters in the elastic region of a material. This law is known as Hooke's Law

$$E = \frac{\sigma}{\varepsilon} \tag{3}$$

Materials, when subjected to stress, first undergo a recoverable deformation, which is known as elastic deformation. The modulus of elasticity is the slope of the stress/strain curve in this elastic zone. If the stress continues to increase and what is known as the elastic limit is exceeded, the material enters a second zone known as the plastic zone. The strain in the plastic zone is not recovered (Figure 5).

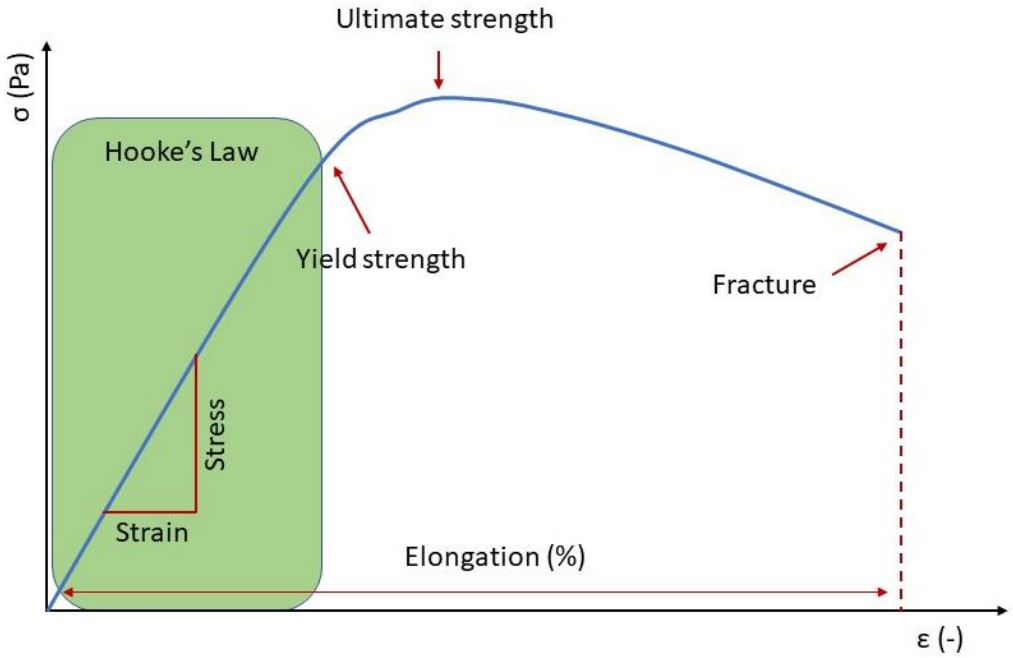

Figure 5.- Typical stress (y-axis)-strain (x-axis) curve of a material.

When a material is subjected to deformation, a relationship appears between the lateral and axial deformations. This relationship is known as Poisson's ratio, which is a dimensionless and positive parameter.

$$\upsilon = \frac{-\varepsilon_x}{\varepsilon_z} = \frac{-\varepsilon_y}{\varepsilon_z} \leq 0.5 \quad (4)$$

Poisson's modulus, in addition, relates the shear modulus (G, in Pa) of a linear isotropic material to its elastic modulus.

$$G = \frac{E}{2(1+\upsilon)} \quad (5)$$

In materials science, composite materials are defined as those materials formed by the union of two or more materials, obtaining a combination of properties that the original materials do not possess. Any tissue in the human body, including the ECM, is composed of a diverse combination of materials (collagen, elastin, etc.). For this reason, the ECM can be considered a composite material. The mechanical properties of a composite material at the macroscopic level are different from the sum of the properties of its components; they even differ depending on the 3D distribution of these components (114, 115, 116).

4.1 Micromechanical properties: Atomic Force Microscopy

Conventional microscopes, due to the diffraction limit of the light (≈200 nm), cannot show structures with nanometer resolution. To overcome this obstacle, in 1931, physicist Ernst Ruska and engineer Max Knoll developed the first prototype of an electron microscope (117). The electron microscope uses a beam of accelerated electrons as an illumination source, achieving a resolution of close to 50 pm. However, these microscopes have the disadvantage that the sample must be coated with a conductive material and the visualization must be carried out in a vacuum chamber.

It was in 1986 that Binning *et al*. (118) invented the atomic force microscope (AFM), a mechano-optical instrument with a resolution capable of detecting forces of the order of nanonewtons. For this purpose, the AFM uses a sharp tip with which it

traces a surface to obtain a 3D topographical map of the sample. The main advantage of AFM is that the sample can be directly characterized under physiological conditions. In addition, the interaction forces generated between the tip and the sample can be quantified with the AFM by applying pressure or by pulling on it. In this way, the AFM can be used as a force sensor, and it has been widely applied in the field of biomedicine to study the mechanics of cells and tissues (119, 120, 121).

AFM uses, as a mapping or measuring element, a beam, called cantilever, which is flexible and ends in a micrometric-shaped tip. The cantilever is positioned by a system of piezoelectric actuators, adjusting the sample-tip position in 3D. For mechanical measurements, the tip is brought close to the sample and a certain compressive force (*F*) is applied to the sample, which produces an indentation (δ) on the surface. In the same way, the sample generates a force of equal magnitude and opposite direction on the cantilever, which produces a deflection (*d*). To quantify this deflection, a laser is projected against the back face of the cantilever. The laser reflects and projects onto a photodiode, which registers the voltage (*V*) that reaches it (122, 123) (Figure 6).

The function of the cantilever is similar to that of a spring. Therefore, by means of Hooke's Law, the force can be obtained from the deflection, the offset (d_0) and the spring's elasticity constant (*k*).

$$F = k \cdot (d - d_0) \tag{6}$$

For accurate force measurements, it is essential to calibrate the spring constant of the cantilever correctly. For this purpose, there are several methods in the literature (124, 125, 126, 127). However, the first and simplest reported method is based on analyzing the thermal noise of the cantilever deflection fluctuations and applying the Energy Equipartition Principle (EEP) (128). As most AFMs measure *d* indirectly, Butt *et al*. (129) introduced a correction factor (Ci ≈ 0.82) that allowed k to be calculated fairly accurately.

$$k = C_i \frac{k_B T}{< \Delta d^2 >} \tag{7}$$

Where:

k_B: Boltzman constant.

T: Temperature (in Kelvin)

$\langle \Delta d^2 \rangle$: Average of the square of the cantilever fluctuations.

Once the cantilever deflection has been calibrated, the indentation on the sample can be calculated.

$$\delta = z - z_c - (d - d_0) \quad (8)$$

Where:

z: Displacement of the cantilever with the piezo actuator.

z_c: Vertical displacement of the cantilever when the tip contacts the sample.

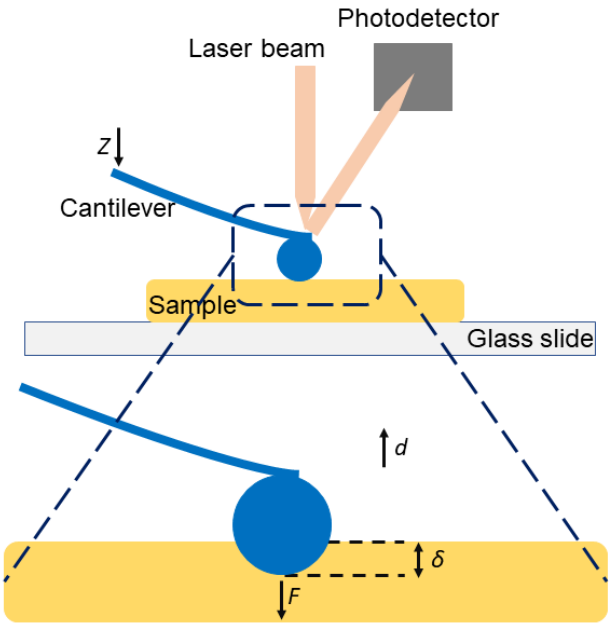

Figure 6.- Schematic view of an AFM system with a spherical tip

Figure 7 shows a typical force/indentation curve. Briefly, the horizontal line is the non-contact zone, so the force in this zone is zero. The point of contact between the tip and the sample is represented as the change in slope between the horizontal line and the upward curve. Once the contact point is reached, the measurement enters the contact zone. In the contact zone, the force grows non-linearly with indentation.

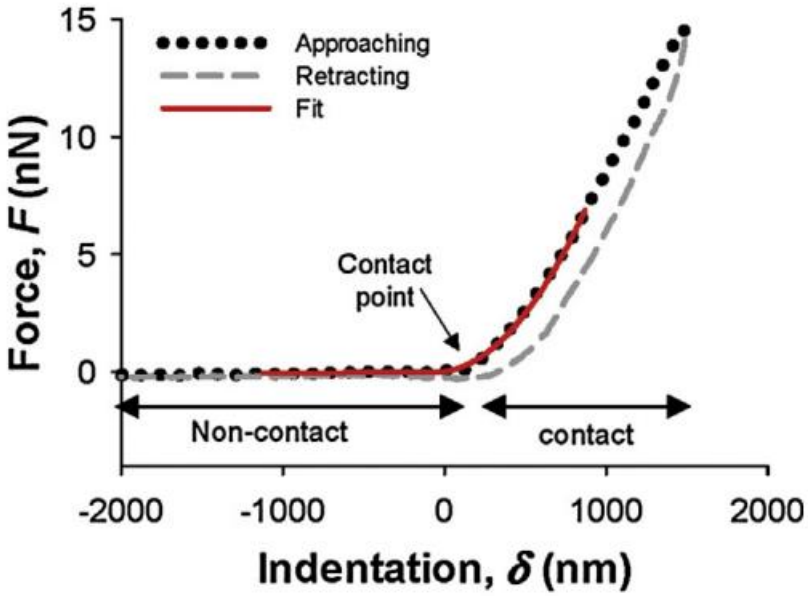

Figure 7.- Force/Indentation curve (130)

The local modulus of elasticity of the sample (E_m) can be calculated by fitting a contact model which depends on the geometry of the tip. The two most commonly used models are the spherical tip model (eq. 9) (122) and the pyramidal tip model (eq. 10) (131).

$$F = \frac{4 \cdot E_m \cdot R^{1/2}}{3(1-\upsilon^2)} \delta^{3/2} \quad (9)$$

$$F = \frac{E_m \cdot \tan(\theta)}{\sqrt{2} \cdot (1-\upsilon^2)} \delta^2 \quad (10)$$

Where:

R: Radius of the sphere.

υ: Poisson's modulus.

Θ: Mean angle of the pyramid.

The AFM contact model makes several assumptions: the sample is elastic and linear, as well as isotropic; the surface area is infinite relative to the tip; the deformations performed on the sample remain in the linear regime; there is no adhesion between the sample and the tip (132).

Spherical tips are generally preferred for mechanical measurements of ECM models of decellularized tissue and soft tissue (133) samples because they have a larger sample contact area, which allows measuring soft samples by averaging several ECM components at the same time while avoiding the large mechanical stresses associated with sharp tips. Pyramidal tips, on the other hand, have a higher lateral resolution due to their smaller sample contact area, but are also more prone to variability in very heterogeneous ECM samples and may cause undesirable mechanical stresses in soft samples (134). However, it is important to point out that contact mechanics models commonly used to analyze AFM measurements assume infinite lateral dimensions of the sample compared to the tip dimensions, or at least an order of magnitude larger. If this requirement is not met with spherical tips, it becomes indispensable to use pyramidal tips (112).

To characterize the mechanical properties of a tissue, 10-50 µm thick slices are cut and adhered to a glass slide. To prevent the stiffness of the support from interfering with the measurement of E_m, the indentation should be less than 10% of the thickness of the sample (typically, 1 µm is indented) (135).

A very common effect is the adhesion between the tip and the sample, especially when characterizing cells or tissue (136, 137). To minimize this, SiO_2 or borosilicate tips are used instead of polystyrene.

4.2 Macromechanical properties: Tensile and compression testing

The union of all the micrometric components of the ECM forms a tissue, which is a composite material with measurable mechanical properties at the macroscopic level. For this purpose, several tests are available. A very common test in materials engineering is the uniaxial test, in which the sample is subjected to unidirectional stress until the desired strain occurs or until the sample breaks (138, 139). The uniaxial test quantifies the resistance of a material to a slowly applied force, with a strain rate that can be adjusted for each individual case.

In soft and physiological tissues, it is common to perform this test horizontally, which allows the sample to be kept immersed in a culture medium and at a physiological

controlled temperature (113, 140). The uniaxial testing device consists of a servomotor capable of stretching the sample to the desired length (*L*) while sensing the force (*F*) applied to it. The tissue strip must be of small dimensions (a few millimeters) to prevent the weight of the sample become bent and thus affecting the measurement.

The mounting of the tissue strip is done applying superglue to two hooks. One of the hooks is attached to the fixed part of the setting while the other hook is attached to the servo-controlled actuator (Figure 8).

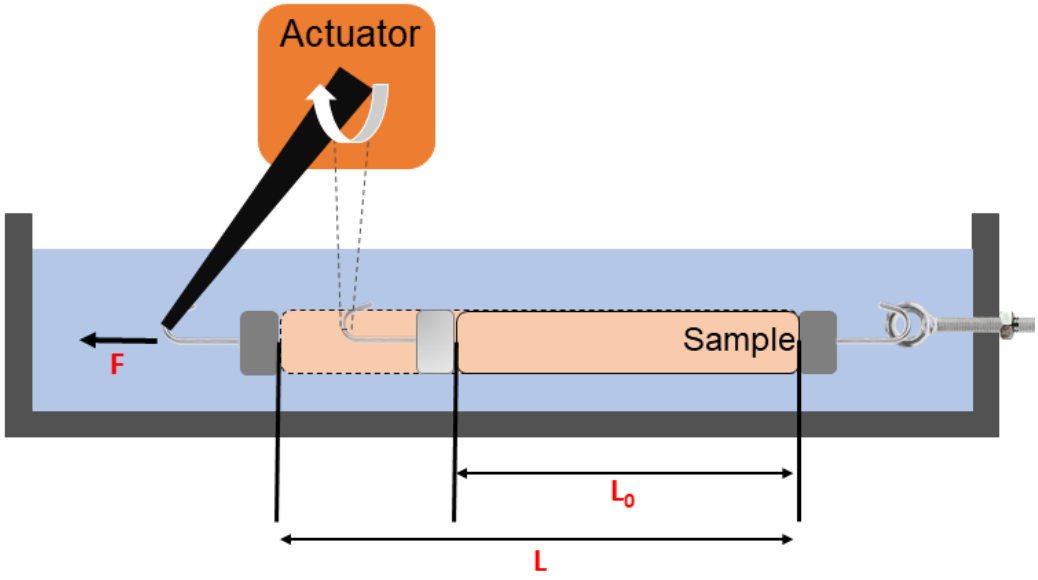

Figure 8.- Diagram of the sample uniaxial tensile setup.

Langrangian strain (ε) can be calculated by the length after deforming the sample (L) and the initial length of the strip (L_0).

$$\varepsilon = \frac{L}{L_0} - 1 \tag{11}$$

Langrangian stress (σ) is calculated by the ratio of the force applied to the end of the strip (F) to the cross-sectional area of the strip (A_0). Since the cross-sectional area is difficult to measure in soft tissue, it is calculated by the mass of the strip (m), its initial length (L_0) and the density (ρ), which is assumed to be equal to that of water (1.06 g/cm^3).

$$\sigma = \frac{F}{A_0} = \frac{F \cdot \rho \cdot L_0}{m} \tag{12}$$

Figure 9 shows a typical stress-strain curve performed by tensile testing. Cyclic deformations are applied to the sample. There is a stretching zone (upward curve) and a relaxation zone (downward curve).

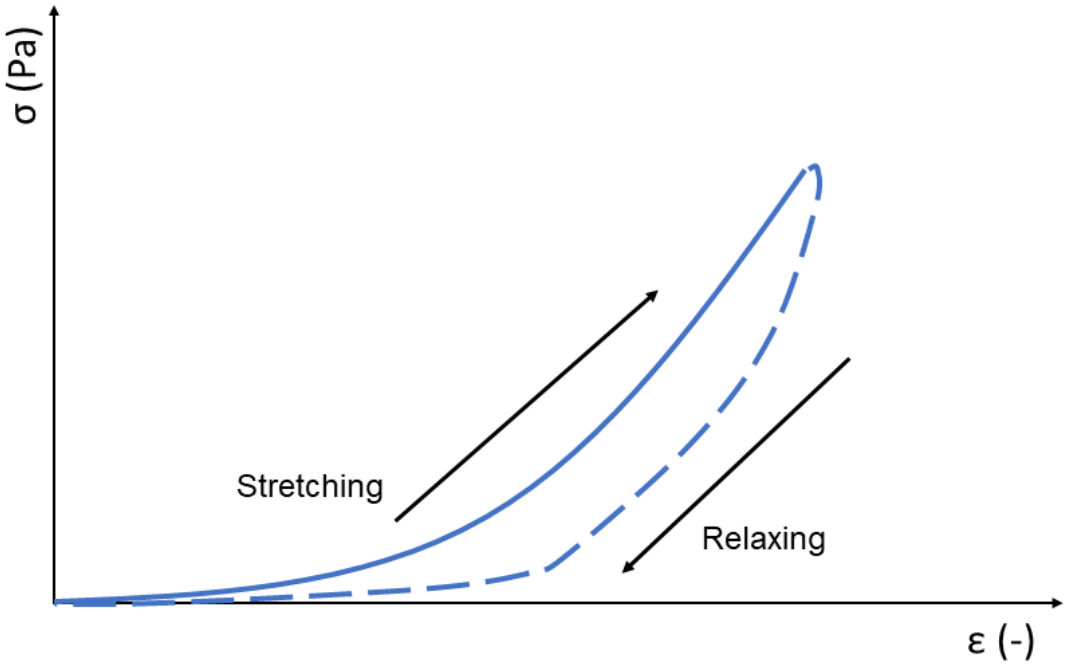

Figure 9.- Typical stress (y-axis) vs strain (x-axis) curve performed by tensile testing.

On the other hand, a compression test on a hydrogel is performed to quantify the force required to compress instead of stretching the sample. For this purpose, the sample is loaded on the support plate and the measuring device is adjusted according to the size and shape of the sample. The load is then applied to the sample in a gradual and controlled manner, using a constant strain rate and recording the data during the compression process. By analyzing the recorded data, the mechanical properties of the hydrogel, such as its Young's modulus, can be obtained.

4.3 Rheological characterization

Flowing materials can be studied by the rheology technique. Rheological characterization is performed from the relationship between stress and strain. The stress applied to a sample in a rheological study is a stress parallel to the area of the sample. The difference with respect to both AFM and the tensile test is that in those

cases the deformation is perpendicular to the area of the sample. Thus, rheology evaluates the transverse modulus of elasticity.

The first scientist to talk about “rheology” was Robert Hooke, in 1678, in his book "True theory of elasticity", where he established the term modulus of elasticity (G) as the proportionality between stress (τ) and strain (γ) for materials in a solid state. Later, in 1687, Isaac Newton, in his work "Philosophiae Naturalis Principia Mathematica", studied the behavior of liquids and named the term viscosity (η) for the first time, defining it as the constant of proportionality between the applied stress and the strain rate. However, only a few fluids behave according to this law of proportionality. These fluids are known as Newtonian fluids, such as water or glycerol.

For many years, materials were classified as Newtonian liquids (eq. 13) or Hooke's solids (eq. 14), depending on their behavior. However, when testing different solid materials, it became clear that Hooke's Law was fulfilled for certain stresses, but above a certain stress, the material did not recover its original length. James Maxwell, in 1867, proposed that the properties of a substance are a combination of an elastic and a viscous component, giving rise to the term "viscoelasticity".

In this way, it was defined that materials can exhibit elastic, viscous or viscoelastic behavior (a combination of both). In addition, in the mid-20th century, the study of rheology was further developed. Viscosity was found to be dependent on other factors, such as time (thixotropy and rheopecty).

$$\tau = \eta \frac{du}{dy} = \eta \dot{\gamma} \tag{13}$$

$$\tau = G \cdot \gamma \tag{14}$$

In contrast to Newtonian fluids, Non-Newtonian fluids show a non-linear relation between shear stress and strain. This relationship defines the shear thinning or shear thickening behavior of the sample. The performance of this association between shear stress and strain defines the parameter n (dimensionless), which represents the fluid flow behavior index (Figure 10). Shear thinning behavior is characterized by a n<1, which means that the biofluid is classified as pseudoplastic, where the viscosity decreases as the strain increases. Shear thickening behavior is characterized by a n>1, which means that the biofluid is classified as dilatant, where viscosity increases as the strain increases.

When n=1, the fluid follows a Newtonian behavior, where viscosity is constant at any strain (141).

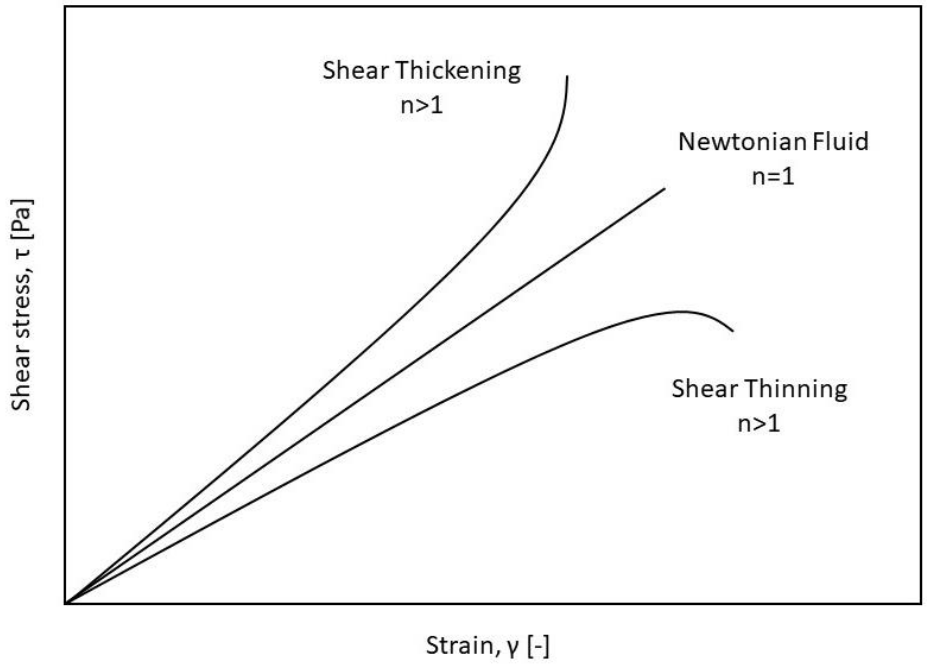

Figure 10.- Fluid flow behavior index.

The shear stress and the strain amplitude are applied to develop a sinusoidal stress (*G**, in Pa), which represents the complex mechanical impedance of the measure. This sinusoidal stress describes the entire viscoelastic behavior of a soft material, and it is defined by the quotient of shear stress (τ, in Pa) by strain (γ, $\mathrm{dimensionless}$).

$$G^* = {}^{\tau}/_{\gamma} \tag{15}$$

The storage modulus (*G'*, which measures the elastic component) is the real part of G* and the loss modulus (*G''*, which measures the viscous component) is the imaginary one; both represent the solid-state and the liquid-state behavior of the sample, respectively. As an indicator of the variation between storage and loss modulus, the phase angle (δ, which represents the relationship between *G'* and *G''*) can be computed, whose tangent angle determines the viscous-elastic response (142).

Complex viscosity (η^*, in Pa·s), which defines the resistance to flow as a function of angular velocity (ω), can be expressed as the relationship between the dynamic viscosity (η') and the storage viscosity (η''). It is also possible to define the dynamic

viscosity (calculated from the loss modulus, *G''*) as the real part of η^*, while the storage viscosity (calculated from the storage modulus, *G'*) represents the imaginary part. Thus, the relationship can be expressed in the following form:

$$\eta^* = \eta' - i\eta'' = \frac{G''}{\omega} - \frac{iG'}{\omega} \quad (16)$$

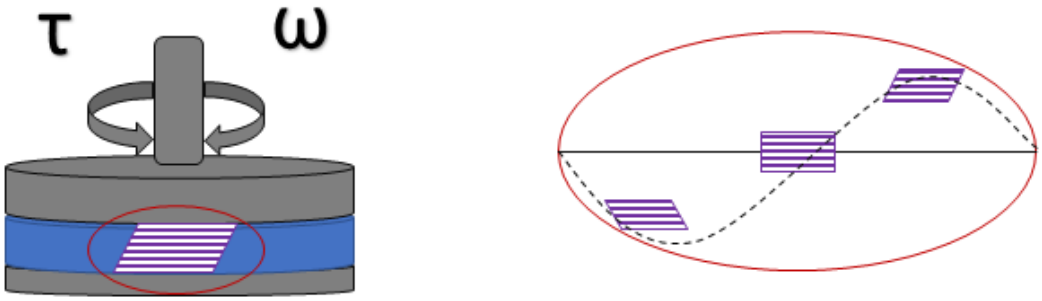

Figure 11.- Illustration of a rheological oscillatory test.

Studying the rheology of ECM-derived hydrogels is essential to develop scaffolds with improved mechanical properties. ECM hydrogels are highly viscoelastic materials (143), so their mechanical behavior varies with time and with variables such as deformation, frequency, or temperature (144). On the other hand, being structures composed of polymeric macromolecules (proteins) and water, their behavior is influenced by the interaction of these two components. Therefore, understanding the rheological behavior of hydrogels is essential to understand how the properties of their components influence their mechanical behavior.

5 3D Bioprinting

3D printing, also known as additive manufacturing (AM), is based on the idea of building a three-dimensional object that has been previously designed or digitized by using a computer. This object is made by depositing material in one layer in the XY plane and then printing more layers in the Z axis. Currently, this technology is used in several fields, such as in the food (145) and fashion industries (146) or in the health sector (bioprinting) (147, 148).

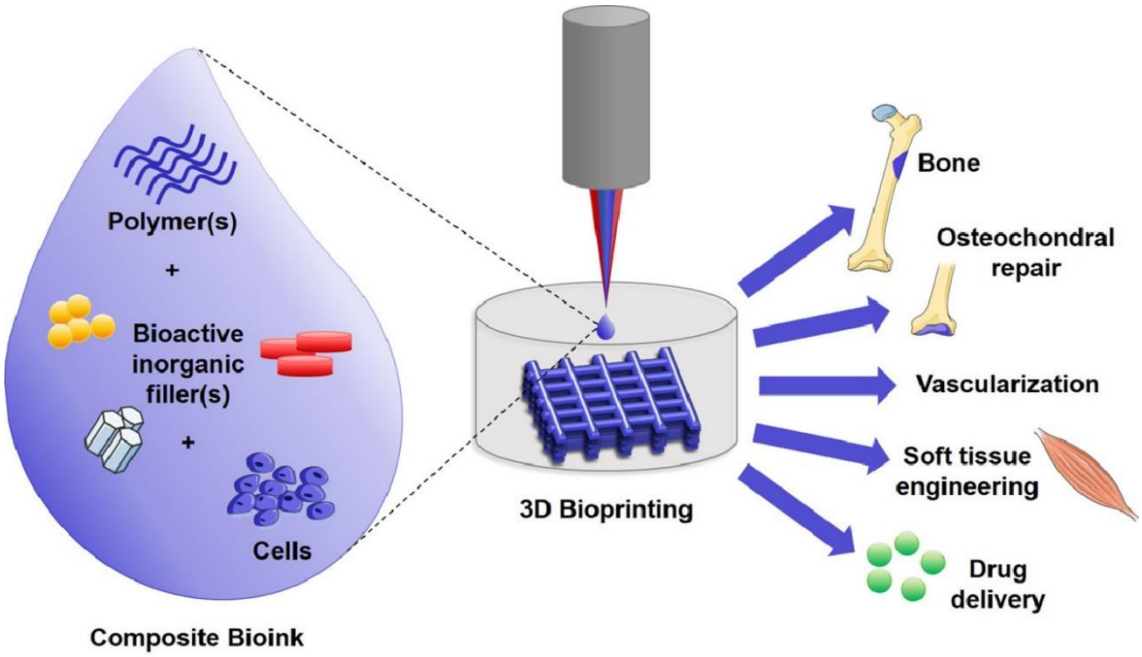

Figure 12.- Scheme of 3D bioprinting process (149).

Bioprinting of scaffolds using AM has been widely used in biomedical research to fabricate, replace, and regenerate damaged tissues. Moreover, this technology, thanks to its ability to faithfully reproduce the structure to be replicated, has opened the door to personalized medicine (150, 151). Thus, thanks to 3D bioprinting, different biomaterials or cell-laden solutions can be deposited layer by layer with great precision (152, 153), both separately and simultaneously. Biomaterials that can be printed, either with or without cells, are usually referred to as bioinks (154, 155).

However, bioinks have different rheological properties depending on the biomaterial they are made of. Therefore, it is mandatory to know the properties of the bioink (rheological properties, gelation kinetics, surface tension, etc.) to optimize the parameters of the printed scaffold (geometry, stiffness, cell density, etc.) (156).

Currently, there are several bioprinting methods, which can be subdivided into three broad categories: material extrusion (piston extrusion, pneumatic extrusion, screw extrusion, etc.), inkjet bioprinting (piezoelectric and thermal) and photopolymerization (stereolithography (SLA), Digital Light Processing (DLP), Laser-Induced Forward Transfer (LIFT), etc.) (157).

Depending on the final application, the bioprinting technique to be used should be different. For example, for skeletal tissue manufacturing, material extrusion

methods, such as Fused Deposition Modelling (FDM), are commonly used (158). On the other hand, the inkjet bioprinting technique is becoming a practical technology for hydrogel-based bioinks (159, 160).

5.1 Extrusion bioprinting

Material extrusion is the most commonly used method in bioprinting (157). Generally, the bioink is introduced into a plastic syringe and extruded mechanically or pneumatically through a nozzle (161). In this method, a bioink filament with a relatively high thickness (approximately 150-300 µm in diameter at least) is extruded (162, 163). Regarding the different extrusion methods, the screw deposition system gives more control over the scaffold definition and can extrude more viscous biomaterials (164); however, the higher pressure generated by this screw system can, due to the higher pressure exerted, break cell membranes, resulting in less cell viability in the developed scaffolds (165). Therefore, thanks to the possibility of adjusting the air pressure, pneumatic deposition is used for a wide range of viscosities.

The main advantage of the extrusion method is the ability to bioprint biomaterials with high viscosity (approximately $3 \cdot 10^5$ mPa·s) with high cell density, even spheroids (156, 166, 167). On the other hand, the main disadvantages of this method are related to its lower resolution than other methods (approximately 1 mm resolution), the possibility of needle clogging and lower cell viability due to shear stress (164, 166, 168).

In the case of bone regeneration, the FDM technique has been used to produce customized bone implants by 3D printing biocompatible materials (169). These implants can be designed to fit the specific shape and size of the defective bone, which can improve patients' ability to heal and reduce the risk of complications (170). In addition, the FDM technique has also been used to produce bone casts for laboratory research (171) and for the production of bio-prostheses to replace damaged or missing body parts (172).

5.2 Inkjet bioprinting

In the inkjet bioprinting method, small droplets of bioink (between 10-50 µm in diameter, equivalent to 1-100 picolitres) are deposited precisely onto a structure or substrate (173). The two most commonly used methods in the inkjet printing of cells are thermal and piezoelectric inkjet bioprinting (174). Although these methods reach very high temperatures locally (over 300 °C), this occurs for a short time (2 µs), and several studies have validated that the cells are not affected by this temperature rise (175, 176, 177).

A key parameter in inkjet bioprinting is surface tension. Surface tension is the result of the cohesive forces that exist between the individual components of the bioink. For reaching droplets in bioprinting by this method, the charges on the surface of the bioink must be weaker than the surface tension (174). However, if cells are added to the bioink, the surface tension decreases, decreasing as the concentration of cells in the bioink increases (178).

One of the main limitations of inkjet bioprinting is the high shear stress it produces on the bioink, which negatively influences cell viability (179). Therefore, bioinks suitable for use with this method must have very low viscosities (<10 mPa-s) and low cell density (<10^6 cells/mL) (156).

5.3 Photopolymerization

In photopolymerization or light-curing, a light source is used to polymerize a biomaterial. This method has been used for several years in the dental field (180). Today, this polymerization is mainly carried out using ultraviolet (UV) light, but also visible light. The wavelengths used range from 254 nm to 800 nm (181). However, when working in the UV region, cell viability can be negatively affected (182). In addition, visible light has been shown to have greater penetration into the material, resulting in more uniform hydrogels (183).

The two most commonly used light-curing methods are Stereolithography (SLA) and Digital Light Processing (DLP). The main difference between both methods is that, in SLA, there is a light source that draws the structure to be crosslinked, while in DLP a

complete image of the layer to be crosslinked is projected at that moment (184). The main advantages of photopolymerization bioprinting are its resolution (50 µm) (185, 186) and the ability to work with bioinks of any viscosity. However, its main limitation is that it does not support working with multicellular structures (187).

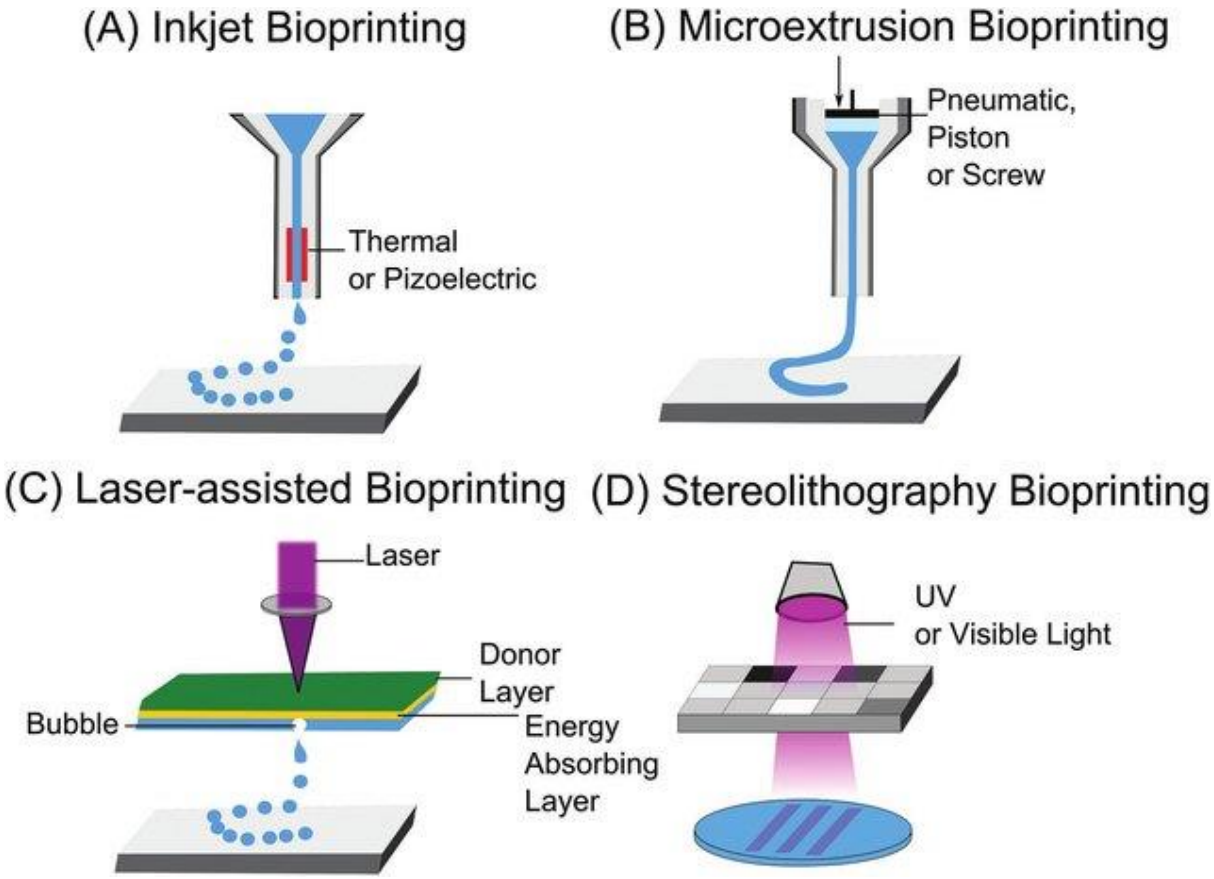

Figure 13.- Schematic view of different bioprinting methods (188).

6 Bioprinted scaffolds for 3D cell culture

6.1 cECM hydrogels in tissue engineering

Several research groups have studied the use of extracellular matrix-derived biomaterials reconstituted in the form of hydrogels, with COL I being the most commonly used material (189, 190, 191, 192). However, the properties of an ideal cellular scaffold should structurally and biologically resemble those present in the ECM of the tissue to be mimicked. Research groups are using decellularized ECM as the main material to make hydrogels nowadays (193, 194, 195).

One of the most studied organs to obtain decellularized ECM is the heart (196); it can be decellularized by perfusion (63) (by cannulating the aorta) or by diffusion (69) (by sectioning the myocardium into thin slices before decellularization).

Wainwright *et al.* developed one of the first protocols for the decellularization of a pig heart by successive retrograde aortic perfusion with hypertonic, hypotonic, enzymatic, acidic, and detergent solutions. They demonstrated how decellularized ECM maintained the collagen, elastin, and GAGs of native tissue, while the biaxial rupture strength of cECM showed no difference compared with native tissue. In addition, they seeded chicken embryonic cardiomyocytes (cCM) on decellularized tissue, showing how the cECM laminin supported the organized formation of cCM sarcomere structure (63).

On the other hand, Singelyn and co-workers reported the first protocol for the decellularization of a pig heart by diffusion and subsequent production of an injectable hydrogel from decellularized cECM. They obtained a hydrogel with a cECM concentration of 8 mg/mL. They compared the cell viability of these hydrogels by seeding neonatal rat cardiomyocytes on top of the structures, demonstrating that the cell viability was comparable to that obtained in collagen hydrogels. In addition, they evaluated the chemo-attractive properties of the hydrogel by analyzing the migration of human coronary artery endothelial cells (HCAECs) and rat aortic smooth muscle cells (RASMCs). The migratory capacity of RASMCs was statistically superior through the cECM-derived hydrogel compared to collagen hydrogels, while no significant differences were seen for HCAECs (197).

Johnson *et al.* extended the work done by Singelyn *et al.* as they analyzed how variations in gelation conditions affected the cECM-derived hydrogel. Specifically, temperature, salt concentration, amount of ECM and pH affect gelation. To do this, they tested hydrogels at two different concentrations (6 mg/mL and 8 mg/mL), pH values (7.4 or 8.5) and salt concentrations (0.5x, 1.0x and 1.5x PBS). Finally, they tried to gel for 24 hours at 4˚C, 22˚C or 37˚C. The first notable result of this study was that, unlike collagen hydrogels, the cECM-derived hydrogels did not form fibrils at 4˚C or 22˚C, remaining liquid at both temperatures; thus, only the material at 37˚C was able to form a hydrogel. Changes in salt concentration proved to be critical in hydrogel stiffness and gelation kinetics. Thus, hydrogels with a 1X PBS concentration required 67.14 ± 3.40 minutes to

gel at 37˚C, while hydrogels with a 0.5X PBS concentration only took 21.27 ± 2.33 minutes. However, hydrogels with a 1.5X PBS concentration required gelation times longer than 8 hours. Changes in pH did not show significant changes. Finally, increasing the cECM concentration from 6 mg/mL to 8 mg/mL showed an increase in the complex viscosity in the liquid state and an increase in the storage modulus once gelled. Therefore, they showed how the properties of cECM-derived hydrogels can be modified by altering their processing conditions (88).

Pati *et al.* used this cECM-derived bioink to bioprint, using a multi-head bioprinter, a three-dimensional cell-laden structure. To print several layers and form a stable structure, they used a support material, polycaprolactone (PCL), which was deposited parallel to the bio-ink to achieve higher resolution. They also managed to bioprint a simple structure using only the cECM-derived bioink, achieving high cell viability (greater than 90% at day 14) and allowing the cells to connect three-dimensionally with each other (198).

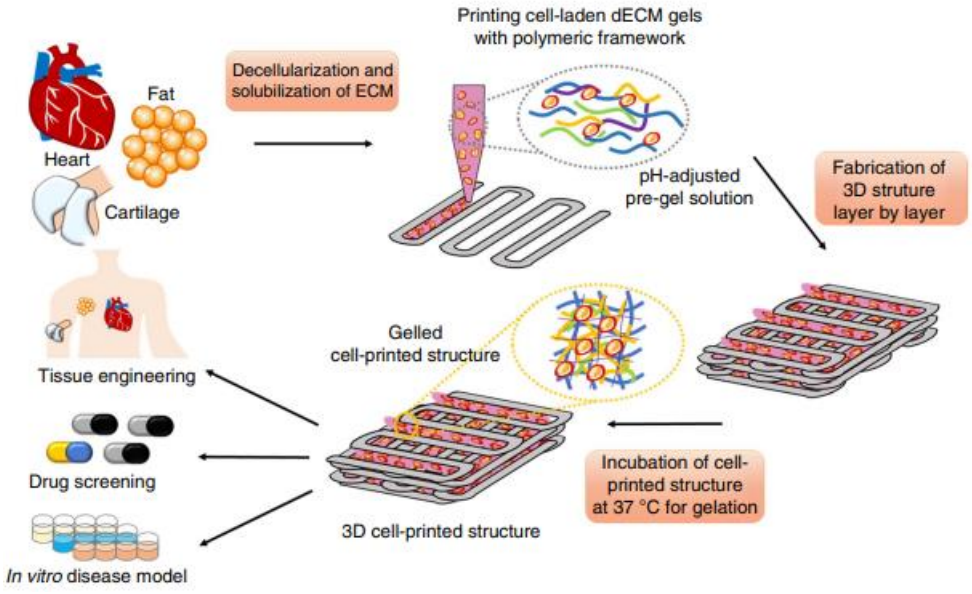

Figure 14.- cECM-derived bioink developed by Pati et al. (198).

Jang and co-workers used the same PCL mechanically supported bioprinting technique to fabricate a patch that could be implanted in vivo on an infarcted heart. To this end, they added Vascular Endothelial Growth Factor (VEGF) intending to achieve rapid vascularization of the cECM-derived scaffold. Cell-laden structures (500 µm of thickness) were bioprinted and implanted *in vivo* on the infarcted area of the left

ventricle. After 28 days, the implanted rats showed improvements in cardiac function compared to the control group (199). This experiment was repeated by Bejleri *et al.*, in this case cross-linking the patch with gelatin methacrylate (GelMA) and adding human cardiac progenitor cells (hCPC) to the bioink. The cell-laden structures were implanted in vivo on infarcted rat hearts and showed improved vascularization and function after 14 days (200).

Recently, Zhu and co-workers described a method for in situ formation of a cECM-derived patch in the intrapericardial region (iPC). To do this, they prepared a pregel with induced pluripotent stem cell-derived cardiac progenitors (iPS-CPCs) and injected it directly into the iPC cavity. In this way, the cavity itself serves as a mold and the body temperature acts as a catalyst for cross-linking the hydrogel, resulting in a cell-laden patch that adheres to the myocardium without the need for surgery or bioglue. Seven days after the injection of the hydrogel into the infarcted heart, they confirmed the differentiation of iPS-CPCs into cardiomyocytes, smooth muscle cells and endothelial cells. In addition, iPC injection of iPS-CPCs promoted angiogenesis, reduction of the infarcted area and decreased the immune response (193) [REF].

Currently, the development of injectable hydrogels is the most studied technique, as can be seen in the most recent published studies on cardiac regeneration (201, 202, 203, 204, 205). However, the drawback of this method is the impossibility of using the scaffold to precondition the cells, since it gels *in situ* at the time of the intervention. Moreover, its use with circulating stem cells, such as Bone Marrow Mesenchymal Stromal Cells (BM-MSCs) (206), means that these may tend to migrate to other tissues if they are not preconditioned in the substrate to be implanted.

6.2 3D printed PLA composite scaffolds

In addition to ECM-derived materials, biocompatible synthetic materials are also available for producing personalized grafts via additive manufacturing. The main advantage of synthetic materials is their tunability. Essential properties such as viscosity, melting temperature, solidification temperature, etc. can be modified. This advantage makes them good candidates for use as a material in 3D printing (207).

One of the fields where most works are being done with synthetic scaffolds is the bioprinting of bone tissue. For this purpose, several materials have been used in bioprinting, including hydroxyapatite (166), zirconia (208), polylactic acid (PLA) (209) or polyvinyl alcohol (PVA) (210), among others. Among them, one of the most widely used in 3D bioprinting is PLA (211). PLA is a polymeric material that is biocompatible, natural, cheap, and biodegradable in the human body (212).

Narayanan *et al.* used PLA nanofibers to reinforce an alginate bioink, resulting in a nano-reinforced hydrogel with human adipose-derived stem cell-laden cells. After testing the cell viability of the hydrogel *in vitro*, they used nuclear magnetic resonance technology to digitally model a patient's meniscus. The meniscus was then bioprinted and evaluated for eight weeks. The results showed higher cell viability in PLA nano-reinforced hydrogels and a 28.5% higher metabolic activity than in hydrogels without PLA nanofibers. Finally, collagen and proteoglycans were present in the area surrounding the cells, showing ECM secretion and chondrogenic differentiation (209). Thus, the use of a biomaterial with the mechanical properties of PLA allows the bioprinting of tissues or organs of complex sizes.

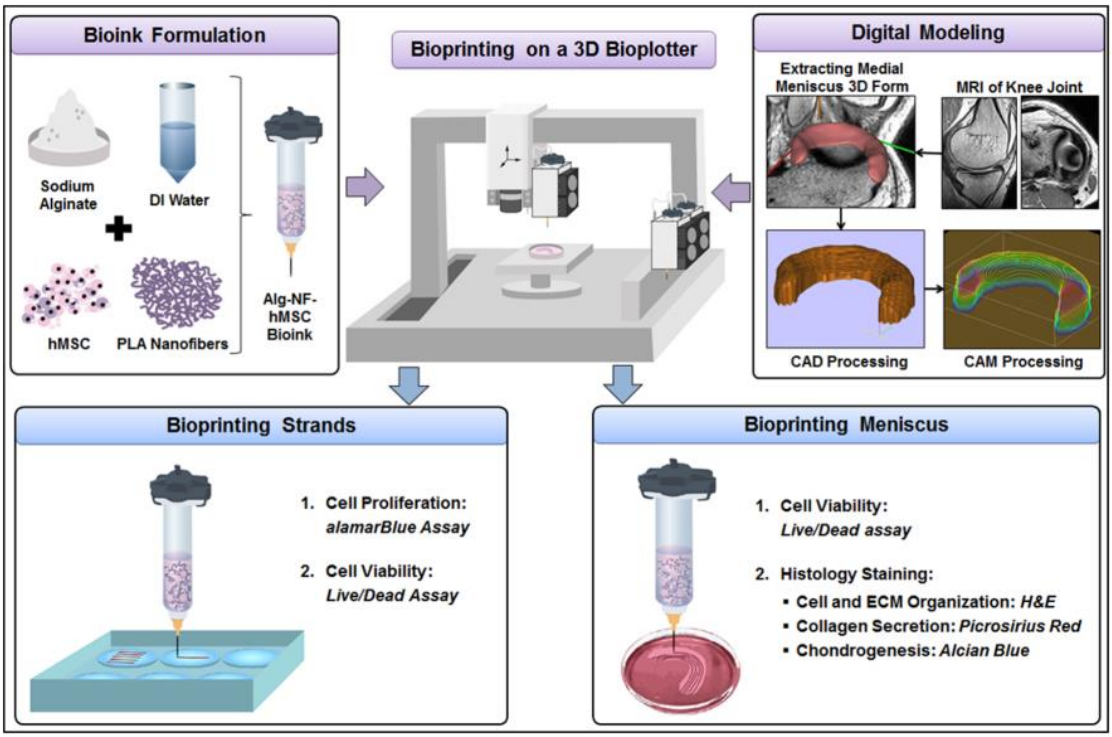

Figure 15.- Bioprinting method for nanofibers-reinforced alginate bioink published by Narayanan et al. (209).

On the other hand, Hu and co-workers used PLA as a rigid and biocompatible support on which to bioprint cell-laden hydrogels. They added murine bone marrow stromal cells to a gelan gum-poly (ethylene glycol) diacrylate (GG-PEGDA) pregel and, using a two-head bioprinter, bioprinted the structure of an intervertebral disc with different patterns and filled them with the bioink. The intervertebral discs bioprinted with this technique tolerated multiple load cycles (0.1 - 3 Mpa) without leaving the elastic zone of the material, thus being able to recover the deformation exerted on them. In addition, the PLA microchannels formed in the printing of the structure facilitated the exchange of nutrients between the cells embedded in the hydrogels (213).

Kolan *et al*. used the same technique of using PLA as a support but added bioactive borate glass (B3) to the PLA. B3 can dissolve rapidly, leaving apatite crystals on the surface, which helped to integrate the scaffolds with soft and hard tissues. To test the cell viability of these scaffolds, they bioprinted a PLA+B3 hybrid structure as support and filled the spaces between lines with a cell-laden gelatin-alginate hydrogel. Cell viability was shown to be over 80% in areas subjected to normoxia (214).

Since metals and alloys have been extensively used as bone substitutes due to their mechanical properties (215, 216), Mohammadizadeh and co-workers developed PLA filaments reinforced with metals such as copper, bronze, or aluminum. Interestingly, the addition of a metal such as copper worsened the mechanical properties (217). In parallel, Liu *et al.* demonstrated that PLA composites with aluminum or copper showed similar or superior mechanical properties compared to pure PLA (218). However, the cell viability of these scaffolds has hardly been studied.

More recently, Hari Rak *et al*. developed a 3D-printed biodegradable PLA orthopedic screw which was surface-modified by the addition of zirconia and titanium oxide to improve the mechanical and biological properties. Since orthopedic implants used to be fabricated using stainless steel or titanium alloys, these materials require replacement after a certain time. Thus, the use of PLA as a matrix material, which has high degradation and biocompatibility properties, solves this problem. The authors used human osteosarcoma cells for analyzing the cell viability of the structures. The scaffold developed in this study showed an improvement in osteointegration and resulted in a suitable composite biomaterial for implants in biomedical applications (219).

Chapter II. Hypothesis of the thesis

THIS THESIS hypothesizes that a hydrogel with tunable stiffness can be developed to mimic the mechanical properties of cardiac tissue, with type I collagen as the main component of the developed scaffold. In addition, this thesis hypothesizes that 3D printed synthetic composite biomaterials are suitable for direct culture of human bone marrow mesenchymal stromal cells, showing positive osteocalcin markers after several days of culture.

Chapter III. Objectives of the thesis

THE MAIN objective of the present work is to develop and characterize novel bioinks for 3D bioprinting in tissue engineering.

Specific objectives:

I) To develop a protocol for the decellularization of porcine myocardium to develop extracellular matrix derived hydrogels.
   a) To optimize the enzymatic digestion time of the matrix to achieve the highest possible stiffness of the resulting hydrogels.
   b) To study the response of cells when cultured in 3D within the developed scaffolds.

II) To study and tune the multiscale biophysical properties of silk reinforced collagen hydrogels to mimic the mechanical properties of the native heart.
   a) To improve the micromechanical stiffness of ECM-derived hydrogels with varying silk content.
   b) To improve the macromechanical stiffness of ECM-derived hydrogels with different silk content.
   c) To enhance the printability of the developed bioinks, measuring the rheological properties of the ECM-derived hydrogels at different strain levels.
   d) To develop bioprinted silk-reinforced hydrogels with fiber diameter ultrastructure similar to tropocollagen fibers.

III) To develop 3D printable composite materials from synthetic materials for bone tissue engineering.
   a) To develop 3D structures suitable for use as *in vitro* models.
   b) To analyze the need of a collagen coating on the developed scaffolds to promote cell adhesion.
   c) To evaluate the response of human bone marrow mesenchymal stromal cells when cultured on the developed scaffolds without collagen coating.
   d) To characterize 3D printed scaffold profilometry by roughness meter analysis to study the suitability for cell culture without the need for post-processing.

Chapter IV. Articles in this thesis

THE SCIENTIFIC articles included in the thesis, in which the Ph.D. candidate was a co-author, are listed below in connection with the different objectives of the thesis:

Aims I and II: To develop and optimize decellularization protocols applicable to complex organs that allow extracting and manipulating their ECM. To study and tune the multiscale biophysical properties of hydrogels developed from ECM of decellularized tissues.

- ***Hector Sanz-Fraile**, Susana Amoros, Irene Mendizabal, Carolina Galvez-Monton, Cristina Prat-Vidal, Antoni Bayes-Genis, Daniel Navajas, Ramon Farre, and Jorge Otero. Silk-Reinforced Collagen Hydrogels with Raised Multiscale Stiffness for Mesenchymal Cells 3D Culture. Tissue Eng Part A. 2020 Mar;26(5-6):358-370. doi:10.1089/ten.TEA.2019.0199. IF: 3.845. Q2 (35/89).*
- **Héctor Sanz-Fraile,** Carolina Herranz-Diez, Anna Ulldemolins, Bryan Falcones, Isaac Almendros, Núria Gavara, Raimon Sunyer, Ramon Farré and Jorge Otero. *Characterization of Bioinks Developed from the Gelification of the Extracelullar Matrix obtained from Decellularized Porcine Myocardia. In manuscript.*

Aim III: To develop additive manufacturing techniques for constructing complex synthetic composite scaffolds.

- *Buj-Corral, Irene; **Sanz-Fraile, Hector**; Tejo Otero, Aitor; Xuriguera, Elena; Otero, Jorge. Biocompatible 3D Yttria-Stabilized Zirconia Parts using Direct Ink Writing. In manuscript.*
- *Irene Buj-Corral, **Héctor Sanz-Fraile**, Anna Ulldemolins, Aitor Tejo-Otero, Alejandro Domínguez-Fernández, Isaac Almendros, Jorge Otero. Characterization of 3D Printed Metal-PLA Composite Scaffolds for Biomedical Applications. Polymers (Basel). 2022 Jul 5;14(13):2754. doi: 10.3390/polym14132754. IF: 4.967. Q1 (16/90).*

Materials, methods, and results

Chapter V. Scientific article I

Silk-Reinforced Collagen Hydrogels with Raised Multiscale Stiffness for Mesenchymal Cells 3D Culture

***Hector Sanz-Fraile**, Susana Amoros, Irene Mendizabal, Carolina Galvez-Monton, Cristina Prat-Vidal, Antoni Bayes-Genis, Daniel Navajas, Ramon Farre, and Jorge Otero*

Tissue Eng Part A. 2020 Mar;26(5-6):358-370

IF: 3.845. Q2 (35/89)

TISSUE ENGINEERING: Part A
Volume 26, Numbers 5 and 6, 2020

DOI: 10.1089/ten.tea.2019.0199

termis
Tissue Engineering
& Regenerative Medicine
International Society

ORIGINAL ARTICLE

Silk-Reinforced Collagen Hydrogels with Raised Multiscale Stiffness for Mesenchymal Cells 3D Culture

Hector Sanz-Fraile, MSc,[1] Susana Amoros, MSc,[23] Irene Mendizabal, MSc,[1] Carolina Galvez-Monton, PhD,[2–4]
Cristina Prat-Vidal, PhD,[2–5] Antoni Bayes-Genis, MD, PhD,[2–4,6] Daniel Navajas, PhD,[1,7,8]
Ramon Farre, PhD,[1,7,9] and Jorge Otero, PhD[1,7]

Type I collagen hydrogels are of high interest in tissue engineering. With the evolution of 3D bioprinting technologies, a high number of collagen-based scaffolds have been reported for the development of 3D cell cultures. A recent proposal was to mix collagen with silk fibroin derived from *Bombyx mori* silkworm. Nevertheless, due to the difficulties in the preparation and the characteristics of the protein, several problems such as phase separation and collagen denaturation appear during the procedure. Therefore, the common solution is to diminish the concentration of collagen although in that way the most biologically relevant component is reduced. In this study, we present a new, simple, and effective method to develop a collagen–silk hybrid hydrogel with high collagen concentration and with increased stiffness approaching that of natural tissues, which could be of high interest for the development of cardiac patches for myocardial regeneration and for preconditioning of mesenchymal stem cells (MSCs) to improve their therapeutic potential. Sericin in the silk was preserved by using a physical solubilizing procedure that results in a preserved fibrous structure of type I collagen, as shown by ultrastructural imaging. The macro- and micromechanical properties of the hybrid hydrogels measured by tensile stretch and atomic force microscopy, respectively, showed a more than twofold stiffening than the collagen-only hydrogels. Rheological measurements showed improved printability properties for the developed biomaterial. The suitability of the hydrogels for 3D cell culture was assessed by 3D bioprinting bone marrow-derived MSCs cultured within the scaffolds. The result was a biomaterial with improved printability characteristics that better resembled the mechanical properties of natural soft tissues while preserving biocompatibility owing to the high concentration of collagen.

[1] Unit of Biophysics and Bioengineering, School of Medicine and Health Sciences, Universitat de Barcelona, Barcelona, Spain.
[2] ICREC Research Program, Germans Trias i Pujol Health Science Research Institute, Badalona, Spain.
[3] Hearth Institute (iCor), Germans Trias i Pujol University Hospital, Badalona, Spain.
[4] CIBER Cardiovascular, Instituto de Salud Carlos III, Madrid, Spain.
[5] Institut d'Investigacio´ Biome`dica de Bellvitge, IDIBELL, L'Hospitalet de Llobregat, Spain.
[6] Department of Medicine, Autonomous University of Barcelona, Barcelona, Spain.
[7] CIBER de Enfermedades Respiratorias, Instituto de Salud Carlos III, Madrid, Spain.
[8] Institute for Bioengineering of Catalonia (IBEC), The Barcelona Institute of Science and Technology, Barcelona, Spain.
[9] Institut d'investigacions Biome`diques Agustı´ Pi i Sunyer, Barcelona, Spain.

Keywords: collagen, silk, hydrogel, mesenchymal cells, 3D bioprinting, multiscale mechanics

Impact Statement

In this study, we report the development of silk microfiber-reinforced type I collagen hydrogels for 3D bioprinting and cell culture. In contrast with previously reported studies, a novel physical method allowed the preservation of the silk sericin protein. Hydrogels were stable, showed no phase separation between the biomaterials, and they presented improved printability. An increase between two- and threefold of the multiscale stiffness of the scaffolds was achieved with no need of using additional crosslinkers or complex methods, which could be of high relevance for cardiac patches development and for preconditioning mesenchymal stem cells (MSCs) for therapeutic applications. We demonstrate that bone marrowderived MSCs can be effectively bioprinted and 3D cultured within the stiffened structures.

Introduction

Hydrogels are hydrophilic polymer networks holding vast quantities of water and presenting mechanical properties similar to those found in soft biological tissues. With the development of 3D bioprinting technology, which allows for customized and high-throughput development of scaffolds, the research interest in naturally derived hydrogels for tissue engineering and regenerative medicine applications has increased dramatically. Scaffolds based on cell-laden hydrogels can be 3D printed layer-by-layer using different technical approaches.[1] Hydrogels mimicking native soft tissue microenvironments and 3D constructs with different shapes can be fabricated in an automated way. In recent years, a high number of different biomaterials have been used as 3D scaffolds for cell culturing and for 3D bioprinting.[2]

Naturally derived type I collagen hydrogels are widely employed since they are biocompatible and biodegradable and, importantly, because they can modulate cell function because their fibrous structure of binding ligands to cell surface receptors.[3] Collagen I hydrogels have the drawback that they experience considerable volume reduction when cells are cultured within them.[4] Another limitation of collagen I hydrogels is that they exhibit a stiffness (a few hundreds of Pa) that is lower than natural tissues such as those in the lung and heart. Given that mesenchymal stem cells (MSCs) are mechanosensitive,[5] it is important to culture them in a physiomimetic mechanical environment, which requires a 3D substrate stiffer than conventional collagen I hydrogels.

Modification of the mechanical properties of the 3D scaffolds where MSCs are cultured is a growing research area for several tissue engineering applications. *In vivo*, one of the most important applications is the generation of cardiac patches for myocardial infarction therapy.[6] Although MSCs have very limited capacity for cardiac differentiation, they have a therapeutic impact in cardiac regeneration mainly due to their immunosuppressive profile and paracrine effects.[7] Scaffolds are needed because it has been shown that only a small percentage of the transplanted cells (by injection or perfusion) engrafts into the host myocardium, with the result that the duration of the therapeutic secreted factors is quite limited[8] if the cells are transplanted without a scaffold for retaining them close to the damaged tissue. Commercially available cardiac patches are based in glutaraldehyde-fixed bovine pericardium,[9] but they present several limitations and *25% of patients need a second surgery after a short period of time.[10] Accordingly, considerable research is currently developed in this field.

In vitro, it is well known that the secretion of several cytokines is regulated by the stiffness of the microenvironment where MSCs are cultured.[11] In cardiac tissue engineering, it has been shown that differentiation requires stiffer scaffolds (with elastic modulus in the range of hundreds of kPa) while beating behavior is better accomplished with softer scaffolds (elastic modulus in the range of kPa).[12] Therefore, the tunability of the mechanical behavior of scaffold is of high importance for the *in vitro* culture of MSCs aimed at therapeutic applications,[13] for instance when culturing cells for cardiac patches where their paracrine effects should be enhanced while differentiation is not an objective.

3D bioprinting is considerably modifying the production processes of scaffolds as it offers the possibility to fabricate a high number of replicates, thus reducing the batch-tobatch variability.[14] Thus, besides having the desired mechanical properties, hydrogels for cardiac patches and for scaffolds to precondition MSCs should be easily bioprintable. Stiffer collagen hydrogels can be obtained by increasing protein concentration,[15] although this procedure makes difficult their manipulation and 3D printability

because of a dramatic decrease in gelation time.[16] Moreover, their viscosity in the pregel phase is not stable, which makes difficult to set up the bioprinter as the pressure applied needs to be adapted during the printing process.

Another possible strategy to obtain stiffer hydrogels is by means of physical (usually with UV radiation) or chemical crosslinking the collagen structure.[17] Nevertheless, such crosslinking processes are known to modify the physiological cell response (or even to be cytotoxic) when culturing MSCs within the scaffolds.[18] However, a common strategy to increase hydrogel stiffness is to mix collagen with other natural or synthetic biomaterials, being alginate,[19] polyethylene glycol, and polycaprolactone[20] the most widely employed.

Recently, silk-derived materials have started to be used with this purpose.[21–23] Although it is possible to obtain silk from spiders,[24] the vast majority of reported studies use silk derived from the *Bombyx mori* silkworm. This material has been used for years in the textile industry, so it is cheap and highly available, and it also has shown its potential as biomaterial for tissue engineering[25,26] due to its high biocompatibility, which is comparable with that of polylactic acid and collagen.[27–29] Silk is a fibrous protein mainly composed of fibroin and sericin. The majority of studies in tissue engineering have used fibroin,[30] because sericin was supposed to have immunogenic activity.[31] Nevertheless, more recent studies have shown no clear differences in immunological response when using silk fibroin or sericin.[32] Moreover, some studies are presenting sericin as a highly interesting biomaterial, mainly due to its positive effects in mesenchymal cells like fibroblasts.[33,34]

The aim of this study was to improve the integration between collagen and sericin-preserved silk to obtain a useful bioink for 3D bioprinting hydrogel scaffolds to be potentially applied in tissue engineering and regenerative medicine, such as the development of stiffened cardiac patches and new microenvironments for the preconditioning of MSCs. To this end, we designed and tested a new, simple, and effective method to dissolve raw silkworm cocoons by physically milling them into liquid nitrogen (LN_2) and using NaOH as solvent. The ultrastructure of the resulting hydrogels and their macro- and microscale properties were assessed by scanning electron microscopy (SEM), tensile stretch (TS) tests, and atomic force microscopy (AFM), respectively. The culture of 3D bioprinted bone marrow-derived MSCs (BM-MSCs) within the resulting scaffolds was also tested.

Materials and Methods

Preparation of silk microfiber-reinforced type I collagen hydrogels

All animal care and experimental procedures were approved by the ethical committee for animal research of the University of Barcelona. Rat-tail type I collagen was extracted by following the protocol described in Rajan *et al.*[35] In brief, tails from Sprague-Dawley rats (male, 350g) were collected as a by-product from other experiments in the animal facilities of the School of Medicine. Tendons were extracted from the tails, rinsed with phosphate-buffered saline (PBS), acetone, and isopropanol, and then dissolved in 0.02N acetic acid at 4C for 48h. The solution was then freeze dried (Telstar Lyoquest-55 Plus, Terrassa, Spain), and the resulting sponge was solubilized in 0.02N acetic acid at a concentration of 10mg/mL and stored at 4C for further use.

Silk was obtained from raw (sericin-preserved) *B. mori* silkworm cocoons (AYARA Health, Yangon, Myanmar). Cocoons were rinsed in deionized (DI) water and then milled in LN_2 by using a cryogenic mill (SPEX 6755, NJ) to obtain a micron-sized powder and stored at -80C for further use. To prepare the pregels, powder was dissolved in 1M NaOH under magnetic stirring until no particles were visible.

Pregel mixtures were prepared by stabilizing the pH of the type I collagen to 7.4–0.4 with 1M NaOH, and by stabilizing the pH of the silk solution with 2M HCl for a final silk concentration of 70mg/mL. For gelation, the collagen pregel was mixed with ice-cold pH-neutralized silk at different ratios of collagen–silk protein (4:1, 2:1, 4:3, and 1:1, which will be referred as 25%, 50%, 75%, and 100% of silk content with respect to the collagen, respectively), resulting in a final concentration of the collagen protein of 7.8mg/mL. For 3D structures formation, the pregels were incubated at 37C for 45min to jellify.

Bioink development

Human BM-MSCs (ATCC, VA) were expanded following the manufacturer's instructions. Expanded BM-MSCs were trypsinized and resuspended in culture media ($1 \cdot 10^6$ cells/mL) and mixed with the collagen control, 50%, and 100% silk-containing collagen pregels before 3D bioprinting (n=3 for each concentration). Control BM-MSCs were cultured on standard plastic substrate. All experiments were conducted with cells at passages 2–4.

Ultrastructure characterization by scanning electron microscopy imaging

The ultrastructure of the constructs was characterized using SEM by adapting the protocol described in Wolf *et al.*[36] In brief, acellular and BM-MSCs laden hydrogel scaffolds (cells cultured for 48h) containing 0%, 50%, and 100% weight silk content with respect to the collagen protein were fixed for 48h in 4% paraformaldehyde in PBS and then washed three times in 0.1M phosphate buffer for 10min each and then incubated in 4% OsO_4 for 90min. The next step was a series of washes with DI water until there was no OsO_4 inside the container where the samples were hanged on. Then, samples were dehydrated in ethanol solutions, with increasing concentrations from 50% till absolute ethanol at 4C, and critical point dried (autosamdri-815 critical point dryer; Tousimis, Rockville, MD). Samples were mounted using conductive adhesive tabs (TED PELLA) and they were carbon coated before imaging with a JSM-6510 (JEOL, Tokyo, Japan) SEM at 3kV.

Swelling and degradation

Swelling and degradation of the scaffolds were studied as described in Wang *et al.*[37] After preparation of the three replicates for each condition of the hydrogels, they were weighted, freeze dried, and immersed in PBS at pH 7.4. During 3 weeks, hydrogels were taken out at certain time points and weighted to determine the amount of water, and the results are expressed as the percentage with respect to the original weight before freeze drying.

Measurement of microscale mechanical properties by atomic force microscopy

The microscale stiffness of silk-containing acellular hydrogels was measured by AFM. Hydrogels with specific geometries for these measurements were developed by bioprinting molds in F-127 hydrogel (pluronic) (3D Discovery bioprinter; RegenHU, Switzerland). Squared structures (5·5· 0.1mm) were bioprinted on top of positively charged glass slides and then the pregels were casted into them. After gelation, pluronic was removed by immersion in PBS at 4C for 10min. All measurements were performed inside a bath with PBS at 37C.

Three batches of three replicates for each sample were fabricated for each silk–collagen mixture of the hydrogels. Measurements were conducted by using a custom-built AFM mounted on an inverted optical microscope (TE2000; Nikon, Tokyo, Japan) equipped with a V-shaped silicon nitride cantilevers (0.03N/m nominal spring constant) ended with a 5mm radius spherical polystyrene bead (Novascan Technologies, Ames, IA). Elastic modulus was computed from the force–displacement curves by adjusting the Hertz model as described in Alcaraz *et al.*[38] The micromechanics of each sample were measured in four randomly

selected zones. Five force curves (1Hz and 10mm amplitude) in four points randomly selected and separated *50–100mm from each other were recorded in each zone.

Micromechanical stiffness (E_m) of each sample was characterized as the average from the different curves recorded in the sample. The values for each batch were calculated as the average of the measurement of three samples (n=3).

Assessment of macroscale mechanical properties by tensile stretch and bulk compression tests

For TS, three batches of four strips of hydrogels, each 5·2·2mm, were fabricated for each concentration mixture condition of the collagen–silk hydrogels following the same procedure than for the AFM samples. One end of the strip was glued with cyanoacrylate to a small hook attached to the lever of a servo-controlled displacement actuator with an integrated force sensor (300C-LR; Aurora Scientific, Aurora, Canada), which permitted stretching the strip and measuring both the stretched length and the applied force simultaneously. The other end of the strip was glued to a fixed hook. The stress and the elastic modulus at 20% of stretch of each strip were computed from a series of 10 force–displacement curves at 0.2Hz frequency and 30% strain, as described in Farre´ *et al.*[39]

In brief, the strain–stress curves were calculated from the force–displacement curves using geometrical measurements to calculate the cross section, and the macroscale elastic modulus (E_M) was computed by local derivation of the curve around the 20% stretching point. The values for each batch were calculated as the average of the measurement of four strip replicates (n=3).

For bulk compression measurements, a batch of three collagen–silk hydrogels was fabricated for the control, 50%, and 100% mixtures. Each hydrogel was shaped as a cylinder of 15.6mm base and 10mm height and covered with a 16mm flat-ended cylindrical indentator. Compression modulus was measured by applying a compressive force with a custom-made base indentator system attached to a servocontrolled displacement actuator with an integrated force sensor (305C; Aurora Scientific), which permitted compressing the sample and measuring both the compressed length and the applied force simultaneously.

A series of 10 force–displacement curves at 0.2Hz frequency were measured using this system for each sample: the first and last curves were discarded for cohesion purposes. The elastic modulus at compression of each sample was computed from the mean of those eight curves given the linear relationship between the penetration and the mean contact pressure due to the constant contact area by using Eq. (1).

$$P_m = \frac{2Eh}{\pi a(1-\upsilon^2)}, \quad (1)$$

where P_m is the mean contact pressure, E the elastic modulus of the sample, h the penetration, a the radius of the indenter, and m the Poisson ratio (assumed 0.5).

Printability characterization

Hydrogel rheological properties were measured by using a HAAKE RheoStress 1 rheometer (ThermoFisher, MA) with 35mm serrated parallel plate geometry. Hydrogels were neutralized just before mechanical testing was done. To test the hydrogels, pregel solution was loaded onto a Peltier plate set at 4C and with a distance between plates of 200mm. The storage modulus ($G¢$), loss modulus ($G†$), and dynamic viscosity (l) were measured at a constant 0.1Hz with a strain of 5%. The temperature of the plates was constant at 4C for 15min, then increased to 37C, and held constant for 15min more.

For 3D bioprinting, a cartridge of the 3D bioprinter (3Ddiscovery; RegenHU) was filled

with the pregel solution mixed with the cells and maintained at 4C during all the printing process. A secondary printing cartridge was filled with Pluronic F127 gel (40% v/v in PBS) at room temperature. Hydrogels were printed at *2 bar of pressure using a nozzle of 330mm (Nordson EFD) and F127 was printed at *4.5 bar using a needle of 200mm (Nordson EFD). The 3D structures were then constructed layer-by-layer by alternatively printing an F127 layer, which served as a template, and a pregel layer that filled the F127 template layer. After the last layer was printed, the 3D structures were incubated at 37C to form the hydrogel. F127 structure was finally dissolved by immersing the structures in culture media at 4C for 10min.

3D bioprinted cell cultures

BM-MSCs were cultured within the scaffolds and imaged after staining them with a Live/Dead viability kit (ThermoFischer) following the manufacturer's instructions. Cells were stained with calcein AM (live cells, green) and EthD-1 (dead cells, red) after 4h and 7 days of 3D bioprinting the scaffolds (1.5mm in height). As silk presented high autofluorescence in the red channel, only qualitative analysis of the green channel of the images was done. For morphological analysis of the cells within the hydrogels, structures at 48h were fixed in 4% paraformaldehyde for 48h and then immersed in optimal cutting temperature compound (OCT; Sigma) and frozen at -80C. Thin tissue slices (*70mm) were obtained by cryosectioning (CM3050; Leica Microsystems, Germany) and placed on top of positively charged glass slides. OCT was removed by thawing and washing the samples in PBS solution at room temperature. Samples were then stained for DNA (NucBlue) and F-actin (phalloidin). Stained scaffolds were then imaged by confocal microscopy (TI-HUBC; Nikon) with a 60·objective.

Statistical analysis

Data are expressed as mean–standard error. One-way analysis of variance (ANOVA) tests were performed to compare changes induced by the different concentrations of silk in the mixture. Statistical significance was considered at p-values <0.05.

Results

Ultrastructure of the scaffolds

Macroscopic images showed no phase separation between both materials in the hydrogels (Fig. 1a). The ultrastructural images (Fig. 1b, c) showed a good integration of BM-MSCs within the scaffolds, as well as the incorporation of the silk fibers in the collagen matrix of the hydrogels. Formation of collagen microfibrils (*100–200nm) did not seem to be affected by the incorporation of the silk fibers (*5–10mm).

Swelling and degradation

Hydrogels formed purely from collagen or with a 50% silk content recovered 70–80% of their original weight, whereas hydrogels with 100% of silk content recovered their full weight after a couple of days. There was no observable degradation of the hydrogels after that during the 3 weeks of the experiment.

Microscale mechanical properties

The microscale elastic moduli of the hydrogels were increased by about twofold in the silk–collagen mixture as compared with pure collagen, increasing with silk concentration up to a maximum that was found at the 50% and 100% of silk content (E_m=1.26–0.17kPa and 1.31–0.23kPa, respectively) with respect to the pure collagen control (E_m= 0.62–0.13kPa). Values for hydrogels with 25% and 75% of silk fell in between, being E_m of 1.05–0.15kPa and 1.14– 0.03kPa, respectively. One-way ANOVA revealed a statistical significant effect of silk in the microscale stiffness of the hydrogels (p=0.019), which was also significant when comparing each individual concentration with the pure collagen control, as shown in Figure 3.

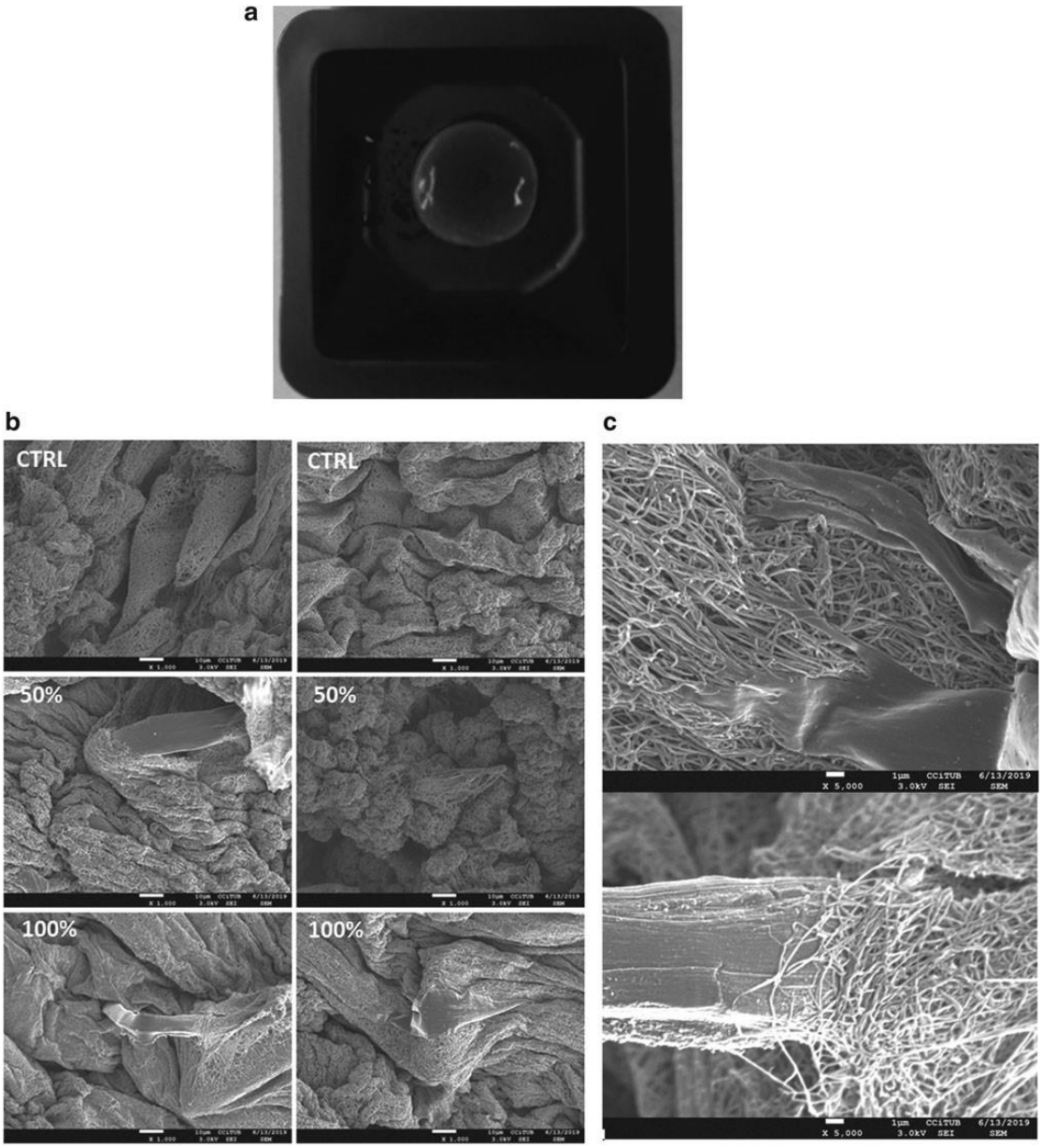

FIG. 1. Ultrastructure images acquired by scanning electron microscopy. (a) Photograph of the 100% silk-containing (with respect to collagen) hydrogels showing that there is no phase separation in the scaffolds between collagen and silk. (b) Different acellular and cellularized scaffolds. (c) Details of the 100% images show how the cell was making junctions with the collagen fibers and the silk microfiber is well integrated within the collagen hydrogel.

Macroscale mechanical properties

At 20% strain, control samples showed a stress of 0.70–0.08kPa and a macroscale elastic modulus E_M of 9.93–2.50kPa. The macroscale mechanical properties were increased by more than twofold in the silk-reinforced hydrogels, increasing with the silk concentration up to a maximum that was found at the 75% (stress of 1.77– 0.05kPa and E_M of

31.16–2.96kPa) and decreasing in the 100% of silk content (stress of 1.11–0.11kPa and E_M of 18.42–2.22kPa). Values at 25% and 50% concentrations fell in between of the control and the 75% (stress = 1.24–0.05kPa and E_M = 19.34–3.41kPa for the 25% and stress = 1.43–0.34kPa and E_M=23.89–5.82 for the 50%).

One-way ANOVA revealed a statistically significant effect of silk in the macroscale stress (p<0.001) and E_M (p<0.001) at 20% of strain of the hydrogels, and for all the groups, as shown in Figure 4b. Compression test results agree with the behavior observed for the tensile tests, with calculated elastic modulus of 2.6kPa (50% silk content), 2.3kPa (100% silk content), and 1.6kPa (control).

Rheological characterization

Viscosity and shear modulus increased with the incorporation of the silk into the hydrogels (Figure 5). Interestingly, at 4C they remain constant for the silk-reinforced hydrogels, while increasing in the pure collagen hydrogels.

Bone marrow derived-mesenchymal stem cells 3D culture within the scaffolds

A high number of viable BM-MSCs were observed at both 4h and 7 days within the collagen scaffolds and no remarkable difference was found for cells cultured in the 50% silk-incorporated scaffolds and with 100% of silk content. Cell distribution was homogeneous in the three directions of the scaffolds as shown in Figure 6. Morphology of the cells cultured in the silk-reinforced scaffolds for 7 days was more elongated with respect to the pure collagen control as shown in Figures 6 and 7.

Discussion

This study presents a novel physical method to solubilize and mix silk from *B. mori* cocoons and type I collagen from rat tails. This straightforward method produces stiffened and stable hydrogel structures that are suitable for 3D bioprinting and culturing of MSCs. Interestingly, incorporation of silk microfibers into the collagen hydrogels results in a twofold increase of their macro- and micromechanical stiffness with no induction of phase separation between the materials nor affecting cell viability in the 3D cultures.

The hydrogels preparation method described here is highly compatible with tissue engineering applications due to the preservation of biocompatibility since no hazardous reagents or high temperatures were used. Cryogenic milling is a physical technique that is widely used in the preparation of extracellular matrix (ECM)-based biomaterials,[40] and alkaline buffer solubilization of silk is a common procedure.[41] Moreover, acid extraction of type I collagen is known to better preserve telopeptides in the tropocollagen molecules than pepsin-based solubilization,[42] and thus it produces collagen fibrils with enhanced capabilities to interact between them and with other proteins,[43] as confirmed by SEM images.

In keeping with the aim of the study, silk-reinforced collagen scaffolds were produced (maximum silk concentration of 100% with respect to collagen concentration) instead of collagen-functionalized silk scaffolds. A multiscale mechanical analysis was carried out to assess the relationship between the increase in hydrogel stiffness and silk content, since this is an adequate methodology to obtain a complete picture of the mechanical response of ECM and ECM-mimicking materials.[44] BM-MSCs, which are nowadays one of the gold standards in regenerative medicine due to their translational potential,[45,46] were cultured within the scaffolds and a high number of viable cells were observed after 1 week.

Type I collagen is a good scaffold for 3D cell culture, and the incorporation of silk in the preparation of the hydrogels showed an improvement in their properties in the presented multiscale study. Some authors have reported methods for

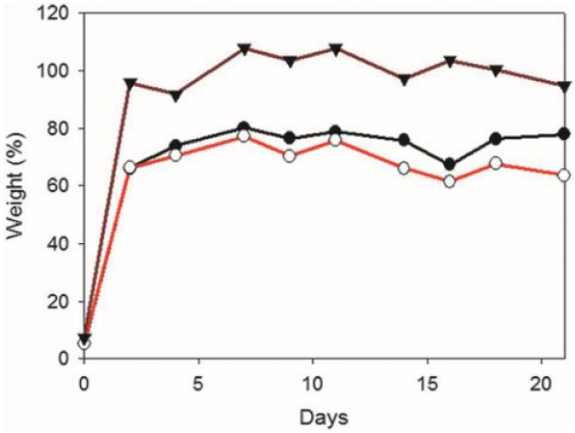

FIG. 2. Swelling and degradation for the control (*black*), 50% (*red*), and 100% (*brown*) silk content hydrogels. At time 0, the hydrogel was freeze dried, and the swelling is expressed in percentage with respect to the original weight before freeze drying. Color images are available online.

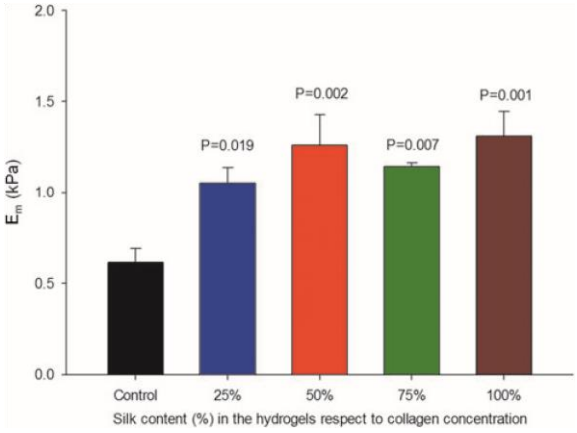

FIG. 3. Local elastic modulus measured with atomic force microscopy (E_m) for the different silk content in the hydrogels. Color images are available online.

mixing type I collagen and purified silk fibroin or degummed silk cocoons (without sericin).[22,47] However, using silk fibroin alone limits the mixture to have low concentrations in collagen, and phase separation between the materials is often observed. The improvement of blending (by inducing electrostatic interactions between the two polymers) is usually carried out by methods requiring considerable changes in temperature,[48] complex techniques such electrospinning,[49] or using additional crosslinkers.[50] Nevertheless, these procedures may result in poor performance or even in denaturation of type I collagen. In addition, phase separation has been observed when mixing collagen with degummed silk cocoons[47] when no additional crosslinkers, such as horseradish peroxidase or genipin, were used to create additional bonds in the structure.[51–53]

The ultrastructural images of the hydrogels developed in this study showed that there is no phase separation between the two biomaterials or denaturation of the collagen fibrils[54] or silk microfibers. As fibroin is mainly hydrophobic[55] and sericin is highly hydrophilic,[56] the presence of sericin in the developed hydrogels may help in the formation of the structures due to its water retention capability,[57] confirmed by the swelling results (Fig. 2). In fact, it has been reported that sericin addition improves the stability of collagen fibrils.[58] The presence of the hydrophilic serine from sericin[56] could aid the interaction between the alanine from the fibroin beta sheets[59] and the proline from the collagen triple helix, because both amino acids are of hydrophobic nature. Therefore, the presence of sericin in the hydrogels seems to help in forming the silk microfiber structures and their interaction with the collagen hydrogel observed in the SEM images (Fig. 1).

Some studies have shown that composite silk scaffolds, developed by mixing fibers and hydrogels, have an impact in the robustness of the constructs,[60] which is in concordance with the results obtained in this study for the silk–collagen composite scaffolds.

Macroscale mechanics of the developed hydrogels was studied by uniaxial tensile testing and bulk compression. By using a bioprinted mold in pluronic to cast the hydrogels before gelation, samples with very similar geometries were obtained, thereby reducing the variability

and artifacts in the experiments. Differences in the macromechanics were quantified by the stress and elastic modulus at 20% strain, which is a strain with physiological relevance in biological application such those involving cardiac[61] and respiratory[62] diseases. The values obtained for pure collagen strips were in agreement with previously reported data.[63] Reinforcing collagen with silk microfibers showed an increase in the values of the stress and elastic modulus up to a maximum found at the 75% of silk concentration, where the increase was between two- and threefold with respect to the control (Figs. 3 and 4).

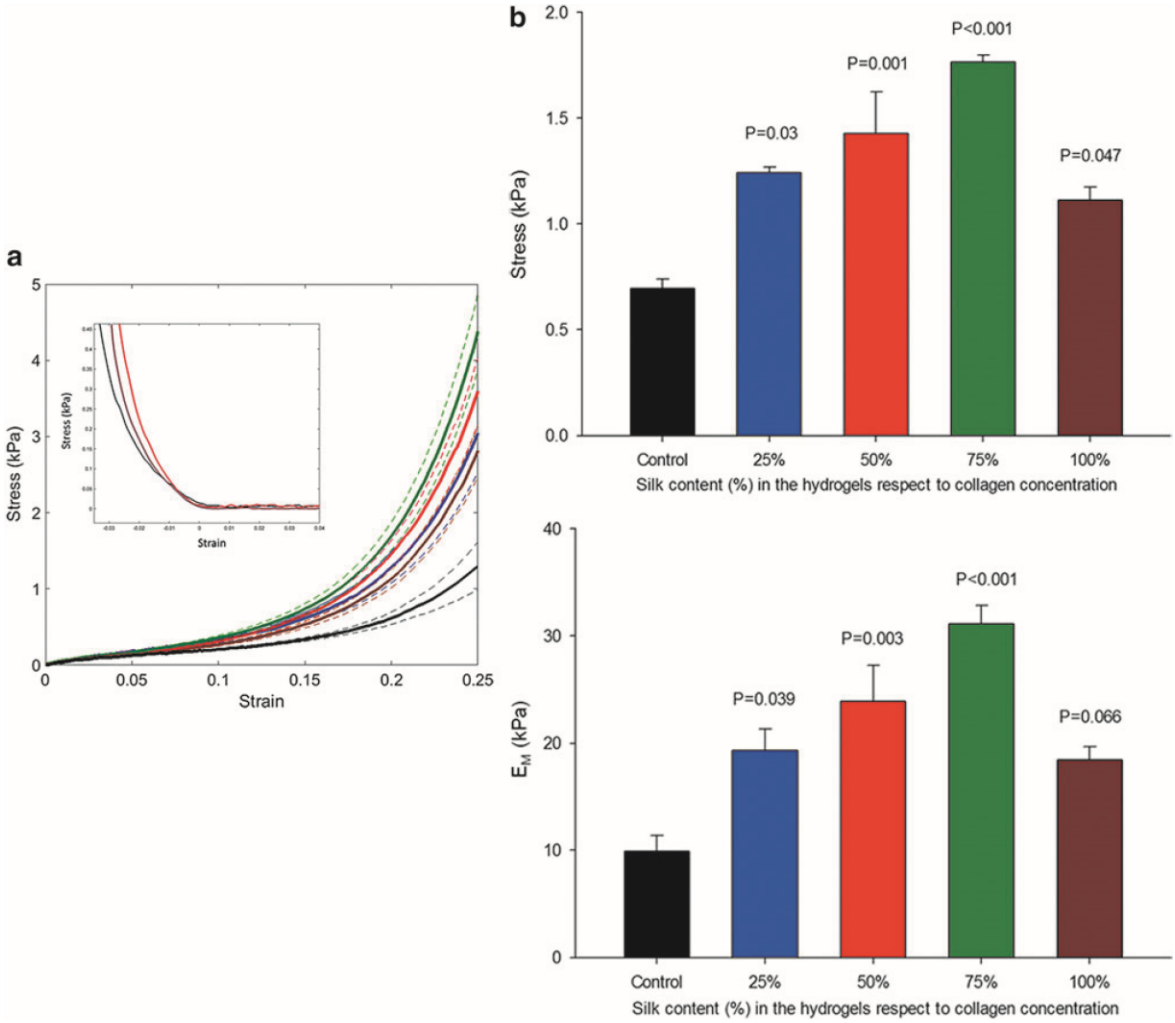

FIG. 4. Macroscale mechanical properties of the hydrogels. (a) Strain–stress curves for the control (*black*), 25% (*blue*), 50% (*red*), 75% (*green*), and 100% (*brown*) silk content. Data are mean (*solid lines*)–standard error (*dashed lines*). Bulk compression data are shown in the *inset* for control and silk concentration of 50% and 100%. (b) Stress and elastic modulus (E_M) at 20% of strain. Color images are available online.

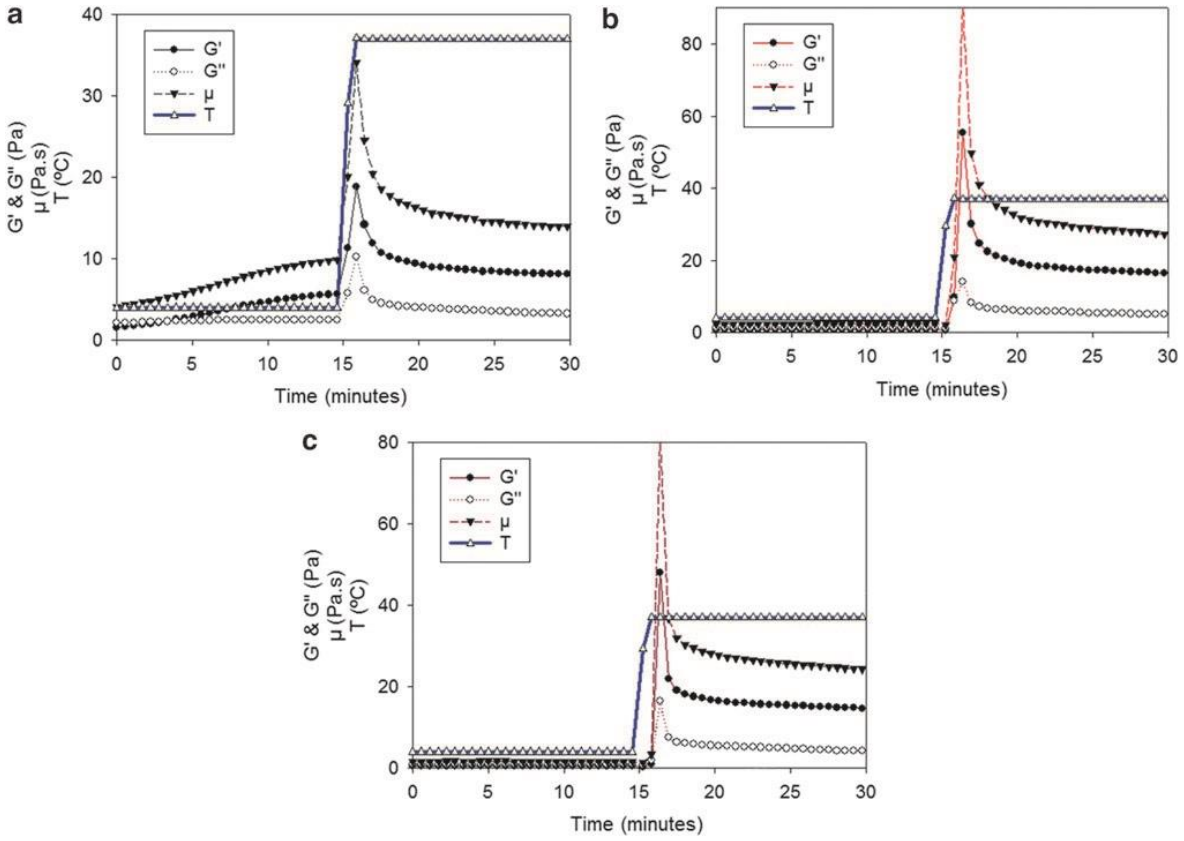

FIG. 5. Rheological data (storage [G¢] and loss [G†] moduli, and dynamic viscosity [l]). Temperature (T) was varied from 4 to 37C. (a) Collagen control. (b) 50% of silk content. (c) 100% of silk content. Color images are available online.

The appearance of a maximum augmentation of elastic modulus for a given silk concentration was already observed in degummed and powdered silk cocoons but with much lower increased stiffness and lower elongation (the samples broke at *20% strain, whereas in our experiments, no samples was broken at 30% strain test).[47] These results are in keeping with the concept that sericin contributes to building the structure. Microscale mechanics of the hydrogels were assessed by AFM, which is the best-suited technique for mechanical measurements in the length scale at which cells sense their micromechanical niche.[64] The results we obtained are consistent with those measured by the macroscale measurements, with an augmentation of the microscale elastic modulus of about twofold in between the 50% and 100% of silk content (Fig. 1). Therefore, it seems that the observed increase in macroscopic stiffness is related to the microstructure of the hydrogel and to the good integration between fibrils and microfibers due to the presence of sericin.

The rise in stiffness (between two- and threefold) achieved with the new method proposed here could seem a modest improvement, but it is of high importance as the main protein in the scaffolds is still type I collagen. Moreover, the ability to tune the mechanical properties without substantially changing the concentration of collagen is of high importance in modeling healthy and diseased soft tissues, as it is well known that mechanical communication in cells is crucial.[65] For example, it has been reported that the microscale elastic modulus of lung parenchyma is ≈0.7– 1.5kPa,[66] but it can be increased twofold with aging.[67] Moreover, the macroscale elastic modulus at 20% of strain of healthy mouse myocardium has

been reported to increase by twofold when the animals were subjected to severe obstructive sleep apnea.[39]

In the case of cardiac patches, increase in scaffold stiffness is needed so that they can be manipulated, sutured, and glued to the native myocardium, but they should be soft enough to not alter the normal function of the heart. It has been reported that the stress at 0.2 strain of the ventricular myocardium in the longitudinal direction is *4kPa,[68] and the elastic modulus at this strain is *20kPa.[69] Collagen scaffolds do not exhibit these mechanical properties. By contrast, the silk-reinforced scaffolds have mechanical properties better resembling those of myocardium. Consequently, they could be good candidates for the development of cardiac patches, since they overcome the common problems related to the mechanical instability of naturally derived biomaterials and to the poor biocompatibility of synthetic materials,[70] which often result in problems such as fibrosis, arrhythmias, and heart failure requiring resurgery as the only viable solution.

In contrast, it is well known that even slight changes in the stiffness of the cell culture microenvironment could result in important changes in stem cell fate.[71–73] It is worth mentioning that the values of stiffness obtained for the pure collagen scaffolds are comparable with the those found in embryos, whereas the values corresponding to the silkreinforced scaffolds are more resembling to adult soft organs such as lung and heart.[5,74] Therefore, the hydrogels presented in this study could be a good model for *in vitro* development studies.

Another important point regarding the tunability of scaffold stiffness is the possibility to optimize the cell microenvironment to optimize the paracrine effects of MSCs for further implantation in a recellularized patch for cardiac regeneration. The morphology of the cells cultured in the scaffolds was qualitatively different when silk microfibers were present (Figs. 6 and 7), which could be caused either by the presence of silk or by the stiffening of the hydrogel. Notwithstanding, BM-MSCs cultured in silk-reinforced scaffolds for 7 days showed a more elongated morphology, which has been recently reported as a predictor of their immunosuppressive capacity.[75] Although out of scope of this study, it is worth noting that silk-reinforced collagen scaffolds could be of interest for preconditioning MSCs.[76,77]

The printability of the developed hydrogels was assessed by rheometry. Rhelogical properties of collagen pregels at 4C changed over time. These changes complicate their use

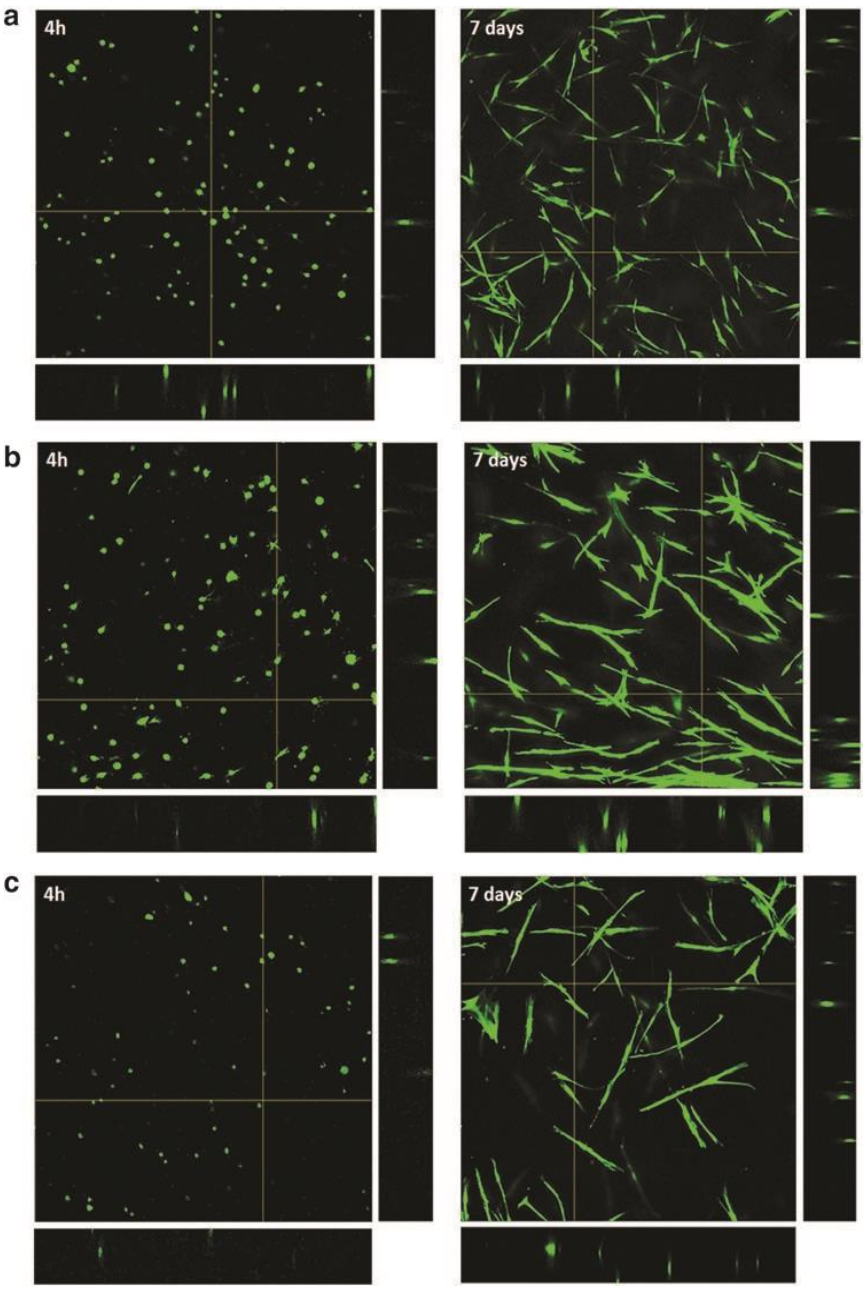

FIG. 6. Live confocal images of the bioprinted bone marrow-derived mesenchymal stem cells cultured within 1.27mm·1.27mm·
200mm scaffolds for 4h and 7 days; Z projection in the center and XZ and YZ views in the sides. (a) Control collagen. (b) 50% of silk with respect to collagen protein. (c) 100% of silk with respect to collagen protein. Color images are available online.

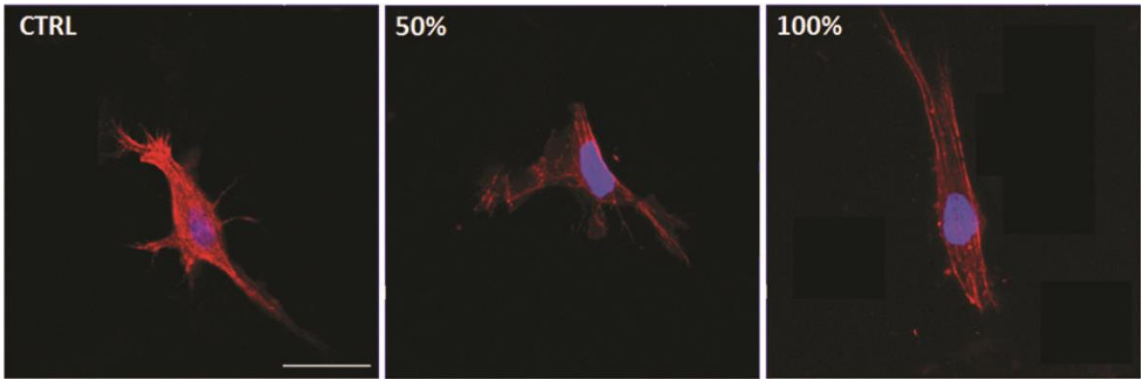

FIG. 7.Images of the cells within the different hydrogels. Scale bar: 100mm. Color images are available online.

as a 3D printing bioink. By contrast, by adding silk to the hydrogels, rheological properties remain stable at low temperature, so the printability of the developed hydrogels is superior to that of collagen hydrogels. This improved printability characteristics will facilitate the development of personalized cardiac patches and the high-throughput fabrication of scaffolds for MSCs preconditioning for further therapeutic applications.

A high number of BM-MSCs were alive within the scaffolds after 3D bioprinting after 7 days of 3D culture (Fig. 6). It has been reported that the presence of sericin in silk scaffolds favors the viability of cultured cells,[78] with endothelial cells surviving twofold more when cultured in silk with lower sericin removal. As the live/dead technique is not intended for quantifying the evolution of cell viability along a period of time, the results show that the main objective for the development of cardiac patches and scaffolds for MSCs preconditioning was accomplished.

This study focused on the development of a simple method to develop collagen–silk scaffolds for 3D bioprinting and cell culture. As already mentioned, preservation of sericin in the silk seems to improve the overall performance of the structures. However, further research is required to optimize sericin–fibroin ratio in the scaffolds, as the proportion that is found in the native silkworm cocoons (3:1 to 4:1 of fibroin–sericin, depending on farming conditions)[79] has been used in this study. Since protocols to extract fibroin[41] and sericin,[37] and to process them to form hydrogels, have been reported, it would be possible to modify the ratio between both proteins in the scaffolds. In contrast, type I collagen[80] and silk are being used in 3D bioprinting applications, and several techniques to build the scaffolds layer-by-layer have been

reported.[81,82]

The developed hydrogels can be effectively bioprinted if the adequate technique is finely tuned (using a pluronic supporting structure in our case) and, when compared with collagen pregels, present the advantage of stable rheological properties when maintained at 4C. One of the most promising techniques is FRESH (freeform reversible embedding of suspended hydrogels), where the pregels are printed in liquid phase within a gelatin-supporting structure that is further removed after the gelation of the scaffold,[83] because the technique can be implemented just by using one printing nozzle.

Potential translation and applicability of the results of this study into the clinics is also promising. For preconditioning of MSCs before cell therapy applications, protocols for the cells to be produced under GMP (good manufacturing practice) have been adapted in the past.[84] In the case of cardiac patches, the protocol described here will need to be adapted to GMP fabrication, but there are

several protocols for producing collagen,[85] and silk is currently used in the clinical practice for sutures, hence translating the developed technology could be feasible.

Conclusions

The results presented in this study show that the hydrogels developed by mixing milled raw silkworm cocoons and rat tail type I collagen can be used as bioink to obtain scaffolds for 3D bioprinting in tissue engineering applications such as development of cardiac patches and scaffolds for MSCs preconditioning. Their mechanical properties are improved to better resemble the structure of soft tissues. The method does not require toxic chemicals, additional crosslinkers, or complex physical methods, hence the procedure could be of high interest for further studies in 3D cell culture and bioprinting. The viability of BM-MSCs when incorporating the silk into the collagen scaffold suggests that the presented biomaterial can be used as a platform for *in vitro* studies where collagen scaffolds with increased stiffness are required. Also, the improved printability of the biomaterial allows high-throughput fabrication of scaffolds to obtain the high number of cells required for therapy, thereby potentially facilitating translation into clinical practice.

Acknowledgments

The authors thank Mr. Miguel A. Rodríguez and Ms. Elisabet Urrea (Unit of Biophysics and Bioengineering) for their excellent technical assistance, Dr. Mateu Pla and Dra. Ramona Bravo (Institute for Bioengineering of Catalonia) for their aid with the 3D bioprinter, and Dr. Josep Rebled and Dra. Eva Prats (Scientific Services of the University of Barcelona) for their aid with the SEM.

Disclosure Statement

No competing financial interests exist.

Funding Information

This work was supported in part by the Spanish Ministry of Sciences, Innovation and Universities (DPI2017-83721-P and PGC2018-097323-A-I00) and by the Marie SklodowskaCurie Action, Innovative Training Networks 2018, EU Grant Agreement no. 812772.

References

1. Mir, T.A., and Nakamura, M. Three-dimensional bioprinting: toward the era of manufacturing human organs as spare parts for healthcare and medicine. Tissue Eng Part B Rev 23, 245, 2017.
2. Zhang, Y.S., and Khademhosseini, A. Advances in engineering hydrogels. Science 356, eaaf3627, 2017.
3. Yannas, I.V., Tzeranis, D.S., Harley, B.A., and So, P.T.Biologically active collagen-based scaffolds: advances in processing and characterization. Philos Trans A Math Phys Eng Sci 368, 2123, 2010.
4. Helary, C., Bataille, I., Abed, A., *et al.* Concentrated collagen hydrogels as dermal substitutes. Biomaterials 31, 481, 2010.
5. Smith, L., Cho, S., and Discher, D.E. Mechanosensing ofmatrix by stem cells: from matrix heterogeneity, contractility, and the nucleus in pore-migration to cardiogenesis and muscle stem cells *in vivo*. Semin Cell Dev Biol 71, 84, 2017.
6. Streeter, B.W., and Davis, M.E. Therapeutic cardiac patches for repairing the myocardium. Adv Exp Med Biol 1144, 1, 2019.
7. Singh, A., and Sen, D. Mesenchymal stem cells in cardiacregeneration: a detailed progress report of the last 6 years (2010–2015). Stem Cell Res Ther 7, 82, 2016.
8. Zhang, J., Zhu, W., Radisic, M., and Vunjak-Novakovic,G. Can we engineer a human cardiac patch for therapy? Circ Res 123, 244, 2018.
9. Bell, D., Prabhu, S., Betts, K., *et al.* Durability of tissueengineered bovine pericardium (CardioCel) for a minimum of 24 months when used for the repair of congenital heart defects. Interact Cardiovasc Thorac Surg 28, 284, 2018.
10. Tao, Z.W., Wu, S., Cosgriff-Hernandez, E.M., and Jacot,J.G. Evaluation of a polyurethane-reinforced hydrogel patch in a rat right ventricle wall replacement model. Acta Biomater 101, 206, 2019.
11. Darnell, M., O'Neil, A., Mao, A., Gu, L., Rubin, L.L., andMooney, D.J. Material microenvironmental properties couple to induce distinct transcriptional programs in mammalian stem cells. Proc Natl Acad Sci U S A 115, E8368, 2018.

12. Hirata, M., and Yamaoka, T. Effect of stem cell nicheelasticity/ECM protein on the self-beating cardiomyocyte differentiation of induced pluripotent stem (iPS) cells at different stages. Acta Biomater 65, 44, 2018.
13. Nonaka, P.N., Falcones, B., Farre, R., Artigas, A., Almendros, I., and Navajas, D. Biophysically preconditioning mesenchymal stem cells improves treatment of ventilatorinduced lung injury. Arch Bronconeumol 2019 [Epub ahead of print]; DOI: 10.1016/j.arbres.2019.08.014.
14. Murphy, S.V., Skardal, A., and Atala, A. Evaluation ofhydrogels for bio-printing applications. J Biomed Mater Res A 101, 272, 2013.
15. Gime´nez, A., Uriarte, J.J., Vieyra, J., Navajas, D., and Alcaraz, J. Elastic properties of hydrogels and decellular-
ized tissue sections used in mechanobiology studies probed by atomic force microscopy. Microsc Res Tech 80, 85, 2017.
16. Holder, A.J., Badiei, N., Hawkins, K., Wright, C., Williams, P.R., and Curtis, D.J. Control of collagen gel mechanical properties through manipulation of gelation conditions near the sol-gel transition. Soft Matter 14, 574, 2018.
17. Sundararaghavan, H.G., Monteiro, G.A., Lapin, N.A.,Chabal, Y.J., Miksan, J.R., and Shreiber, D.I. Genipininduced changes in collagen gels: correlation of mechanical properties to fluorescence. J Biomed Mater Res A 87, 308, 2008.
18. Delgado, L.M., Fuller, K., and Zeugolis, D.I. Collagencross-linking: biophysical, biochemical, and biological response analysis. Tissue Eng Part A 23, 1064, 2017.
19. Liu, C., Lewin Mejia, D., Chiang, B., Luker, K.E., andLuker, G.D. Hybrid collagen alginate hydrogel as a platform for 3D tumor spheroid invasion. Acta Biomater 75, 213, 2018.
20. Fu, S., Ni, P., Wang, B., *et al.* Injectable and thermosensitive PEG-PCL-PEG copolymer/collagen/n-HA hydrogel composite for guided bone regeneration. Biomaterials 33, 4801, 2012.
21. Buitrago, J.O., Patel, K.D., El-Fiqi, A., *et al.* Silk fibroin/ collagen protein hybrid cell-encapsulating hydrogels with tunable gelation and improved physical and biological properties. Acta Biomater 69, 218, 2018.
22. Long, K., Liu, Y., Li, W., *et al.* Improving the mechanical properties of collagen-based membranes using silk fibroin for corneal tissue engineering. J Biomed Mater Res A 103, 1159, 2015.
23. Zhang, X., Zhai, C., Fei, H., *et al.* Composite silkextracellular matrix scaffolds for enhanced chondrogenesis of mesenchymal stem cells. Tissue Eng Part C Methods 24, 645, 2018.
24. Steiner, D., Lang, G., Fischer, L., *et al.* Intrinsic vascularization of recombinant eADF4(C16) spider silk matrices in the arteriovenous loop model. Tissue Eng Part A 25, 1504, 2019.
25. Affas, S., Scha¨fer, F.M., Algarrahi, K., *et al.* Augmentation cystoplasty of diseased porcine bladders with bi-layer silk fibroin grafts. Tissue Eng Part A 25, 855, 2019.
26. Frauchiger, D.A., Tekari, A., Wo¨ltje, M., Fortunato, G., Benneker, L.M., and Gantenbein, B. A review of the application of reinforced hydrogels and silk as biomaterials for intervertebral disc repair. Eur Cell Mater 34, 271, 2017.
27. Altman, G.H., Diaz, F., Jakuba, C., *et al.* Silk-based biomaterials. Biomaterials 24, 401, 2003.
28. Thurber, A.E., Omenetto, F.G., and Kaplan, D.L. *In vivo* bioresponses to silk proteins. Biomaterials 71, 145, 2015.
29. Font Tellado, S., Bonani, W., Balmayor, E.R., *et al.* Fabrication and characterization of biphasic silk fibroin scaffolds for tendon/ligament-to-bone tissue engineering. Tissue Eng Part A 23, 859, 2017.
30. Cai, H., Wu, B., Li, Y., *et al.* Local delivery of silkcellulose incorporated with SDF-1a functionally improves the uterus repair. Tissue Eng Part A 25, 1514, 2019.
31. Yang, Y., Chen, X., Ding, F., Zhang, P., Liu, J., and Gu,X. Biocompatibility evaluation of silk fibroin with peripheral nerve tissues and cells *in vitro*. Biomaterials 28, 1643, 2007.
32. Liu, B., Song, Y.W., Jin, L., *et al.* Silk structure and degradation. Colloids Surf B Biointerfaces 131, 122, 2015.
33. Lamboni, L., Gauthier, M., Yang, G., and Wang, Q. Silksericin: a versatile material for tissue engineering and drug delivery. Biotechnol Adv 33, 1855, 2015.
34. Sapru, S., Das, S., Mandal, M., Ghosh, A.K., and Kundu,S.C. Nonmulberry silk protein sericin blend hydrogels for skin tissue regeneration—*in vitro* and *in vivo*. Int J Biol Macromol 137, 545, 2019.
35. Rajan, N., Habermehl, J., Cote´, M.F., Doillon, C.J., and Mantovani, D. Preparation of ready-to-use, storable and reconstituted type I collagen from rat tail tendon for tissue engineering applications. Nat Protoc 1, 2753, 2006.
36. Wolf, M.T., Daly, K.A., Brennan-Pierce, E.P., *et al.* A hydrogel derived from decellularized dermal extracellular matrix. Biomaterials 33, 7028, 2012.
37. Wang, Z., Zhang, Y., Zhang, J., *et al.* Exploring natural silk protein sericin for regenerative medicine: an injectable, photoluminescent, cell-adhesive 3D hydrogel. Sci Rep 4, 7064, 2014.

38. Alcaraz, J., Otero, J., Jorba, I., and Navajas, D. Bidirectional mechanobiology between cells and their local extracellular matrix probed by atomic force microscopy. Semin Cell Dev Biol 73, 71, 2018.
39. Farre´ N, Otero, J., Falcones, B., *et al*. Intermittent hypoxia mimicking sleep apnea increases passive stiffness of myocardial extracellular matrix. A multiscale study. Front Physiol 9, 1143, 2018.
40. Freytes, D.O., O'Neill, J.D., Duan-Arnold, Y., Wrona,E.A., and Vunjak-Novakovic, G. Natural cardiac extracellular matrix hydrogels for cultivation of human stem cell-derived cardiomyocytes. Methods Mol Biol 1181, 69, 2014.
41. Rockwood, D.N., Preda, R.C., Yu¨cel, T., Wang, X., Lovett, M.L., and Kaplan, D.L. Materials fabrication from *Bombyx mori* silk fibroin. Nat Protoc 6, 1612, 2011.
42. Meyer, M. Processing of collagen based biomaterials andthe resulting materials properties. Biomed Eng Online 18, 24, 2019.
43. Shayegan, M., Altindal, T., Kiefl, E., and Forde, N.R. Intacttelopeptides enhance interactions between collagens. Biophys J 111, 2404, 2016.
44. Jorba, I., Beltra´n, G., Falcones, B., *et al*. Nonlinear elasticity of the lung extracellular microenvironment is regulated by macroscale tissue strain. Acta Biomater 92, 265, 2019.
45. Mendicino, M., Bailey, A.M., Wonnacott, K., Puri, R.K.,and Bauer, S.R. MSC-based product characterization for clinical trials: an FDA perspective. Cell Stem Cell 14, 141, 2014.
46. Samsonraj, R.M., Raghunath, M., Nurcombe, V., Hui, J.H.,van Wijnen, A.J., and Cool, S.M. Concise review: multifaceted characterization of human mesenchymal stem cells for use in regenerative medicine. Stem Cells Transl Med 6, 2173, 2017.
47. de Moraes, M.A., Paternotte, E., Mantovani, D., andBeppu, M.M. Mechanical and biological performances of new scaffolds made of collagen hydrogels and fibroin microfibers for vascular tissue engineering. Macromol Biosci 12, 1253, 2012.
48. Lu, Q., Feng, Q., Hu, K., and Cui, F. Preparation of threedimensional fibroin/collagen scaffolds in various pH conditions. J Mater Sci Mater Med 19, 629, 2008.
49. Zhou, J., Cao, C., Ma, X., and Lin, J. Electrospinning ofsilk fibroin and collagen for vascular tissue engineering. Int J Biol Macromol 47, 514, 2010.
50. Lv, Q., Hu, K., Feng, Q., and Cui, F. Fibroin/collagenhybrid hydrogels with crosslinking method: preparation, properties, and cytocompatibility. J Biomed Mater Res A 84, 198, 2008.
51. McGill, M., Coburn, J.M., Partlow, B.P., Mu, X., and Kaplan, D.L. Molecular and macro-scale analysis of enzymecrosslinked silk hydrogels for rational biomaterial design. Acta Biomater 63, 76, 2017.
52. Chirila, T.V., Suzuki, S., and Papolla, C. A comparativeinvestigation of *Bombyx mori* silk fibroin hydrogels generated by chemical and enzymatic cross-linking. Biotechnol Appl Biochem 64, 771, 2017.
53. Liu, C., Jin, Z., Ge, X., Zhang, Y., and Xu, H. Decellularized annulus fibrosus matrix/chitosan hydrogels for annulus fibrous tissue engineering. Tissue Eng Part A 25, 1605, 2019.
54. Antoine, E.E., Vlachos, P.P., and Rylander, M.N. Reviewof collagen I hydrogels for bioengineered tissue microenvironments: characterization of mechanics, structure, and transport. Tissue Eng Part B Rev 20, 683, 2014.
55. Vepari, C., and Kaplan, D.L. Silk as a biomaterial. ProgPolym Sci 32, 991, 2007.
56. Kunz, R.I., Brancalha˜o, R.M., Ribeiro, L.F., and Natali, M.R. Silkworm sericin: properties and biomedical applications. Biomed Res Int 2016, 8175701, 2016.
57. Ghaeli, I., de Moraes, M.A., Beppu, M.M., *et al.* Phase behaviour and miscibility studies of collagen/silk fibroin macromolecular system in dilute solutions and solid state. Molecules 22, E1368, 2017.
58. Duan, L., Yuan, J., Yang, X., Cheng, X., and Li, J. Interaction study of collagen and sericin in blending solution. Int J Biol Macromol 93(Pt A), 468, 2016.
59. Hayashi, C.Y., Shipley, N.H., and Lewis, R.V. Hypothesesthat correlate the sequence, structure, and mechanical properties of spider silk proteins. Int J Biol Macromol 24, 271, 1999.
60. Yodmuang, S., McNamara, S.L., Nover, A.B., *et al.* Silk microfiber-reinforced silk hydrogel composites for functional cartilage tissue repair. Acta Biomater 11, 27, 2015.
61. Park, J.H., Lee, J.H., Lee, S.Y., *et al.* Normal 2dimensional strain values of the left ventricle: a substudy of the normal echocardiographic measurements in Korean population study. J Cardiovasc Ultrasound 24, 285, 2016.
62. Pen˜uelas, O., Melo, E., Sa´nchez, C., *et al.* Antioxidant effect of human adult adipose-derived stromal stem cells in alveolar epithelial cells undergoing stretch. Respir Physiol Neurobiol 188, 1, 2013.
63. Valero, C., Amaveda, H., Mora, M., and Garcı´a-Aznar, J.M. Combined experimental and computational characterization of crosslinked collagen-based hydrogels. PLoS One 13, e0195820, 2018.

64. Andreu, I., Luque, T., Sancho, A., *et al.* Heterogeneous micromechanical properties of the extracellular matrix in healthy and infarcted hearts. Acta Biomater 10, 3235, 2014.
65. Sapir, L., and Tzlil, S. Talking over the extracellular matrix: how do cells communicate mechanically? Semin Cell Dev Biol 71, 99, 2017.
66. Liu, F., and Tschumperlin, D.J. Micro-mechanical characterization of lung tissue using atomic force microscopy. J Vis Exp 2911, 2011.
67. Sicard, D., Haak, A.J., Choi, K.M., Craig, A.R., Fredenburgh, L.E., and Tschumperlin, D.J. Aging and anatomical variations in lung tissue stiffness. Am J Physiol Lung Cell Mol Physiol 314, L946, 2018.
68. Engelmayr, G.C., Cheng, M., Bettinger, C.J., Borenstein,J.T., Langer, R., and Freed, L.E. Accordion-like honeycombs for tissue engineering of cardiac anisotropy. Nat Mater 7, 1003, 2008.
69. Perea-Gil, I., Ga´lvez-Monto´n, C., Prat-Vidal, C., *et al.* Head-to-head comparison of two engineered cardiac grafts for myocardial repair: from scaffold characterization to preclinical testing. Sci Rep 8, 6708, 2018.
70. Pok, S., and Jacot, J.G. Biomaterials advances in patchesfor congenital heart defect repair. J Cardiovasc Transl Res 4, 646, 2011.
71. Zakrzewski, W., Dobrzyn´ski, M., Szymonowicz, M., and Rybak, Z. Stem cells: past, present, and future. Stem Cell Res Ther 10, 68, 2019.
72. Lane, S.W., Williams, D.A., and Watt, F.M. Modulatingthe stem cell niche for tissue regeneration. Nat Biotechnol 32, 795, 2014.
73. Z˘igon-Branc, S., Markovic, M., Van Hoorick, J., *et al.* Impact of hydrogel stiffness on differentiation of human adipose-derived stem cell microspheroids. Tissue Eng Part A 25, 1369, 2019.
74. Discher, D.E., Mooney, D.J., and Zandstra, P.W. Growthfactors, matrices, and forces combine and control stem cells. Science 324, 1673, 2009.
75. Klinker, M.W., Marklein, R.A., Lo Surdo, J.L., Wei, C.H.,and Bauer, S.R. Morphological features of IFN-gstimulated mesenchymal stromal cells predict overall immunosuppressive capacity. Proc Natl Acad Sci U S A 114, E2598, 2017.
76. Hu, C., and Li, L. Preconditioning influences mesenchymalstem cell properties *in vitro* and *in vivo*. J Cell Mol Med 22, 1428, 2018.
77. Ezquer, F.E., Ezquer, M.E., Vicencio, J.M., and Calligaris,S.D. Two complementary strategies to improve cell engraftment in mesenchymal stem cell-based therapy: increasing transplanted cell resistance and increasing tissue receptivity. Cell Adh Migr 11, 110, 2017.
78. Wray, L.S., Hu, X., Gallego, J., *et al.* Effect of processing on silk-based biomaterials: reproducibility and biocompatibility. J Biomed Mater Res B Appl Biomater 99, 89, 2011.
79. Zhang, Y., Zhao, D., Meng, Z., *et al.* Wild silkworm cocoon contains more metabolites than domestic silkworm cocoon to improve its protection. J Insect Sci 17, 2017.
80. Osidak, E.O., Karalkin, P.A., Osidak, M.S., *et al.* Viscoll collagen solution as a novel bioink for direct 3D bioprinting. J Mater Sci Mater Med 30, 31, 2019.
81. Rodriguez, M.J., Dixon, T.A., Cohen, E., Huang, W.,Omenetto, F.G., and Kaplan, D.L. 3D freeform printing of silk fibroin. Acta Biomater 71, 379, 2018.
82. Chawla, S., Midha, S., Sharma, A., and Ghosh, S. Silkbased bioinks for 3D bioprinting. Adv Healthc Mater 7, e1701204, 2018.
83. Hinton, T.J., Jallerat, Q., Palchesko, R.N., *et al.* Threedimensional printing of complex biological structures by freeform reversible embedding of suspended hydrogels. Sci Adv 1, e1500758, 2015.
84. Vigano`, M., Budelli, S., Lavazza, C., *et al.* Tips and tricks for validation of quality control analytical methods in good manufacturing practice mesenchymal stromal cell production. Stem Cells Int 2018, 3038565, 2018.
85. Hartmann-Fritsch, F., Marino, D., and Reichmann, E. About ATMPs, SOPs and GMP: the Hurdles to produce novel skin grafts for clinical use. Transfus Med Hemother 43, 344, 2016.

Address correspondence to:
Jorge Otero, PhD
Unit of Biophysics and Bioengineering
School of Medicine and Health Sciences
Universitat de Barcelona
Casanova 143
Barcelona 08036
Spain

E-mail: jorge.otero@ub.edu

Received: July 31, 2019
Accepted: February 11, 2020
Online Publication Date: March 18, 2020

Chapter VI. Scientific article II

Characterization of Bioinks Developed from the Gelification of the Extracelullar Matrix obtained from Decellularized Porcine Myocardia

Héctor Sanz-Fraile, Carolina Herranz-Diez, Anna Ulldemolins, Bryan Falcones, Isaac Almendros, Núria Gavara, Raimon Sunyer, Ramon Farré and Jorge Otero

In manuscript

Article

Characterization of Bioinks Developed from the Gelification of the Extracellular Matrix obtained from Decellularized Porcine Myocardia

Héctor Sanz-Fraile 10,+, Carolina Herranz-Diez 1,+, Anna Ulldemolins 1, Bryan Falcones 1, Isaac Almendros 1,2,3, Núria Gavara 1,4, Raimon Sunyer 1,4, Ramon Farré 1,2,3 and Jorge Otero 1,2,4,*

[1] Unitat de Biofísica i Bioenginyeria, Facultat de Medicina i Ciències de la Salut, Universitat de Barcelona, 08036 Barcelona, Spain; hector.sanz.fraile@hotmail.com (H.S-F.); anna.ulldemolins@ub.edu (A.U.); carolinaherranz@ub.edu (C.H.); bfalco86@gmail.com (B.F.); ialmendros@ub.edu (I.A.); ngavara@ub.edu (N.G.); rsunyer@ub.edu (R.S.); rfarre@ub.edu (R.F.)

[2] CIBER de Enfermedades Respiratorias, 28029 Madrid, Spain

[3] Institut d'Investigacions Biomèdiques August Pi i Sunyer, 08036 Barcelona, Spain

[4] The Institute for Bioengineering of Catalonia (IBEC), The Barcelona Institute of Science and Technology (BIST), 08028 Barcelona, Spain

+ Equally contributed to this work

* Correspondence: jorge.otero@ub.edu (J.O.)

Abstract: With the rise of 3D bioprinting, synthetic and natural materials have been used to develop bioinks to mimic the 3D environments for cell culture. In the case of the heart, many of the strategies have been focused on the development of patches for cardiac repair but they present limitations that can be solved with the use of extracellular matrix (ECM)-derived hydrogels. In this study a physiomimetic cardiac bioinks based on hydrogels made from decellularized porcine myocardia are presented. Scaffold ultrastructure revealed that a typical ECM fiber structure was achieved. Mechanical properties were characterized by rheometry to optimize the bioink production, specifically the matrix enzymatic digestion time. Human bone marrow mesenchymal stromal cells were used to determine the response of cells when cultured in 3D within the developed hydrogels. Results showed that hydrogels promoted the

1. Introduction

There is an important lack of organs and replacements in implantology, mainly due to population aging in developed countries. In the last decades, tissue engineering has emerged as a potential solution to overcome this progressive reduction of viable donors [1]. In the specific case of the heart, although engineering an implantable heart in the laboratory is still far away [2], novel grafts based on decellularized tissue [3] or electroconductive scaffolds [4] have been recently developed. The main idea is to produce recellularized patches to ameliorate the function of diseased hearts [5]. Ideally, the biomaterial used to develop these cardiac grafts should mimic as much as possible the natural environment of the native myocardium. Synthetic materials have been used to develop scaffolds for heart tissue repair, but still present limitations related with immune responses and biodegradability of the scaffolds [6,7]. Naturally-derived materials, on the other hand, have been being explored with the idea that they could resemble better the natural environment of cardiac cells [8,9]. Among the different natural sources to develop these biomaterials, decellularized tissues are one of the main promising ones [10]. Decellularization is the process of removing the cells from an organ or tissue while maintaining its extracellular matrix (ECM) proteins [11]. In recent years, protocols for obtaining decellularized ECM (dECM) from virtually every organ and tissue have been developed [12]. In the case of the heart, dECM from pericardium has been used to engineer patches for the treatment of myocardial infarct [3]. Rat dECM patches have successfully replaced the right ventricular outflow tract defect in Lewis rat models, showing no differences between the area in contact with the patch and the healthy ventricles [13]. Patches have also shown signs of

crosstalk between cells and between cells and hydrogel. In conclusion, the bioink presented in this work can be used to develop hydrogels which are promising candidates to be used in cardiac 3D bioprinting for tissue engineering applications.

neovascularization and nerve sprouting in the infarcted area that were in contact with either human pericardial or porcine myocardial dECM scaffolds [14]. An interesting aspect of the dECM patches is that, because of their biomimetic nature, they are able to be repopulated with human mesenchymal stromal cells (hMSCs) to enhance their repairing potential by reducing the scar mass in the threated area [3,14]. It has been demonstrated that hMSCs have the capability to release agents as paracrine factors and extracellular vesicles (EVs) with immunomodulatory, anti-inflammatory, and antimicrobial effects [15–19]. Although these cardiac patches developed have shown good outcomes, they still present certain limitations such as their mechanical properties and the lack of customized patient-specific shapes [20,21].

The problem of developing customized-shape patches can be overcome by the use of 3D bioprinting technology by using the adequate biomaterials [22]. Recently, it has been shown that the dECM of different organs and tissues can be pulverized and solubilized to form bioprintable hydrogels [23–25]. These bioinks have the capability to be loaded with cells or other bioactive molecules in order to enhance the cell proliferation [26] or be used as physiomimetic vehicles for applying MSCs or MSCs-derived release agents [27,28]. Nevertheless, in the case of cardiac bioinks, their weak mechanical properties prevent their use without the need of mixing the ECM hydrogel with other biomaterials [29] or the use of additional crosslinkers [30].

In the present work, an optimized protocol to produce hydrogels from decellularized porcine myocardium ECM (cECM) is presented. Scaffolds can be developed without the need of mixing the cECM with other biomaterial or the incorporation of additional crosslinkers in the protocol. The developed bioink was studied to produce scaffolds for 3D cell culture in cardiac tissue engineering. The rheological properties of the hydrogel were assessed by rheometry as well as its ultrastructure by imaging with a Scanning Electron Microscope. The cECM bioink was prepared by loading the hydrogel with Human Bone Marrow-derived Mesenchymal Stem Cells (hBM-MSCs) and the behavior of the cells when cultured in 3D in the developed bioink was studied by immunostaining.

2. Results and Discussion

2.1. Macro and ultrastructure of the scaffolds developed with cECM bioinks

Hydrogels showed a homogeneous structure with not macroscopically visible fiber board clusters. Structures formed with the developed bioink showed enough strength to be manipulated with tweezers without breaking them and with the capability of recover the original shape after a manipulation (figure 1A). This improvement with respect previous reported works are due to working at higher powder concentration and the optimization of the digestion time respect to the commonly protocol originally published by Freytes and coworkers [31]. Thanks to these improved mechanics, a 3D bioprinted scaffold could be manipulated and implanted *in vivo* by bio-glue with the goal of restoring cardiac functions after myocardial infarction, which is one of the current challenges in cardiac tissue research [3,14,20].

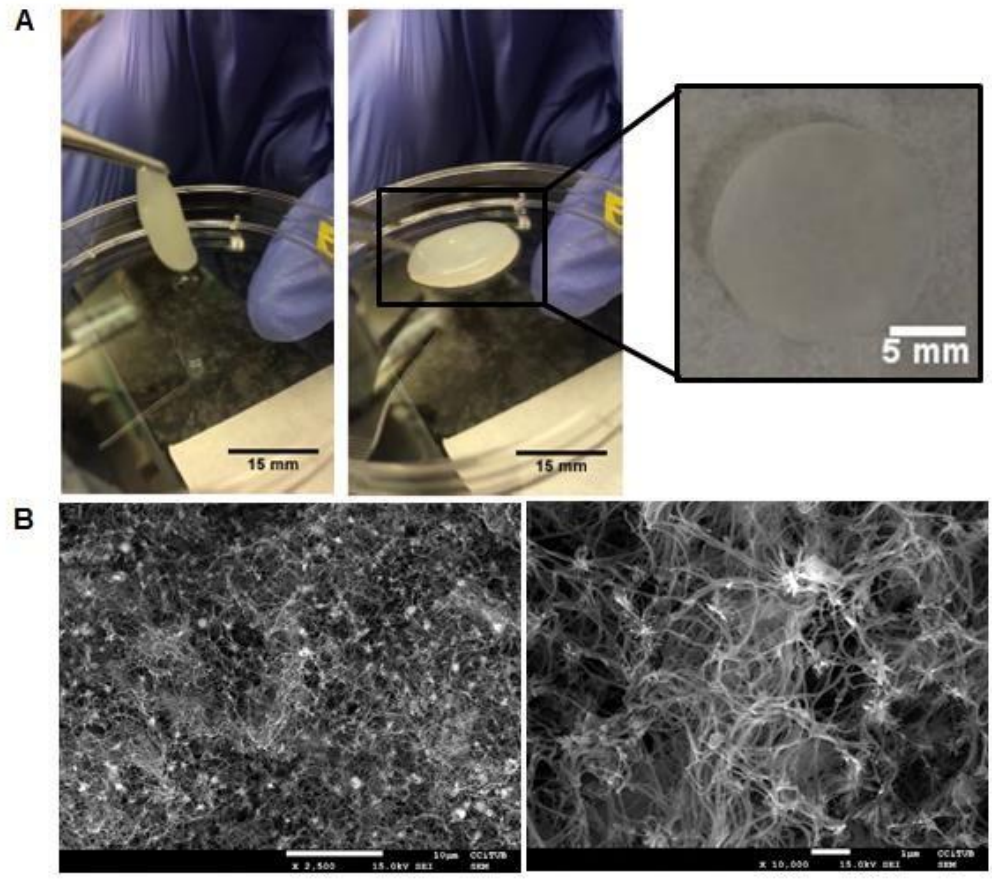

Figure 1. Structural characterization of the cECM hydrogels. Macro image of the cECM hydrogel, showing a homogeneous structure and its surgical tool manipulation (a). SEM images of cECM hydrogel (b).

Regarding to ultrastructure, SEM images of the acellular hydrogels (figure 1B) showed a fibrillary structure as expected. The average diameter of the fibers of the cECM hydrogel was 126 ± 8 nm. These data coincide with the diameter of tropocollagen fibers [32], which is consistent with the collagen I fibrils, reported to be in the 100-nm diameter range [33]. The structure observed in cECM hydrogels is closer to that of the native ECM compared with previous works [34] which fibers presented a diameter slightly below than that of tropocollagen and collagen present in the ECM. As it can be observed in Figure 1B, structures obtained with the developed bioink presented a disposition of the fibers that resembles that of the original ECM and, thanks to the small diameter of the fibers, the hydrogel presented a high contact area and porosity, which had been reported to improve cell attachment and proliferation [35,36].

2.2. Rheological propeties of the cECM bioinks depending on the pepsin digestion time

Rheological properties of the cECM hydrogels showed to be dependent on the digestion time, as shown in Figure 2. Interestingly, for digestion times above 24h, the hydrogel does not reach the gelation after thermal crosslinking. For the rest of studied digestion times, the gelation started gradually, being the hydrogel digested for 24h the one showing the highest storage modulus (G'=23.95 Pa) and the hydrogel digested for 16h the one with the lowest storage modulus (G'= 4.78 Pa).

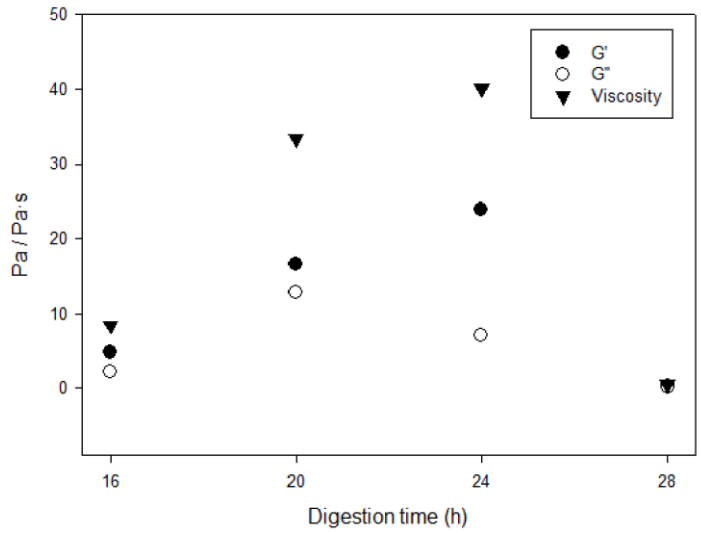

Figure 2. Rheological properties of the cECM bioink in function of the pepsin digestion time.

Obtained values for G′ after 24h digestion are in line (even slightly higher) with values reported previously for other natural organ-derived hydrogels, such as lung extracellular matrix or type I collagen hydrogels [37], so 24h was the chosen digestion time the bioinks used in the rest of experiments of the present work.

2.3. 3D cultures of hBM-MSCs

When cultured in 3D, hBM-MSCs contracted the cECM hydrogels, as measured by the hydrogel contraction assay (Figure 3). As expected, the shrinkage of the structures increased with the cultured time. After 1 day of 3D culture the measured area of the cECM hydrogels with hBM-MSCs was reduced to 158.5 ± 8.27 mm^2 (12.9 ± 4.5 percent of contraction; p=0.076). At day 4, the measured value was 111.2 ± 11.21 mm^2 (38.9 ± 6.2 percent of contraction; p=0.005), and after 7 days in culture the area was 85.7 ± 7.43 mm^2 (52.9 ± 4.1 percent of contraction; p<0.001).

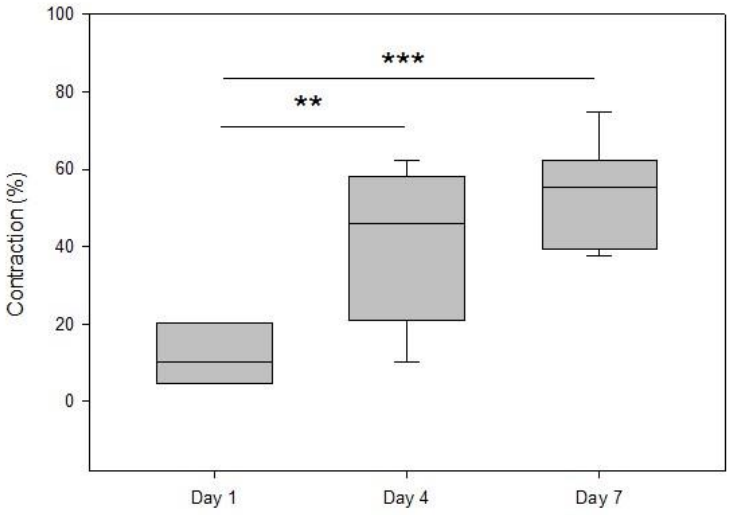

Figure 3. Contraction of the 3D-cultured hydrogels (hBM-MSC) against acellular ones (control) for 1, 4 and 7 days. **: p<0.01; ***: p<0.001.

The contraction observed in the structures indicated an active crosstalk between the cECM hydrogels matrix and the cells cultured within. Various effects could be overlapping for the observed contraction, as cells can be effectively pulling the fibers of the

structure while, at the same time, degrading matrix proteins by secreting metalloproteinases. Although out of the scope of the present study, further work should be done to determine which of the factors is dominating for this kind of cells in cECM hydrogels. Previous studies done with fibroblasts and stromal cells cultured in collagen matrices have shown that the combination of both factors strongly depends on structure mechanics and other stimuli that may alter cell contractility [38–40]. To better understand these cell-matrix interactions, the alteration of the mechanical properties of the structures due to the cell culture was studied by rheometry. As shown in figure 4, cell-laden structures were softened when compared with the acellular ones. As expected, values for the shear modulus and viscosity decreased with the applied strain. Measured rheological properties were in the same range of values previously reported for other cECM hydrogels [21]. Interestingly, cell-laden scaffolds showed to be softer than acellular ones. This could be due to the fact that cells are generally softer than their surrounding ECM, or by the fact that cells are degrading the ECM where they are cultured.

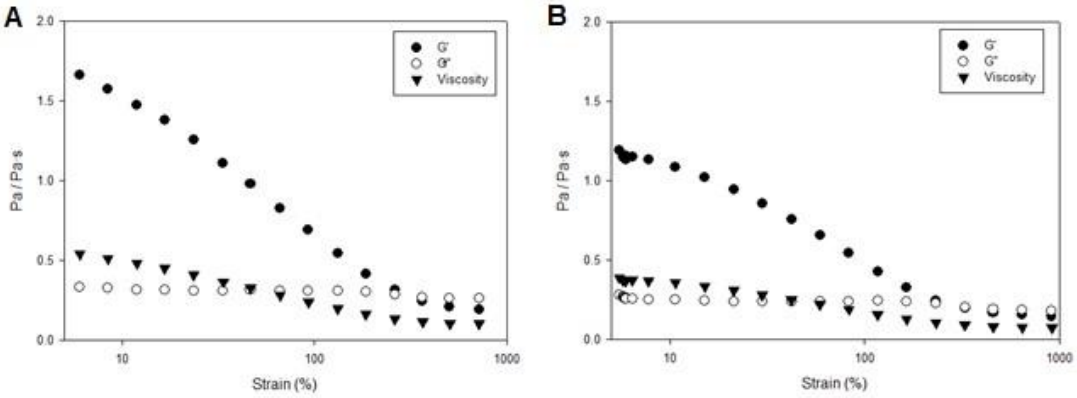

Figure 4. A) Comparison of the storage modulus (G′) in acellular and cellular hydrogels. B) Comparison of the Complex Viscosity of the acellular and cellular hydrogels

Immunofluorescence images of 3D cultured hBM-MSCs for 7 days can be observed in figure 5. Cells were stained for Connexin 43 (Cx43) and α-Smooth muscle actin (α-SMA) in green. The actin filaments of the cytoskeleton and the nuclei were also stained.

Cells showed a well formed cytoskeleton with the characteristic spindle shape of MSCs. 3D cultured cells expressed Cx43 and α-SMA as confirmed by immunostaining.

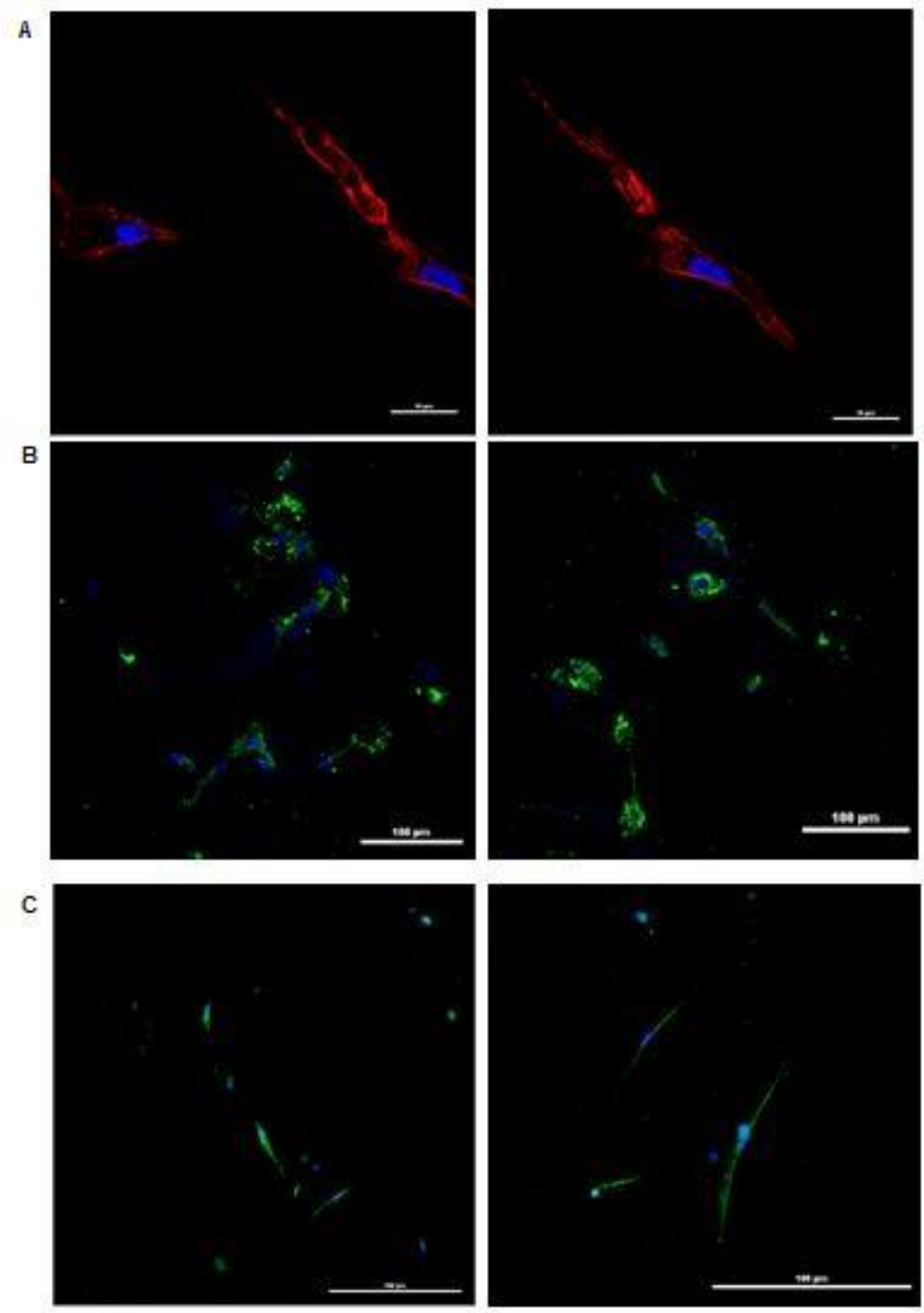

Figure 5. Immunostaining of hBM-MSC cultured in 3D in the cECM hydrogels for 7 days. A)Phalloidin (red). B) α-SMA (green). C) Cx43 (green). The nucleus is counter-stained in all the images (blue).

Cell-laden hydrogels are a promising therapeutic approach. Using this physiomimetic cardiac hydrogel, cells were able to grow and proliferate. In figure 5, the expression of Cx43 reveals a cell-cell communication that plays an important role in the physiology of the heart [28,41]. The cells, at the same time, showed a spindle-like morphology of the cytoskeleton, typical of MSCs [42]. Furthermore, the contractile phenotype of the cells located in the heart during a healing process is characterized

by the expression of α-SMA, which promotes focal adhesions and therefore cell – matrix interaction and ECM remodeling [43,44]. The positive expression of αSMA in hBM-MSC within the cECM hydrogel suggests interplay between the cells and the matrix.

A major part of the regenerative potential of using MSCs relies in their capacity to secrete factors [45]. Nevertheless, their proliferation and interaction both with the cells themselves and the ECM, makes the cECM hydrogel a good candidate for tissue engineering approaches, priming the paracrine signaling of MSCs.

Several studies have shown that the cardiac differentiation capacity of MSCs is very low and that they can only assume cardiomyocyte-like cell fates. Interestingly, the limited differentiation capacity of MSCs seemingly has minimal impact on the therapeutic effects cell therapy confers on the infarcted heart. MSCs release exosomes and vesicles that play an important role in cardiac tissue repair. This characteristic makes MSCs good candidates to be used as part of the hydrogels with therapeutic purpose [46].

It is well stablished that MSCs sense the biomechanical cues of the microenvironment leading to a several physiological responses related to cell function, fate, and phenotype [47,48]. Accordingly, ECM-based therapies have been used in cardiac tissue engineering [27,28]. In this context, cardiac ECM-based hydrogels could be further enhanced to be used as physiomimetic vehicle for applying MSCs or MSCs-derived release agents.

Pati *et al.* [49] printed a three-dimensional cardiac tissue with cECM hydrogel made by porcine dECM and human adipose-derived MSCs, achieving high cell viability; Jang *et al.* [50] added Vascular Endothelial Growth Factor (VEGF) and MSCs to a porcine dECM pregel with the aim of promoting a rapid vascularization of cells-laden heart cECM bioink. In both cases, to fabricate the prevascularized constructs, intercalated layers of polycaprolactone (PCL) were printed to provide mechanical support to the structure, due to the weak mechanical properties of the cECM hydrogel itself. To confer better supporting structure to the hydrogels, several crosslinkers [51] from natural and synthetic origin, such as silk, genipin [30] or gelatin methacrylate (GelMA) [20] are added to the dECM hydrogels. Basara *et al*. showed that adding GelMA to a human-dECM enhanced the mechanical properties and maintained good biocompatibility [52]. Following this trend, our research group developed a silk-reinforced collagen hydrogel that presented two-fold stiffening compared to collagen hydrogels, an improved printability properties and a suitable substrate for hBM-MSCs 3D culture [8].

3. Conclusions

The aim of the engineered scaffolds is to resemble as much as possible the extracellular matrix of the tissue. In this work, decellularized porcine myocardial tissue has been used to engineer bioink which is totally formed by ECM components. When developing a decellularization method it is important to maintain a balance between the thickness of the tissue pieces and the time they are in contact with the chemicals and enzymes to ensure decellularization without damaging the ECM tissues. Additionally, SEM images showed a woven fiber structure typical of the ECM with size fibers. The contraction observed in the hydrogels seems to indicate an active crosstalk between the cells and the scaffold. Regarding to the characterization, rheology has shown that the hydrogel developed shown mechanical properties similar to other ECM-derived hydrogels in the literature. Finally, the expression of Cx43 reveals a cell-cell communication, while the expression of αSMA suggests interplay between the cells and the ECM.

4. Materials and Methods

All the reagents were obtained from Sigma Aldrich (Missouri, US) unless otherwise specified.

4.1. Preparation of the cECM bioinks from the decellularization of porcine myocardia

Porcine hearts were obtained from a local slaughterhouse and then washed with deionized water before freezing them at -80 ˚C for storage and to aid in cell lysis. The decellularization method was adapted from a protocol developed for human hearts [53] with slight modifications. Briefly, hearts were thawed to room temperature (RT) and the left ventricular myocardium was sectioned into 1x1x1cm cubes and stored at -80 ˚C for further cryosectioning into 300 µm-thickness slices by using a cryostat (HM 560, Thermo Fisher Scientific, Waltham, MA). Resulting myocardial slices were then decellularized by their sequential immersion in lysis solution (10 mM Tris, 0.1% w/v ethylenediaminetetraacetic acid (EDTA), pH 7.4 in dH_2O, 2 h at RT), 0.5% sodium dodecyl sulfate (SDS) (6 h at RT), and fetal bovine serum (FBS) (3 h at 37 ˚C) with intermediate washes in phosphate buffered saline (PBS) 1X. At the end of the decellularization, slices were drained and dried before storing them at -80 ˚C. To produce the cECM powder, slices were freeze-dried for 48 h (Lyoquest-55 Plus, Telstar, Terrasa, Spain) and pulverized into a micrometic powder by using a cryogenic miller (6775 Freezer/Mill, SPEX, Metuchen, NJ, US).

The resulting cECM powder was digested at a concentration of 20 mg/mL in a 0.1M HCl solution with pepsin from porcine gastric mucosa (1:10 concentration) under magnetic stirring at room temperature for different times (for experiments other than rheology, 24 h digestions was chosen as it showed to have the higher storage modulus). The pregel solution was then pH-stabilized to 7.4 ± 0.4 by using 0.1M NaOH and PBS 10X. For 3D bioprinting, the dual-printhead method described in [37] was used. Briefly, one printhead of the 3D bioprinter (3Ddiscovery, RegenHU, Switzerland) was filled with the pregel while a secondary printhead was filled with Pluronic F-127 gel. Structures were then bioprinted by alternatively printing an F127 layer, which served as a template, and a pregel layer. At the end of the process, scaffolds were incubated at 37 ˚C for 45 min to form the hydrogel. Finally, pluronic was dissolved by immersing the structures in culture media at 4 ˚C for 10 min.

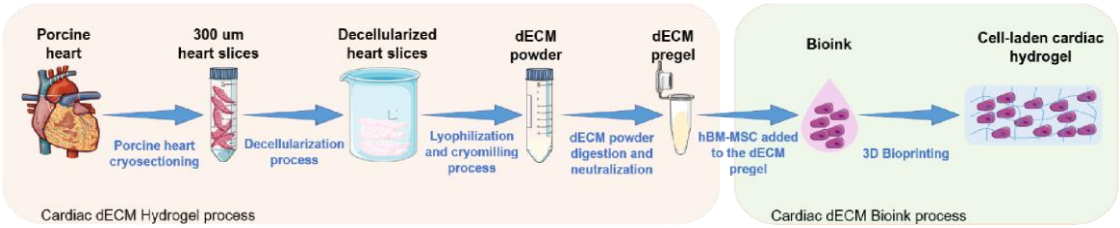

Figure 6. Schematic description of the process followed to obtain cECM heart hydrogel.

4.2. Ultrastructural characterization by Scanning Electron Microscopy

The ultrastructure of the cECM hydrogel scaffolds was visualized with a JSM-6510 (JEOL, Tokyo, Japan) Scanning Electron Microscopy (SEM). cECM scaffolds of 20x9x3 mm were produced by 3D bioprinting casting

The 3D scaffolds were fixed in 4% paraformaldehyde (PFA) in PBS for 48h and then washed three times with 0.1M phosphate buffer (PB). Next, the samples were incubated in 4% osmium tetroxide for 90 min and then rinsed with deionized water. Subsequently, samples were dehydrated by washing them with ethanol 80% (x2), 90% (x3), 96% (x3) and 100% (x3) and preserved in absolute ethanol at 4 ˚C until critical point drying (Autosamdri-815 critical point dryer, Tousimis, Rockville, MD, US). Samples were then carbon coated and mounted using conductive adhesive tabs (TED PELLA, Redding, CA, US). Imaging was performed by using a SEM (JSM-6510, JEOL, Tokyo, Japan) at 15 kV.

The diameter of the fibers was calculated following the method developed in [54]. Briefly, 10 fibers of three different zone of

each sample were randomly selected and their diameter was computed with ImageJ Software (National Institute of Health, Bethesda, MD, US).

4.3. Bioink rheology

The rheology of the developed bioinks was measured by using a Haake RheStress1 rheometer (Thermo Fisher, MA, US) with a 35mm serrated parallel plate. The storage modulus (G′) and loss modulus (G′′) were measured, and the modulus of the complex viscosity (|η*|) was calculated by using equation 1 for a given frequency ω.

$$\eta^* = \eta' - i\eta'' = \frac{G''}{\omega} - \frac{iG'}{\omega} \quad (1)$$

Hydrogels were digested for 16h, 20h, 24h, and 28h. The gelation kinetics of the acellular hydrogels was assessed by loading a pregel solution onto a Peltier plate at 4 °C for 10 min at 0.628 rad/s frequency. Temperature was kept constant for 10 minutes and then increased to 37 °C and kept constant for 15 min while measuring the rheology of the different samples.

4.4. 3D Cell Culture of hBM-MSCs

Human Bone-Marrow Mesenchymal Stromal cells (ATCC, VA, US) were expanded in tissue cultures plates by following the manufacturer instructions. Cells at passages 3-5 were used for conducting all the experiments presented herein.

The bioink hydrogel was prepared at 4 °C by mixing the pregel with the cells resuspended in culture media at a relation 10:1 v/v. To form the cell-laden hydrogel structures, the pregel was then incubated at 37 °C for 45 min to form disk-shaped structures of 1.9 cm^2 of surface area. Final cell concentration in the scaffolds was $2.5 \cdot 10^5$ cells/mL. Cells were cultured for 7 days, changing the medium every 3 days.

Diameter of cell-laden structures was assessed at day 1, 4 and 7 after cell seeding. Bottom-adhered cECM hydrogels were imaged with a high-resolution camera fixed to a tripod after aspirate the culture media to avoid image errors due to movement of the structure. The surface area of the 3D cultures was measured with ImageJ Software and the contraction was quantified as the percentage of reduction respect to the acellular controls [37].

The influence of the cells on the rheological properties once structures were gellified was assessed for the cultures at 7 days. Then, rheometry on the cell-laden hydrogels (24h of pepsin digestion) was characterized at 37 °C by using an amplitude sweep from 5% (which showed to be the deformation for the cell-laden hydrogels when applying the lowest value for tension that the equipment allowed) to 1000% at a frequency 3.14 rad/s.

For immunohistochemical analysis of the cells cultured in 3D within the cardiac bioinks, cell-laden hydrogels at day 1, 4 and 7 were immersed in Optimal Cutting Temperature (OCT) and frozen at -80 °C. Thin hydrogel slices (≈12 µm) were obtained by cryosectioning (HM 560, Thermo Fisher Scientific, MA, US) and placed on top of positively charged glass slides. OCT was removed by thawing and washing the samples in PBS 1X solution at room temperature. After that, cells were fixed with 4% PFA for 15 min. Primary and secondary antibodies were incubated overnight and for 2h at 37 °C, respectively. Nuclei were stained with Hoechst 33342 (Thermo Fisher Scientific, MA, US) for 15 min. Primary antibodies employed were anti-Cx43 (ab11370, abcam, Cambridge, UK) and anti-αSMA (ab32575, abcam, Cambridge, UK). Secondary antibodies used were Alexa 488 goat anti-rabbit (ab150081, abcam, Cambridge, UK) and Alexa 488 goat anti-mouse antibody (ab150117, abcam, Cambridge, UK). Images were acquired with a Nikon D-Eclipse Ci confocal microscope with a 100x Plan Apo objective (Nikon, Tokyo, Japan).

4.5. Statistical analysis.

Data are expressed as mean ± SE. For contraction analysis, one-way analysis of variance (ANOVA) followed by the Holm-Sidak's post hoc test was done, while paired

T-test was performed for rheological characterization. Statistical significance was considered at p-values < 0.05.

Author Contributions: Conceptualization, H.S-F., C.H., R.F. and J.O.; Formal analysis, H.S-F., C.H., A.U., R.S., N.G., R.F., I.A. and J.O.; Funding acquisition, R.F., I.A., N.G. and J.O..; Investigation, H.S-F., C.H., B.F., N.G., I.A., R.S., R.F. and J.O.; Methodology, H.S-F., C.H., A.U., B.F., R.F. and J.O.; Project administration, R.F. and J.O.; Resources, N.G., R.S., R.F., N.G., I.A. and J.O.; Software, H.S-F., C.H., A.U. and J.O.; Supervision, R.F. and J.O.; Writing of original draft, H.S-F., C.H. and J.O. All authors have read and agreed to the published version of the manuscript.

Data Availability Statement: The datasets generated for this study are available on request from the corresponding author.

Acknowledgments: The authors wish to thank Mr. Miguel A. Rodríguez and Ms. Elisabet Urrea (Unit of Biophysics and Bioengineering) for their excellent technical assistance, and Dr. Josep Rebled and Dra. Eva Prats (Scientific Services of the University of Barcelona) for their aid with the Scanning Electron Microscope.

Conflicts of Interest: The authors declare no conflict of interest.

References

1. Muzzio, N.; Moya, S.; Romero, G. Multifunctional Scaffolds and Synergistic Strategies in Tissue Engineering and Regenerative Medicine. *Pharmaceutics* 2021, *13*.
2. Yadid, M.; Oved, H.; Silberman, E.; Dvir, T. Bioengineering Approaches to Treat the Failing Heart: From Cell Biology to 3D Printing. *Nat Rev Cardiol* 2022, *19*, 83–99.
3. Prat-Vidal, C.; Rodríguez-Gómez, L.; Aylagas, M.; Nieto-Nicolau, N.; Gastelurrutia, P.; Agustí, E.; Gálvez-Montón, C.; Jorba, I.; Teis, A.; Monguió-Tortajada, M.; et al. First-in-Human PeriCord Cardiac Bioimplant: Scalability and GMP Manufacturing of an Allogeneic Engineered Tissue Graft. *EBioMedicine* **2020**, *54*, doi:10.1016/j.ebiom.2020.102729.
4. Esmaeili, H.; Patino-Guerrero, A.; Hasany, M.; Ansari, M.O.; Memic, A.; Dolatshahi-Pirouz, A.; Nikkhah, M. Electroconductive Biomaterials for Cardiac Tissue Engineering. *Acta Biomater* 2022, *139*, 118–140.
5. Kc, P.; Hong, Y.; Zhang, G. Cardiac Tissue-Derived Extracellular Matrix Scaffolds for Myocardial Repair: Advantages and Challenges. *Regen Biomater* **2019**, *6*, 185–199, doi:10.1093/rb/rbz017.
6. Peña, B.; Laughter, M.; Jett, S.; Rowland, T.J.; Taylor, M.R.G.; Mestroni, L.; Park, D. Injectable Hydrogels for Cardiac Tissue Engineering. *Macromol Biosci* 2018, *18*.
7. Sadtler, K.; Wolf, M.T.; Ganguly, S.; Moad, C.A.; Chung, L.; Majumdar, S.; Housseau, F.; Pardoll, D.M.; Elisseeff, J.H. Divergent Immune Responses to Synthetic and Biological Scaffolds. *Biomaterials* **2019**, *192*, 405–415, doi:10.1016/j.biomaterials.2018.11.002.
8. Sanz-Fraile, H.; Amoros, S.; Mendizabal, I.; Galvez-Monton, C.; Prat-Vidal, C.; Bayes-Genis, A.; Navajas, D.; Farre, R.; Otero, J. Silk-Reinforced Collagen Hydrogels with Raised Multiscale Stiffness for Mesenchymal Cells 3D Culture. *Tissue Eng Part A* **2020**, *26*, 358–370, doi:10.1089/ten.tea.2019.0199.
9. Elkhoury, K.; Morsink, M.; Sanchez-Gonzalez, L.; Kahn, C.; Tamayol, A.; Arab-Tehrany, E. Biofabrication of Natural Hydrogels for Cardiac, Neural,

and Bone Tissue Engineering Applications. *Bioact Mater* 2021, *6*, 3904– 3923.

10. Taylor, D.A.; Sampaio, L.C.; Ferdous, Z.; Gobin, A.S.; Taite, L.J. Decellularized Matrices in Regenerative Medicine. *Acta Biomater* 2018, *74*, 74–89.
11. Bejleri, D.; Davis, M.E. Decellularized Extracellular Matrix Materials for Cardiac Repair and Regeneration. *Adv Healthc Mater* 2019, *8*.
12. Saldin, L.T.; Cramer, M.C.; Velankar, S.S.; White, L.J.; Badylak, S.F. Extracellular Matrix Hydrogels from Decellularized Tissues: Structure and Function. *Acta Biomater* 2017, *49*, 1–15.
13. Wainwright, J.M.; Hashizume, R.; Fujimoto, K.L.; Remlinger, N.T.; Pesyna, C.; Wagner, W.R.; Tobita, K.; Gilbert, T.W.; Badylak, S.F. Right Ventricular Outflow Tract Repair with a Cardiac Biologic Scaffold. *Cells Tissues Organs* **2011**, *195*, 159–170, doi:10.1159/000331400.
14. Perea-Gil, I.; Gálvez-Montón, C.; Prat-Vidal, C.; Jorba, I.; Segú-Vergés, C.; Roura, S.; Soler-Botija, C.; Iborra-Egea, O.; Revuelta-López, E.; Fernández, M.A.; et al. Head-to-Head Comparison of Two Engineered Cardiac Grafts for Myocardial Repair: From Scaffold Characterization to Pre-Clinical Testing. *Sci Rep* **2018**, *8*, doi:10.1038/s41598-018-25115-2.
15. Lee, J.W.; Krasnodembskaya, A.; McKenna, D.H.; Song, Y.; Abbott, J.; Matthay, M.A. Therapeutic Effects of Human Mesenchymal Stem Cells in Ex Vivo Human Lungs Injured with Live Bacteria. *Am J Respir Crit Care Med* **2013**, *187*, 751–760, doi:10.1164/rccm.201206-0990OC.
16. Gore, A. v.; Bible, L.E.; Song, K.; Livingston, D.H.; Mohr, A.M.; Sifri, Z.C. Mesenchymal Stem Cells Increase T-Regulatory Cells and Improve Healing Following Trauma and Hemorrhagic Shock. *Journal of Trauma and Acute Care Surgery* **2015**, *79*, 48–52, doi:10.1097/TA.0000000000000681.
17. Curley, G.F.; Hayes, M.; Ansari, B.; Shaw, G.; Ryan, A.; Barry, F.; O'Brien, T.; O'Toole, D.; Laffey, J.G. Mesenchymal Stem Cells Enhance Recovery and Repair Following Ventilator-Induced Lung Injury in the Rat. *Thorax* **2012**, *67*, 496–501, doi:10.1136/thoraxjnl-2011-201059.
18. Devaney, J.; Horie, S.; Masterson, C.; Elliman, S.; Barry, F.; O'brien, T.; Curley, G.F.; O'toole, D.; Laffey, J.G. Human Mesenchymal Stromal Cells Decrease the Severity of Acute Lung Injury Induced by E. Coli in the Rat. **2068**, doi:10.1136/thoraxjnl-2015.
19. Laffey, J.G.; Matthay, M.A. Cell-Based Therapy for Acute Respiratory Distress Syndrome: Biology and Potential Therapeutic Value. *Am J Respir Crit Care Med* 2017, *196*, 266–273.
20. Bejleri, D.; Streeter, B.W.; Nachlas, A.L.Y.; Brown, M.E.; Gaetani, R.; Christman, K.L.; Davis, M.E. A Bioprinted Cardiac Patch Composed of Cardiac-Specific Extracellular Matrix and Progenitor Cells for Heart Repair. *Adv Healthc Mater* **2018**, *7*, doi:10.1002/adhm.201800672.

21. Johnson, T.D.; Lin, S.Y.; Christman, K.L. Tailoring Material Properties of a Nanofibrous Extracellular Matrix Derived Hydrogel. *Nanotechnology* **2011**, *22*, doi:10.1088/0957-4484/22/49/494015.

22. Cui, H.; Miao, S.; Esworthy, T.; Zhou, X.; Lee, S. jun; Liu, C.; Yu, Z. xi; Fisher, J.P.; Mohiuddin, M.; Zhang, L.G. 3D Bioprinting for Cardiovascular Regeneration and Pharmacology. *Adv Drug Deliv Rev* 2018, *132*, 252–269.

23. Shin, Y.J.; Shafranek, R.T.; Tsui, J.H.; Walcott, J.; Nelson, A.; Kim, D.H. 3D Bioprinting of Mechanically Tuned Bioinks Derived from Cardiac Decellularized Extracellular Matrix. *Acta Biomater* **2021**, *119*, 75–88, doi:10.1016/j.actbio.2020.11.006.

24. Falcones, B.; Sanz-Fraile, H.; Marhuenda, E.; Mendizábal, I.; Cabrera-Aguilera, I.; Malandain, N.; Uriarte, J.J.; Almendros, I.; Navajas, D.; Weiss, D.J.; et al. Bioprintable Lung Extracellular Matrix Hydrogel Scaffolds for 3D Culture of Mesenchymal Stromal Cells. **2021**, doi:10.3390/polym1314.

25. Ravichandran, A.; Murekatete, B.; Moedder, D.; Meinert, C.; Bray, L.J. Photocrosslinkable Liver Extracellular Matrix Hydrogels for the Generation of 3D Liver Microenvironment Models. *Sci Rep* **2021**, *11*, doi:10.1038/s41598-021-94990-z.

26. Saludas, L.; Pascual-Gil, S.; Prósper, F.; Garbayo, E.; Blanco-Prieto, M. Hydrogel Based Approaches for Cardiac Tissue Engineering. *Int J Pharm* **2017**, *523*, 454–475, doi:10.1016/j.ijpharm.2016.10.061.

27. Sun, X.; Nunes, S.S. Overview of Hydrogel-Based Strategies for Application in Cardiac Tissue Regeneration. *Biomedical Materials* **2015**, *10*, 034005, doi:10.1088/1748-6041/10/3/034005.

28. Camci-Unal, G.; Annabi, N.; Dokmeci, M.R.; Liao, R.; Khademhosseini, A. Hydrogels for Cardiac Tissue Engineering. *NPG Asia Mater* 2014, *6*.

29. Basara, G.; Gulberk Ozcebe, S.; Ellis, B.W.; Zorlutuna, P. Tunable Human Myocardium Derived Decellularized Extracellular Matrix for 3d Bioprinting and Cardiac Tissue Engineering. *Gels* **2021**, *7*, doi:10.3390/gels7020070.

30. Efraim, Y.; Sarig, H.; Cohen Anavy, N.; Sarig, U.; de Berardinis, E.; Chaw, S.Y.; Krishnamoorthi, M.; Kalifa, J.; Bogireddi, H.; Duc, T.V.; et al. Biohybrid Cardiac ECM-Based Hydrogels Improve Long Term Cardiac Function Post Myocardial Infarction. *Acta Biomater* **2017**, *50*, 220–233, doi:10.1016/j.actbio.2016.12.015.

31. Freytes, D.O.; O'Neill, J.D.; Duan-Arnold, Y.; Wrona, E.A.; Vunjak-Novakovic, G. Natural Cardiac Extracellular Matrix Hydrogels for Cultivation of Human Stem Cell-Derived Cardiomyocytes. *Methods in Molecular Biology* **2014**, *1181*, 69–81, doi:10.1007/978-1-4939-1047-2_7.

32. Buehler, M.J. Nature Designs Tough Collagen: Explaining the Nanostructure of Collagen Fibrils. *Proc Natl Acad Sci U S A* **2006**, *103*, 12285–12290, doi:10.1073/pnas.0603216103.

33. Vesentini, S.; Redaelli, A.; Gautieri, A. Nanomechanics of Collagen Microfibrils. *Muscles Ligaments Tendons J* **2013**, *3*, 23–34, doi:10.11138/mltj/2013.3.1.023.
34. Pouliot, R.A.; Link, P.A.; Mikhaiel, N.S.; Schneck, M.B.; Valentine, M.S.; Gninzeko, F.J.K.; Herbert, J.A.; Sakagami, M.; Heise, R.L. Development and Characterization of a Naturally Derived Lung Extracellular Matrix Hydrogel. **2016**, 1922–1935, doi:10.1002/jbm.a.35726.
35. Wang, B.; Borazjani, A.; Tahai, M.; de Jongh Curry, A.L.; Simionescu, D.T.; Guan, J.; To, F.; Elder, S.H.; Liao, J. Fabrication of Cardiac Patch with Decellularized Porcine Myocardial Scaffold and Bone Marrow Mononuclear Cells. *J Biomed Mater Res A* **2010**, *94*, 1100–1110, doi:10.1002/jbm.a.32781.
36. Singelyn, J.M.; DeQuach, J.A.; Seif-Naraghi, S.B.; Littlefield, R.B.; Schup-Magoffin, P.J.; Christman, K.L. Naturally Derived Myocardial Matrix as an Injectable Scaffold for Cardiac Tissue Engineering. *Biomaterials* **2009**, *30*, 5409–5416, doi:10.1016/j.biomaterials.2009.06.045.
37. Falcones, B.; Sanz-Fraile, H.; Marhuenda, E.; Mendizábal, I.; Cabrera-Aguilera, I.; Malandain, N.; Uriarte, J.J.; Almendros, I.; Navajas, D.; Weiss, D.J.; et al. Bioprintable Lung Extracellular Matrix Hydrogel Scaffolds for 3d Culture of Mesenchymal Stromal Cells. *Polymers (Basel)* **2021**, *13*, 1–18, doi:10.3390/polym13142350.
38. Kobayashi, N.; Yasu, T.; Ueba, H.; Sata, M.; Hashimoto, S.; Kuroki, M.; Saito, M.; Kawakami, M. *Mechanical Stress Promotes the Expression of Smooth Muscle-like Properties in Marrow Stromal Cells*; 2004; Vol. 32;.
39. Rouabhia, M.; Park, H.; Meng, S.; Derbali, H.; Zhang, Z. Electrical Stimulation Promotes Wound Healing by Enhancing Dermal Fibroblast Activity and Promoting Myofibroblast Transdifferentiation. *PLoS One* **2013**, *8*, doi:10.1371/journal.pone.0071660.
40. Grinnell, F. Fibroblast Biology in Three-Dimensional Collagen Matrices. *Trends Cell Biol* 2003, *13*, 264–269.
41. Kotini, M.; Barriga, E.H.; Leslie, J.; Gentzel, M.; Rauschenberger, V.; Schambon, A.; Mayor, R. Gap Junction Protein Connexin-43 Is a Direct Transcriptional Regulator of N-Cadherin in Vivo. *Nat Commun* **2018**, *9*, doi:10.1038/s41467-018-06368-x.
42. Ichinose, S.; Tagami, M.; Muneta, T.; Sekiya, I. Morphological Examination during in Vitro Cartilage Formation by Human Mesenchymal Stem Cells. *Cell Tissue Res* **2005**, *322*, 217–226, doi:10.1007/s00441-005-1140-6.
43. Shinde, A. v.; Humeres, C.; Frangogiannis, N.G. The Role of α-Smooth Muscle Actin in Fibroblast-Mediated Matrix Contraction and Remodeling. *Biochim Biophys Acta Mol Basis Dis* **2017**, *1863*, 298–309, doi:10.1016/j.bbadis.2016.11.006.
44. Dye, B.K.; Butler, C.; Lincoln, J. Smooth Muscle α-Actin Expression in Mitral Valve Interstitial Cells Is Important for Mediating Extracellular Matrix Remodeling. *J Cardiovasc Dev*

Dis **2020**, *7*, doi:10.3390/JCDD7030032.

45. Laffey, J.G.; Matthay, M.A. Cell-Based Therapy for Acute Respiratory Distress Syndrome: Biology and Potential Therapeutic Value. *Am J Respir Crit Care Med* 2017, *196*, 266–273.
46. Kawaguchi, N.; Nakanishi, T. Stem Cell Studies in Cardiovascular Biology and Medicine: A Possible Key Role of Macrophages. *Biology (Basel)* 2022, *11*.
47. Darnell, M.; O'Neil, A.; Mao, A.; Gu, L.; Rubin, L.L.; Mooney, D.J. Material Microenvironmental Properties Couple to Induce Distinct Transcriptional Programs in Mammalian Stem Cells. *Proc Natl Acad Sci U S A* **2018**, *115*, E8368–E8377, doi:10.1073/pnas.1802568115.
48. Kusuma, G.D.; Carthew, J.; Lim, R.; Frith, J.E. Effect of the Microenvironment on Mesenchymal Stem Cell Paracrine Signaling: Opportunities to Engineer the Therapeutic Effect. *Stem Cells Dev* 2017, *26*, 617–631.
49. Pati, F.; Cho, D.-W. Bioprinting of 3D Tissue Models Using Decellularized Extracellular Matrix Bioink. In *3D Cell Culture: Methods and Protocols*; Koledova, Z., Ed.; Springer New York: New York, NY, 2017; pp. 381–390 ISBN 978-1-4939-7021-6.
50. Jang, J.; Park, H.J.; Kim, S.W.; Kim, H.; Park, J.Y.; Na, S.J.; Kim, H.J.; Park, M.N.; Choi, S.H.; Park, S.H.; et al. 3D Printed Complex Tissue Construct Using Stem Cell-Laden Decellularized Extracellular Matrix Bioinks for Cardiac Repair. *Biomaterials* **2017**, *112*, 264–274, doi:10.1016/j.biomaterials.2016.10.026.
51. Gu, L.; Shan, T.; Ma, Y. xuan; Tay, F.R.; Niu, L. Novel Biomedical Applications of Crosslinked Collagen. *Trends Biotechnol* 2019, *37*, 464–491.
52. Basara, G.; Yue, X.; Zorlutuna, P. Dual Crosslinked Gelatin Methacryloyl Hydrogels for Photolithography and 3D Printing. *Gels* **2019**, *5*, doi:10.3390/gels5030034.
53. Becker, M.; Maring, J.A.; Oberwallner, B.; Kappler, B.; Klein, O.; Falk, V.; Stamm, C. Processing of Human Cardiac Tissue toward Extracellular Matrix Self-Assembling Hydrogel for in Vitro and in Vivo Applications. *Journal of Visualized Experiments* **2017**, *2017*, doi:10.3791/56419.
54. Baker, S.C.; Atkin, N.; Gunning, P.A.; Granville, N.; Wilson, K.; Wilson, D.; Southgate, J. Characterisation of Electrospun Polystyrene Scaffolds for Three-Dimensional in Vitro Biological Studies. *Biomaterials* **2006**, *27*, 3136–3146, doi:10.1016/j.biomaterials.2006.01.026.

Chapter VII. Scientific article III

Biocompatible 3D Yttria-Stabilized Zirconia Parts using Direct Ink Writing

Buj-Corral, Irene; ***Sanz-Fraile, Hector****; Tejo Otero, Aitor; Xuriguera, Elena; Otero, Jorge*

In manuscript

Biocompatible 3D Printed Yttria-Stabilized Zirconia parts using Direct Ink Writing

Irene Buj-Corral[1,*], Hector Sanz-Fraile[2], Aitor Tejo-Otero[1], Daniel Vidal[1], José Antonio Padilla[3], Elena Xuriguera[3], Jorge Otero [2,4]

[1] Department of Mechanical Engineering, School of Engineering of Barcelona (ETSEIB), Universitat Politècnica de Catalunya, Av. Diagonal, 647, 08028 Barcelona, Spain

[2]Unit of Biophysics and Bioengineering. School of Medicine and Health Sciences. Universitat de Barcelona. Barcelona. Spain.

[3] Department of Materials Science and Physical Chemistry, Universitat de Barcelona, Carrer Martí i Franquès 1, 08028 Barcelona, Spain

[4] CIBER de Enfermedades Respiratorias, Madrid, Spain

*Corresponding author: irene.buj@upc.edu

Abstract

Metals such as titanium or Cr-Co alloys have been the most widely used materials in biomedical applications that require high mechanical properties, like implants. However, these materials present the disadvantage of releasing ion metals into the body. As an alternative, prostheses made of ceramic materials have been developed, as they produce less debris and have better durability. The aim of the present work is to test the biocompatibility of 3D-prinred yttria-stabilized zirconia parts by culturing human bone-marrow-derived mesenchymal stem cells. Results on surface roughness and biocompatibility tests confirmed that 3 mol % yttria-stabilized zirconia is the most promising material as it presented high biocompatibility.

Introduction

Metals have been the most widely used materials in biomedical applications that require excellent mechanical properties. Among the different applications, personalized medical implants [1] or dental teeth [2] are the most common.

However, a major disadvantage of these materials is related to the release of ion metals. These may cause inflammatory and hypersensitivity reactions [3]. Additionally, a failure in medical implants such as hip or knee would require the removal of the device to implant a new one. On the other hand, research has also been carried out by using 3D-printed metal-PLA (poly lactic acid) composite scaffolds for implants [4]. As an alternative, research in the use of ceramics is growing in popularity. Prostheses made from ceramic materials produce less debris and have better durability than those made from metals or plastics [5].

Amongst the different ceramics used in prosthetics (such as hydroxyapatite [6], or alumina [7,8]), zirconia [7] offers several advantages: (1) reduction in the wear rate of implants [9] and the risk of toxicity [10]; (2) excellent biocompatibility [11] and corrosion resistance [12]; (3) outstanding mechanical properties for the manufacture of prostheses [11]. Zirconia has a monoclinic structure at room temperature. As temperature increases, it changes to tetragonal and later to cubic structures. The transition between monoclinic and tetragonal leads to an important volume change. For this reason, yttria is often added to zirconia to stabilize it with a mix of tetragonal and cubic structures at room temperature [13]. Among the different parameters that can affect the performance of the ceramic grafts, surface roughness is of high importance. For example, a lower layer height corresponds to a lower lateral roughness [14].

Ceramics can be manufactured using different Additive Manufacturing technologies depending on the feedstock form according to Chen *et al*. [15]: 1) slurry-based (stereolithography -SLA-, digital light processing -DLP-, two-photon polymerization -2PP-, inkjet printing and direct ink writing -DIW-), 2) powder-based (selective laser sintering -SLS and selective laser melting -SLM-) and 3) bulk-solid based (laminated object manufacturing -LOM- and fused deposition modelling -FDM-). One of the most employed AM techniques for ceramics is Direct Ink Writing (DIW), an extrusion technique in which a ceramic paste is extruded and subsequently deposited layer-by-layer [16–18]. Different ceramic materials can be printed with DIW, for example, kaolinite clay ceramics[19], zirconia[20], zirconia-toughened alumina[21], or hydroxyapatite [22].

Yttria-stabilized zirconia (YSZ) is a biocompatible ceramic with high mechanical properties. A major advantage of YSZ is that it can be 3D printed to manufacture complex shapes such as prostheses or dental implants [23,24]. Nevertheless, to the author's knowledge, few *in vitro* studies are known for proving the biocompatibility of 3D-printed YSZ [25,26]. On the other hand, the surface finish of ceramics is known to affect their mechanical properties [27] and also influence their biocompatibility[28]. In addition, surface roughness is related to bacterial growth in dental implants[29]. The aim of the present research study is to culture human bone-marrow-derived mesenchymal stem cells (hBM-MSCs) on 3D-printed yttria-stabilized zirconia parts with different surface roughness values to assess their suitability to be used as biomedical material in implants.

Materials and Methods

1.1. Zirconia parts preparation for cell culture

Zirconia pastes were prepared in a mixer. Mixing time was 2 min and rotational speed was 2000 min^{-1}. Vacuum pressure was used to enable both dispersion of materials and the removal of bubbles (ARV-310P Thinky Corporation, Tokyo, Japan). Yttria-stabilized zirconia (YSZ) with a 3 mol% concentration (HSY-3B, Daiichi Kigenso Kagaku Kogyo Co., Ltd., Japan) and a 0.5 % wt dispersant (Dolapix PC75, Zschimmer & Schwarz, Germany) were mixed to a Pluronic F-127 (Sigma-Aldrich, UK) stock solution of 25 wt% concentration. The final solid percentage was 40 v%. The d50 value of the ceramic powder ranged between 0.7 and 1.5 µm (50% of the particles are smaller than that size).

Disk-shaped samples of diameter 10 mm and height 4 mm were printed (see Figure 1A) and subsequently sintered at 1550 °C, with a heating rate of 5 °C/min (see Figure 1B). The final dimensions of the disks were around 8.5 mm in diameter and 3 mm in height. As can be seen there is a shrinkage in the samples of 15% and 25% in the horizontal plane and vertical plane, respectively. A linear infill pattern of raster angle 0° was used, with different infill values of 80% and 95% respectively. Three replicates were considered for each experiment.

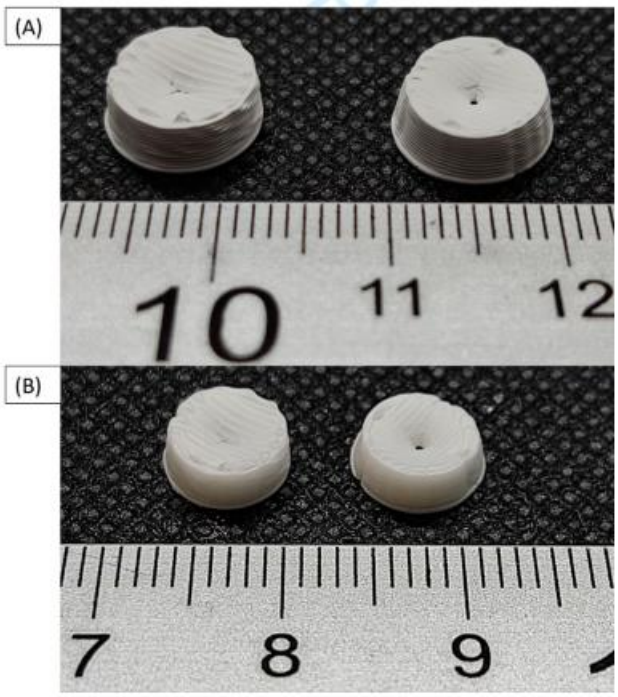

Figure 1. *3D printed zirconia samples (A) before and (B) after sintering treatment.*

A customized 3D printer was used, Dual Paste Extruder, from CIM-UPC (Figure 2). The nozzle diameter was 0.58 mm, the layer height was 0.3 mm, the printing speed was 5 mm/s and the extrusion multiplier was 100%.

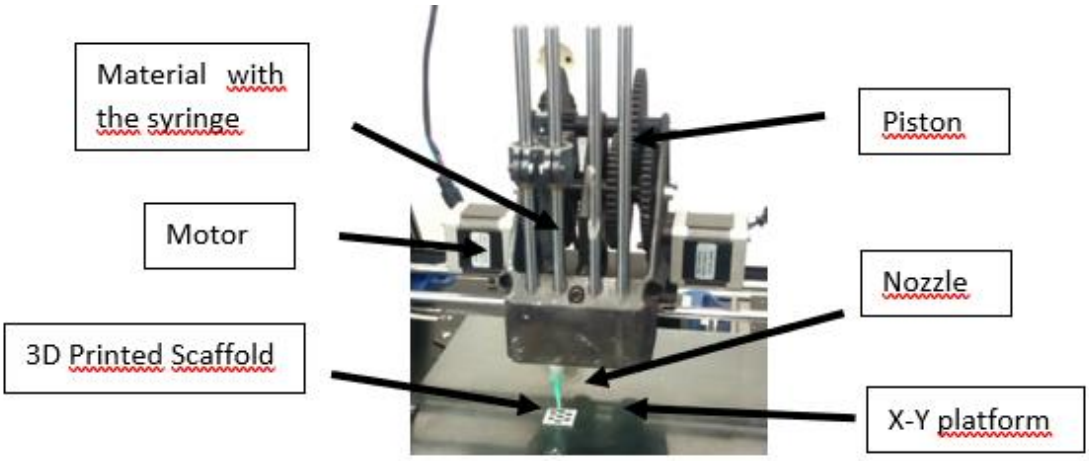

Figure 2. *Printing head of the Dual Paste extruder from CIM-UPC*

1.2. Surface roughness characterization

According to the work of Deltombe and co-workers [30], the different roughness parameters can be divided into six groups: (1) amplitude, (2) spatial, (3) hybrid, (4) functional, (5) feature, and (6) other 3D parameters. In the present study, not only areal arithmetical mean has been studied, but also skewness (S_{sk}) and kurtosis (S_{ku}) values were measured. S_a (Equation 1) is the average value of the heights, expressed as an absolute value, regarding the central plane [20]. S_{sk} (Equation 2) corresponds to the symmetry of the heights concerning the central plane. A positive S_{sk} value indicates the predominance of peaks, while a negative value corresponds to the predominance of valleys [31]. Kurtosis parameter S_{ku} (Equation 3) is related to the peakedness of the surface. Sharp peaks and valleys correspond to S_{ku} >3, while rounded peaks and valleys are related to S_{ku} <3 [31]. Both parameters are related to the friction control of surfaces [32].

A Smartproof 5 confocal microscope (Zeiss, Oberkochen, Germany) with a 20X magnification lens was used to measure areal roughness. Optical equipment was used, to prevent damage to the samples and/or to the tip of a contact roughness meter [33]. The uncertainty of the microscope in the vertical direction is ± (0.1 µm + 0.008 × L), whereas in the horizontal direction it is ± (0.1 µm + 0.012 × L). Areal parameters were determined according to ISO 25178 standard [34].

$$S_a = \frac{1}{A} \iint_A |Z\,(x,y)|\, dxdy \qquad (1)$$

$$S_{ku} = \frac{1}{A_q^4} \iint_A |Z\,(x,y)|^4\, dxdy \qquad (2)$$

$$S_{sk} = \frac{1}{A_q^3} \iint_A |Z\,(x,y)|^3\, dxdy \qquad (3)$$

where A is the measured area and Z (x, y) is a function that corresponds to the surface topography.

Roughness was measured on the upper surface of the disks, within an area of 0.5 x 0.5 mm.

1.3. BM-MSCs culture

hBM-MSCs are widely used in regenerative medicine and they are a widely accepted model to test the biocompatibility of new scaffold developments, as they have been used previously to test the biocompatibility of novel scaffolds based, for example, in silk composites [35]. hBM-MSCs were expanded and cultured following the manufacturer's instructions (ATCC, VA). The medium was replaced every 2 days and cells were split from T-75 flasks at reaching 80% confluence. Cells in passage 5 were used for this study. 3D printed zirconia scaffolds were sterilized by high pressure and vapor using an autoclave (Tomy SX-700E) before seeding the cells, and half of them were coated with type I collagen at a concentration of 0.1 mg/mL (Merck, US). Cells were seeded on the sterilized parts with a density of $4 \cdot 10^4$ cells/cm^2 and cultured for 24h and 72h. At the endpoint, samples were stained for DNA (NucBlue) to identify cell nuclei and imaged with a confocal microscope with a monitored X-Y stage (Nikon TI-HUBC, Japan) with a 10x objective.

Results and Discussion

1.4. 3D Printed Samples Shrinkage

The 3D printed samples showed, as mentioned before, a shrinkage of 15% and 25% in the horizontal plane and vertical plane, respectively. This is in accordance with a previous study by Buj *et al*. [14], in which the shrinkage percentage values ranged between 19% and 28%. On the other hand, He *et al*. [36] 3D printed using a DLP printer samples which displayed significant shrinkage after sintering, with the maximum shrinkage being 35.26%.

1.5. Surface Roughness

Table 1 shows the average values of areal arithmetic mean, skewness, and kurtosis of both 80% and 95% density experiments. Overall, both porosities tested showed a smooth roughness, no sharp or rounded valley or as well as the presence of high peaks or deep valleys. Figure 3 shows the surface topography of the 3D-printed parts.

Table 1. Surface roughness of the upper surface of the yttria-stabilized zirconia samples.

	Sa [µm]	Ssk	Sku
80% porosity	0.30±0.026	-0.002±0.48	10.35±8.37
95% porosity	0.69±0.007	-0.14±0.05	5.03±0.41

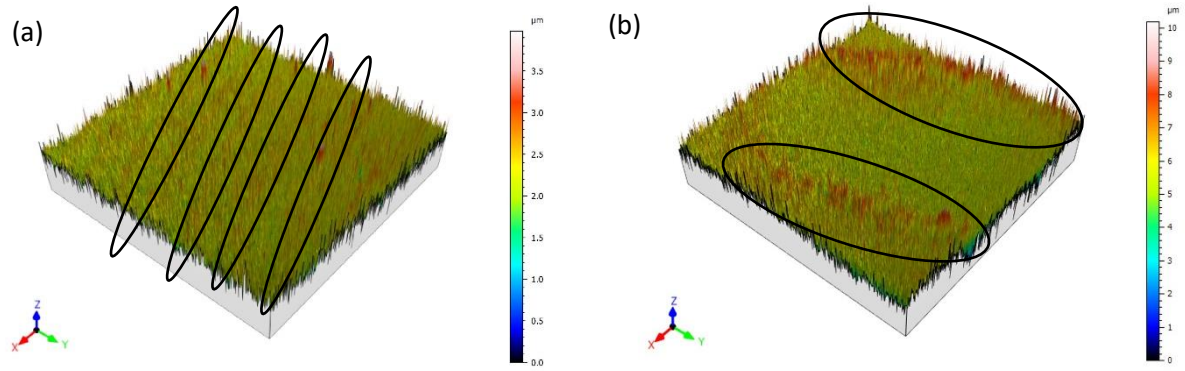

Figure 3. *Surface topography of YSZ parts printed with: (a) 80% infill, (b) 95% infill*

The surface topographies showed that the different printed lines were fused, showing no holes among them. In Figure 3a, several parallel crests can be observed, corresponding to the deposition of material along parallel lines in the linear structure. In Figure 3b only some crests can be observed, showing that, due to an excess of material, the paste became mixed. As for S_a values in Table 1, higher roughness values were observed for 95 % infill (Figure 3b) than for 80 % infill (Figure 3a). This suggests that for a high infill value of 95 % there was an excess of material that leaded to higher crests. A slightly negative value for S_{sk} was reported for 95 % infill (Figure 3b), showing higher valleys than peaks. As for S_{ku}, a high value of 10.35 was obtained for 80 % infill, corresponding to sharp peaks and valleys, with a lower value of 5.03 for 95 % infill. In both cases, S_{ku} was higher than 3, which corresponds to a normal distribution of heights.

Shao *et al*. [37] reported surface roughness close to 8 µm for zirconia-based gel materials. For implants, S_a values below or equal to 1 µm are considered to be smooth, while values above 1 µm are rough, from the point of view of osseointegration [38]. Therefore, the samples in the present study can be considered smooth and, therefore, it is not necessary to undertake a subsequent polishing operation. Additionally, the surface roughness obtained in lateral walls of yttria-stabilized zirconia pastes depends on layer height and on print speed [20]. The lower layer height and speed, the smoother the surface is as demonstrated by our previous findings [14]. In the present work, however, the roughness was measured on the upper surface of the printed parts to assess its influence on cell compatibility.

1.6. *In vitro* biocompatibility assessment

As it can be observed in Figure 4, hBM-MSCs were able to attach to the 3D-printed zirconia scaffolds and showed good viability after 3 days of culture (no differences were observed between 24h and 72h of culture). It is noticeable that no differences were observed

between uncoated and coated samples (type I collagen), showing that the bare material is biocompatible enough to allow direct cell culture on top without the need for functionalization, so unspecific adhesions formed by MSCs on bare scaffolds are enough for them to proliferate. Collagen has been proven to enhance corrosion resistance and biocompatibility mainly on metallic substrates such as titanium[39] or magnesium alloys[40] but it might not be so effective on ceramic substrates. Cells attached to the bare surface, suggesting that unspecific adhesions are being formed, although more tests should be done to confirm which cell proteins are mediating those adhesions to the surface. On the other hand, although a higher proliferation might be observed in the higher infill scaffolds, the difference is not significant enough to extract conclusions about the most appropriate infill parameter. Further tests on proliferation should be done to confirm these hypotheses.

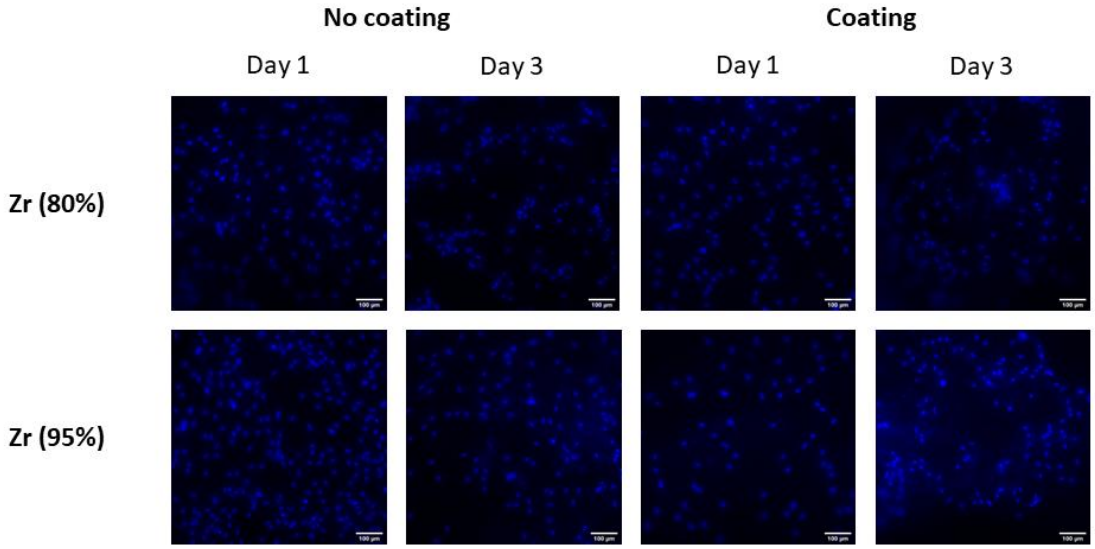

Figure 4. *Fluorescent images (DAPI, cell nuclei) of hBM-MSCs cultured for 24h or 72h on zirconia scaffolds (80% or 95% of porosity) with and without type I collagen coating.*

The surface properties of the scaffolds directly affect cellular behavior. A too-smooth or too-rough scaffold could cause the cells not to adhere or to modify their behavior. For example, in soft hydrogels osteodifferentiation increased with surface roughness, being important from Rq values around 0.38 µm, while in stiff hydrogels higher osteodifferentiation was observed for intermediate roughness values[41]. In this work, the areal average roughness S_a measured in the above scaffolds, between 0.30±.026 µm and 0.69±0.0 µm, led to a good cell proliferation behavior as shown in Figure 4. Thus, it seems that scaffolds' roughness makes them suitable for MSCs culture, even when the material remains uncoated. This indicated that cells are generating unspecific adhesions with the printed parts that allow them to engraft.

Conclusions

In the present work, 3D-printed yttria-stabilized zirconia parts are presented to be used as a novel material in implants. We found that the physical properties of the material, such as the surface topography, made the material a suitable candidate for prosthetics. Human BM-MSCs cultured on top of the printed scaffolds showed to be highly viable. Interestingly, we observed no differences between bare printed parts and those coated with an extracellular matrix protein to increase cell adhesion, thus indicating that the 3D-printed scaffolds could be used without further processing. This opens a door in the field of personalized medicine, as scaffolds could be directly printed with the needed shape before the intervention in the patient. Further research *in vivo*, by implanting the developed scaffolds in animals, would be needed to evaluate the scaffolds presented herein, but *in vitro* results suggest that biocompatibility would not be a limiting factor in those experiments.

Acknowledgments

This work was co-financed by the European Union Regional Development Fund within the framework of the ERDF Operational Program of Catalonia 2014–2020 with a grant of 50% of total cost eligible, project BASE3D, grant number 001-P-001646. Authors would like to thank Alejandro Domínguez for his help with the experimental tests.

References

1. Buj-Corral I, Tejo-Otero A, Fenollosa-Artés F. Development of am technologies for metals in the sector of medical implants. *Metals (Basel)* 2020; 10: 1–30.

2. Bozkurt Y, Karayel E. 3D printing technology; methods, biomedical applications, future opportunities and trends. *J Mater Res Technol* 2021; 14: 1430–1450.

3. Czarnek K, Terpilowska S, Siwicki AK. Selected aspects of the action of cobalt ions in the human body. *Cent Eur J Immunol* 2015; 40: 236–242.

4. Garcia J, Yang ZL, Mongrain R, et al. 3D printing materials and their use in medical education: A review of current technology and trends for the future. *BMJ Simul Technol Enhanc Learn* 2018; 4: 27–40.

5. Lerouge S, Huk O, Yahia L, et al. Characterization of in vivo wear debris from ceramic-ceramic total hip arthroplasties. *J Biomed Mater Res* 1996; 32: 627–633.

6. Hamdi DA, Jiang ZT, No K, et al. Biocompatibility study of multi-layered hydroxyapatite coatings synthesized on Ti-6Al-4V alloys by RF magnetron sputtering for prosthetic-orthopaedic

implant applications. *Appl Surf Sci* 2019; 463: 292–299.

7. De Aza AH, Chevalier J, Fantozzi G, et al. Crack growth resistance of zirconia toughened alumina ceramics for joint prostheses. *Key Eng Mater* 2001; 23: 1535–1538.

8. Zeng P. *Biocompatible alumina ceramic for total hip replacements*. 2008. Epub ahead of print 2008. DOI: 10.1179/174328408X287682.

9. Jiang L, Liao Y, Wan Q, et al. Effects of sintering temperature and particle size on the translucency of zirconium dioxide dental ceramic. *J Mater Sci Mater Med* 2011; 22: 2429–2435.

10. Bearden LJ, Cooke FW. Growth inhibition of cultured fibroblasts by cobalt and nickel. *J Biomed Mater Res* 1980; 14: 289–309.

11. Gautam C, Joyner J, Gautam A, et al. Zirconia based dental ceramics: structure, mechanical properties, biocompatibility and applications. *Dalt Trans* 2016; 45: 19194–19215.

12. Bergman M, Bergman B, Söremark R. Tissue accumulation of nickel released due to electrochemical corrosion of non-precious dental casting alloys. *J Oral Rehabil* 1980; 7: 325–330.

13. Hayashi H, Saitou T, Maruyama N, et al. Thermal expansion coefficient of yttria stabilized zirconia for various yttria contents. *Solid State Ionics*. Epub ahead of print 2005. DOI: 10.1016/j.ssi.2004.08.021.

14. Buj-corral I, Vidal D, Tejo-otero A, et al. Characterization of 3D Printed Yttria-Stabilized Zirconia Parts for Use in Prostheses. 2021; 1–12.

15. Chen Z, Li Z, Li J, et al. 3D printing of ceramics: A review. *J Eur Ceram Soc* 2019; 39: 661-687.

16. Lewis JA. Direc ink writing of 3D functional materials. *Adv Funct Mater* 2006; 16: 2193-2204.

17. Fenollosa-artes F, Jorand L, Tejo-otero A, et al. Soft 3D printing of thermoplastic polyurethane : Preliminary study. Epub ahead of print 2022. DOI: 10.1177/09544054221100077.

18. Tejo-otero A, Colly A, Courtial E, et al. Soft-tissue-mimicking using silicones for the manufacturing of soft phantoms by fresh 3D printing. Epub ahead of print 2021. DOI: 10.1108/RPJ-04-2021-0079.

19. Revelo CF, Colorado HA. 3D printing of kaolinite clay ceramics using the Direct Ink Writing (DIW) technique. *Ceram Int*. Epub ahead of print 2018. DOI: 10.1016/j.ceramint.2017.12.219.

20. Buj-Corral I, Domínguez-Fernández A,

Gómez-Gejo A. Effect of printing parameters on dimensional error and surface roughness obtained in direct ink writing (DIW) processes. *Materials (Basel)*; 13. Epub ahead of print 2020. DOI: 10.3390/ma13092157.

21. Stanciuc AM, Sprecher CM, Adrien J, et al. Robocast zirconia-toughened alumina scaffolds: Processing, structural characterisation and interaction with human primary osteoblasts. *J Eur Ceram Soc*. Epub ahead of print 2018. DOI: 10.1016/j.jeurceramsoc.2017.08.031.

22. Cesarano J, Dellinger JG, Saavedra MP, et al. Customization of load-bearing hydroxyapatite lattice scaffolds. *Int J Appl Ceram Technol* 2005; 2: 212–220.

23. Pieralli S, Kohal RJ, Jung RE, et al. Clinical Outcomes of Zirconia Dental Implants: A Systematic Review. *J Dent Res* 2017; 96: 38–46.

24. Pieralli S, Kohal RJ, Lopez Hernandez E, et al. Osseointegration of zirconia dental implants in animal investigations: A systematic review and meta-analysis. *Dent Mater* 2018; 34: 171–182.

25. Hodásová L, Sans J, Molina BG, et al. Polymer infiltrated ceramic networks with biocompatible adhesive and 3D-printed highly porous scaffolds. *Addit Manuf*; 39. Epub ahead of print 2021. DOI: 10.1016/j.addma.2021.101850.

26. Chen F, Zhu H, Wu JM, et al. Preparation and biological evaluation of ZrO2 all-ceramic teeth by DLP technology. *Ceram Int* 2020; 46: 11268–11274.

27. Shukla PP, Lawrence J, Wu H. Fracture toughness of a zirconia engineering ceramic and the effects thereon of surface processing with fibre laser radiation. *Proc Inst Mech Eng Part B J Eng Manuf*. Epub ahead of print 2010. DOI: 10.1243/09544054JEM1887.

28. Li M, Zhang L, Zhang C, et al. Effect of Y2O3 on the physical properties and biocompatibility of β–SiAlON ceramics. *Ceram Int* 2020; 46: 23427–23432.

29. Rashid H. The effect of surface roughness on ceramics used in dentistry: A review of literature. *European Journal of Dentistry*. Epub ahead of print 2014. DOI: 10.4103/1305-7456.143646.

30. Deltombe R, Kubiak KJ, Bigerelle M. How to select the most relevant 3D roughness parameters of a surface. *Scanning* 2014; 36: 150–160.

31. LLC MM. 3D S Parameters - Height (Amplitude) Parameters, https://www.michmet.com/3d_s_height_parameters_sssksku.htm (2021).

32. Sedlaček M, Gregorčič P, Podgornik B.

Use of the Roughness Parameters S sk and S ku to Control Friction—A Method for Designing Surface Texturing. *Tribol Trans* 2017; 60: 260–266.

33. Oonishi H, Wakitani S, Murata N, et al. Clinical Experience With Ceramics in Total Hip Replacement. *Clin Orthop Relat Res* 2000; 77–84.

34. ISO25178. *ISO, I. (2010). 25178-6 Geometrical product specifications (GPS)-Surface texture: Areal-Part 6: Classification of methods for measuring surface texture. Geneva, Switzerland.* 2010.

35. Sanz-Fraile H, Amoros S, Mendizabal I, et al. Silk-Reinforced Collagen Hydrogels with Raised Multiscale Stiffness for Mesenchymal Cells 3D Culture. *Tissue Eng - Part A* 2020; 26: 358–370.

36. He R, Liu W, Wu Z, et al. Fabrication of complex-shaped zirconia parts via a DLP-stereolithography-based 3D printing method. *Ceram int* 2018; 44: 3412-3416.

37. Shao H, Zhao D, Lin T, et al. 3D gel-printing of zirconia ceramic parts. *Ceram Int* 2017; 43: 13938–13942.

38. Sykaras N, Iacopino AM, Marker VA, et al. Implant materials, designs, and surface topographies: their effect on osseointegration. A literature review. *Int J Oral Maxillofac Implants*; 15.

39. Chen J, Chen C, Chen Z, et al. Collagen/heparin coating on titanium surface improves the biocompatibility of titanium applied as a blood-contacting biomaterial. *J Biomed Mater Res - Part A* 2010; 95 A: 341–349.

40. Guo Y, Su Y, Gu R, et al. Enhanced corrosion resistance and biocompatibility of biodegradable magnesium alloy modified by calcium phosphate/collagen coating. *Surf Coatings Technol*; 401. Epub ahead of print 2020. DOI: 10.1016/j.surfcoat.2020.126318.

41. Hou Y, Yu L, Xie W, et al. Surface Roughness and Substrate Stiffness Synergize to Drive Cellular Mechanoresponse. *Nano Lett* 2020; 20: 748–757.

Chapter VIII. Scientific article IV

Characterization of 3D Printed Metal-PLA Composite Scaffolds for Biomedical Applications

*Irene Buj-Corral, **Héctor Sanz-Fraile**, Anna Ulldemolins, Aitor Tejo-Otero, Alejandro Domínguez-Fernández, Isaac Almendros, Jorge Otero*

Polymers (Basel). 2022 Jul 5;14(13):2754.

IF: 4.967. Q1 (16/90)

polymers

MDPI

Communication

Characterization of 3D Printed Metal-PLA Composite Scaffolds for Biomedical Applications

Irene Buj-Corral [1,*], Héctor Sanz-Fraile [2], Anna Ulldemolins [2], Aitor Tejo-Otero [1], Alejandro Domínguez-Fernández [1], Isaac Almendros [2,3] and Jorge Otero [2,3,*]

check for updates

May 2022 Accepted: 1 July 2022
Published: 5 July 2022

Citation: Buj-Corral, I.; Sanz-Fraile, H.; Ulldemolins, A.; Tejo-Otero, A.; Domínguez-Fernández, A.; Almendros, I.; Otero, J. Characterization of 3D Printed Metal-PLA Composite Scaffolds for Biomedical Applications. *Polymers* **2022**, *14*, 2754. https://doi.org/10.3390/polym14132754

Academic Editors: Hamid Reza Vanaei, Sofiane Khelladi and Abbas Tcharkhtchi

Received: 31

[1] Department of Mechanical Engineering, School of Engineering of Barcelona (ETSEIB), Universitat Politècnica de Catalunya, Av. Diagonal 647, 08028 Barcelona, Spain; aitor.tejo@upc.edu (A.T.-O.); alejandro.dominguez-fernandez@upc.edu (A.D.-F.)

[2] Unitat de Biofísica i Bioenginyeria, Facultat de Medicina i Ciències de la Salut, Universitat de Barcelona, 08036 Barcelona, Spain; hector.sanz.fraile@hotmail.com (H.S.-F.); anna.ulldemolins@ub.edu (A.U.); isaac.almendros@ub.edu (I.A.)

[3] CIBER de Enfermedades Respiratorias, 28029 Madrid, Spain

* Correspondence: irene.buj@upc.edu (I.B.-C.); jorge.otero@ub.edu (J.O.)

Abstract: Three-dimensional printing is revolutionizing the development of scaffolds due to their rapid-prototyping characteristics. One of the most used techniques is fused filament fabrication (FFF), which is fast and compatible with a wide range of polymers, such as PolyLactic Acid (PLA). Mechanical properties of the 3D printed polymeric scaffolds are often weak for certain applications. A potential solution is the development of composite materials. In the present work, metal-PLA composites have been tested as a and 0.8 mm, respectively. The porosity of the samples was measured from cross-sectional images. Biocompatibility was assessed by culturing Human Bone Marrow-Derived Mesenchymal Stromal on the surface of the printed scaffolds. The results showed that, for identical line spacing value, the highest porosity corresponded to bronzefilled material and the lowest one to steel-filled material. Steel-filled PLA polymers showed good cytocompatibility without the need to coat the material with biomolecules. Moreover, human bone marrow-derived mesenchymal stromal cells differentiated towards osteoblasts when cultured on top of the developed scaffolds. Therefore, it can be concluded that steel-filled PLA bioprinted parts are valid scaffolds for bone tissue engineering.

Keywords: steel-filled PLA; FFF; scaffold; grid structure; cell culture

material for 3D printing scaffolds. Three different materials were tested: copper-filled PLA, bronze-filled PLA, and steel-filled PLA. Disk-shaped samples were printed with linear infill patterns and line spacing of 0.6, 0.7,

1. Introduction

Additive manufacturing (AM) is a group of techniques in which three-dimensional structures are manufactured layer-by-layer in an automated way. It offers several advantages over the traditional subtractive or forming techniques: (1) it allows manufacturing complex shapes and even porous structures, (2) cheaper parts are produced if low-cost machines are employed; (3) it implies material, waste, and energy savings. Within the AM field, there are seven different categories [1]: binder jetting (BJ) [2], directed energy deposition (DED) [3], material extrusion (includes FFF—Fused Filament Fabrication and DIW—Direct Ink Writing) [4,5], material jetting (MJ) [6], powder bed fusion (PBF) (includes SLM—Selective Laser Melting and SLS—Selective Laser Sintering) [7], sheet lamination [8], and vat photopolymerization (includes SLA—stereolithography and Digital Light Processing (DLP) printing, as well as volumetric 3D printing) [9,10].

Within the different AM techniques, FFF is one of the most widely used technologies for rapid prototyping within the biomedical field, as it presents several advantages in terms of costs and the range of materials that can be used [11]. Also known as FDM (Fused Deposition Modelling), FFF uses a continuous filament of a thermoplastic material such as PolyLactic Acid (PLA) to build complex 3D structures in an automated way. One of the main disadvantages of FFF technology is the difficulty to ensure the correct bonding between layers [12]. The FFF 3D printing technique was patented in 1989 [13] and it bloomed up after its patent expired in 2009. After the technique became available to the general public, it has been used in different fields: automation, aeronautics, medicine, etc. Regarding the biomedical area, different applications could be highlighted, such as implants [14,15], 3D surgical planning prototypes [16,17], scaffolding [18,19], and regeneration of tissues [20].

There are numerous materials in the market for FFF 3D printing, for example acrylonitrile butadiene styrene (ABS) or Nylon, being PLA one of the most widely used, both alone and in combination with other materials such as wood, metals, or ceramics. Very little data have so far been published on systematic studies regarding the use of metal-filled filaments, since selecting compatible filler materials for the sake of improving the performance of polymeric composite materials is a difficult task [21]. In the present study, copper-, bronze-, and steel-filled PLA filaments are studied. Copper has an excellent heat and electric conductivity, it is easy to machine, bio-fouling resistant, and corrosion resistant [22]. Bronze alloy consists primarily of Cu, commonly with between 12 and 12.5% of Sn. It is a ductile alloy. Stainless steel is made of iron with typically a few tenths of carbon percentage, and with anti-corrosion elements such as Ni or Cr. It has high tensile strength, high corrosion resistance, and high biocompatibility. Therefore, it is used in a wide range of biomedical applications such as prostheses.

Regarding the mechanical properties of the metal-filled filaments, in some cases, increasing the metal content reduces the tensile strength and increases the thermal conductivity of the composite material studied. For example, Mohammadizadeh *et al*. [23] manufactured PLA filaments that contained copper, bronze, stainless steel, high carbon iron, and aluminum powders. They stated that the mechanical proper4ies of copper-filled-PLA were worse than those of PLA 3D printed parts. Additionally, they showed that the larger the layer height was, the lower the tensile strength, elastic modulus, and yield stress were. On the contrary, in different works, the mechanical properties were observed to increase when adding metals to the base polymer. Liu *et al*. [24] found that ceramic, copper, and aluminum-based PLA composite parts had similar or even superior mechanical properties when compared to bare PLA-made parts. Fafenrot *et al*. [25] developed polymer-metal materials 3D printed by FFF and concluded that the mechanical properties were similar to those of the PLA parts. On the other hand, there are other available options for the polymer matrix such as the use of ceramics. For instance, glass fiber-reinforced PLA can be employed in a wide range of applications, particularly in the biomedical, energy, and electronics industry [26]. In another example, Mahmoud *et al*. [27] studied the incorporation of two carbon fillers into the polypropylene: carbon nanotubes and synthetic graphite. The results showed that graphite-filled composites are more conductive than carbon nanotubesfilled composites. The flexural and tensile strength for both composites increased with the increase in the filler materials weight percentage. Later, the same authors [28] showed that flame-retardant MPP (melamine polyphosphate) had remarkable effects

on the mechanical properties of the LLDPE (low-density polyethylene) composites. Five weight percentages of MPP were embedded into LLDPE, ranging from 5 to 30 wt%. It was concluded that the Young's modulus increased, and the tensile break strength and the tensile yield strength increased monotonically with the increase in MPP content.

The addition of metal components to the polymers used in FFF printing opens a new world in different fields such as bioengineering, but more knowledge needs to be obtained on the optimization of the production of these biomaterials for the fabrication of novel scaffolds. Although there are some studies about cell growth on 3D printed ceramic zirconia toughened alumina (ZTA) scaffolds [29], few and non-concluding studies have been done with metal-filled polymeric materials. Moreover, previous studies have not focused on the biological response of cells in metal-PLA 3D printed parts, as cells were cultured on metal-based scaffolds, such as titanium 3D printed bases [30]. On the other hand, several studies have evaluated the cytocompatibility of 3D printed iron-based scaffolds for bone regeneration [11,31,32] so we hypothesize that composite polymers incorporating metals will be appropriate for cell growth, since metals and alloys have been used extensively as bone substitutes [33,34]. These iron-based alloys have better mechanical properties than those based on lighter materials, such as magnesium.

Porosity is another key parameter that must be taken into consideration during the design and synthesis of a biomaterial [35]. The 3D printed porous materials should ideally fulfil conditions such as biocompatibility, noninflammatory response, tunable biodegradability, appropriate mechanic properties, defined pore structure, and, above all, promote a health improvement [36].

Table 1. 3D printing parameters.

Variable	**Value**
Infill pattern	Linear
Layer height (mm)	0.15
Nozzle diameter (mm)	0.4
Print speed (mm/s)	7
Extrusion multiplier (%)	100
Temperature (° C)	190

This work presents the characterization of three metal-reinforced PLA biomaterials for 3D printing biomedical scaffolds regarding porosity, surface roughness and cell culture. For that purpose, first the surface of the parts was analyzed, and the line spacing was measured. Surface roughness was then measured on the upper surface of the specimens. Regarding biological characterization, human-derived bone marrow mesenchymal stromal cells (hBM-MSC) were cultured on the composite scaffolds to assess their biocompatibility and the effect of the 3D printing scaffolds on determining cell fate, specifically in osteogenic differentiation.

2. Materials and Methods

2.1. Materials

The materials used in the present study were metal-filled PLA filaments of 2.85 mm diameter manufactured by ColorFabb (Belfeld, Netherlands). The specific materials used were: (1) steel-filled PLA, (2) bronze-filled PLA, and (3) copper-filled PLA. As stated by the manufacturer, these materials were developed for aesthetic purposes and need a polishing treatment after being printed if a brilliant appearance is to be required. All reagents were purchased from Sigma-Aldrich (Saint Louis, MO, USA), unless specified otherwise.

2.2. 3D Printing Process

Parts were additively manufactured by using a Sigma R19 3D printer (BCN3D Technologies, Gavà, Spain). The 3D printing parameters are presented in Table 1. Figure 1 shows a scheme of an FFF 3D printer. Cura BCN3D software was used to generate the G-code that is required to print the parts.

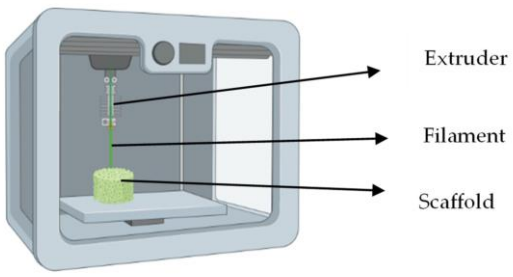

Figure 1. FFF 3D printer scheme.

Disk-shaped samples of 6 mm in diameter and 2 mm in height were manufactured.

The linear infill pattern was selected, using three different line spacing values: 0.6 mm, 0.7 mm, and 0.8 mm (Figure 2). The shell width was set to 0.4 mm and the bottom width was set to 1.2 mm. No top layer was used.

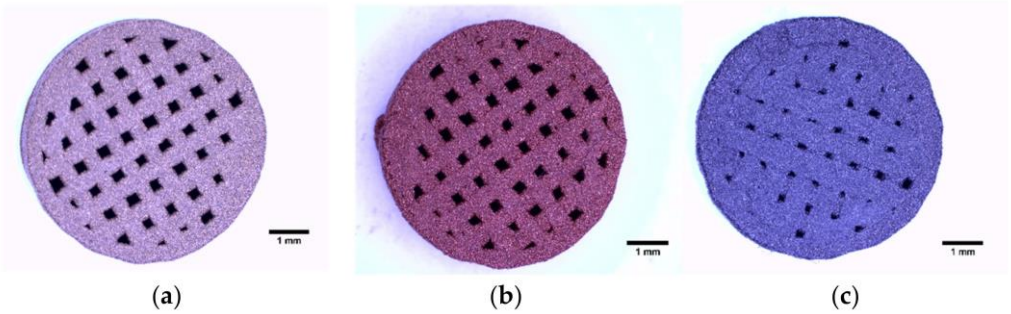

Figure 2. Disk-shaped 3D printed samples with line spacing of 0.7 mm of (**a**) bronze-filled PLA, (**b**) copper-filled PLA, (**c**) steel-filled PLA. Scale bars correspond to 1 mm.

2.3. Pictures

Pictures of the 3D printed scaffolds were obtained by using a Leica S8AP0 binocular magnifier (Leica Camera AG, Wetzlar, Germany) with 8× (Figure 2) and 16× (Figure 3) magnification, respectively.

2.4. Porosity

The porosity of the disk samples was quantified from the images of the cross section of the scaffolds, assuming that the length of the pores corresponds to the length of the sample and using Equation (1):

$$Pt = \frac{V_p}{V_t} \quad (1)$$

where *Pt* is the porosity, *Vp* the pore volume, and *Vt* the total volume of the scaffold. The software used for cross-sectional images quantification was ImageJ.

2.5. Roughness

Roughness was measured with a Talysurf 2 contact roughness meter from Taylor Hobson Ltd., Leicester, UK. A diamond tip was used with tip angle of 90° and tip radius of 2 µm. The measuring force was 0.8 mN and speed was 0.5 mm/s. A Gaussian filter was employed. A cut-off value of 0.8 mm was used according to ISO 4288 [37]. Total sampling length was 4.8 mm (6 × 0.8 mm). Roughness was measured on the upper surface of the disks, along the generatrices of the filaments in the two perpendicular directions, in order to assess if there were differences regarding their surface finish. As an example, the steel-filled samples were measured with line spacing 0.6 and 0.7 mm. Two different samples were measured for each line spacing value.

The roughness parameters that were analyzed in this present study are:

1. Arithmetical mean roughness value or arithmetical mean of the absolute values of the profile deviations from the mean line of the roughness profile (Ra) (Equation (2)), which is one of the most commonly employed parameters in industry;

$$Ra = \frac{1}{L}\int_0^L |Z(x)|dx \quad (2)$$

2. Mean roughness depth or average maximum peak to valley of five consecutive sampling lengths of the profile within a sampling length (Rz);
3. Kurtosis (Rku), which is a measure of the sharpness of the profile (Equation (3));

$$Rku = \frac{1}{R_q^4}\left[\frac{1}{L}\int_0^L |Z^4(x)|dx\right] \quad (3)$$

4. Skewness (Rsk), which measures the symmetry of the profile (Equation (4));

$$Rsk = \frac{1}{R_q^3}\left[\frac{1}{L}\int_0^L |Z^3(x)|dx\right] \quad (4)$$

These parameters are defined in the UNE-EN-ISO 4287:1999 standard [38].

2.6. Human Bone Marrow-Derived Mesenchymal Stromal Cells Culture on the Developed Scaffolds

Primary human Bone Marrow-Derived Mesenchymal Stromal cells (hBM-MSCs, ATCC PCS-500-012, ATCC, Manassas, VA, USA) were expanded following the manufacturers' instructions. Cells from passage 3–6 were used for all the experiments presented herein.

Printed parts were coated by incubating with rat tail-derived type I collagen at a concentration of 0.1 mg/mL for 30 min at 37 °C. hBM-MSCs were cultured on the scaffolds at a seeding density of 4 × 10^4 cells/cm^2 for 24 and 72 h. Cells seeded on uncoated parts were cultured in parallel. At the defined time points, cells were fixed with paraformaldehyde (PFA) 4% for further immunohistochemical imaging.

In a subsequent set of experiments, hBM-MSCs were cultured with a seeding density of 9.4 × 10^4 cells/cm^2 for 1, 4, and 7 days, respectively, on the different collagencoated/uncoated samples and then fixed with PFA 4%.

Finally, to evaluate the impact of the developed scaffolds on the cell fate, hBM-MSCs were cultured with αMEM (12509069, Gibco, Waltham, MA, USA) 10% FBS (Gibco) on the steel-filled PLA scaffolds with 0.6, 0.7, and 0.8 mm line spacing, respectively, with a seeding density of 1.3 × 10^4 cells/cm^2. Control cells were cultured in parallel on conventional culture plates. After 21 days, the cells were fixed with PFA 4% for further analysis.

2.7. Immunohistochemical Analysis

After PFA fixation, samples were permeabilized with Triton 0.1%, blocked with 10% FBS solution, and incubated overnight at 4 °C with primary antibodies (anti-hOsteocalcein 967801, R&D Systems, Minneapolis, MN, USA) and subsequently, incubated for 2 h at 37 °C with the secondary Alexa 488 anti-rabbit antibody for differentiation studies. For morphology analysis, nuclei were stained with NucBlue (Thermo Scientific, Waltham, MA, USA) and actin cytoskeleton with phalloidin (Thermo Scientific, Waltham, MA, USA). Images were acquired with a Nikon D-Eclipse Ci confocal microscope (Nikon, Tokyo, Japan) with 10× and 20× Plan Apo objectives (Nikon).

3. Results and Discussion

3.1. 3D Printed Samples

Figure 3 shows the pictures of bronze-filled, copper-filled, and steel-filled samples manufactured with 0.6, 0.7, and 0.8 mm line spacing, respectively. Achieving 0.6 mm line spacing was more difficult than 0.8 mm, because of smaller pores. Despite that, appropriate scaffolds were achieved for the three different materials.

Additionally, scaffolds for biomedical applications should have a porous architecture. This porosity provides the necessary environment for promoting cell migration, proliferation, etc. [39].

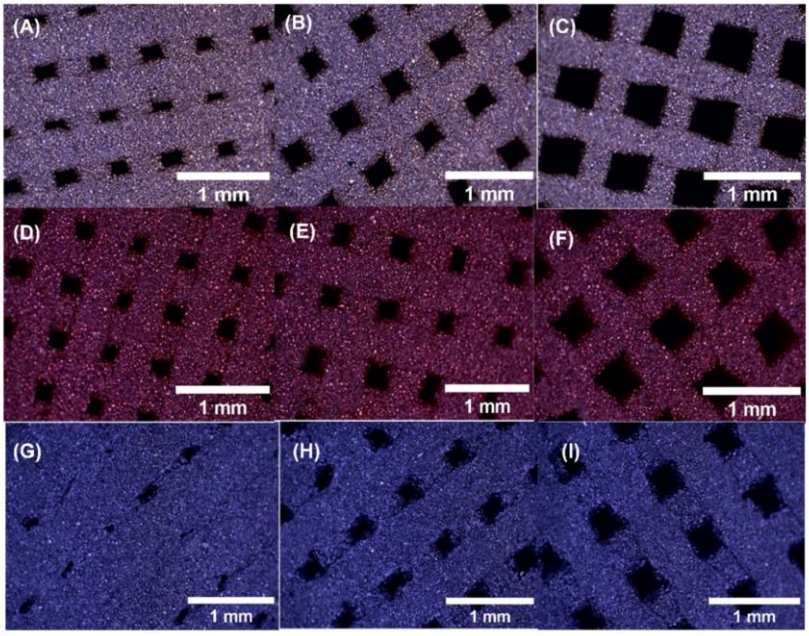

Figure 3. Surface of the samples with 16× magnification: (**A**) bronze-filled 0.6 mm, (**B**) bronze-filled 0.7 mm, (**C**) bronze-filled 0.8 mm, (**D**) copper-filled 0.6 mm. (**E**) copper-filled 0.7 mm, (**F**) copperfilled 0.7 mm, (**G**) steel-filled 0.6 mm, (**H**) steel-filled 0.7 mm, (**I**) steel-filled 0.8 mm. The scale bars correspond to 1 mm.

3.2. Porosity

As shown in Figure 4, the higher the line spacing, the higher the porosity of the 3D printed scaffolds is. Among the different scaffolds, for a certain line spacing value, most porous scaffolds are the bronze-filled ones, followed by the copper-filled ones, although they were manufactured with the same 3D printing conditions:

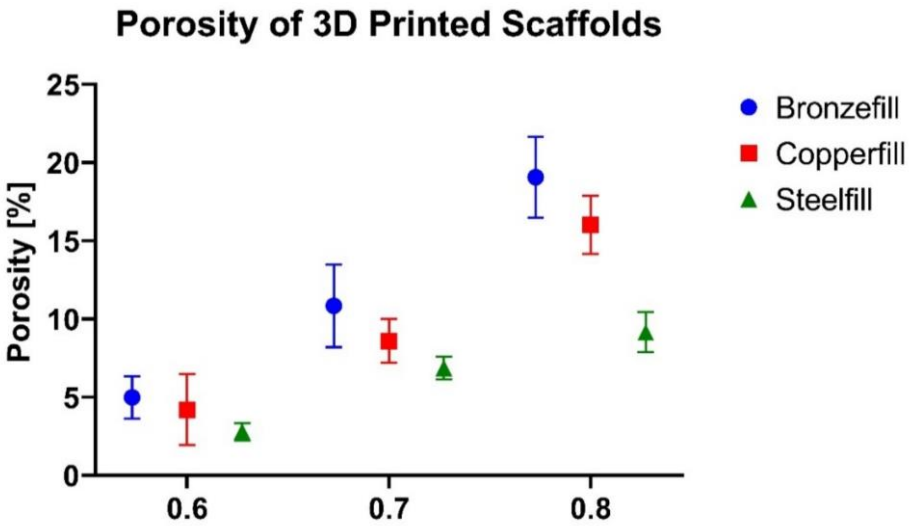

Figure 4. Porosity of the 3D printed scaffolds: bronze-filled, copper-filled and steel-filled. *N* = 3.

3.3. Roughness

Table 2 presents the roughness results for both the internal and the external surfaces of the 3D printed samples. One measurement was performed on each surface.

Table 2. Roughness on the external and internal layer of 3D printed steel-filled samples.

Line Spacing	Sample	External Roughness				Internal Roughness			
		Ra (μm)	Rz (μm)	Rku	Rsk	Ra (μm)	Rz (μm)	Rku	Rsk
0.6 mm	1	25.36	128.90	3.12	−1.00	7.99	38.67	2.91	0.24
	2	25.60	129.11	3.14	−1.03	7.97	37.16	3.29	0.44
0.7 mm	1	32.38	142.63	2.54	−0.73	12.13	52.91	2.60	−0.09
	2	35.04	158.71	2.73	−0.80	15.68	78.31	2.89	0.04

Figure 5 depicts the roughness profiles of samples with a line spacing of 0.6 and 0.7 mm, on the external (first) and internal (second) layers, respectively, starting from the top of the part. Higher Ra values were obtained on the external (first) layer (Table 2 and Figure 5a,c) than on the internal (second) layer (Table 2 and Figure 5b,d). On the external layer, slightly higher Ra values (up to 35.04 μm) were found for line spacing 0.7 mm than for line spacing 0.6 mm (up to 25.60 μm). The Rz parameter shows a similar trend than Ra.

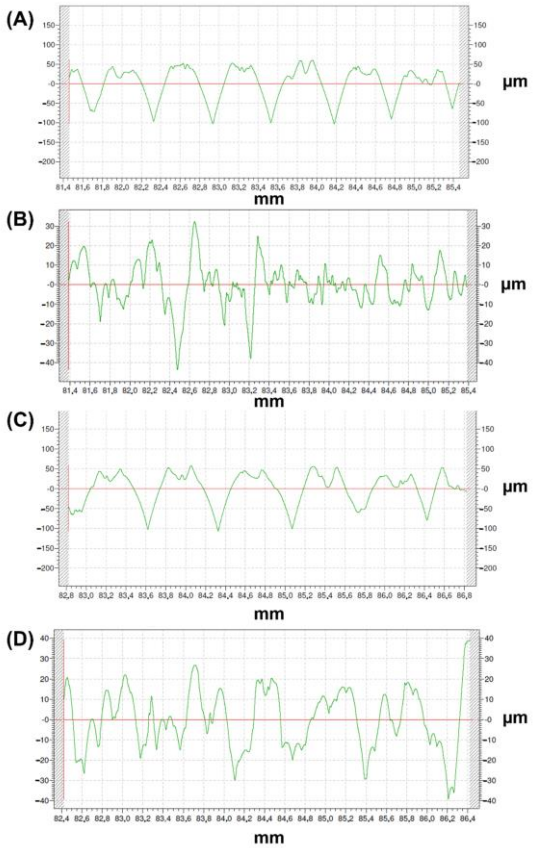

Figure 5. Roughness profiles of the steel-filled 3D printed samples. (**A**) 0.6 mm external roughness (first layer). (**B**) 0.6 mm internal roughness (second layer). (**C**) 0.7 mm external roughness (first layer). (**D**) 0.7 mm internal roughness (second layer).

Rku values around 3 were found in all cases, corresponding to a normal distribution of the roughness heights in each profile. On the external layer, slightly negative Rsk values were obtained, corresponding to longer valleys than crests. On the contrary, on the second layer Rsk values are close to 0, corresponding to symmetric profiles.

The external or first layers show more regular roughness profiles (Figure 5a,c) than the internal or second layers (Figure 5b,d).

3.4. Human Bone Marrow-Derived Mesenchymal Stromal Cells Cultured on the Developed Scaffolds

hBM-MSCs showed good adhesion to both collagen-coated and untreated 3D printed steel-filled PLA samples. Cells cultured for both 24 and 72 h were well-adhered to the 3D printed PLA composites (Figure 6a,b), with no observed differences between both conditions.

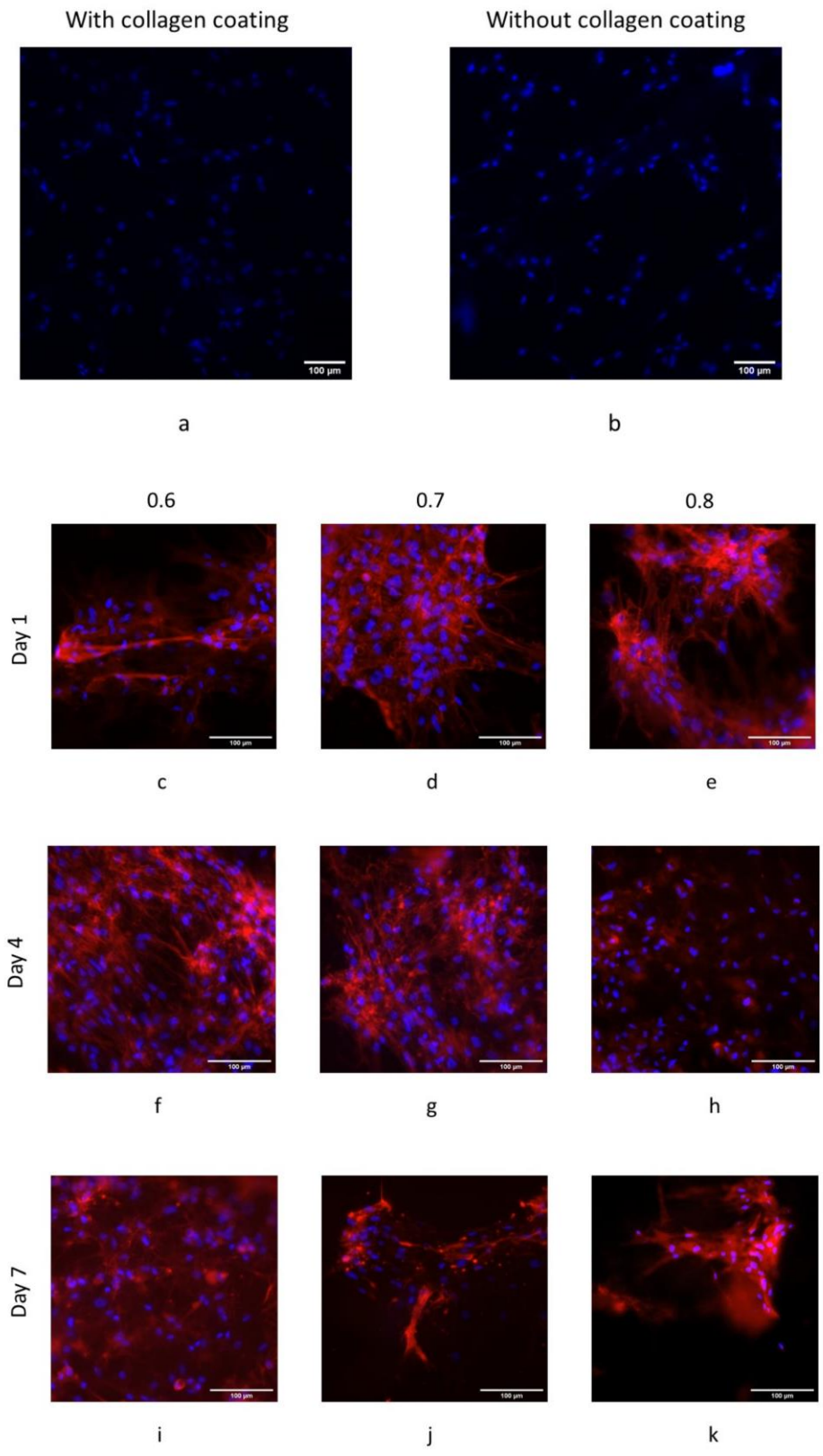

Figure 6. (**a**,**b**) Adhesion test to PLA with and without collagen coating. (**c**–**e**) Viability test at day 1 of cell culture. (**f**–**h**) Viability test at day 4 of cell culture. (**i**–**k**) Viability test at day 7 of cell culture.

Steel-filled PLA samples showed a very good cytocompatibility, especially on 0.6 and 0.7 line spacing (Figure 6c,d,f,g,i,j). On the contrary, copper-filled and bronze-filled PLA presented higher cytotoxicity since there were no cells

adhered to the scaffolds after 24 h of culture (data not shown).

Steel-filled scaffolds showed high biocompatibility, unlike copper-filled and bronzefilled materials. This is in concordance with Kuroda *et al*. [39]. Additionally, the best biological behavior was found with the lowest porosity achieved (0.6 mm line spacing). This is in accordance with data presented by Chen *et al*. [40], who concluded that samples with 30% porosity exhibit the best biocompatibility, which were the lowest porosity scaffolds of their research.

The different scaffolds manufactured by means of FFF showed to have different behavior. As mentioned, bronze-filled as well as copper-filled scaffolds presented high cytotoxicity since there were no cells adhered to the scaffolds after 24 h of culture.

It is interesting to highlight that there were no differences observed when a specific protein coating was used in the parts. Cells form specific adhesions to the collagen protein while they are expected to form unspecific adhesions to uncoated materials. From the experiments presented herein, it can be concluded that steel-filled PLA promotes the formation of unspecific adhesion in MSCs, while this is not happening with copper- or bronze-filled polymers.

3.5. hBM-MSCs Differentiated towards Osteoblasts When Cultured on the Developed Scaffolds hBM-MSCs cultured on the steel-filled 3D printed scaffolds (0.6 and 0.7 mm line spacing) without osteogenic supplements showed the presence of osteocalcin after 21 days of culture (Figure 6). Moreover, cells exhibited a broad spreading area compared with those cultured under conventional culture conditions (Figure 7).

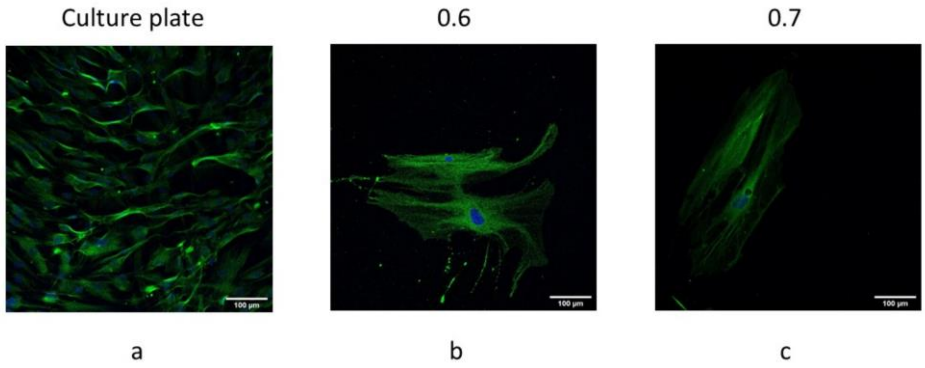

Figure 7. Osteocalcin detection by immunofluorescence in hBM-MSCs (at day 21) cultured on (**a**) conventional culture conditions, steel-filled PLA scaffolds of (**b**) 0.6 mm and (**c**) 0.7 mm line spacing. Osteocalcin (green) and nucleus (blue). Scale bars correspond to 100 µm.

The images show the classical spindle-like shape of MSCs, so it seems that the steelfilled 3D printed structures are a suitable scaffold for cell culturing. The enlarged phenotype is similar to differentiated osteoblasts when cultured on rigid substrates [41–43].

4. Conclusions

In the present work, results are presented for the cell growth of stem cells on metalfilled PLA composites that were printed with a grid structure by means of the FFF technique. Three different composites were tested: bronze, copper, and stainless steel, respectively. The main conclusions are as follows:

- Given a certain line spacing, higher porosity was observed for the copper-filled scaffolds than for the bronze-filled scaffolds and the steel-filled scaffolds, although they were 3D printed with similar printing conditions;
- Steel-filled composite showed important cell growth, both with and without protein coating, so it is promoting the formation of unspecific adhesions in MSCs;
- Neither bronze-filled nor copper-filled composites favored cell growth, so they cannot be considered to be biocompatible;
- When considering steel-filled composite, line spacing of 0.6 and 0.7 mm provided the best results, while line spacing of 0.8 mm is not recommended.

In future work, the effect of the use of other infill patterns on both cell growth and the mechanical strength of the structures will be addressed.

Author Contributions: Conceptualization, I.B.-C. and J.O.; methodology, A.U., H.S.-F., A.D.-F. and A.T.-O.; software, A.D.-F. and H.S.-F.; validation, I.B.-C. and J.O.; formal analysis, A.U., H.S.-F., I.A. and A.T.-O.; investigation, A.U., H.S.-F., I.A. and A.T.-O.; resources, I.A., I.B.-C. and J.O.; data curation, A.T.-O.; writing—original draft preparation, all; writing—review and editing, all; visualization, I.B.C., A.D.-F. and J.O.; supervision, I.B.-C. and J.O.; project administration, I.B.-C. and J.O.; funding acquisition, I.B.-C., I.A. and J.O. All authors have read and agreed to the published version of the manuscript.

Funding: This research was co-funded by the European Union Regional Development Fund within the framework of the ERDF Operational Program of Catalonia 2014–2020 with a grant of 50% of total cost eligible, project BASE3D, grant number 001-P-001646. Research was also funded in part by the Spanish Ministry of Science, Innovation and Universities, grants numbers PID2019-108958RB-I00 and PGC2018-097323-A-I00.

Institutional Review Board Statement: Not applicable.

Informed Consent Statement: Not applicable.

Data Availability Statement: Data supporting the findings of this study are available from the corresponding authors upon reasonable request.

Acknowledgments: The authors thank Ramón Casado for his help with the experimental tests.

Conflicts of Interest: The authors declare no conflict of interest.

References

1. *ISO/ASTM 52900:2021*; Additive Manufacturing—General Principles—Fundamentals and Vocabulary. International Organization for Standardization: Geneva, Switzerland, 2021; pp. 1–28.
2. Ziaee, M.; Crane, N.B. Binder jetting: A review of process, materials, and methods. *Addit. Manuf.* **2019**, *28*, 781–801. [CrossRef]
3. Ryu, D.J.; Sonn, C.-H.; Hong, D.H.; Kwon, K.B.; Park, S.J.; Ban, H.Y.; Kwak, T.Y.; Lim, D.; Wang, J.H. Titanium Porous Coating Using 3D Direct Energy Deposition (DED) Printing for Cementless TKA Implants: Does It Induce Chronic Inflammation? *Materials* **2020**, *13*, 472. [CrossRef] [PubMed]
4. Lewis, J.A.; Smay, J.E.; Stuecker, J.; Cesarano, J. Direct Ink Writing of Three-Dimensional Ceramic Structures. *J. Am. Ceram. Soc.* **2006**, *89*, 3599–3609. [CrossRef]
5. Tejo-Otero, A.; Colly, A.; Courtial, E.-J.; Fenollosa-Artés, F.; Buj-Corral, I.; Marquette, C.A. Soft-tissue-mimicking using silicones for the manufacturing of soft phantoms by fresh 3D printing. *Rapid Prototyp. J.* **2021**, *28*, 285–296. [CrossRef]
6. Tee, Y.L.; Tran, P.; Leary, M.; Pille, P.; Brandt, M. 3D Printing of polymer composites with material jetting: Mechanical and fractographic analysis. *Addit. Manuf.* **2020**, *36*, 101558. [CrossRef]
7. Murr, L.E. Metallurgy principles applied to powder bed fusion 3D printing/additive manufacturing of personalized and optimized metal and alloy biomedical implants: An overview. *Integr. Med. Res.* **2019**, *9*, 1087–1103. [CrossRef]
8. Bhatt, P.M.; Kabir, A.M.; Peralta, M.; Bruck, H.A.; Gupta, S.K. A robotic cell for performing sheet lamination-based additive manufacturing. *Addit. Manuf.* **2019**, *27*, 278–289. [CrossRef]
9. Zhu, Y.; Ramadani, E.; Egap, E. Thiol ligand capped quantum dot as an efficient and oxygen tolerance photoinitiator for aqueous phase radical polymerization and 3D printing under visible light. *Polym. Chem.* **2021**, *12*, 5106–5116. [CrossRef]
10. Shi, X.; Zhang, J.; Corrigan, N.A.; Boyer, C. Controlling mechanical properties of 3D printed polymer composites through photoinduced reversible addition–fragmentation chain transfer (RAFT) polymerization. *Polym. Chem.* **2021**, *13*, 44–57. [CrossRef]
11. Bozkurt, Y.; Karayel, E. 3D printing technology; methods, biomedical applications, future opportunities and trends. *J. Mater. Res. Technol.* **2021**, *14*, 1430–1450. [CrossRef]
12. Vanaei, H.R.; Khelladi, S.; Deligant, M.; Shirinbayan, M.; Tcharkhtchi, A. Numerical Prediction for Temperature Profile of Parts Manufactured Using Fused Filament Fabrication. *J. Manuf. Process.* **2022**, *76*, 548–558. [CrossRef]
13. Deckard, C.R. Method and Apparatus for Producing Parts by Selective Sintering. U.S. Patent No. 4,863,538, 5 September 1989.
14. Buj-Corral, I.; Bagheri, A.; Petit-Rojo, O. 3D Printing of Porous Scaffolds with Controlled Porosity and Pore Size Values. *Materials* **2018**, *11*, 1532. [CrossRef]
15. Bagheri, A.; Buj-Corral, I.; Ferrer, M.; Pastor, M.M.; Roure, F. Determination of the Elasticity Modulus of 3D-Printed Octet-Truss Structures for Use in Porous Prosthesis Implants. *Materials* **2018**, *11*, 2420. [CrossRef]
16. Tejo-Otero, A.; Buj-Corral, I.; Fenollosa-Artés, F. 3D Printing in Medicine for Preoperative Surgical Planning: A Review. *Ann. Biomed. Eng.* **2020**, *48*, 536–555. [CrossRef]

17. Tejo-Otero, A.; Lustig-Gainza, P.; Fenollosa-Artés, F.; Valls, A.; Krauel, L.; Buj-Corral, I. 3D printed soft surgical planning prototype for a biliary tract rhabdomyosarcoma. *J. Mech. Behav. Biomed. Mater.* **2020**, *109*, 103844. [CrossRef]
18. Polonio-Alcalá, E.; Rabionet, M.; Guerra, A.J.; Yeste, M.; Ciurana, J.; Puig, T. Screening of Additive Manufactured Scaffolds Designs for Triple Negative Breast Cancer 3D Cell Culture and Stem-like Expansion. *Int. J. Mol. Sci.* **2018**, *19*, 3148. [CrossRef]
19. Polonio-Alcalá, E.; Rabionet, M.; Gallardo, X.; Angelats, D.; Ciurana, J.; Ruiz-Martínez, S.; Puig, T. PLA Electrospun Scaffolds for Three-Dimensional Triple-Negative Breast Cancer Cell Culture. *Polymers* **2019**, *11*, 916. [CrossRef]
20. Nejad, Z.M.; Zamanian, A.; Saeidifar, M.; Vanaei, H.R.; Amoli, M.S. 3D Bioprinting of Polycaprolactone-Based Scaffolds for Pulp-Dentin Regeneration: Investigation of Physicochemical and Biological Behavior. *Polymers* **2021**, *13*, 4442. [CrossRef]
21. Yousry, M.; Zaghloul, M.; Mahmoud, M.; Zaghloul, Y.; Mahmoud, M.; Zaghloul, Y. Developments in polyester composite materials—An in-depth review on natural fibres and nano fillers. *Compos. Struct.* **2021**, *278*, 114698.
22. Fuseini, M.; Mahmoud, M.; Zaghloul, Y.; El-shazly, A.H. Evaluation of synthesized polyaniline nanofibres as corrosion protection film coating on copper substrate by electrophoretic deposition. *J. Mater. Sci.* **2022**, *57*, 6085–6101. [CrossRef]
23. Mohammadizadeh, M.; Lu, H.; Fidan, I.; Tantawi, K.; Gupta, A. Mechanical and Thermal Analyses of Metal-PLA. *Inventions* **2020**, *5*, 44. [CrossRef]
24. Liu, Z.; Lei, Q.; Xing, S. Mechanical characteristics of wood, ceramic, metal and carbon fiber-based PLA composites fabricated by FDM. *J. Mater. Res. Technol.* **2019**, *8*, 3743–3753. [CrossRef]
25. Fafenrot, S.; Grimmelsmann, N.; Wortmann, M.; Ehrmann, A. Three-Dimensional (3D) Printing of Polymer-Metal Hybrid Materials by Fused Deposition Modeling. *Materials* **2017**, *10*, 1199. [CrossRef]
26. Mahmoud, M.; Zaghloul, Y.; Mohamed, Y.S. Fatigue and tensile behaviors of fiber-reinforced thermosetting composites embedded with nanoparticles. *J. Compos. Mater.* **2019**, *53*, 709–718.
27. Mahmoud, M.; Zaghloul, Y.; Yousry, M.; Zaghloul, M.; Mahmoud, M.; Zaghloul, Y. Experimental and modeling analysis of mechanical-electrical behaviors of polypropylene composites fi lled with graphite and MWCNT fillers. *Polym. Test.* **2017**, *63*, 467–474.
28. Mahmoud, M.; Mahmoud, Y. Mechanical properties of linear low-density polyethylene fi re-retarded with melamine polyphosphate. *J. Appl. Polym. Sci.* **2018**, *135*, 46770.
29. Stanciuc, A.-M.; Sprecher, C.M.; Adrien, J.; Roiban, L.I.; Alini, M.; Gremillard, L.; Peroglio, M. Robocast zirconia-toughened alumina scaffolds: Processing, structural characterisation and interaction with human primary osteoblasts. *J. Eur. Ceram. Soc.* **2018**, *38*, 845–853. [CrossRef]
30. Rifai, A.; Tran, N.; Reineck, P.; Elbourne, A.; Mayes, E.L.H.; Sarker, A.; Dekiwadia, C.; Ivanova, E.P.; Crawford, R.J.; Ohshima, T.; et al. Engineering the Interface: Nanodiamond Coating on 3D-Printed Titanium Promotes Mammalian Cell Growth and Inhibits *Staphylococcus aureus* Colonization. *ACS Appl. Mater. Interfaces* **2019**, *11*, 24588–24597. [CrossRef]
31. Ma, H.; Li, T.; Huan, Z.; Zhang, M.; Yang, Z.; Wang, J.; Chang, J.; Wu, C. 3D printing of high-strength bioscaffolds for the synergistic treatment of bone cancer. *NPG Asia Mater.* **2018**, *10*, 31–44. [CrossRef]
32. Yang, C.; Huan, Z.; Wang, X.; Wu, C.; Chang, J. 3D Printed Fe Scaffolds with HA Nanocoating for Bone Regeneration. *ACS Biomater. Sci. Eng.* **2018**, *4*, 608–616. [CrossRef]
33. Hermawan, H. Updates on the research and development of absorbable metals for biomedical applications. *Prog. Biomater.* **2018**, *7*, 93–110. [CrossRef] [PubMed]
34. Han, H.-S.; Loffredo, S.; Jun, I.; Edwards, J.; Kim, Y.-C.; Seok, H.-K.; Witte, F.; Mantovani, D.; Glyn-Jones, S. Current status and outlook on the clinical translation of biodegradable metals. *Mater. Today* **2018**, *23*, 57–71. [CrossRef]
35. Ahumada, M.; Jacques, E.; Calderon, C.; Martínez-Gómez, F. Porosity in biomaterials: A key factor in the development of applied materials in biomedicine. *Handb. Ecomater.* **2019**, *5*, 3503–3522.
36. Chai, Q.; Jiao, Y.; Yu, X. Hydrogels for Biomedical Applications: Their Characteristics and the Mechanisms behind Them. *Gels* **2017**, *3*, 6. [CrossRef] [PubMed]
37. *ISO 4288:1996*; Geometrical Product Specifications (GPS)—Surface Texture: Profile Method—Rules and Procedures for the Assessment of Surface Texture. International Organization for Standardization: Geneva, Switzerland, 1996.
38. *ISO 4287:1997*; Geometrical Product Specifications (GPS)—Surface Texture: Profile Method—Terms, Definitions and Surface Texture Parameters. International Organization for Standardization: Geneva, Switzerland, 1997.
39. Zimina, A.; Senatov, F.; Choudhary, R.; Kolesnikov, E.; Anisimova, N.; Kiselevskiy, M.; Orlova, P.; Strukova, N.; Generalova, M.; Manskikh, V.; et al.

Biocompatibility and Physico-Chemical Properties of Highly Porous PLA/HA Scaffolds for Bone Reconstruction. *Polymers* **2020**, *12*, 2938. [CrossRef]

40. Chen, Y.; Frith, J.E.; Dehghan-Manshadi, A.; Attar, H.; Kent, D.; Soro, N.D.M.; Bermingham, M.J.; Dargusch, M.S. Mechanical properties and biocompatibility of porous titanium scaffolds for bone tissue engineering. *J. Mech. Behav. Biomed. Mater.* **2017**, *75*, 169–174. [CrossRef]
41. Matta, C.; Szu˝cs-Somogyi, C.; Kon, E.; Robinson, D.; Neufeld, T.; Altschuler, N.; Berta, A.; Hangody, L.; Veréb, Z.; Zákány, R. Osteogenic differentiation of human bone marrow-derived mesenchymal stem cells is enhanced by an aragonite scaffold. *Differentiation* **2019**, *107*, 24–34. [CrossRef]
42. Mazzoni, E.; Mazziotta, C.; Iaquinta, M.R.; Lanzillotti, C.; Fortini, F.; D'Agostino, A.; Trevisiol, L.; Nocini, R.; Barbanti-Brodano, G.; Mescola, A.; et al. Enhanced Osteogenic Differentiation of Human Bone Marrow-Derived Mesenchymal Stem Cells by a Hybrid Hydroxylapatite/Collagen Scaffold. *Front. Cell Dev. Biol.* **2021**, *8*, 610570. [CrossRef]
43. Zhang, T.; Lin, S.; Shao, X.; Zhang, Q.; Xue, C.; Zhang, S.; Lin, Y.; Zhu, B.; Cai, X. Effect of matrix stiffness on osteoblast functionalization. *Cell Prolif.* **2017**, *50*, e12338. [CrossRef]

Chapter IX. Results summary

Informe del director

Ramon Farré Ventura, Catedrático de Fisiología del Departamento de Biomedicina de la Facultat de Medicina i Ciències de la Salut de la Universitat de Barcelona, y director de la Tesis Doctoral del Sr. Héctor Sanz Fraile, y Jorge Otero Díaz, Profesor Lector del departamento de Biomedicina de la Facultat de Medicina i Ciències de la Salut de la Universitat de Barcelona, y directos de la Tesis Doctoral del Sr. Héctor Sanz Fraile,

INFORMAN sobre la participación personal del doctorando en los artículos científicos incluidos en su Tesis Doctoral, que se presenta en el formato de compendio de artículos. A continuación se hace referencia a los artículos en el mismo orden en que, por razones de coherencia, aparecen en la memoria de la Tesis Doctoral:

- ***Hector Sanz-Fraile**, Susana Amoros, Irene Mendizabal, Carolina Galvez-Monton, Cristina Prat-Vidal, Antoni Bayes-Genis, Daniel Navajas, Ramon Farre, and Jorge Otero. Silk-Reinforced Collagen Hydrogels with Raised Multiscale Stiffness for Mesenchymal Cells 3D Culture. Tissue Eng Part A. 2020 Mar;26(5-6):358-370. doi:10.1089/ten.TEA.2019.0199. IF: 3.845. Q2 (35/89)*

Este es el trabajo principal de la Tesis Doctoral de Héctor Sanz. El doctorando fue responsable de todo el desarrollo experimental. Va a llevar a cabo el desarrollo y caracterización mecánica de hidrogeles de colágeno reforzado con seda. Puso a punto la técnica para disolver correctamente la seda de tal manera que preserve la sericina. Realizó todas las medidas mecánicas tanto a nivel micro (AFM) como macromecánico (ensayo de tracción) y reológico. Además, analizó la viabilidad celular de los hidrogeles. Efectuó el análisis global de los resultados y discutió las medidas mecánicas multiescalares de la rigidez de dichos hidrogeles. Además, tuvo un papel importante en la redacción del artículo. *Este artículo no se ha utilizado ni formará parte, implícita o explícitamente, de ninguna otra tesis doctoral.*

- *Irene Buj-Corral, **Héctor Sanz-Fraile**, Anna Ulldemolins, Aitor Tejo-Otero, Alejandro Domínguez-Fernández, Isaac Almendros, Jorge Otero. Characterization of 3D Printed Metal-PLA Composite Scaffolds for Biomedical Applications. Polymers (Basel). 2022 Jul 5;14(13):2754. doi: 10.3390/polym14132754.*
  IF: 4.967. Q1 (16/90)

Héctor Sanz realizó los análisis de viabilidad celular de las muestras impresas en 3D. Además, puso a punto los experimentos para comprobar si las células se adherían bien a los sustratos utilizados, además de comprobar si expresaban marcadores de osteocalcina tras el cultivo sobre dichos sustratos. También participó en la redacción del artículo. *Este artículo no se ha utilizado ni formará parte, implícita o explícitamente, de ninguna otra tesis doctoral.*

Además, cabe que el doctorando, durante el desarrollo de su Tesis Doctoral, ha colaborado muy activamente en otros trabajos de investigación del laboratorio en los que ha llevado a cabo técnicas puestas a punto por el doctorado, como queda reflejado en el listado de otros artículos del Apéndice A de la memoria de la Tesis Doctoral.

Así lo hacemos constar para los efectos que sean pertinentes antes la correspondiente Comisión de Doctorado de la Universitat de Barcelona.

Ramon Farré Jorge Otero

THE MAIN results of the present thesis have been disseminated through four scientific papers. The overall aim of these works has been to develop and characterize new bioinks for 3D bioprinting in tissue engineering. Regarding soft biomaterials, a decellularization protocol has been developed and optimized to extract and manipulate the ECM from native pig myocardial tissue, optimizing the matrix digestion time to achieve improved mechanical properties of the hydrogel obtained. In addition, multiscale mechanical characterization techniques have been developed using hydrogels composed of type I collagen and cocoon silk. Finally, hBM-MSCs have been seeded inside the developed hydrogels to study their biocompatibility.

On the other hand, FDM-based 3D printing techniques have been developed to produce synthetic composite scaffolds. For this purpose, an yttria-doped zirconia composite biomaterial and a steel-reinforced PLA biomaterial have been developed and printed. In both materials, the surface has been characterized and the cell adhesion capacity with and without collagen coating has been evaluated. Finally, in the case of steel-reinforced PLA, stromal cell differentiation was studied.

The first article of this thesis (**Chapter V**) reported the development and characterization of composite hydrogels from rat tail type I collagen and *B. Mori* silkworm cocoons silk. The aim was to reach mechanical properties similar to those of native myocardium. The developed hydrogels did not show phase separation between both biomaterials. The microscale elastic moduli (Em) were measured at different silk collagen ratios as well as in pure collagen. Pure collagen (Em = 0.62 ± 0.13 kPa) showed lower values than reinforced ones. Maximum values were found at 50% and 100% of silk content (Em = 1.26 ± 0.17 kPa and 1.31 ± 0.23 kPa, respectively). Values for hydrogels with 25% and 75% of silk content fell in between (Em = 1.05 ± 0.15 kPa and 1.14 ± 0.03 kPa, respectively). One-way ANOVA revealed a statistically significant effect of silk on the microscale stiffness of the hydrogels.

Regarding macroscale mechanical properties, they were increased in silk-reinforced hydrogel versus non-reinforced ones. At 20% strain, control samples showed a stress of 0.70 ± 0.08 kPa and a macroscale elastic modulus (EM) EM = 9.93 ± 2.50 kPa. Regarding silk-collagen hydrogels, maximum values were found at 75% of silk content (stress of 1.77 ± 0.05 kPa and EM = 31.16 ± 2.96 kPa) and decreasing at 100% of silk content (stress of 1.11 ± 0.11 kPa and EM = 18.42 ± 2.22 kPa). One-way ANOVA revealed a statistically significant effect of silk on the macroscale properties at 20% of strain.

The rheological properties were improved in silk-reinforced hydrogels. On the one hand, storage modulus showed an increase from non-reinforced hydrogels to reinforced ones. On the other hand, the viscosity in control bioinks slowly increased at 4 ^{o}C while it showed no changes in silk-reinforced collagen, which is a key factor for the printability of the biomaterial.

hBM-MSCs were cultured in 3D within the developed bioinks. Cell viability was studied at different times within collagen hydrogel as control and collagen hydrogel silk-reinforced at 50% and 100% of silk content. Cells were mostly viable after 1 week of culture and homogeneously distributed.

The second article of the thesis (**Chapter VI**) focused on the development of a decellularized porcine myocardium-derived ECM bioink for 3D culture in cardiac tissue engineering with improved mechanical properties. To do so, ECM was solubilized at different pepsin digestion times to evaluate the optimum time for getting hydrogels as stiffer as possible. The macroscopic structure of the hydrogel showed a structure without fiber clusters and with the capacity to be manipulated by surgical tools without breaking and recovering its original shape. The study of the ultrastructure showed a fibrillary mesh with an average fiber diameter of 126 ± 8 nm.

The bioinks were characterized by rheological analysis. Digestion times above 24h did not reach gelation after thermal crosslinking, while for digestion times between 12h and 24h, the gelation started gradually after reaching physiological temperature. Furthermore, the cell-laden hydrogels were rheologically compared versus acellular hydrogels after 7 days of cell culture, showing a softening when MSCs were cultured in 3D within the developed scaffolds.

To evaluate the active crosstalk between the cECM and the hBM-MSCs, the area of cell-laden hydrogel was measured at different days of culture (1, 4 and 7 days) and compared versus acellular hydrogels, reaching almost 60% of contraction after 7 days of cell culture. Cell-laden hydrogels were fixed and stained for Connexin 43 (Cx43), α-Smooth muscle actin (α-SMA) and phalloidin, while they were counterstained by DAPI (figure 9). Cells showed a characteristic spindle shape of MSC, while they showed a well-formed cytoskeleton. The expression of Cx43 and α-SMA was positive in the cultured hBM-MSCs within the hydrogel.

The third article of the thesis (**Chapter VII**) shows the development of a Yttria-stabilized zirconia (YSZ) material which is 3D printed by an extrusion method and the subsequent study of the viability of hBM-MSCs on the printed samples with different surface roughness. The surface roughness on the top face of two 3D-printed zirconia samples (with different infill values of 80% and 95%, respectively) was compared. The average values of areal arithmetic mean (Sa), skewness (Ssk) and kurtosis (Sku) were studied. Regarding the 80%, the values obtained were: Sa = 0.30±0.03 µm, Ssk = -0.002±0.48 µm and Sku = 10.35±8.37 µm, while to 95% infill density, the values obtained were Sa = 0.69±0.01 µm, Ssk = -0.14±0.05 µm and Sku = 5.03±0.41 µm.

Surface topography images revealed crests corresponding to the deposition of material in parallel lines, typical of the FDM-based printing system. However, when increasing the infill, only a few crests were observed, while these crests were more pronounced.

Printed YSZ samples were coated with type I collagen at a concentration of 0.1 mg/mL. hBM-MSC were seeded on coated and uncoated samples, studying whether the cells adhered to the uncoated substrate or whether they needed coating to adhere. Cells were well-adhered to both coated and uncoated surfaces for 80% and 95% infill.

Finally, in the last article of this thesis (**Chapter VIII**), three PLA/metal composite materials were fabricated by 3D extrusion printing and their surface was characterized. Furthermore, the biocompatibility of the material was studied by the evaluation of its osteogenic differentiation capacity. However, although steel, copper and bronze reinforcements were studied, only steel showed cytocompatibility.

Samples with different line spacing were printed. The higher the line spacing, the greater the porosity of the materials analyzed. The arithmetical mean roughness (Ra), the mean roughness depth (Rz), the kurtosis (Rku) and the skewness (Rsk) of the internal and external layer of 3D printed steel-filled samples were quantified as well as the profilometry of these samples.

To analyze cytocompatibility, a coating was performed with type I collagen at a concentration of 0.1 mg/mL and adhesion was found to show no significant difference. Therefore, cell behavior was analyzed after 1, 4 and 7 days. Finally, hBMMSCs were cultured for 21 days on the steel/PLA scaffolds and the cells showed the presence of osteocalcin, thus indicating their differentiation towards osteoblasts.

Chapter X. Discussion

TISSUE ENGINEERING is the discipline that works on supplying, from an engineering point of view, the health deficiencies that the human body acquires as a result of diseases and aging. One of the main areas of development in tissue engineering is biomaterials. Thus, research in the field of biomaterials has for many years focused on developing materials that influence cellular behavior (220), so engineered tissues can be developed by using them as scaffolds for the cells. Most biomaterials developed in tissue engineering are composed of two or more materials (they are composites), either to achieve better mechanical properties or to improve qualities such as bioprintability, biocompatibility, etc (221).

Concretely, they are formed by joining two or more materials of different natures with a combination of properties; a matrix material and one or more reinforcing materials. These composite biomaterials can be composed of natural (such as collagen, elastin, silk, etc.) or synthetic (such as polycaprolactone, PLGA, PET, etc.) materials.

In the present thesis biomaterials that can be used as bioinks for the 3D bioprinting of scaffolds have been developed. Their structural and biological properties have been evaluated by a multiscale analysis of their biomechanics and the culture of Mesenchymal Stromal Cells in the developed scaffolds.

Sericin-preserved silk improves the mechanical properties of collagen scaffolds for tissue engineering.

One of the main goals of tissue engineering is to develop biomaterials that mimic the mechanical properties of native tissue. Therefore, one of the first objectives of this thesis was to develop a biomaterial composed of type I collagen from rat tails reinforced with silk from *B. mori* cocoons which could mimic the mechanical properties of the native heart. (Chapter V).

The methodology presented herein produced mechanically-tunable hydrogel-based bioinks suitable for the development of scaffolds by 3D bioprinting. In this study, the reinforcement of COL I structures with silk microfibers resulted in an increase of more than two-fold in the macro- and micromechanical properties of the developed scaffolds. Furthermore, the final hydrogels did not show phase separation at the macroscopical level, which was one of the main problems detected with other methods used in studies published before (222).

Since no aggressive physical or chemical methods were used to prepare the composite hydrogels developed in Chapter V, the biomaterials obtained were suitable for 3D cell culture. To reach a good silk-collagen mixture, it was necessary to solubilize the silk with an alkaline buffer, which is a common procedure (223) after cryogenic milling of the material. Cryogenic milling is a very common technique for the preparation of ECM-derived biomaterials (224). Regarding type I collagen extraction, a well-known acid extraction method was used (225). This method is suitable to preserve the telopeptides in tropocollagen molecules (226), obtaining collagen fibrils capable of interacting with each other and with other proteins.

Natural COL I hydrogels present an elastic modulus of ≈1 kPa (194, 227). However, the mechanical properties observed in native tissues of different organs, such as the heart, are often above this value, as demonstrated by previous studies (228, 229). To achieve hydrogels with an elastic modulus closer to that of the heart, a multiscale mechanical analysis was performed at different silk concentrations (from 25% to 100%).

For this purpose, hydrogels with a silk reinforcement content of 0% (control), 25%, 50%, 75% and 100% were produced. The macroscopic properties were analyzed at a strain of 20%, which is a strain with physiological relevance in biological applications involving cardiac diseases (230). To avoid the variability inherent to the geometry of the sample analyzed, the characterized hydrogels were fabricated by 3D bioprinting.

One of the key factors when a composite biomaterial is developed is the interface at the microscopic level of the different materials. As observed in the ultrastructure characterization carried out by SEM, there was a good integration of the silk fibers within the collagen matrix, which resulted in no phase separation between

both biomaterials at the macroscopic level as well as no denaturation of the collagen fibrils was appreciated (231).

Interestingly, the mechanical properties of the composite hydrogels increased as the reinforcement content present in the hydrogels increased until reaching a maximum at 75% of silk content. At macromechanical level, when the hydrogels were reinforced with the same weight percentage of silk (100% silk content) as type I collagen, the stiffness decreased. It seemed that there is a limit in silk content that, when it is surpassed, affects the formation of the collagen matrix. In the formation of composite materials, as the content of reinforcing material increases, the mechanical properties of the composite material also increase, but only to a certain extent. After that point, a decrease in mechanical properties may occur due to the interface between the reinforced material and the reinforcing material, or the formation of discontinuities in the material (232). Similar effects have been seen in other studies in hydrogels (222, 233) and other composite materials (234).

However, at the micromechanical level, the Young's modulus reached twice the value of control collagen when reinforcing hydrogels with silk, remaining relatively stable for all silk concentrations. This difference regarding the mechanical properties at the macroscopic level could be because, in a composite material, the properties of the whole are greater than the mechanical properties separately. When performing the analysis using AFM equipped with a cantilever with a spherical tip, the stiffness analysis is performed on a few fibers and not on the whole material. This same effect appears in various multiscale mechanical studies (112, 235, 236).

One of the most important physical parameters of bioinks is their printability. In the case of collagen-based bioinks, they start to form a hydrogel under physiological conditions (neutral pH and 37 ˚C) (237). However, numerous studies have highlighted several issues that arise when using bioprinting with bioinks based solely on collagen: the difficulty of using it at high concentrations (the higher the concentration, the stronger the mechanical properties) (231, 238, 239). Various techniques have been used to overcome this problem, such as using collagen at low concentrations (240) or combining it with other materials (241). Thus, the printability of the developed composite hydrogels was evaluated by rheometry. Remarkably, rheological properties

(viscosity) of collagen pregels changed before reaching 37 ˚C over time, which was in concordance with previous studies (242, 243). This feature of the pregel complicates its use as a bioink, as obstructions may appear in the needle or syringe. Nevertheless, silk-reinforced bioink maintains constant rheological properties for temperatures below 37 ˚C, facilitating its use as material for 3D bioprinting.

Regarding 3D cell culturing within the developed composite hydrogels, the experiment showed that a high number of hBM-MSCs were alive after 7 days of 3D cell culture in the reinforced hydrogels. Therefore, the developed structures seem to be suitable for the development of cardiac patches or MSCs preconditioning. Although some studies highlight the immunogenic activity of sericin (244), more recent studies not only show that the immunogenicity of fibroin and sericin do not differ (245), but also that sericin may have positive effects on mesenchymal cells (246).

In summary, the novel aspect of this developed composite biomaterial is that sericin is preserved, resulting in better integration between fibrils and microfibers. Nevertheless, most studies where silk has been used in tissue engineering have focused solely on the use of fibroin (247). However, in our study, we have shown that preserving sericin has positive effects on the development of mechanically more stable structures. In addition, an increase between two- and threefold in stiffness is of high importance, reaching the elastic modulus of native myocardium while type I collagen is still the main protein of the developed scaffolds.

Cardiac ECM-derived hydrogels can be optimized for developing 3D bioscaffolds.

One of the most commonly used matrix-derived materials in tissue engineering is organ-derived ECM (248). Therefore, it is mandatory to develop a proper decellularization protocol for the native ECM while maximizing the removal of cell debris and DNA as well as minimizing tissue damage. However, unlike the obtention of rat-tail derived type I collagen, which is performed by solubilization of the tendons in weak acids, the decellularization of tissues is commonly performed by using different reagents before digesting the resulting matrix with pepsin and strong acids. It is then important to evaluate and characterize the mechanical properties of the structures after different

digestion times with pepsin as well as to study the response of cells when cultured in 3D within the developed scaffolds. This was another objective of this thesis, which has been studied and developed in Chapter VI.

The biomaterial presented in Chapter VI is a native porcine cardiac-derived hydrogel. It is suitable for 3D bioprinting scaffolds for 3D cell culture of MSCs. The protocol for obtaining a well-decellularized ECM from the native myocardium was tuned up, as well as the matrix enzymatic digestion process was adjusted to get a hydrogel as stiffer as possible. The main feature of the hydrogels developed from this bioink is that they do not require additional reinforcements or crosslinkers, achieving structures with sufficient rigidity to be manipulated with surgical material and implanted *in vivo* without breaking, which is one of the major challenges in cardiac tissue engineering (200, 228, 249).

Several research groups are developing cardiac ECM-derived hydrogels. However, bioinks obtained from pure cardiac ECM (cECM) have only been developed at low concentrations (88, 250), resulting in scaffolds with weak mechanical characteristics (251). Therefore, fine-tuning a protocol with which to obtain a pure cardiac matrix hydrogel, capable of being thermally crosslinked at a concentration of 20 mg/mL, is an important achievement for the advancement of cardiac engineering research.

Concerning the macroscopic structure of the developed scaffolds, there was no evidence of macroscopically-visible fiber board clusters. In addition, SEM images showed the typical fibrillar structure of ECM-derived hydrogels (252). The diameter of the fibers obtained in the cECM hydrogels (126 ± 8 nm) coincided with the diameter of tropocollagen fibers (253) and they were in the same diameter range of COL I fibrils (109) as well as similar to the diameter of the collagen fibers obtained in the hydrogel developed in the Chapter V. Furthermore, the structure of this cECM scaffolds showed to be similar to that of the native ECM (252).

Another important factor in the study was to characterize the optimal digestion time. Interestingly, the cECM hydrogels only reached gelation with an enzymatic digestion time between 16 and 24 hours. For longer digestion times, the hydrogel did not gel. This differs from other investigations where ECM-derived hydrogels have been

developed, in which much longer digestion times are used for lower ECM concentrations (250). However, the longer the ECM is solubilized in a strong acid and the longer the enzymatic digestion lasts, the more damage the proteins that compose the matrix are suffering (82). Thus, hydrogels digested for 24 hours showed the highest storage modulus (G' = 24 Pa), which is in the same range of other natural organ-derived hydrogels, such us lung ECM (194) or cardiac ECM hydrogels (88).

To test the biocompatibility of the scaffolds developed in Chapter VI, hBM-MSCs were cultured within the hydrogels for 7 days. After one day of cell culture, the scaffolds already showed an approximate 20% shrinkage of their size as compared to the acellular hydrogel. This contraction was higher than 50% after one week of cell culture. The observed shrinkage may be due to several factors beyond the scope of the study (degradation of the matrix proteins or physical interaction between the cells and the matrix, where cells could be pulling the fibers of the structure (254, 255)); likewise, to try to better understand the mechanism of cell-matrix interaction within these hydrogels, the rheology of the cellular and acellular structures was analyzed after 7 days of cell culture.

The measured rheological properties of the cell-laden hydrogels were in the same range as other cECM-derived hydrogels studied in the literature (88). However, the cellular scaffolds showed lower mechanical properties than the acellular scaffolds. This finding, together with the contraction observed in the cell-laden hydrogels, points out the active crosstalk between the cECM and the hBM-MSCs.

Cells cultured within the developed hydrogels were stained with Connexin 43 (Cx43) and α-Smooth muscle actin (α-SMA) and counterstained with DAPI and phalloidin to study the cell viability of the hBM-MSCs within the structures as well as the behavior of the cells after seven days of cell culture. Thus, a positive expression of Cx43 was observed, pointing out cell-cell communication, which plays a key role in the physiology of the heart (256, 257). In addition, a positive expression of α-SMA was revealed too, showing that there were interactions between the cells and the matrix, which is an indicator of ECM remodeling (258, 259).

Yttria-Stabilized Zirconia scaffolds can be 3D printed by using direct ink writing.

Although soft tissue bioprinting is very important for the development of tissue engineering in organs such as the heart, which has mechanical properties already analyzed in this thesis, rigid tissue bioprinting is also an important challenge in tissue engineering. Therefore, as discussed in Chapter I, materials such as zirconia (260) or PLA (211) are emerging as suitable synthetic materials for the repair and replacement of rigid organs, such as bone (261). Therefore, another objective of this thesis was to develop additive manufacturing techniques for constructing complex synthetic composite scaffolds. Thus, developing a scaffold of yttria-stabilized zirconia (YSZ) by 3D bioprinting with high biocompatibility was the first step for reaching this aim (Chapter VII).

The biomaterial presented in Chapter VII is a 3D-printed YSZ scaffold with different surface roughness suitable for using it as biomedical material in an implant. Although metallic materials have been commonly used in biomedical applications due to their optimal mechanical properties, they have the disadvantage of releasing metal ions over time. This release of metal ions can cause biological alterations, such as inflammatory reactions (262). As an alternative to metals, the use of ceramic materials is growing. Ceramic implants or prostheses produce less debris and have greater durability (263).

To study the surface physical properties of extrusion-bioprinted YSZ scaffolds, the roughness of the top face of the samples was characterized. For this purpose, three physical properties were measured: surface arithmetic mean (S_a), skewness (S_{sk}) and kurtosis (S_{ku}). Tests were performed on samples with 80% and 95% infill patterns.

In both types of samples, S_a showed values lower than 1, which implies that the material is considered smooth, from the point of view of osteointegration (264). This implies that the bioprinted scaffolds with the parameters designed in Chapter VII do not require a final polishing operation. In addition, S_{sk} value was slightly negative in both cases, indicating a predominance of valleys instead of peaks (265). Furthermore, S_{ku} was greater than 3 for both the 80% and 95% infill samples, showing a normal distribution of surface roughness heights (265). Both S_{sk} and S_{ku} are parameters related to controlling the surface friction of the samples (266).

Regarding the study of the biocompatibility of the scaffolds developed in Chapter VII, it was evaluated by culturing of hBM-MSCs on the surface of the samples. Since metal alloys require a collagen coating to improve biocompatibility and cell attachment as well as corrosion resistance (267, 268), it was important to characterize the cell attachment on the developed structures. As previously shown in Chapter VII, hBM-MSCs were able to attach to the 3D-bioprinted YSZ scaffolds with and without collagen coating. After 3 days of cell culture no differences in cell survival were observed in the scaffolds. Consequently, it seems that the roughness obtained in the developed scaffolds, as well as the nature of the materials used, make them suitable candidates for culturing MSCs.

Therefore, the developed material showed good biocompatibility, allowing direct cell culture on top of the bioprinted scaffolds without the need of covering the surface with ECM proteins. This result suggests that unspecific adhesions are being formed between the material and the cells, opening the door to its use for *in vitro* experiments. Anyway, more extensive studies on cell viability and proliferation should be performed to confirm this hypothesis.

From the experiments presented herein, 3D-printed YSZ showed to be a suitable material in implants. The topological properties of the material showed a good surface roughness, allowing the use of the scaffolds for a prosthesis. In addition, the need of coating the surface, as happens in other materials used in prosthesis printing, is avoided with the developed material, thus minimizing the need for complex post-processing processes.

3D Printed Metal-PLA composite scaffolds induce osteogenic differentiation of Mesenchymal Stromal Cells.

PLA is emerging as a suitable synthetic material for bioprinting applications (211). However, their low stiffness has led to adding metals to the polymeric matrix to improve its characteristics (218, 269). Although the use of zirconia as a viable material for cell growth in 3D scaffolds has been studied in Chapter VII of this thesis, very few or non-concluding studies have evaluated the biological response of MSCs in metal-PLA

composite materials. Thus, the last step for achieving all the objectives of this thesis was to develop and characterize a 3D printed metal-PLA composite scaffold for tissue engineering (Chapter VIII).

Although metals and metal alloys have been widely used as bone substitutes or implants (215, 216), numerous studies have shown the cytocompatibility of 3D-printed iron-based scaffolds with polymeric coating for bone regeneration (270, 271, 272). Therefore, we hypothesized that the development of metal-reinforced polymeric materials would be suitable for cell growth. In addition, porosity is a key element to consider for the development and synthesis of biomaterials (273). Hence, developing a polymer-based, metal-reinforced composite biomaterial that can be 3D printed to control the porosity of the scaffold was the objective of the study presented in Chapter VIII of this thesis.

To find the best material to mix with PLA to develop printed structures, the biocompatibility of copper, bronze and steel as reinforcement within the scaffold was first analyzed. For this purpose, the samples were divided into collagen-coated and uncoated samples. hBM-MSCs were seeded on the coated and uncoated samples and cell survival was analyzed after 24 h and 72 h of culture. However, both the copper-filled and bronze-filled materials exhibited high cytotoxicity as no cells were adhering to these scaffolds after 24 h of cell culture. On the other hand, steel-filled PLA samples showed high cytocompatibility in both collagen-coated and non-collagen-coated samples, especially in samples with a line spacing of 0.6mm and 0.7 mm. This toxicity found in bronze and copper is in agreement with other published studies, where copper (and therefore bronze, being an alloy of copper and tin) was shown to be highly cytotoxic (274, 275).

As with the material studied in Chapter VIII, the steel-filled PLA scaffolds allowed direct cell culture on the samples without the need for surface coverage. This is an improvement over other metallic alloys used in tissue engineering, which require this collagen coating to achieve both proper cell attachment and good biocompatibility (267, 268). Therefore, it seems that the material properties of the structures printed in Chapter VIII promote the formation of nonspecific adhesions between hBM-MSCs and the surface of the samples. On the other hand, cell viability was affected in steel-filled

PLA structures with a line spacing of 0.8 mm. Therefore, it seems that as the porosity of the structure increases, cell viability decreases, which is in agreement with other published studies (276).

From the physical characterization, the external face showed the highest results (up to 35 mm), and all of them greater than 1, which is the value previously shown to be defined for a smooth surface from the point of view of osteointegration (264). It can be seen that the value obtained in S_a is much higher than that obtained for the YSZ structures studied in Chapter VII. This is because the steel-filled PLA scaffolds were printed without a top layer to favor cell migration toward the interior of the structure. However, S_{ku} values turned out to be around 3 in all cases, which was previously discussed as corresponding to a normal distribution of the roughness heights in each profile. Finally, S_{sk} values were negative on the outside of the scaffolds, corresponding to a greater presence of valleys than crests.

Once it was defined that the best composite material, in terms of biocompatibility of the materials studied in Chapter VIII, was steel-reinforced PLA, the impact of the developed material on the cell fate was analyzed. For this purpose, hBM-MSCs were seeded on the 3D-printed structures and cultured without osteogenic supplements for 21 days. After that time the cells showed an elevated presence of osteocalcin as well as an increased broad spreading area compared to control cells. In addition, the cells showed the characteristic spindle-like shape of mesenchymal cells and the enlarged phenotype was similar to those found in differentiated osteoblasts when they are cultured on rigid structures (277, 278, 279).

Chapter XI. Conclusions

1. A protocol for the decellularization of native porcine myocardium was optimized for developing cardiac ECM hydrogels (Objective I).
    a) The optimal enzymatic digestion time to achieve the best mechanical properties of the resulting hydrogel was studied and evaluated.
    b) The developed hydrogel showed active crosstalk between the cells and the scaffold as well as cell-cell communication.

2. ECM-derived hydrogels were developed and modified by reinforcing them with another natural material (silk) to modify their multiscale biophysical proprieties (Objective II).
    a) The micromechanical stiffness was increased by adding different concentrations of silk to the type I collagen hydrogel, which was characterized by Atomic Force Microscopy.
    b) The macromechanical stiffness was increased by adding silk at different concentrations to the type I collagen scaffolds until the maximum Young's modulus was reached at a concentration of 75% silk to collagen. These mechanical properties were evaluated by tensile testing.
    c) The printability of the developed bioink was improved by the addition of silk, which could be verified by kinetic analysis using the rheology of bioink gelation.
    d) The ultrastructure of the bioprinted hydrogels showed a fiber diameter similar to the diameter of tropocollagen fibers and in the same range as type I collagen fibrils.

3. Different composite biomaterials for bone tissue engineering were developed and studied, which were 3D printed to build custom-shaped scaffolds (Objective III).
    a) The developed 3D structures were suitable for use as *in vitro* models.
    b) The need for using a collagen coating on the printed parts was analyzed. It was found that the uncoated parts showed a high capacity to generate unspecific adhesion in human bone marrow mesenchymal stromal cells.

c) Human bone marrow mesenchymal stromal cells seeded on scaffolds 3D printed with both yttria-stabilized zirconia and steel-reinforced polylactide showed high cell viability after several days of culture. In addition, osteocalcin markers on steel-filled polylactide scaffolds were positive after 21 days of culture.
d) The roughness of the printed structures was analyzed, showing a surface suitable for cell culture without the need for any post-processing.

Chapter XII. References

1. Theocharis AD, Skandalis SS, Gialeli C, Karamanos NK. Extracellular matrix structure. Advanced Drug Delivery Reviews. 2016;97:4-27.
2. Bonnans C, Chou J, Werb Z. Remodelling the extracellular matrix in development and disease. Nat Rev Mol Cell Biol. 2014;15(12):786-801.
3. Alberts B, Johnson A, Lewis J, Raff M, Roberts K, Walter P. Molecular biology of the cell. 6th ed. United States of America: Garland Science; 2017. 1464 p.
4. Frantz C, Stewart KM, Weaver VM. The extracellular matrix at a glance. Journal of Cell Science. 2010;123(24):4195-200.
5. Clause KC, Barker TH. Extracellular matrix signaling in morphogenesis and repair. Current Opinion in Biotechnology. 2013;24(5):830-3.
6. Theocharis A, Gialeli C, Hascall V, Karamanos NK. Extracellular Matrix: Pathobiology and Signaling

1.1 Extracellular matrix: a functional scaffold. In: Karamanos N, editor.: De Gruyter; 2012. p. 3-20.
7. Di Lullo GA, Sweeney SM, Korkko J, Ala-Kokko L, San Antonio JD. Mapping the ligand-binding sites and disease-associated mutations on the most abundant protein in the human, type I collagen. J Biol Chem. 2002;277(6):4223-31.
8. Ricard-Blum S. The collagen family. Cold Spring Harb Perspect Biol. 2011;3(1):a004978.
9. Shoulders MD, Raines RT. Collagen structure and stability. Annu Rev Biochem. 2009;78:929-58.
10. Brodsky B, Persikov AV. Molecular structure of the collagen triple helix. Adv Protein Chem. 2005;70:301-39.
11. Corsi A, Xu T, Chen XD, Boyde A, Liang J, Mankani M, et al. Phenotypic effects of biglycan deficiency are linked to collagen fibril abnormalities, are synergized by decorin deficiency, and mimic Ehlers-Danlos-like changes in bone and other connective tissues. J Bone Miner Res. 2002;17(7):1180-9.
12. Varma S, Orgel JP, Schieber JD. Nanomechanics of Type I Collagen. Biophys J. 2016;111(1):50-6.
13. Hulmes DJ, Jesior JC, Miller A, Berthet-Colominas C, Wolff C. Electron microscopy shows periodic structure in collagen fibril cross sections. Proc Natl Acad Sci U S A. 1981;78(6):3567-71.
14. Orgel JP, Miller A, Irving TC, Fischetti RF, Hammersley AP, Wess TJ. The in situ supermolecular structure of type I collagen. Structure. 2001;9(11):1061-9.
15. Orgel JP, Irving TC, Miller A, Wess TJ. Microfibrillar structure of type I collagen in situ. Proc Natl Acad Sci U S A. 2006;103(24):9001-5.
16. Lin K, Zhang D, Macedo MH, Cui W, Sarmento B, Shen G. Advanced Collagen-Based Biomaterials for Regenerative Biomedicine. Advanced Functional Materials. 2019;29(3):1804943.
17. Dutov P, Antipova O, Varma S, Orgel JP, Schieber JD. Measurement of Elastic Modulus of Collagen Type I Single Fiber. PLoS One. 2016;11(1):e0145711.
18. Shen ZL, Kahn H, Ballarini R, Eppell SJ. Viscoelastic properties of isolated collagen fibrils. Biophys J. 2011;100(12):3008-15.
19. Yang L, van der Werf KO, Fitié CF, Bennink ML, Dijkstra PJ, Feijen J. Mechanical properties of native and cross-linked type I collagen fibrils. Biophys J. 2008;94(6):2204-11.
20. Sasaki N, Odajima S. Elongation mechanism of collagen fibrils and force-strain relations of tendon at each level of structural hierarchy. J Biomech. 1996;29(9):1131-6.

21. Sasaki N, Odajima S. Stress-strain curve and Young's modulus of a collagen molecule as determined by the X-ray diffraction technique. J Biomech. 1996;29(5):655-8.
22. Sun YL, Luo ZP, Fertala A, An KN. Direct quantification of the flexibility of type I collagen monomer. Biochem Biophys Res Commun. 2002;295(2):382-6.
23. Lovelady HH, Shashidhara S, Matthews WG. Solvent specific persistence length of molecular type I collagen. Biopolymers. 2014;101(4):329-35.
24. Vesentini S, Fitié CF, Montevecchi FM, Redaelli A. Molecular assessment of the elastic properties of collagen-like homotrimer sequences. Biomech Model Mechanobiol. 2005;3(4):224-34.
25. Mithieux SM, Weiss AS. Elastin. Advances in Protein Chemistry. 70: Academic Press; 2005. p. 437-61.
26. Thomson J, Singh M, Eckersley A, Cain SA, Sherratt MJ, Baldock C. Fibrillin microfibrils and elastic fibre proteins: Functional interactions and extracellular regulation of growth factors. Semin Cell Dev Biol. 2019;89:109-17.
27. Keeley FW, Bellingham CM, Woodhouse KA. Elastin as a self-organizing biomaterial: use of recombinantly expressed human elastin polypeptides as a model for investigations of structure and self-assembly of elastin. Philos Trans R Soc Lond B Biol Sci. 2002;357(1418):185-9.
28. Romberger DJ. Fibronectin. The International Journal of Biochemistry & Cell Biology. 1997;29(7):939-43.
29. Wierzbicka-Patynowski I, Schwarzbauer JE. The ins and outs of fibronectin matrix assembly. J Cell Sci. 2003;116(Pt 16):3269-76.
30. Lenselink EA. Role of fibronectin in normal wound healing. International Wound Journal. 2015;12(3):313-6.
31. Al Jamal R, Roughley PJ, Ludwig MS. Effect of glycosaminoglycan degradation on lung tissue viscoelasticity. American Journal of Physiology-Lung Cellular and Molecular Physiology. 2001;280(2):L306-L15.
32. Hopwood JJ, Dorfman A. Glycosaminoglycan synthesis by cultured human skin fibroblasts after transformation with simian virus 40. Journal of Biological Chemistry. 1977;252(14):4777-85.
33. Trowbridge JM, Gallo RL. Dermatan sulfate: new functions from an old glycosaminoglycan. Glycobiology. 2002;12(9):117R-25R.
34. Papakonstantinou E, Roth M, Karakiulakis G. Hyaluronic acid: A key molecule in skin aging. Dermato-Endocrinology. 2012;4(3):253-8.
35. Wang DA, Varghese S, Sharma B, Strehin I, Fermanian S, Gorham J, et al. Multifunctional chondroitin sulphate for cartilage tissue-biomaterial integration. Nat Mater. 2007;6(5):385-92.
36. Korducki JM, Loftus SJ, Bahn RS. Stimulation of glycosaminoglycan production in cultured human retroocular fibroblasts. Investigative Ophthalmology & Visual Science. 1992;33(6):2037-42.
37. DeAngelis PL. Glycosaminoglycan polysaccharide biosynthesis and production: today and tomorrow. Applied Microbiology and Biotechnology. 2012;94(2):295-305.
38. Ford AJ, Rajagopalan P. Extracellular matrix remodeling in 3D: implications in tissue homeostasis and disease progression. Wiley Interdiscip Rev Nanomed Nanobiotechnol. 2018;10(4):e1503.
39. García JR, García AJ. Cellular mechanotransduction: sensing rigidity. Nat Mater. 2014;13(6):539-40.
40. Doyle AD, Yamada KM. Mechanosensing via cell-matrix adhesions in 3D microenvironments. Exp Cell Res. 2016;343(1):60-6.
41. Mouw JK, Ou G, Weaver VM. Extracellular matrix assembly: a multiscale deconstruction. Nat Rev Mol Cell Biol. 2014;15(12):771-85.
42. Wells RG. Tissue mechanics and fibrosis. Biochim Biophys Acta. 2013;1832(7):884-90.
43. Pickup MW, Mouw JK, Weaver VM. The extracellular matrix modulates the hallmarks of cancer. EMBO Rep. 2014;15(12):1243-53.

44. Gilbert TW, Sellaro TL, Badylak SF. Decellularization of tissues and organs. Biomaterials. 2006;27(19):3675-83.
45. Fu R-H, Wang Y-C, Liu S-P, Shih T-R, Lin H-L, Chen Y-M, et al. Decellularization and Recellularization Technologies in Tissue Engineering. Cell Transplantation. 2014;23(4-5):621-30.
46. Badylak SF, Lantz GC, Coffey A, Geddes LA. Small intestinal submucosa as a large diameter vascular graft in the dog. J Surg Res. 1989;47(1):74-80.
47. Lantz GC, Badylak SF, Coffey AC, Geddes LA, Blevins WE. Small intestinal submucosa as a small-diameter arterial graft in the dog. J Invest Surg. 1990;3(3):217-27.
48. Lantz GC, Badylak SF, Coffey AC, Geddes LA, Sandusky GE. Small intestinal submucosa as a superior vena cava graft in the dog. J Surg Res. 1992;53(2):175-81.
49. Crapo PM, Gilbert TW, Badylak SF. An overview of tissue and whole organ decellularization processes. Biomaterials. 2011;32(12):3233-43.
50. Funamoto S, Nam K, Kimura T, Murakoshi A, Hashimoto Y, Niwaya K, et al. The use of high-hydrostatic pressure treatment to decellularize blood vessels. Biomaterials. 2010;31(13):3590-5.
51. Hashimoto Y, Funamoto S, Sasaki S, Honda T, Hattori S, Nam K, et al. Preparation and characterization of decellularized cornea using high-hydrostatic pressurization for corneal tissue engineering. Biomaterials. 2010;31(14):3941-8.
52. Flynn LE. The use of decellularized adipose tissue to provide an inductive microenvironment for the adipogenic differentiation of human adipose-derived stem cells. Biomaterials. 2010;31(17):4715-24.
53. Prasertsung I, Kanokpanont S, Bunaprasert T, Thanakit V, Damrongsakkul S. Development of acellular dermis from porcine skin using periodic pressurized technique. J Biomed Mater Res B Appl Biomater. 2008;85(1):210-9.
54. Phillips M, Maor E, Rubinsky B. Nonthermal irreversible electroporation for tissue decellularization. J Biomech Eng. 2010;132(9):091003.
55. Sano MB, Neal RE, Garcia PA, Gerber D, Robertson J, Davalos RV. Towards the creation of decellularized organ constructs using irreversible electroporation and active mechanical perfusion. Biomed Eng Online. 2010;9:83.
56. Reing JE, Brown BN, Daly KA, Freund JM, Gilbert TW, Hsiong SX, et al. The effects of processing methods upon mechanical and biologic properties of porcine dermal extracellular matrix scaffolds. Biomaterials. 2010;31(33):8626-33.
57. Lumpkins SB, Pierre N, McFetridge PS. A mechanical evaluation of three decellularization methods in the design of a xenogeneic scaffold for tissue engineering the temporomandibular joint disc. Acta Biomater. 2008;4(4):808-16.
58. Rieder E, Kasimir MT, Silberhumer G, Seebacher G, Wolner E, Simon P, et al. Decellularization protocols of porcine heart valves differ importantly in efficiency of cell removal and susceptibility of the matrix to recellularization with human vascular cells. J Thorac Cardiovasc Surg. 2004;127(2):399-405.
59. Kasimir MT, Rieder E, Seebacher G, Silberhumer G, Wolner E, Weigel G, et al. Comparison of different decellularization procedures of porcine heart valves. Int J Artif Organs. 2003;26(5):421-7.
60. Ott HC, Matthiesen TS, Goh SK, Black LD, Kren SM, Netoff TI, et al. Perfusion-decellularized matrix: using nature's platform to engineer a bioartificial heart. Nat Med. 2008;14(2):213-21.
61. Uygun BE, Soto-Gutierrez A, Yagi H, Izamis ML, Guzzardi MA, Shulman C, et al. Organ reengineering through development of a transplantable recellularized liver graft using decellularized liver matrix. Nat Med. 2010;16(7):814-20.
62. Stern MM, Myers RL, Hammam N, Stern KA, Eberli D, Kritchevsky SB, et al. The influence of extracellular matrix derived from skeletal muscle tissue on the proliferation and differentiation of myogenic progenitor cells ex vivo. Biomaterials. 2009;30(12):2393-9.

63. Wainwright JM, Czajka CA, Patel UB, Freytes DO, Tobita K, Gilbert TW, et al. Preparation of cardiac extracellular matrix from an intact porcine heart. Tissue Eng Part C Methods. 2010;16(3):525-32.
64. Hopkinson A, Shanmuganathan VA, Gray T, Yeung AM, Lowe J, James DK, et al. Optimization of amniotic membrane (AM) denuding for tissue engineering. Tissue Eng Part C Methods. 2008;14(4):371-81.
65. He M, Callanan A. Comparison of methods for whole-organ decellularization in tissue engineering of bioartificial organs. Tissue Eng Part B Rev. 2013;19(3):194-208.
66. Guyette JP, Gilpin SE, Charest JM, Tapias LF, Ren X, Ott HC. Perfusion decellularization of whole organs. Nat Protoc. 2014;9(6):1451-68.
67. Gupta SK, Mishra NC, Dhasmana A. Decellularization Methods for Scaffold Fabrication. Methods Mol Biol. 2018;1577:1-10.
68. Remlinger NT, Wearden PD, Gilbert TW. Procedure for decellularization of porcine heart by retrograde coronary perfusion. J Vis Exp. 2012(70):e50059.
69. Becker M, Maring JA, Oberwallner B, Kappler B, Klein O, Falk V, et al. Processing of Human Cardiac Tissue Toward Extracellular Matrix Self-assembling Hydrogel for In Vitro and In Vivo Applications. J Vis Exp. 2017(130).
70. Bilodeau C, Goltsis O, Rogers IM, Post M. Limitations of recellularized biological scaffolds for human transplantation. J Tissue Eng Regen Med. 2020;14(3):521-38.
71. Ullah F, Othman MB, Javed F, Ahmad Z, Md Akil H. Classification, processing and application of hydrogels: A review. Mater Sci Eng C Mater Biol Appl. 2015;57:414-33.
72. Wichterle O, LÍM D. Hydrophilic Gels for Biological Use. Nature. 1960;185(4706):117-8.
73. Li J, Mooney DJ. Designing hydrogels for controlled drug delivery. Nat Rev Mater. 2016;1(12).
74. Overstreet DJ, Dutta D, Stabenfeldt SE, Vernon BL. Injectable hydrogels. Journal of Polymer Science Part B: Polymer Physics. 2012;50(13):881-903.
75. Lee KY, Mooney DJ. Hydrogels for Tissue Engineering. Chemical Reviews. 2001;101(7):1869-80.
76. Huleihel L, Hussey GS, Naranjo JD, Zhang L, Dziki JL, Turner NJ, et al. Matrix-bound nanovesicles within ECM bioscaffolds. Sci Adv. 2016;2(6):e1600502.
77. Reing JE, Zhang L, Myers-Irvin J, Cordero KE, Freytes DO, Heber-Katz E, et al. Degradation products of extracellular matrix affect cell migration and proliferation. Tissue Eng Part A. 2009;15(3):605-14.
78. Londono R, Badylak SF. Biologic scaffolds for regenerative medicine: mechanisms of in vivo remodeling. Ann Biomed Eng. 2015;43(3):577-92.
79. Brightman AO, Rajwa BP, Sturgis JE, McCallister ME, Robinson JP, Voytik-Harbin SL. Time-lapse confocal reflection microscopy of collagen fibrillogenesis and extracellular matrix assembly in vitro. Biopolymers. 2000;54(3):222-34.
80. Keane TJ, Londono R, Turner NJ, Badylak SF. Consequences of ineffective decellularization of biologic scaffolds on the host response. Biomaterials. 2012;33(6):1771-81.
81. Saldin LT, Cramer MC, Velankar SS, White LJ, Badylak SF. Extracellular matrix hydrogels from decellularized tissues: Structure and function. Acta Biomater. 2017;49:1-15.
82. Mat DJL, Cattenoz T, Souchon I, Michon C, Le Feunteun S. Monitoring protein hydrolysis by pepsin using pH-stat: In vitro gastric digestions in static and dynamic pH conditions. Food Chem. 2018;239:268-75.
83. Freytes DO, Martin J, Velankar SS, Lee AS, Badylak SF. Preparation and rheological characterization of a gel form of the porcine urinary bladder matrix. Biomaterials. 2008;29(11):1630-7.
84. Voytik-Harbin SL, Brightman AO, Waisner BZ, Robinson JP, Lamar CH. Small Intestinal Submucosa: A Tissue-Derived Extracellular Matrix That Promotes Tissue-Specific Growth and Differentiation of Cells in Vitro. Tissue Engineering. 1998;4(2):157-74.
85. Hulmes D. Collagen. 2008.

86. Pouliot RA, Young BM, Link PA, Park HE, Kahn AR, Shankar K, et al. Porcine Lung-Derived Extracellular Matrix Hydrogel Properties Are Dependent on Pepsin Digestion Time. Tissue Engineering Part C: Methods. 2020;26(6):332-46.
87. Parkinson J, Kadler KE, Brass A. Simple physical model of collagen fibrillogenesis based on diffusion limited aggregation. J Mol Biol. 1995;247(4):823-31.
88. Johnson TD, Lin SY, Christman KL. Tailoring material properties of a nanofibrous extracellular matrix derived hydrogel. Nanotechnology. 2011;22(49):494015.
89. Fernández-Pérez J, Ahearne M. The impact of decellularization methods on extracellular matrix derived hydrogels. Sci Rep. 2019;9(1):14933.
90. Gaetani R, Aude S, DeMaddalena LL, Strassle H, Dzieciatkowska M, Wortham M, et al. Evaluation of Different Decellularization Protocols on the Generation of Pancreas-Derived Hydrogels. Tissue Eng Part C Methods. 2018;24(12):697-708.
91. Delgado LM, Pandit A, Zeugolis DI. Influence of sterilisation methods on collagen-based devices stability and properties. Expert Rev Med Devices. 2014;11(3):305-14.
92. Charulatha V, Rajaram A. Influence of different crosslinking treatments on the physical properties of collagen membranes. Biomaterials. 2003;24(5):759-67.
93. Dias J, Diakonis VF, Lorenzo M, Gonzalez F, Porras K, Douglas S, et al. Corneal stromal elasticity and viscoelasticity assessed by atomic force microscopy after different cross linking protocols. Exp Eye Res. 2015;138:1-5.
94. Li X, Xue W, Zhu C, Fan D, Liu Y, XiaoxuanMa. Novel hydrogels based on carboxyl pullulan and collagen crosslinking with 1, 4-butanediol diglycidylether for use as a dermal filler: initial in vitro and in vivo investigations. Mater Sci Eng C Mater Biol Appl. 2015;57:189-96.
95. Chen YC, Chen M, Gaffney EA, Brown CP. Effect of crosslinking in cartilage-like collagen microstructures. J Mech Behav Biomed Mater. 2017;66:138-43.
96. Arora B, Tandon R, Attri P, Bhatia R. Chemical Crosslinking: Role in Protein and Peptide Science. Curr Protein Pept Sci. 2017;18(9):946-55.
97. Wu X, Liu A, Wang W, Ye R. Improved mechanical properties and thermal-stability of collagen fiber based film by crosslinking with casein, keratin or SPI: Effect of crosslinking process and concentrations of proteins. Int J Biol Macromol. 2018;109:1319-28.
98. Wu X, Liu Y, Liu A, Wang W. Improved thermal-stability and mechanical properties of type I collagen by crosslinking with casein, keratin and soy protein isolate using transglutaminase. Int J Biol Macromol. 2017;98:292-301.
99. Hecht H, Srebnik S. Structural Characterization of Sodium Alginate and Calcium Alginate. Biomacromolecules. 2016;17(6):2160-7.
100. Casassa EZ, Sarquis AM, Van Dyke CH. The gelation of polyvinyl alcohol with borax: A novel class participation experiment involving the preparation and properties of a "slime". Journal of Chemical Education. 1986;63(1):57.
101. Wu Y, Chen S, Luo P, Deng S, Shan Z, Fang J, et al. Optimizing the bio-degradability and biocompatibility of a biogenic collagen membrane through cross-linking and zinc-doped hydroxyapatite. Acta Biomater. 2022;143:159-72.
102. Veríssimo DM, Leitão RF, Ribeiro RA, Figueiró SD, Sombra AS, Góes JC, et al. Polyanionic collagen membranes for guided tissue regeneration: Effect of progressive glutaraldehyde cross-linking on biocompatibility and degradation. Acta Biomater. 2010;6(10):4011-8.
103. Fessel G, Cadby J, Wunderli S, van Weeren R, Snedeker JG. Dose- and time-dependent effects of genipin crosslinking on cell viability and tissue mechanics - toward clinical application for tendon repair. Acta Biomater. 2014;10(5):1897-906.
104. Vidal CM, Leme AA, Aguiar TR, Phansalkar R, Nam JW, Bisson J, et al. Mimicking the hierarchical functions of dentin collagen cross-links with plant derived phenols and phenolic acids. Langmuir. 2014;30(49):14887-93.
105. Krishnakumar GS, Gostynska N, Dapporto M, Campodoni E, Montesi M, Panseri S, et al. Evaluation of different crosslinking agents on hybrid biomimetic collagen-hydroxyapatite composites for regenerative medicine. Int J Biol Macromol. 2018;106:739-48.

106. Liu Y, Niu H, Wang C, Yang X, Li W, Zhang Y, et al. Bio-inspired, bio-degradable adenosine 5'-diphosphate-modified hyaluronic acid coordinated hydrophobic undecanal-modified chitosan for hemostasis and wound healing. Bioact Mater. 2022;17:162-77.
107. Kamkin A, Kiseleva I. Mechanosensitivity of Cells from Various Tissues. In: Kamkin A, Kiseleva I, editors. Mechanosensitivity in Cells and Tissues. Moscow: Academia

108. Attwood SJ, Cortes E, Haining AW, Robinson B, Li D, Gautrot J, et al. Adhesive ligand tether length affects the size and length of focal adhesions and influences cell spreading and attachment. Sci Rep. 2016;6:34334.
109. Vesentini S, Redaelli A, Gautieri A. Nanomechanics of collagen microfibrils. Muscles Ligaments Tendons J. 2013;3(1):23-34.
110. Júnior C, Narciso M, Marhuenda E, Almendros I, Farré R, Navajas D, et al. Baseline Stiffness Modulates the Non-Linear Response to Stretch of the Extracellular Matrix in Pulmonary Fibrosis. Int J Mol Sci. 2021;22(23).
111. Jorba I, Mostert D, Hermans LHL, van der Pol A, Kurniawan NA, Bouten CVC. Methods to Model Cardiac Mechanobiology in Health and Disease. Tissue Eng Part C Methods. 2021;27(3):139-51.
112. Jorba I, Beltrán G, Falcones B, Suki B, Farré R, García-Aznar JM, et al. Nonlinear elasticity of the lung extracellular microenvironment is regulated by macroscale tissue strain. Acta Biomater. 2019;92:265-76.
113. Sanz-Fraile H, Amoros S, Mendizabal I, Galvez-Monton C, Prat-Vidal C, Bayes-Genis A, et al. Silk-Reinforced Collagen Hydrogels with Raised Multiscale Stiffness for Mesenchymal Cells 3D Culture. Tissue Eng Part A. 2020;26(5-6):358-70.
114. Pham L, Lu G, Tran P. Influences of Printing Pattern on Mechanical Performance of Three-Dimensional-Printed Fiber-Reinforced Concrete. 3D Print Addit Manuf. 2022;9(1):46-63.
115. Rho J-Y, Kuhn-Spearing L, Zioupos P. Mechanical properties and the hierarchical structure of bone. Medical Engineering & Physics. 1998;20(2):92-102.
116. Lau K-t, Gu C, Hui D. A critical review on nanotube and nanotube/nanoclay related polymer composite materials. Composites Part B: Engineering. 2006;37(6):425-36.
117. Bogner A, Jouneau PH, Thollet G, Basset D, Gauthier C. A history of scanning electron microscopy developments: towards "wet-STEM" imaging. Micron. 2007;38(4):390-401.
118. Binnig G, Quate CF, Gerber C. Atomic force microscope. Phys Rev Lett. 1986;56(9):930-3.
119. Kontomaris SV, Stylianou A, Malamou A. Atomic Force Microscopy Nanoindentation Method on Collagen Fibrils. Materials (Basel). 2022;15(7).
120. Severov V, Tsvetkov V, Barinov N, Babenko V, Klinov D, Pozmogova G. Spontaneous DNA Synapsis by Forming Noncanonical Intermolecular Structures. Polymers (Basel). 2022;14(10).
121. Petit C, Karkhaneh Yousefi AA, Guilbot M, Barnier V, Avril S. Atomic Force Microscopy Stiffness Mapping in Human Aortic Smooth Muscle Cells. J Biomech Eng. 2022;144(8).
122. Jorba I, Uriarte JJ, Campillo N, Farré R, Navajas D. Probing Micromechanical Properties of the Extracellular Matrix of Soft Tissues by Atomic Force Microscopy. J Cell Physiol. 2017;232(1):19-26.
123. Heinz WF, Hoh JH. Spatially resolved force spectroscopy of biological surfaces using the atomic force microscope. Trends Biotechnol. 1999;17(4):143-50.
124. Rodriguez-Ramos J, Rico F. Determination of calibration parameters of cantilevers of arbitrary shape by finite element analysis. Rev Sci Instrum. 2021;92(4):045001.
125. Langlois ED, Shaw GA, Kramar JA, Pratt JR, Hurley DC. Spring constant calibration of atomic force microscopy cantilevers with a piezosensor transfer standard. Review of Scientific Instruments. 2007;78(9):093705.
126. Lubarsky GV, Hähner G. Hydrodynamic methods for calibrating the normal spring constant of microcantilevers. Nanotechnology. 2008;19(32):325707.

127. Sumbul F, Hassanpour N, Rodriguez-Ramos J, Rico F. One-Step Calibration of AFM in Liquid. Frontiers in Physics. 2020;8.
128. Hutter J, Bechhoefer J. Calibration of Atomic-Force Microscope Tips. Review of Scientific Instruments. 1993;64:1868-73.
129. Butt HJ, Jaschke M. Calculation of thermal noise in atomic force microscopy. Nanotechnology. 1995;6(1):1.
130. Alcaraz J, Otero J, Jorba I, Navajas D. Bidirectional mechanobiology between cells and their local extracellular matrix probed by atomic force microscopy. Semin Cell Dev Biol. 2018;73:71-81.
131. Rico F, Roca-Cusachs P, Gavara N, Farré R, Rotger M, Navajas D. Probing mechanical properties of living cells by atomic force microscopy with blunted pyramidal cantilever tips. Phys Rev E Stat Nonlin Soft Matter Phys. 2005;72(2 Pt 1):021914.
132. Johnson KL. Contact mechanics: Cambridge university press; 1987.
133. Dimitriadis EK, Horkay F, Maresca J, Kachar B, Chadwick RS. Determination of elastic moduli of thin layers of soft material using the atomic force microscope. Biophys J. 2002;82(5):2798-810.
134. Otero J, Navajas D, Alcaraz J. Characterization of the elastic properties of extracellular matrix models by atomic force microscopy. Methods Cell Biol. 2020;156:59-83.
135. Gavara N, Chadwick RS. Determination of the elastic moduli of thin samples and adherent cells using conical atomic force microscope tips. Nat Nanotechnol. 2012;7(11):733-6.
136. Radmacher M. Studying the mechanics of cellular processes by atomic force microscopy. Methods Cell Biol. 2007;83:347-72.
137. Acerbi I, Luque T, Giménez A, Puig M, Reguart N, Farré R, et al. Integrin-specific mechanoresponses to compression and extension probed by cylindrical flat-ended AFM tips in lung cells. PLoS One. 2012;7(2):e32261.
138. Walsh MT, Cunnane EM, Mulvihill JJ, Akyildiz AC, Gijsen FJ, Holzapfel GA. Uniaxial tensile testing approaches for characterisation of atherosclerotic plaques. J Biomech. 2014;47(4):793-804.
139. Sutherland DW, McEleney A, de Almeida M, Kajimoto M, Ventura G, Isenberg BC, et al. Characterization of main pulmonary artery and valve annulus region of piglets using echocardiography, uniaxial tensile testing, and a novel non-destructive technique. Front Cardiovasc Med. 2022;9:884116.
140. Farré N, Otero J, Falcones B, Torres M, Jorba I, Gozal D, et al. Intermittent Hypoxia Mimicking Sleep Apnea Increases Passive Stiffness of Myocardial Extracellular Matrix. A Multiscale Study. Front Physiol. 2018;9:1143.
141. Hess O, Hess S. Nonlinear fluid behavior: from shear thinning to shear thickening. Physica A: Statistical Mechanics and its Applications. 1994;207(4):517-40.
142. Mezger T. The Rheology Handbook

Oscillatory tests. For users of rotational and oscillatory rheometers: Vincentz Network; 2020. p. 153-247.
143. Chaudhuri O, Cooper-White J, Janmey PA, Mooney DJ, Shenoy VB. Effects of extracellular matrix viscoelasticity on cellular behaviour. Nature. 2020;584(7822):535-46.
144. Song G, Zhao Z, Peng X, He C, Weiss RA, Wang H. Rheological Behavior of Tough PVP-in Situ-PAAm Hydrogels Physically Cross-Linked by Cooperative Hydrogen Bonding. Macromolecules. 2016;49(21):8265-73.
145. Liu Z, Zhang M, Bhandari B, Wang Y. 3D printing: Printing precision and application in food sector. Trends in Food Science & Technology. 2017;69:83-94.
146. Vanderploeg A, Lee S-E, Mamp M. The application of 3D printing technology in the fashion industry. International Journal of Fashion Design, Technology and Education. 2017;10(2):170-9.

147. Read S, Domingos M. 3D Bioprinting: A Short Overview and Future Prospects in Healthcare Engineering. In: Dash M, editor. Biomimetic Biomaterials for Tissue Regeneration and Drug Delivery. Singapore: Springer Singapore; 2022. p. 149-56.
148. Jovic TH, Combellack EJ, Jessop ZM, Whitaker IS. 3D Bioprinting and the Future of Surgery. Front Surg. 2020;7:609836.
149. Heid S, Boccaccini AR. Advancing bioinks for 3D bioprinting using reactive fillers: A review. Acta Biomater. 2020;113:1-22.
150. Debnath SK, Debnath M, Srivastava R, Omri A. Intervention of 3D printing in health care: transformation for sustainable development. Expert Opinion on Drug Delivery. 2021;18(11):1659-72.
151. Langer R, Tirrell DA. Designing materials for biology and medicine. Nature. 2004;428(6982):487-92.
152. Kačarević Ž, Rider PM, Alkildani S, Retnasingh S, Smeets R, Jung O, et al. An Introduction to 3D Bioprinting: Possibilities, Challenges and Future Aspects. Materials (Basel). 2018;11(11).
153. Jiang T, Munguia-Lopez JG, Flores-Torres S, Kort-Mascort J, Kinsella JM. Extrusion bioprinting of soft materials: An emerging technique for biological model fabrication. Applied Physics Reviews. 2019;6(1):011310.
154. Groll J, Boland T, Blunk T, Burdick JA, Cho DW, Dalton PD, et al. Biofabrication: reappraising the definition of an evolving field. Biofabrication. 2016;8(1):013001.
155. Mironov V, Reis N, Derby B. Review: Bioprinting: A Beginning. Tissue Engineering. 2006;12(4):631-4.
156. Hölzl K, Lin S, Tytgat L, Van Vlierberghe S, Gu L, Ovsianikov A. Bioink properties before, during and after 3D bioprinting. Biofabrication. 2016;8(3):032002.
157. Yilmaz B, Al Rashid A, Mou YA, Evis Z, Koç M. Bioprinting: A review of processes, materials and applications. Bioprinting. 2021;23:e00148.
158. Wang Y, Gao M, Wang D, Sun L, Webster TJ. Nanoscale 3D Bioprinting for Osseous Tissue Manufacturing. Int J Nanomedicine. 2020;15:215-26.
159. Suntornnond R, Ng WL, Huang X, Yeow CHE, Yeong WY. Improving printability of hydrogel-based bio-inks for thermal inkjet bioprinting applications via saponification and heat treatment processes. Journal of Materials Chemistry B. 2022;10(31):5989-6000.
160. Li X, Liu B, Pei B, Chen J, Zhou D, Peng J, et al. Inkjet Bioprinting of Biomaterials. Chemical Reviews. 2020;120(19):10793-833.
161. Ozbolat IT, Hospodiuk M. Current advances and future perspectives in extrusion-based bioprinting. Biomaterials. 2016;76:321-43.
162. Duarte Campos DF, Blaeser A, Weber M, Jäkel J, Neuss S, Jahnen-Dechent W, et al. Three-dimensional printing of stem cell-laden hydrogels submerged in a hydrophobic high-density fluid. Biofabrication. 2013;5(1):015003.
163. Shor L, Güçeri S, Chang R, Gordon J, Kang Q, Hartsock L, et al. Precision extruding deposition (PED) fabrication of polycaprolactone (PCL) scaffolds for bone tissue engineering. Biofabrication. 2009;1(1):015003.
164. Malda J, Visser J, Melchels FP, Jüngst T, Hennink WE, Dhert WJ, et al. 25th anniversary article: Engineering hydrogels for biofabrication. Adv Mater. 2013;25(36):5011-28.
165. Dababneh AB, Ozbolat IT. Bioprinting Technology: A Current State-of-the-Art Review. Journal of Manufacturing Science and Engineering. 2014;136(6).
166. Murphy SV, Atala A. 3D bioprinting of tissues and organs. Nat Biotechnol. 2014;32(8):773-85.
167. Peltola SM, Melchels FP, Grijpma DW, Kellomäki M. A review of rapid prototyping techniques for tissue engineering purposes. Ann Med. 2008;40(4):268-80.
168. Chang R, Nam J, Sun W. Effects of dispensing pressure and nozzle diameter on cell survival from solid freeform fabrication-based direct cell writing. Tissue Eng Part A. 2008;14(1):41-8.

169. Li Z, Wang Q, Liu G. A Review of 3D Printed Bone Implants. Micromachines (Basel). 2022;13(4).
170. Garot C, Bettega G, Picart C. Additive Manufacturing of Material Scaffolds for Bone Regeneration: Toward Application in the Clinics. Adv Funct Mater. 2021;31(5).
171. Winarso R, Anggoro PW, Ismail R, Jamari J, Bayuseno AP. Application of fused deposition modeling (FDM) on bone scaffold manufacturing process: A review. Heliyon. 2022;8(11):e11701.
172. Cuellar JS, Plettenburg D, Zadpoor AA, Breedveld P, Smit G. Design of a 3D-printed hand prosthesis featuring articulated bio-inspired fingers. Proc Inst Mech Eng H. 2021;235(3):336-45.
173. Wu D, Xu C. Predictive Modeling of Droplet Formation Processes in Inkjet-Based Bioprinting. Journal of Manufacturing Science and Engineering. 2018.
174. Lemarchand J, Bridonneau N, Battaglini N, Carn F, Mattana G, Piro B, et al. Challenges, Prospects, and Emerging Applications of Inkjet-Printed Electronics: A Chemist's Point of View. Angew Chem Int Ed Engl. 2022;61(20):e202200166.
175. Xu T, Jin J, Gregory C, Hickman JJ, Boland T. Inkjet printing of viable mammalian cells. Biomaterials. 2005;26(1):93-9.
176. Cui X, Dean D, Ruggeri ZM, Boland T. Cell damage evaluation of thermal inkjet printed Chinese hamster ovary cells. Biotechnol Bioeng. 2010;106(6):963-9.
177. Gao G, Yonezawa T, Hubbell K, Dai G, Cui X. Inkjet-bioprinted acrylated peptides and PEG hydrogel with human mesenchymal stem cells promote robust bone and cartilage formation with minimal printhead clogging. Biotechnol J. 2015;10(10):1568-77.
178. Xu C, Zhang M, Huang Y, Ogale A, Fu J, Markwald RR. Study of droplet formation process during drop-on-demand inkjetting of living cell-laden bioink. Langmuir. 2014;30(30):9130-8.
179. Nair K, Gandhi M, Khalil S, Yan KC, Marcolongo M, Barbee K, et al. Characterization of cell viability during bioprinting processes. Biotechnol J. 2009;4(8):1168-77.
180. Kowalska A, Sokolowski J, Bociong K. The Photoinitiators Used in Resin Based Dental Composite-A Review and Future Perspectives. Polymers (Basel). 2021;13(3).
181. Chiulan I, Heggset EB, Voicu Ş, Chinga-Carrasco G. Photopolymerization of Bio-Based Polymers in a Biomedical Engineering Perspective. Biomacromolecules. 2021;22(5):1795-814.
182. Khoshakhlagh P, Bowser DA, Brown JQ, Moore MJ. Comparison of visible and UVA phototoxicity in neural culture systems micropatterned with digital projection photolithography. J Biomed Mater Res A. 2019;107(1):134-44.
183. Petta D, Armiento AR, Grijpma D, Alini M, Eglin D, D'Este M. 3D bioprinting of a hyaluronan bioink through enzymatic-and visible light-crosslinking. Biofabrication. 2018;10(4):044104.
184. Truxova V, Šafka J, Seidl M, Kovalenko I, Volensky L, Ackermann M. CERAMIC 3D PRINTING: COMPARISON OF SLA AND DLP TECHNOLOGIES. MM Science Journal. 2020;2020:3905-11.
185. Wang Z, Abdulla R, Parker B, Samanipour R, Ghosh S, Kim K. A simple and high-resolution stereolithography-based 3D bioprinting system using visible light crosslinkable bioinks. Biofabrication. 2015;7(4):045009.
186. Lim KS, Levato R, Costa PF, Castilho MD, Alcala-Orozco CR, van Dorenmalen KMA, et al. Bio-resin for high resolution lithography-based biofabrication of complex cell-laden constructs. Biofabrication. 2018;10(3):034101.
187. Zheng Z, Eglin D, Alini M, Richards GR, Qin L, Lai Y. Visible Light-Induced 3D Bioprinting Technologies and Corresponding Bioink Materials for Tissue Engineering: A Review. Engineering. 2021;7(7):966-78.
188. Foyt DA, Norman MDA, Yu TTL, Gentleman E. Exploiting Advanced Hydrogel Technologies to Address Key Challenges in Regenerative Medicine. Adv Healthc Mater. 2018;7(8):e1700939.
189. Liu M, Zeng X, Ma C, Yi H, Ali Z, Mou X, et al. Injectable hydrogels for cartilage and bone tissue engineering. Bone Res. 2017;5:17014.

190. Lee YB, Polio S, Lee W, Dai G, Menon L, Carroll RS, et al. Bio-printing of collagen and VEGF-releasing fibrin gel scaffolds for neural stem cell culture. Exp Neurol. 2010;223(2):645-52.
191. Nguyen BB, Moriarty RA, Kamalitdinov T, Etheridge JM, Fisher JP. Collagen hydrogel scaffold promotes mesenchymal stem cell and endothelial cell coculture for bone tissue engineering. J Biomed Mater Res A. 2017;105(4):1123-31.
192. Yang Z, Cao H, Gao S, Yang M, Lyu J, Tang K. Effect of Tendon Stem Cells in Chitosan/β-Glycerophosphate/Collagen Hydrogel on Achilles Tendon Healing in a Rat Model. Med Sci Monit. 2017;23:4633-43.
193. Zhu D, Li Z, Huang K, Caranasos TG, Rossi JS, Cheng K. Minimally invasive delivery of therapeutic agents by hydrogel injection into the pericardial cavity for cardiac repair. Nat Commun. 2021;12(1):1412.
194. Falcones B, Sanz-Fraile H, Marhuenda E, Mendizábal I, Cabrera-Aguilera I, Malandain N, et al. Bioprintable Lung Extracellular Matrix Hydrogel Scaffolds for 3D Culture of Mesenchymal Stromal Cells. Polymers (Basel). 2021;13(14).
195. Ravichandran A, Murekatete B, Moedder D, Meinert C, Bray LJ. Photocrosslinkable liver extracellular matrix hydrogels for the generation of 3D liver microenvironment models. Sci Rep. 2021;11(1):15566.
196. Wu T, Liu W. Functional hydrogels for the treatment of myocardial infarction. NPG Asia Materials. 2022;14(1):9.
197. Singelyn JM, DeQuach JA, Seif-Naraghi SB, Littlefield RB, Schup-Magoffin PJ, Christman KL. Naturally derived myocardial matrix as an injectable scaffold for cardiac tissue engineering. Biomaterials. 2009;30(29):5409-16.
198. Pati F, Jang J, Ha DH, Won Kim S, Rhie JW, Shim JH, et al. Printing three-dimensional tissue analogues with decellularized extracellular matrix bioink. Nat Commun. 2014;5:3935.
199. Jang J, Park HJ, Kim SW, Kim H, Park JY, Na SJ, et al. 3D printed complex tissue construct using stem cell-laden decellularized extracellular matrix bioinks for cardiac repair. Biomaterials. 2017;112:264-74.
200. Bejleri D, Streeter BW, Nachlas ALY, Brown ME, Gaetani R, Christman KL, et al. A Bioprinted Cardiac Patch Composed of Cardiac-Specific Extracellular Matrix and Progenitor Cells for Heart Repair. Adv Healthc Mater. 2018;7(23):e1800672.
201. Wu Y, Chang T, Chen W, Wang X, Li J, Chen Y, et al. Release of VEGF and BMP9 from injectable alginate based composite hydrogel for treatment of myocardial infarction. Bioactive Materials. 2021;6(2):520-8.
202. Li Y, Chen X, Jin R, Chen L, Dang M, Cao H, et al. Injectable hydrogel with MSNs/microRNA-21-5p delivery enables both immunomodification and enhanced angiogenesis for myocardial infarction therapy in pigs. Sci Adv. 2021;7(9).
203. Martin JR, Patil P, Yu F, Gupta MK, Duvall CL. Enhanced stem cell retention and antioxidative protection with injectable, ROS-degradable PEG hydrogels. Biomaterials. 2020;263:120377.
204. Zhang X, Lyu Y, Liu Y, Yang R, Liu B, Li J, et al. Artificial apoptotic cells/VEGF-loaded injectable hydrogel united with immunomodification and revascularization functions to reduce cardiac remodeling after myocardial infarction. Nano Today. 2021;39:101227.
205. Liu Y, Guo R, Wu T, Lyu Y, Xiao M, He B, et al. One zwitterionic injectable hydrogel with ion conductivity enables efficient restoration of cardiac function after myocardial infarction. Chemical Engineering Journal. 2021;418:129352.
206. Shi Q, Rafii S, Wu MH, Wijelath ES, Yu C, Ishida A, et al. Evidence for circulating bone marrow-derived endothelial cells. Blood. 1998;92(2):362-7.
207. Khoeini R, Nosrati H, Akbarzadeh A, Eftekhari A, Kavetskyy T, Khalilov R, et al. Natural and Synthetic Bioinks for 3D Bioprinting. Advanced NanoBiomed Research. 2021;1(8):2000097.
208. Weng W, Wu W, Hou M, Liu T, Wang T, Yang H. Review of zirconia-based biomimetic scaffolds for bone tissue engineering. Journal of Materials Science. 2021;56(14):8309-33.

209. Narayanan LK, Huebner P, Fisher MB, Spang JT, Starly B, Shirwaiker RA. 3D-Bioprinting of Polylactic Acid (PLA) Nanofiber-Alginate Hydrogel Bioink Containing Human Adipose-Derived Stem Cells. ACS Biomater Sci Eng. 2016;2(10):1732-42.
210. Luo Y, Luo G, Gelinsky M, Huang P, Ruan C. 3D bioprinting scaffold using alginate/polyvinyl alcohol bioinks. Materials Letters. 2017;189:295-8.
211. Singh S, Prakash C, Singh M, Mann GS, Gupta MK, Singh R, et al. Poly-lactic-Acid: Potential Material for Bio-printing Applications. In: Prakash C, Singh S, Singh R, Ramakrishna S, Pabla BS, Puri S, et al., editors. Biomanufacturing. Cham: Springer International Publishing; 2019. p. 69-87.
212. Brézulier D, Chaigneau L, Jeanne S, Lebullenger R. The Challenge of 3D Bioprinting of Composite Natural Polymers PLA/Bioglass: Trends and Benefits in Cleft Palate Surgery. Biomedicines. 2021;9(11).
213. Hu D, Wu D, Huang L, Jiao Y, Li L, Lu L, et al. 3D bioprinting of cell-laden scaffolds for intervertebral disc regeneration. Materials Letters. 2018;223:219-22.
214. Kolan KCR, Semon JA, Bindbeutel AT, Day DE, Leu MC. Bioprinting with bioactive glass loaded polylactic acid composite and human adipose stem cells. Bioprinting. 2020;18:e00075.
215. Han H-S, Loffredo S, Jun I, Edwards J, Kim Y-C, Seok H-K, et al. Current status and outlook on the clinical translation of biodegradable metals. Materials Today. 2019;23:57-71.
216. Hermawan H. Updates on the research and development of absorbable metals for biomedical applications. Prog Biomater. 2018;7(2):93-110.
217. Mohammadizadeh M, Lu H, Fidan I, Tantawi K, Gupta A, Hasanov S, et al. Mechanical and Thermal Analyses of Metal-PLA Components Fabricated by Metal Material Extrusion. Inventions [Internet]. 2020; 5(3).
218. Liu Z, Lei Q, Xing S. Mechanical characteristics of wood, ceramic, metal and carbon fiber-based PLA composites fabricated by FDM. Journal of Materials Research and Technology. 2019;8(5):3741-51.
219. Hari Raj K, Gnanavel S, Ramalingam S. Investigation of 3D printed biodegradable PLA orthopedic screw and surface modified with nanocomposites (Ti–Zr) for biocompatibility. Ceramics International. 2022.
220. Tibbitt MW, Anseth KS. Hydrogels as extracellular matrix mimics for 3D cell culture. Biotechnol Bioeng. 2009;103(4):655-63.
221. Salernitano E, Migliaresi C. Composite Materials for Biomedical Applications: A Review. Journal of Applied Biomaterials and Biomechanics. 2003;1(1):3-18.
222. de Moraes MA, Paternotte E, Mantovani D, Beppu MM. Mechanical and biological performances of new scaffolds made of collagen hydrogels and fibroin microfibers for vascular tissue engineering. Macromol Biosci. 2012;12(9):1253-64.
223. Rockwood DN, Preda RC, Yücel T, Wang X, Lovett ML, Kaplan DL. Materials fabrication from Bombyx mori silk fibroin. Nat Protoc. 2011;6(10):1612-31.
224. Freytes DO, O'Neill JD, Duan-Arnold Y, Wrona EA, Vunjak-Novakovic G. Natural cardiac extracellular matrix hydrogels for cultivation of human stem cell-derived cardiomyocytes. Methods Mol Biol. 2014;1181:69-81.
225. Rajan N, Habermehl J, Coté MF, Doillon CJ, Mantovani D. Preparation of ready-to-use, storable and reconstituted type I collagen from rat tail tendon for tissue engineering applications. Nat Protoc. 2006;1(6):2753-8.
226. Shayegan M, Altindal T, Kiefl E, Forde NR. Intact Telopeptides Enhance Interactions between Collagens. Biophys J. 2016;111(11):2404-16.
227. Valero C, Amaveda H, Mora M, García-Aznar JM. Combined experimental and computational characterization of crosslinked collagen-based hydrogels. PLoS One. 2018;13(4):e0195820.
228. Prat-Vidal C, Rodríguez-Gómez L, Aylagas M, Nieto-Nicolau N, Gastelurrutia P, Agustí E, et al. First-in-human PeriCord cardiac bioimplant: Scalability and GMP manufacturing of an allogeneic engineered tissue graft. EBioMedicine. 2020;54:102729.

229. Garcia-Puig A, Mosquera JL, Jiménez-Delgado S, García-Pastor C, Jorba I, Navajas D, et al. Proteomics Analysis of Extracellular Matrix Remodeling During Zebrafish Heart Regeneration. Mol Cell Proteomics. 2019;18(9):1745-55.
230. Park JH, Lee JH, Lee SY, Choi JO, Shin MS, Kim MJ, et al. Normal 2-Dimensional Strain Values of the Left Ventricle: A Substudy of the Normal Echocardiographic Measurements in Korean Population Study. J Cardiovasc Ultrasound. 2016;24(4):285-93.
231. Antoine EE, Vlachos PP, Rylander MN. Review of collagen I hydrogels for bioengineered tissue microenvironments: characterization of mechanics, structure, and transport. Tissue Eng Part B Rev. 2014;20(6):683-96.
232. Composite Materials Handbook. In: Corporation MS, editor. Volume 3. Polymer matrix composites materials usage, design, and analysis.1997. p. 693.
233. Ambrosio L, De Santis R, Nicolais L. Composite hydrogels for implants. Proceedings of the Institution of Mechanical Engineers, Part H: Journal of Engineering in Medicine. 1998;212(2):93-9.
234. Ju H, Lee D, Kim JR, Kim KS. Maximum torsional reinforcement ratio of reinforced concrete beams. Structures. 2020;23:481-93.
235. Juliano TF, Forster AM, Drzal PL, Weerasooriya T, Moy P, VanLandingham MR. Multiscale mechanical characterization of biomimetic physically associating gels. Journal of Materials Research. 2006;21(8):2084-92.
236. Liparoti S, Sorrentino A, Speranza V, Titomanlio G. Multiscale mechanical characterization of iPP injection molded samples. European Polymer Journal. 2017;90:79-91.
237. Osidak EO, Kozhukhov VI, Osidak MS, Domogatsky SP. Collagen as Bioink for Bioprinting: A Comprehensive Review. Int J Bioprint. 2020;6(3):270.
238. Włodarczyk-Biegun MK, Del Campo A. 3D bioprinting of structural proteins. Biomaterials. 2017;134:180-201.
239. Hospodiuk M, Dey M, Sosnoski D, Ozbolat IT. The bioink: A comprehensive review on bioprintable materials. Biotechnol Adv. 2017;35(2):217-39.
240. Murphy SV, Skardal A, Atala A. Evaluation of hydrogels for bio-printing applications. J Biomed Mater Res A. 2013;101(1):272-84.
241. Isaacson A, Swioklo S, Connon CJ. 3D bioprinting of a corneal stroma equivalent. Exp Eye Res. 2018;173:188-93.
242. Vulpe R, Le Cerf D, Dulong V, Popa M, Peptu C, Verestiuc L, et al. Rheological study of in-situ crosslinkable hydrogels based on hyaluronanic acid, collagen and sericin. Materials Science and Engineering: C. 2016;69:388-97.
243. Djabourov M, Lechaire J-P, Gaill F. Structure and rheology of gelatin and collagen gels. Biorheology. 1993;30:191-205.
244. Yang Y, Chen X, Ding F, Zhang P, Liu J, Gu X. Biocompatibility evaluation of silk fibroin with peripheral nerve tissues and cells in vitro. Biomaterials. 2007;28(9):1643-52.
245. Liu B, Song Y-w, Jin L, Wang Z-j, Pu D-y, Lin S-q, et al. Silk structure and degradation. Colloids and Surfaces B: Biointerfaces. 2015;131:122-8.
246. Sapru S, Das S, Mandal M, Ghosh AK, Kundu SC. Nonmulberry silk protein sericin blend hydrogels for skin tissue regeneration - in vitro and in vivo. Int J Biol Macromol. 2019;137:545-53.
247. Cai H, Wu B, Li Y, Liu Y, Shi L, Gong L, et al. Local Delivery of Silk-Cellulose Incorporated with Stromal Cell-Derived Factor-1α Functionally Improves the Uterus Repair. Tissue Eng Part A. 2019;25(21-22):1514-26.
248. Mobaraki M, Ghaffari M, Yazdanpanah A, Luo Y, Mills DK. Bioinks and bioprinting: A focused review. Bioprinting. 2020;18:e00080.
249. Perea-Gil I, Gálvez-Montón C, Prat-Vidal C, Jorba I, Segú-Vergés C, Roura S, et al. Head-to-head comparison of two engineered cardiac grafts for myocardial repair: From scaffold characterization to pre-clinical testing. Sci Rep. 2018;8(1):6708.

250. Noor N, Shapira A, Edri R, Gal I, Wertheim L, Dvir T. 3D Printing of Personalized Thick and Perfusable Cardiac Patches and Hearts. Adv Sci (Weinh). 2019;6(11):1900344.
251. Chachques JC, Lila N, Soler-Botija C, Martinez-Ramos C, Valles A, Autret G, et al. Elastomeric cardiopatch scaffold for myocardial repair and ventricular support. European Journal of Cardio-Thoracic Surgery. 2020;57(3):545-55.
252. Pouliot RA, Link PA, Mikhaiel NS, Schneck MB, Valentine MS, Kamga Gninzeko FJ, et al. Development and characterization of a naturally derived lung extracellular matrix hydrogel. J Biomed Mater Res A. 2016;104(8):1922-35.
253. Buehler MJ. Nature designs tough collagen: explaining the nanostructure of collagen fibrils. Proc Natl Acad Sci U S A. 2006;103(33):12285-90.
254. Grinnell F. Fibroblast biology in three-dimensional collagen matrices. Trends Cell Biol. 2003;13(5):264-9.
255. Kobayashi N, Yasu T, Ueba H, Sata M, Hashimoto S, Kuroki M, et al. Mechanical stress promotes the expression of smooth muscle-like properties in marrow stromal cells. Exp Hematol. 2004;32(12):1238-45.
256. Camci-Unal G, Annabi N, Dokmeci MR, Liao R, Khademhosseini A. Hydrogels for cardiac tissue engineering. NPG Asia Materials. 2014;6(5):e99-e.
257. Kotini M, Barriga EH, Leslie J, Gentzel M, Rauschenberger V, Schambony A, et al. Gap junction protein Connexin-43 is a direct transcriptional regulator of N-cadherin in vivo. Nat Commun. 2018;9(1):3846.
258. Shinde AV, Humeres C, Frangogiannis NG. The role of α-smooth muscle actin in fibroblast-mediated matrix contraction and remodeling. Biochim Biophys Acta Mol Basis Dis. 2017;1863(1):298-309.
259. Dye BK, Butler C, Lincoln J. Smooth Muscle α-Actin Expression in Mitral Valve Interstitial Cells is Important for Mediating Extracellular Matrix Remodeling. J Cardiovasc Dev Dis. 2020;7(3).
260. Rahimnejad M, Rezvaninejad R, França R. Biomaterials in bone and mineralized tissue engineering using 3D printing and bioprinting technologies. Biomed Phys Eng Express. 2021;7(6).
261. Genova T, Roato I, Carossa M, Motta C, Cavagnetto D, Mussano F. Advances on Bone Substitutes through 3D Bioprinting. Int J Mol Sci. 2020;21(19).
262. Czarnek K, Terpiłowska S, Siwicki AK. Selected aspects of the action of cobalt ions in the human body. Cent Eur J Immunol. 2015;40(2):236-42.
263. Lerouge S, Huk O, Yahia LH, Sedel L. Characterization of in vivo wear debris from ceramic-ceramic total hip arthroplasties. J Biomed Mater Res. 1996;32(4):627-33.
264. Sykaras N, Iacopino AM, Marker VA, Triplett RG, Woody RD. Implant materials, designs, and surface topographies: their effect on osseointegration. A literature review. Int J Oral Maxillofac Implants. 2000;15(5):675-90.
265. Dong WP, Sullivan PJ, Stout KJ. Comprehensive study of parameters for characterising three- dimensional surface topography: III: Parameters for characterising amplitude and some functional properties. Wear. 1994;178(1):29-43.
266. Sedlaček M, Gregorčič P, Podgornik B. Use of the Roughness Parameters Ssk and Sku to Control Friction—A Method for Designing Surface Texturing. Tribology Transactions. 2017;60(2):260-6.
267. Chen J, Chen C, Chen Z, Li Q, Huang N. Collagen/heparin coating on titanium surface improves the biocompatibility of titanium applied as a blood-contacting biomaterial. J Biomed Mater Res A. 2010;95(2):341-9.
268. Guo Y, Su Y, Gu R, Zhang Z, Li G, Lian J, et al. Enhanced corrosion resistance and biocompatibility of biodegradable magnesium alloy modified by calcium phosphate/collagen coating. Surface and Coatings Technology. 2020;401:126318.
269. Fafenrot S, Grimmelsmann N, Wortmann M, Ehrmann A. Three-Dimensional (3D) Printing of Polymer-Metal Hybrid Materials by Fused Deposition Modeling. Materials (Basel). 2017;10(10).

270. Bozkurt Y, Karayel E. 3D printing technology; methods, biomedical applications, future opportunities and trends. Journal of Materials Research and Technology. 2021;14:1430-50.
271. Ma H, Li T, Huan Z, Zhang M, Yang Z, Wang J, et al. 3D printing of high-strength bioscaffolds for the synergistic treatment of bone cancer. NPG Asia Materials. 2018;10(4):31-44.
272. Yang C, Huan Z, Wang X, Wu C, Chang J. 3D Printed Fe Scaffolds with HA Nanocoating for Bone Regeneration. ACS Biomater Sci Eng. 2018;4(2):608-16.
273. Ahumada M, Jacques E, Calderon C, Martínez-Gómez F. Porosity in Biomaterials: A Key Factor in the Development of Applied Materials in Biomedicine. In: Martínez LMT, Kharissova OV, Kharisov BI, editors. Handbook of Ecomaterials. Cham: Springer International Publishing; 2019. p. 3503-22.
274. Zimina A, Senatov F, Choudhary R, Kolesnikov E, Anisimova N, Kiselevskiy M, et al. Biocompatibility and Physico-Chemical Properties of Highly Porous PLA/HA Scaffolds for Bone Reconstruction. Polymers (Basel). 2020;12(12).
275. Kuroda D, Niinomi M, Morinaga M, Kato Y, Yashiro T. Design and mechanical properties of new β type titanium alloys for implant materials. Materials Science and Engineering: A. 1998;243(1):244-9.
276. Chen Y, Frith JE, Dehghan-Manshadi A, Attar H, Kent D, Soro NDM, et al. Mechanical properties and biocompatibility of porous titanium scaffolds for bone tissue engineering. Journal of the Mechanical Behavior of Biomedical Materials. 2017;75:169-74.
277. Matta C, Szűcs-Somogyi C, Kon E, Robinson D, Neufeld T, Altschuler N, et al. Osteogenic differentiation of human bone marrow-derived mesenchymal stem cells is enhanced by an aragonite scaffold. Differentiation. 2019;107:24-34.
278. Mazzoni E, Mazziotta C, Iaquinta MR, Lanzillotti C, Fortini F, D'Agostino A, et al. Enhanced Osteogenic Differentiation of Human Bone Marrow-Derived Mesenchymal Stem Cells by a Hybrid Hydroxylapatite/Collagen Scaffold. Front Cell Dev Biol. 2020;8:610570.
279. Zhang T, Lin S, Shao X, Zhang Q, Xue C, Zhang S, et al. Effect of matrix stiffness on osteoblast functionalization. Cell Prolif. 2017;50(3).
280. Chawla S, Midha S, Sharma A, Ghosh S. Silk-Based Bioinks for 3D Bioprinting. Adv Healthc Mater. 2018;7(8):e1701204.
281. Cheng G, Wang X, Wu M, Wu S, Cheng L, Zhang X, et al. Insignificant Difference in Biocompatibility of Regenerated Silk Fibroin Prepared with Ternary Reagent Compared with Regenerated Silk Fibroin Prepared with Lithium Bromide. Polymers (Basel). 2022;14(18).

Chapter XIII. Appendices

Appendix A. Other publications and conference communications

DURING THE time that I have been working on this thesis, I have had the opportunity to collaborate with other researchers from both the Biophysics and Bioengineering Unit and other research groups. In this way, I have been able to learn and develop different techniques that have allowed me to participate as a co-author in other articles. In addition, I have also had the opportunity to present my work at several international congresses.

Other research articles:

- López-Alonso I, López-Martínez C, Martín-Vicente P, Amado-Rodríguez L, González-López A, Mayordomo-Colunga J, Del Busto C, Bernal M, Crespo I, Astudillo A, Arias-Guillén M, Fueyo A, Almendros I, Otero J, **Sanz-Fraile H**, Farré R, Albaiceta GM. *Mechanical Ventilation Promotes Lung Tumour Spread by Modulation of Cholesterol Cell Content.* Eur Respir J. 2022 Jul 21;60(1):2101470. **IF = 33.801. Q1 (02/66).**
- López-Mengual A, Segura-Feliu M, Sunyer R, **Sanz-Fraile H**, Otero J, Mesquida-Veny F, Gil V, Hervera A, Ferrer I, Soriano J, Trepat X, Farré R, Navajas D, Del Río JA. *Involvement of Cechanical Cues in the Migration of Cajal-Retzius Cells in the Marginal Zone During Neocortical Development*. Front Cell Dev Biol. 2022 May 16;10:886110. **IF = 6.081. Q1 (06/39).**
- Falcones B, **Sanz-Fraile H**, Marhuenda E, Mendizábal I, Cabrera-Aguilera I, Malandain N, Uriarte JJ, Almendros I, Navajas D, Weiss DJ, Farré R, Otero J. *Bioprintable lung extracelular matrix Hydrogels Scaffolds for 3D Culture of Mesenchymal Stromal Cells*. Polymers (Basel). 2021 Jul 18;13(14):2350. **IF = 4.967. Q1 (16/90).**
- Osuna A, Ulldemolins A, **Sanz-Fraile H**, Otero J, Farré N, Farré R, Almendros I. Experimental Setting for Applying Mechanical Stimuli to Study the Endothelial Response of Ex Vivo Vessels under Realistic Pathophysiological Environments. Life (Basel). 2021 Jul 8;11(7):671. **IF = 3.253. Q2 (39/94).**

International and national conferences:

Oral presentation "Development and Characterization of Extracellular Matrix Bioinks from Decellularized Porcine Hearts", at the World Congress of Biomechanics (WCB) 2022. (Taipei-Taiwan).

Co-author of the oral presentation "Association between the viscoelastic characteristics and sputum colour in patients with bronchiectasis", at the European Respiratory Society (ERS) 2022 (Barcelona-Spain), **abstract awarded** with "The Zambon award on NCFB"

Co-author of the poster presentation "Bacterial Nanocellulose-Reinforced Type I Collagen Hydrogels as Scaffolds for 3D Cell Culture", at the European Polysaccharide Network of Excellence (EPNOE) 2021 (Online Congress).

Poster presentation "Standardization of Viscoelasticity of Sputum from Bronchiectasis Patients", at the CIBERES 2021 (Online Congress).

Poster presentation "Non-Newtonian Fluid Properties of Sputum from Bronchiectasis Patients", at the American Thoracic Society (ATS) 2021. (Online Congress).

Poster presentation "3D Bioprinted Lung Extracellular Matrix Hydrogels as Scaffolds for Mesenchymal Stromal Cells Culture", at the Congreso Anual de la Sociedad Española de Ingeniería Biomédica (CASEIB) 2020 (Santander-Spain).

Co-author of the poster presentation "Carbon Nanotubes-incorporated Collagen Hydrogels for Soft Actuators 3D Bioprinting", at the WBC 2020.

Co-author of the poster presentation "Three-dimensional Decellularized Extracellular Matrix Hydrogels for Acute Lung Injury Modelling", at the WBC 2020.

Poster presentation "Development of 3D hydrogels from Decellularized Cardiac Porcine Hearts", at the WBC 2020.

Oral presentation "Development of Composite Silk-Collagen Hydrogels with Enhanced Mechanical Properties", at the World Biomaterials Congress (WBC) 2020. (Glasgow-Scotland)

Co-author of the poster presentation "3D Bioprinted Nanocomposite Collagen Hydrogels for Soft Actuators Development", at the CASEIB 2019.

Co-author of the poster presentation "Extracellular Matrix Bioengineered Hydrogels as Scaffolds for Acute Lung Injury 3D Modelling", at the CASEIB 2019.

Poster presentation "Silk-Collagen Hydrogels Development for the Biofabrication of Scaffolds with Increased Stiffnes", at the CASEIB 2019.

Poster presentation "Development and Characterization of Cardiac Bioinks from Decellularized Porcine Hearts", at the CASEIB 2019.

Appendix B. Step-by-step protocol for silk solubilization

THIS APPENDIX describes in detail the protocol for the solubilization of silk from *B. Mori* silkworm cocoons, which is the method used in chapter five of this thesis. Several protocols for silk extraction and solubilization have been published, but most of them use lithium bromide in high concentrations to promote protein solubility (280). However, this solvent is highly cytotoxic (281). Therefore, the protocol developed during my PhD studies uses only sodium hydroxide (NaOH) as a solvent, which is widely used as a neutralizer in the digestion of ECM-derived hydrogels.

MATERIALS

- *B. Mori* silkworm cocoons (AYARA Health, Yangon, Myanmar).
- MilliQ water.
- PBS 1X (Gibco, Massachusetts, cat. no. 10010-015).
- Sodium Hydroxide (Sigma, cat. no. 1310-73-2).
- Hydrochloric acid (Sigma, cat. no. 320331).

EQUIPMENT

- Micro-spoon (DD BioLab, cat. no. 076190).
- Dissecting scissors (Fisher Scientific, Fisherbrand model, cat. no. 15277168).
- Plastic Pasteur pipette (Sigma, cat. no. Z331740).
- 15 mL sterile Falcon tube (Corning, cat. no. 652095).
- 50 mL centrifuge tube (Sigma, cat. no. CLS430829).
- 10 µL pipette tips (Eppendorf, cat. no. 0030000854).
- 200 µL pipette tips (Eppendorf, cat. no. 0030000897).
- 1000 µL pipette tips (Eppendorf, cat. no. 0030000927).
- 0.5-10 µL micropipette (Eppendorf, cat. no. ES-10).
- 20-200 µL micropipette (Eppendorf, cat. no. ES-200).
- 100-1000 µL micropipette (Eppendorf, cat. no. ES-1000).
- pH-indicator strips (Sigma, cat. no. 1095350001).
- Analytical balance (PCE Instruments, Germany, PCE-BSH-6000).
- Freezer miller (Spex, 6775 model).
- Small grinding vial set (Spex, 6751 model).
- Cryo-Gloves (Tempshield, cat. no. MAMWP).
- Magnetic stirring bar, cylindrical (VWR, cat. no. 442-4520).
- Magnetic stirrer (Cimarec i, Poly 15 model, cat. no. 10145751).

PROCEDURE

1. **Cryomilling of *B. Mori* silkworm cocoons.**
   1.1. Cut cocoons with dissecting scissors into 0.5 x 0.5 cm.
   1.2. Open the small grinding vial and insert the cocoon pieces cut to cover a quarter of the vial (including the metal piece).
   1.3. Fill the freezer miller tank with liquid nitrogen. Close the top of the freezer miller (without inserting the vial) so that all internal components reach the same temperature as the liquid nitrogen.
   1.4. Reopen the top of the freezer miller and insert the small grinding vial with silk.
   1.5. Press the "Start" button. The protocol must be set with the following parameters:
      1.5.1. PRE-COOL: 2
      1.5.2. RUN TIME: 6:00
      1.5.3. COOL-TIME: 1
      1.5.4. CYCLES: 1
      1.5.5. RATE: 10 CPS
   1.6. When the cycle is complete, open the top of the freezer miller, remove the small grinding vial with cryo-gloves, and place the vial in water to temper it.
   1.7. Open the vial and use the micro-spoon to scoop out the silk powder and place it in a 50 mL centrifuge tube.
   1.8. Repeat the above steps until all cocoons are cryomilled.
2. **Solubilization of silk.**
   2.1. Take the desired amount of silk powder and place it in a new 50 mL centrifuge tube.
   2.2. Use a 100-1000 micropipette with a 1000 µL tip to add 1 mL of sodium hydroxide 1M per 100 mg of silk powder.
   2.3. Using a plastic Pasteur pipette, make an up-and-down motion into the tube.
   2.4. Insert a magnetic stirring bar (3 mm in diameter and 6 mm length) into the 50 mL tube, close the tube and place it on the magnetic stirrer at 450 rpm until the silk dissolves macroscopically (usually less than 1 hour).
3. **Neutralization.**
   3.1. When the silk is dissolved, neutralize the solution with hydrochloric acid 2M (0.45 µL per 1 mL of solution).
   3.2. Finish the neutralization adjustment by checking the pH of the solution with a pH-indicator strip (pH ≈ 7.4).
   3.3. Once neutralization is complete, take the desired amount to use the silk as reinforcement in a pregel.

Appendix C. Step-by-step protocol for porcine-derived hydrogel development

THIS APPENDIX describes in detail the protocol for obtaining a cardiac extracellular matrix derived hydrogel from porcine myocardia. This protocol is based on the one published by Becker M. *et al.* (69), which works with myocardium from human hearts. This protocol was stablished in the laboratory during my PhD studies, and it was implemented in the laboratory by me.

MATERIALS

- MilliQ water.
- PBS 10X (Gibco, Massachusetts, cat. no. 70011044).
- PBS 1X (Gibco, Massachusetts, cat. no. 10010-015).
- Sodium Hydroxide (Sigma, cat. no. 1310-73-2).
- Hydrochloric acid (Sigma, cat. no. 320331).
- Tris (Bio-Rad, cat. no. 1610719).
- Ethylenediaminetetra-acetic acid (EDTA) (VWR Chemical, cat. no. 20294.294).
- Sodium dodecyl sulfate (SDS) (Sigma, cat. no. 75746).
- Fetal Bovine Serum (FBS) (Gibco, cat. no. 10270106).
- Pepsin from porcine gastric mucosa, ≥2500 unit/mg (Sigma, cat. no. P7012-250MG)

EQUIPMENT

- Micro-spoon (DD BioLab, cat. no. 076190).
- Precision tweezers (BIONIC, cat. no. 91197-00)
- Dissecting scissors (Fisher Scientific, Fisherbrand model, cat. no. 15277168).
- Plastic Pasteur pipette (Sigma, cat. no. Z331740).
- 15 mL sterile Falcon tube (Corning, cat. no. 652095).
- 50 mL centrifuge tube (Sigma, cat. no. CLS430829).
- Polypropylene beaker 1000 mL (Kartell, cat. no. 0180800).
- 10 µL pipette tips (Eppendorf, cat. no. 0030000854).
- 200 µL pipette tips (Eppendorf, cat. no. 0030000897).
- 1000 µL pipette tips (Eppendorf, cat. no. 0030000927).
- 0.5-10 µL micropipette (Eppendorf, cat. no. ES-10).
- 20-200 µL micropipette (Eppendorf, cat. no. ES-200).
- 100-1000 µL micropipette (Eppendorf, cat. no. ES-1000).
- 5 mL serological pipette (Corning, cat. no. CLS4487).

- Pipette controller (Corning, cat. no. CLS4099).
- pH-indicator strips (Sigma, cat. no. 1095350001).
- Analytical balance (PCE Instruments, Germany, PCE-BSH-6000).
- Freeze-dryer (Telstar, LyoQuest model).
- Freezer miller (Spex, 6775 model).
- Small grinding vial set (Spex, 6751 model).
- Cryo-Gloves (Tempshield, cat. no. MAMWP).
- Magnetic stirring bar, cylindrical (VWR, cat. no. 442-4520).
- Magnetic stirrer (Cimarec i, Poly 15 model, cat. no. 10145751).
- Orbital shaker (IKA KS, 130 basic model, cat. no. Z341800).
- Cryostat (Thermo, HM 560 model).
- Embedding matrix for frozen sections (OCT) (CellPatch, cat. no. KMA-0100-00A).
- Centrifuge (Heraeus Instruments, Labofuge 400R model).
- Vortex (Scientific Industries, Vortex-Genie 2 model).
- Scalpel (Swann Morton, cat. no. 0206).
- Scalpel no. 20 blade (Swann Morton, cat. no. 0306).
- 6-well cell culture plates (Corning, cat. no. 3506).

PROCEDURE

1. **Preparation of porcine left myocardium for cryosectioning.**
   1.1. Collect the whole heart from a local slaughterhouse.
   1.2. Wash the heart with de-ionized water before freezing them at -80 ˚C for at least one overnight for storage and to aid in cell lysis.
   1.3. Slowly thaw the heart (from -80 ˚C to 4 ˚C) and dissect the left myocardium with a scalpel with a no. 20 blade.
   1.4. Once the left myocardium has been dissected, it is cut into 1 x 1 x 1 cm cubes and placed in the wells of 6-well cell culture plates.
   1.5. Store the 6-well cell culture plates containing the cubes at (-80 ˚C). The tissue can be stored for several months, until the cryosectioning.
2. **Cryosectioning of the left myocardium cubes into slices.**
   2.1. The day before cryosectioning, place 6 empty 50 mL tubes at -80 ˚C (6 tubes per each 6-well plate to be cryosectioned).
   2.2. Set the object and chamber temperature of the cryostat (-21 ˚C and -19 ˚C, respectively).
   2.3. Place the precision tweezer inside the cryostat.
   2.4. Transfer six empty tubes and one 6-well plate from the freezer to the cryostat.
   2.5. Fix a left myocardial cube on the cold stamp with OCT.
   2.6. Set the cryostat to 300 µm.
   2.7. Start the cryosectioning of the left myocardial cube in 300 µm slices.
   2.8. Take each slide with the cold precision tweezer and place it in a 50 mL cold tube.
   2.9. Cut the entire left myocardial cube into slices and place them all in the same 50 mL tube. **IMPORTANT**: If the tube fills up and you have not finished slicing the left myocardial cube, do not squeeze the slices to fit more; use a new tube.

2.10. When the entire left myocardial cube is cryosectioned, close the 50 mL tube and store it at -80 ˚C until the decellularization steps are initiated.

2.11. Repeat the steps from 2.5 to 2.9 for every left myocardial cube.

3. Decellularization of porcine myocardium slices.

3.1. Take six 50 mL tubes from the -80 ˚C freezer for each decellularization protocol you wish to begin.

3.2. Add 300 mL of lysis solution (10 mM Tris, 0.1% w/v EDTA, pH 7.4 in dH2O) to a 1000 mL beaker. **IMPORTANT**: 300 mL of lysis solution in 1000 mL beaker will work properly with six 50 mL tubes filled with heart slides. To decellularize more tubes, use multiple beakers containing the same amount of solution.

3.3. Transfer the slices from the six 50 mL tubes to the beaker and shake it for 2 hours at room temperature (160 rpm).

3.4. Transfer the slices to a new beaker containing 300 mL of 0.5% SDS in PBS and shake it for 6 hours at room temperature (160 rpm).

3.5. Strain the solution and wash the slices three times with 300 mL PBS for 10 minutes each while shaking at room temperature (160 rpm).

3.6. Leave the slices in PBS at 4 ˚C overnight while shaking (160 rpm). **IMPORTANT**: Steps 3.1 through 3.6 should be performed on the same day.

3.7. Discard the PBS and transfer the slices to a new beaker containing 150 mL of FBS at 37 ˚C.

3.8. Incubate the slices for 3h at 37 ˚C.

3.9. Discard FBS and wash the slices three times with 300 mL PBS for 10 minutes each while shaking at room temperature (160 rpm).

3.10. Transfer the slices decellularized to a 15 mL tube and store it at -80 ˚C until the freeze-drying process begins. **IMPORTANT**: Do not fill the 15 mL tube more than three-quarters full. Use as many 15 mL tubes as needed.

4. Freeze-drying

4.1. Transfer the 15 mL tubes of decellularized heart tissue from the -80 ˚C freezer to a freeze dryer and allow the tubes to freeze dry for 48 hours.

4.2. After 48 hours, store the 15 mL tubes of freeze-dried decellularized heart tissue at -80 ˚C until the cryomilling process begins.

5. Cryomilling

5.1. Take out the decellularized tissue from the -80 ˚C and cut each sponge into small pieces with dissecting scissors into ≈0.5 x 0.5 cm cubes.

5.2. Open the small grinding vial and insert the heart pieces cut to cover a quarter of the vial (including the metal piece).

5.3. Fill the freezer miller tank with liquid nitrogen. Close the top of the freezer miller (without inserting the vial) so that all internal components reach the same temperature as the liquid nitrogen.

5.4. Reopen the top of the freezer miller and insert the small grinding vial containing the freeze-dried heart.

5.5. Press the "Start" button. The protocol must be set with the following parameters:

5.5.1. PRE-COOL: 1

5.5.2. RUN TIME: 5:00
5.5.3. COOL-TIME: 1
5.5.4. CYCLES: 1
5.5.5. RATE: 10 CPS

5.6. When the cycle is complete, open the top of the freezer miller, remove the small grinding vial with cryogenic gloves, and place the vial in water to temper it.
5.7. Open the vial and use the microspoon to scoop out the cardiac ECM (cECM) powder and place it in a 50 mL centrifuge tube.
5.8. Repeat the above steps until all freeze-dried decellularized cardiac slice sponges are cryomilled.
5.9. Store the powder at -80 ˚C until the digestion protocol is initiated.

6. Enzyme based digestion of cECM powder.

6.1. Take out the powder from the freezer and place the required amount (for a concentration of 20 mg/mL) in a 50 mL tube. To do so, tare a balance with the empty tube and add powder until the desired weight is reached. For example, to obtain 5 mL of final pregel, weigh 100 mg of powder.
6.2. Tare the balance again and add pepsin from porcine gastric mucosa to a concentration of 10% w/w. For example, if you used 100 mg of cardiac powder, add 10 mg of pepsin.
6.3. Use pipette controller with a 5 mL serological pipette to add 5 mL of hydrochloric acid 0.1M.
6.4. Using a plastic Pasteur pipette, make an up-and-down motion into the tube.
6.5. Insert a magnetic stirring bar (3 mm in diameter and 6 mm length) into the 50 mL tube, close the tube and place it on the magnetic stirrer at 450 rpm for 48 hours at room temperature.

7. Neutralization of the digestion and hydrogel development.

7.1. Stop magnetic stirring. **TIP**: The following steps show the neutralization protocol. It is advisable to neutralize in 1 mL aliquots because some of the initial 5 mL solution will have evaporated in the exothermic process created with the hydrochloric acid and there will be less of the initial amount.
7.2. Using a 100-1000 micropipette with a 1000 µL tip, transfer 1 mL of the pepsin digested solution to a 15 mL tube.
7.3. Add 1/9 of cold 10X PBS (pH 7.4). Example: To neutralize 1 mL of pepsin digested solution, add 111 µL of 10X PBS.
7.4. Add 1/8 of cold 1M NaOH. Example: To neutralize 1 mL of pepsin digested solution, add 125 µL of 1M NaOH.
7.5. Vortex the tube containing the solution.
7.6. Complete the neutralization adjustment by checking the pH of the solution with a pH-indicator strip (pH ≈ 7.4).
7.7. Mix the final volume of neutralized solution with 1X culture media with suspended cells (or 1/10 of cold PBS for acellular hydrogels) and introduce it into the desired mold at 37 ˚C, 5% CO_2 and 21% O_2 for 60 minutes.

Appendix D. Implementation of rheological measurements

RHEOLOGICAL MEASUREMENTS were first implemented and established in the laboratory by me during my PhD studies. Through a collaboration with the pneumology team at the Hospital Clinic (Prof. Antoni Torres), we had access to a HAAKE RheoStress 1 rheometer (ThermoFisher, Massachusetss, United States). The rheometer was recently purchased had not been used when I set it up to characterize both the rheology of hydrogels and physiological samples for the Pneumology group, in a collaboration that is still active today. Here I explain how to characterize extracellular matrix-derived hydrogels using the rheometer's software (RheoWin).

All tests were performed by loading the sample onto a Peltier plate set at 37 ˚C when a hydrogel is characterized or at 4 ˚C when a pregel is characterized. In addition, all tests were performed by oscillatory testing with a 35 mm serrated parallel plate geometry.

Oscillatory frequency sweep.

To select a measurement frequency within the viscoelastic range of the hydrogel, it is important to analyze the values of the storage modulus (G') and the loss modulus (G') by performing an oscillatory frequency sweep test. For this purpose, a test is carried out with the following values:

- Gap: 1 mm
- Strain: 0.5 % ± 0.025 %
- Frequency start: 0.1 Hz (0.6283 rad/s).
- Frequency end: 100 Hz (628.3 rad/s).
- Temperature: 37 ˚C.
- Break criteria: No

The end of the linear viscoelastic region can be found when G' decreases by 5% from the initial value.

Oscillatory amplitude sweep.

Once the ideal frequency within the viscoelastic region is obtained (X), an oscillatory amplitude sweep test is performed to obtain the rheological properties of the characterized hydrogel.

- Gap: 1 mm
- Strain start: 0.1 % ($5.71 \cdot 10^{-5}$ rad).
- Strain end: 1000 % (0.5714 rad).

- Frequency: X Hz (X rad/s). **NOTE**: X is the value obtained in the previous test.
- Temperature: 37 ˚C.
- Break criteria: No

Analysis of gelation kinetics of ECM-derived hydrogels.

One of the most important properties when characterizing a bioink is its printability. For this purpose, it is essential to start the analysis in the pregel state and to perform the rheological characterization of the entire gelation process.

1. Rheological measurement in the pregel state
   1.1. Temperature: 4 ˚C.
   1.2. Gap: 0.2 mm
   1.3. Strain: 0.5 % ± 0.1250 %.
   1.4. Frequency: 0.1 Hz (0.6283 rad/s).
   1.5. Duration: 600 s.
   1.6. Break criteria: No.
2. Analysis of gelation kinetics
   2.1. Temperature: 37 ˚C
   2.2. Gap: 0.2 mm
   2.3. Strain: 0.5 % ± 0.1250 %.
   2.4. Frequency: 0.1 Hz (0.6283 rad/s).
   2.5. Duration: 1200 s. **NOTE**: Longer times may affect mechanical properties due to water evaporation.
   2.6. Break criteria: No

IMPORTANT: All the above steps must be performed during the same test; with no pause in between.